Max-Planck-Institut für Physik komplexer Systeme Dresden

Mesoscopic wave phenomena in electronic and optical ring structures

der Fakultät für Mathematik und Naturwissenschaften
der Technischen Universität Dresden vorgelegte

Dissertation

zur Erlangung des
Doktorgrades der Naturwissenschaften
(Doctor rerum naturalium)

vorgelegt von

Martina Hentschel

geboren am 5.11.1971 in Dresden

Dresden 2002

Eingereicht am 12. Juli 2001

1. Gutachter: Prof. Dr. Klaus Richter

2. Gutachter: Prof. Dr. Peter Fulde

3. Gutachter: Prof. Dr. Matthias Brack

Verteidigt am 29. Oktober 2001

Abstract

In this work we investigate wave phenomena in mesoscopic systems using different theoretical approaches. In Part I, we focus on effectively one-dimensional electronic ring structures and address the phenomenon of geometric phases in spin-dependent electronic transport in the presence of non-uniform magnetic fields. In the general non-adiabatic case, exact solutions of the Schrödinger equation are used in a transfer matrix formalism to compute the transmission probability through the ring. In the magneto-conductance we identify clear signatures of interference effects due to geometric phases, for example in rings where the non-uniform field is created by a central micromagnet. For the special case of an in-plane magnetic field we predict an interesting spin-flip effect that allows one to control the spin polarization of electrons by applying an external Aharonov-Bohm flux. Optical mesoscopic systems are the subject of Part II. We consider two-dimensional annular structures characterized by different refractive indices, and apply classical methods from geometric optics as well as wave concepts based on Maxwell's equations. For the first time, an S-matrix approach is successfully employed in the description of resonances in optical microresonators; in particular we propose the dielectric annular billiard as an attractive model system. Comparing ray and wave pictures, we find general agreement, except for large wavelengths of the order of the system size, where corrections to the ray model are necessary. The Goos-Hänchen effect as an extension of the ray picture is shown to quantitatively account for wave modifications of Fresnel's laws due to curved interfaces. We derive novel analytical expressions for the corrected Fresnel formulas for both polarizations of light. Motivated by the successful ray description, we give a conclusive interpretation of a recent filter experiment on a quadrupolar glass fibre, and suggest novel concepts for microresonator-based lasers.

Kurzfassung

Gegenstand dieser Arbeit sind Wellenphänomene in mesoskopischen Ringstrukturen. In Teil I der Arbeit befassen wir uns mit spinabhängigem Transport von Elektronen in effektiv eindimensionalen Ringen in Gegenwart inhomogener Magnetfelder. Wir benutzen die exakten Lösungen der Schrödinger-Gleichung im allgemeinen nicht-adiabatischen Fall in einem Transfer-Matrix-Formalismus und untersuchen Auswirkungen von geometrischen Phasen auf den Magnetwiderstand. Für den Spezialfall eines Magnetfeldes in der Ringebene sagen wir einen interessanten Spin-Flip-Effekt vorher, der die Steuerung der Polarisationsrichtung von Elektronen über einen externen Aharonov-Bohm-Fluß erlaubt. Optische mesoskopische Systeme sind Thema von Teil II dieser Arbeit. Wir betrachten zweidimensionale annulare Strukturen, charakterisiert durch unterschiedliche Brechungsindizes, sowohl im klassischen Bild der geometrischen Optik als auch mit Wellenmethoden auf der Grundlage der Maxwellschen Gleichungen. Insbesondere diskutieren wir erstmals eine Streumatrixbeschreibung optischer Mikroresonatoren und wenden sie auf das dielektrische annulare Billard an. Ein Vergleich der Ergebnisse des Wellen- und Strahlenbildes liefert eine gute Übereinstimmung, jedoch sind im Grenzfall großer Wellenlängen von der Ordnung der Systemabmessungen Korrekturen zum Strahlenbild nötig. Wir zeigen am Beispiel von Fresnel-Gesetzen für gekrümmte Oberflächen erstmals, daß der Goos-Hänchen-Effekt diese Korrekturen quantitativ erfaßt. Ausgehend von der Wellenbeschreibung leiten wir neue analytische Formeln für verallgemeinerte Fresnel-Gesetze für beide möglichen Polarisationsrichtungen ab. Die Anwendung des Strahlenbildes erlaubt eine schlüssige Interpretation eines Experiments mit einer quadrupolaren Glasfaser, außerdem schlagen wir Strahlenkonzepte als Grundlage der Konstruktion von Mikrolasern mit maßgeschneiderten Charakteristika vor.

Contents

1 **Mesoscopic ring structures** 7

Part I – Spin-dependent electronic transport in non-uniform magnetic fields 9

2 **Introduction** 11
- 2.1 Geometric phases 11
- 2.2 Electronic mesoscopic systems and interference phenomena 13

3 **Geometric phases in one-dimensional mesoscopic rings** 17
- 3.1 Model system and Hamiltonian 17
- 3.2 Magnetic field configurations and corresponding eigenstates 18
- 3.3 Geometric vector potential $\vec{A}_g$ 21
- 3.4 Adiabatic case 22
  - 3.4.1 Effective Hamiltonian for orbital motion 23
  - 3.4.2 Eigenstates and Berry phase 24
- 3.5 Non-adiabatic case 26

4 **Ballistic quantum transport** 33
- 4.1 Spinless transport 33
  - 4.1.1 Transfer and scattering matrices 33
  - 4.1.2 Transmission probability 35
  - 4.1.3 Aharonov-Bohm oscillations in a 1d ring 37
- 4.2 Spin-dependent transport 39
  - 4.2.1 Transmission probability 39
  - 4.2.2 Transfer matrices 42
- 4.3 Uniform field perpendicular to the ring as limiting case 48
- 4.4 Transformations in spin space and symmetries of the transmission matrix 52

5 **Transmission in non-uniform magnetic fields: Examples** 55
- 5.1 In-plane magnetic field 55
  - 5.1.1 Aharonov-Bohm ring as a spin switch 55
  - 5.1.2 Averaged transmission probabilities 61
  - 5.1.3 Comparison with a two-dimensional model 68
  - 5.1.4 Limiting situations: Adiabatic and diabatic regime 69
- 5.2 Central micromagnet 70

Part II – Chaos and regularity in optical systems 79

6 **Introduction** 81
- 6.1 Quantum chaos 81
- 6.2 Optics 82
- 6.3 Fusion: Chaotic light 83

7 Ray and wave description of the open dielectric disk 87
7.1 Ray picture: Classical billiards with total internal reflection 87
7.1.1 Billiards in terms of Poincaré's surface of section 87
7.1.2 Total internal reflection and Fresnel's law 91
7.2 Wave picture: From Maxwell to Schrödinger 93
7.2.1 Maxwell's equations for the dielectric disk 93
7.2.2 Eigenvalues of the closed disk 97
7.2.3 Quasibound states of the dielectric disk 99
7.3 Scattering approach to the dielectric disk 102
7.3.1 Scattering matrix 102
7.3.2 Wigner delay time 104
7.3.3 Comparison of wave-based methods 107
7.4 Quantum – classical correspondence: Ray versus wave picture 110

8 Fresnel laws at curved interfaces 117
8.1 Extending the ray picture: Goos-Hänchen shift 117
8.2 Description of narrow resonances in the wave picture 123

9 Ray-wave correspondence in the dielectric annular billiard 131
9.1 Classical and dielectric annular billiard: Ray picture 131
9.2 Dielectric annular billiard in the wave picture 133
9.2.1 Scattering matrix 133
9.2.2 Concentric case and exact solution 138
9.2.3 Eccentric case: Perturbation of whispering gallery modes 141
9.3 Correspondence of ray and wave picture beyond whispering gallery modes 147
9.3.1 Dielectric ring embedded in air 147
9.3.2 Eccentric dielectric inclusion in a lower-index coating 151
9.3.3 Open problems 158

10 Achievements of the ray model in microcavities: Examples 159
10.1 Multiple beam interference in a quadrupolar glass fibre 159
10.2 Microlaser in the ray picture 167

11 Summary & Outlook 173

Appendix 177
A Conserved quantities in a closed ring 177
B Electrons in a closed ring and Aharonov-Bohm effect 177
C Magnetic field of a bar magnet 179
D Parabolic cylinder functions 184

Bibliography 185

1 Mesoscopic ring structures

Wave phenomena in ring-like structures receive a lot of interest both in theoretical and experimental physics. The reason for this are the special properties of these systems. On one hand, a ring is formed if we concatenate both ends of a line – we obtain an (effective) one-dimensional system with periodic boundary conditions. On the other hand, we can cut a hole into a disk – resulting in a two-dimensional system of changed topology: for example, a loop or closed curve enclosing the hole cannot be contracted to a point. Such spaces are said to be non-singly connected. This special topology is, of course, also present in one-dimensional rings that we can understand as the zero-width limit of two-dimensional rings. In Part I of this work we will study electrons in such an one-dimensional ring, an example where both aspects, periodic boundary conditions and special topology, are relevant. In contrast, in Part II we will investigate the dielectric annular billiard as a system where the two-dimensional character is of importance.

Physical phenomena depend fundamentally on the topology. Famous examples of these topological effects are the Aharonov-Bohm effect [1] or Berry's phase [2], that we will discuss in detail in Part I. However, the property of ring structures to constitute a system with periodic boundary conditions is likewise important, and used in a great variety of systems. The evolution of sand ripples under a water shear flow is experimentally investigated in an annular channel where a continuous flow is easily realized [3]. Electrons confined to a ring will, under suitable conditions, may travel without dissipation, giving rise to persistent currents [4]. A light ray tracing its path near the outer boundary of a glass ring will do so forever if we assume that it is subject to (perfect) total internal reflection, and the ring is wide enough to avoid intersection with the hole boundary. Then we could even fill the hole, obtaining a glass *disk*, without changing the ray dynamics. On the contrary, if we increase the size of the hole, the ray path eventually will be affected.

We have to keep in mind the huge difference in size of physically interesting ring systems. The annular channel in the sand ripple experiment [3] has a diameter of $30\,cm$, and glass disks or lenses used in ray optics experiments have a size of typically several cm. However, throughout this work we will investigate systems orders of magnitude *smaller* than this – so-called *mesoscopic systems* with typical dimensions in the μm-scale. Here, the physical properties are no longer described by classical physics alone, and *wave corrections*, stemming from quantum mechanics in electronic systems or from Maxwell's electromagnetism for light, are of importance. The rich interplay of classical and quantum effects is an important ingredient to the relatively young fields of *mesoscopic physics* and *quantum chaos*. In the present work we will study electronic and optical mesoscopic systems that represent examples of ring structures.

The dynamics of (non-relativistic) electrons in a narrow (one-dimensional) ring subject to an inhomogeneous magnetic field is considered in Part I of the thesis. The electron dynamics is governed by the Schrödinger equation with an additional Zeeman term that describes the interaction between the spin of the electron and the magnetic field. This can lead to *geometric phases* [8], and their appearance and consequences for electronic transport through one-dimensional ballistic rings are investigated throughout Part I.

Optical, or dielectric, two-dimensional mesoscopic systems, so-called microcavities, are the subject of Part II. The theoretical basis for the description of light, i.e., electromagnetic waves, is provided by Maxwell's equations. We will discuss the formal relation between electromagnetism and quantum mechanics. The crucial difference is the *energy-dependence* of the potential, which has large implications – e.g., states to different energy cannot be discussed using the same potential. For fixed energy, the potential depends on the refractive indices of the involved materials, and variation of their ratio allows one to control the openness of the system. Planck's constant $\hbar$, which does not occur in the description of electromagnetism, has to be given some meaning when discussing light in terms of quantum mechanics, and we will refer to this issue in Part II.

Many phenomena inherent to mesoscopic and semiclassical physics as well as to quantum chaos have been observed in both electronic and optical systems, as for example the scarring of wave functions along classically unstable periodic paths in open quantum dots and billiard systems, see e.g. [5, 6]. We postpone further introductory remarks to the detailed introductions given in each of the two parts. In particular, we will explain the phenomenon of geometric phases in the beginning of Part I that comprises Chapters 2 - 5. An introduction to mesoscopic optical systems as well as classical geometric optics constitutes the beginning of the second part with Chapters 6 - 10. Subsequent to this, a summary of both parts and an outlook are given in Chapter 11.

Part I:

SPIN-DEPENDENT ELECTRONIC TRANSPORT IN NON-UNIFORM MAGNETIC FIELDS

2 Introduction

2.1 Geometric phases

The first predictions of geometric or topological phases that probe *geometric* rather than dynamical properties of a given system were made by M. V. Berry [2] in 1984, and by Y. Aharonov and J. Anandan [7] in 1987. Geometric phases were first investigated in time-dependent quantum mechanical systems described by a Hamiltonian $H(t)$ where, under certain conditions, they can exist together with the familiar *dynamical phase* $\sim \exp\left(-\frac{i}{\hbar}\int H(t)dt\right)$. The concept of geometric phases was not only successfully applied to various quantum systems, but also allowed a new interpretation of well-known classical phenomena like Foucault's pendulum. Geometric phases provide a profound insight into the geometric and topological peculiarities of a system. One of the first examples where geometric phases were investigated is the cyclic adiabatic evolution of the electron spin in a non-uniform magnetic field – and it is precisely this example that gave the motivation for this first part of the present work, with the goal to explain and guide the experimental verification of geometric phases in magnetotransport measurements in mesoscopic rings.

Notably, the phenomenon of geometric phases can be understood well in familiar settings like classical parallel transport on the sphere. The situation is illustrated in Fig. 2.1a. A pencil (or arrow) is transported on a sphere from the north pole to the equator along a certain longitude and always pointing southwards. Keeping this direction ("parallel transport") we follow the equator and eventually return to the north pole thus *closing the loop.* Although the arrow *always* pointed to the south, we find its final position rotated by an angle γ with respect to (w.r.t.) its initial orientation, see Fig. 2.1a. The size of this angle γ depends on the loop chosen – it will be the larger the further we travel along a meridian. We find that the orientation of the arrow or, more generally, of some variable does *not return to its original value after one round cycle* – this geometric phenomenon is referred to as *anholonomy.* The change in the direction of swing in Foucault's pendulum after one rotation of the earth belongs to this class, as well as phenomena related to *quantum parallel transport.* One way to realize quantum parallel transport is *adiabaticity*, that is, slow change. The variables subject to cyclic evolution are parameters in the Hamiltonian of the system, for example a (non-uniform) magnetic field as shown in Fig. 3.1. The adiabatic theorem [9] guarantees that the system returns to its original state (the north pole in the example above) but it usually acquires a geometric phase as a manifestation of anholonomy. Hence, cyclic, adiabatic evolution and an anholonomic environment are the conditions under which we expect geometric phases to exist[1].

Berry phases have been observed in optical systems, in the context of nuclear magnetic resonance, and in molecular and atomic physics. They are anticipated to be generated in the dynamic quantum Zeno effect [20] and have been suggested as a means for quantum computation [21]. Geometric phases appear as a universal feature in dynamic Jahn-Teller systems [19] and can induce persistent currents in mesoscopic rings [32]. Many phenomena like the writhe of a

---

[1] The conditions of adiabaticity and cyclic evolution can in principle be relaxed, see [7, 8].

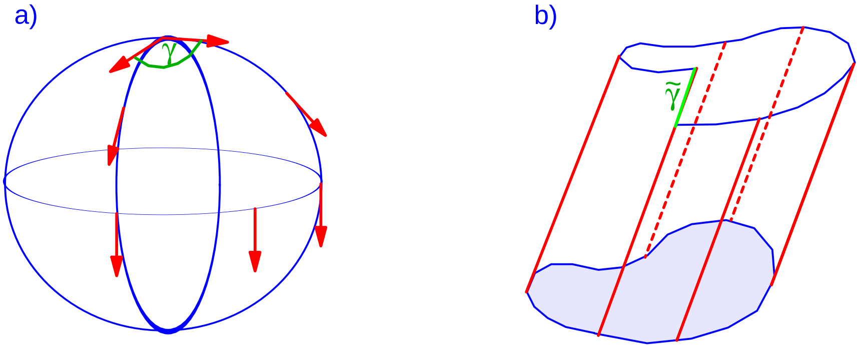

Figure 2.1: Concept of geometric phases. a) A classical vector transported along a closed loop on a sphere has changed its orientation after one round cycle. b) The concept of projective space and the appearance of geometric phases in this picture, see text for details.

polymer [10] are now explained in terms of geometric phases, and it is hard to distinguish between classical and quantum geometric phases [8]. In experiments with polarized light in coiled optical fibres a change in the direction of linear polarized light is measured [14], typically by interference or filtering. Other experiments are performed with polarized neutrons in a varying magnetic field [13]. However, experiments with the electron spin subject to an inhomogeneous magnetic field are not yet found in this line, partly because the condition of adiabaticity is hard to achieve with present experimental arrangements.

There had been indications for the existence of geometric phases before 1984 and furthermore, well-known optical effects have experienced a new interpretation in the last years. One example is the *Gouy phase shift* [12], found by Gouy in 1890. It is an additional 180° phase shift that all waves (including electromagnetic and sound waves) passing through a focus acquire in comparison with a plane wave. Its recent interpretation as geometric or Berry phase is based on a cyclic parameter as usual, namely the complex wave front radius of curvature associated with a Gaussian beam [12]. In 1955 Pancharatman [11] considered the phase shift in a beam of coherent linearly polarized light subject to a sequence of polarization changes. He found a contribution that was determined by the geometry of the cycle on the Poincaré sphere, the so-called Pancharatnam phase.

We would like to finish this introduction to geometric phases with two remarks on their mathematical description. First, there is a classical analogue of the quantal phase factor, namely Hannay's angle that describes the *additional* shift in the classical adiabatic angle variables after one closed cycle of evolution. It is semiclassically related to the quantum geometric phase [15]. The other point concerns the relation to topology and differential geometry. The concept of *projective spaces* was successfully applied to quantum mechanics – a flavour is given in Fig. 2.1. The lower closed loop represents a cycle in quantum mechanical state space (or *projective* Hilbert space) [17]. The corresponding Hilbert space is a fibre bundle over the state space, symbolized by the parallel lines. Without going further into details we just state that the trajectory in Hilbert space (the so-called horizontal lift) does not have to be closed as indicated by the offset $\tilde{\gamma}$ [18]. Finally, we mention that the Berry phase can be thought of resulting from a geometric vector potential, an idea that we will deepen and exploit later on. It is based on the concept of gauge transformations that is well-known from quantum field theory. In differential geometry, the geometric vector potential is called a *connection*. The geometric phase then results as the *curvature* of the connection. This approach emphasizes yet again the geometric nature of Berry and related phases.

Throughout this work we shall use the notations "geometric" and "topological" phase synonymously and reserve the term Berry phase for geometric phases in adiabatic situations. Geometric phases in non-adiabatic regimes are sometimes referred to as Aharonov-Anandan phases.

2.2 Electronic mesoscopic systems and interference phenomena

Many efforts have been made to prove the existence of topological phases in experiments, and as stated above these were successful in many cases. However, clear experimental verification of the paradigmatic Berry phase that electrons acquire upon adiabatic evolution in a non-uniform magnetic field remains to be found [25]. The latest developments in experimental techniques raise hope that this gap will soon be filled. The first part of this thesis is devoted to the theoretical description of quantities accessible to experiments that furthermore lead to the prediction of a spin-flip effect not known so far.

Recent advances in the field of semiconductor heterostructures have allowed for the fabrication of two-dimensional model systems containing high mobility electrons [22]. The idea is to combine two layers of semiconductor material (like, e.g., GaAs and AlGaAs or InAs and AlInAs) into a heterostructure with the resulting band structure allowing for movement of the charge carriers in two dimensions only. These so-called two-dimensional electron gases (2DEG) have opened a large field of experimental research. Microelectronic devices of all kinds are based on these semiconductor heterostructures. Both well-known as well as new effects found in those systems are under theoretical and experimental investigation. One example is the quantum Hall effect [23], another one a possible metal insulator transition [24]. Of particular interest w.r.t. the present work are experiments on Berry phase effects in these electronic systems [25, 35]. However, the results are not yet fully conclusive and are still under debate. Having in mind the successful detection of geometric phases in other systems opens the field to accompanying theoretical investigations aimed at identifying experimentally accessible signatures of geometric phases.

Let us return to the electrons in a 2DEG. In the absence of impurities that would cause electron scattering, the electrons can move freely and the system is called *ballistic*. In experiments, the ballistic regime can be observed only in very clean and small samples, and at low temperatures. Then the scattering length, i.e., the distance between two scattering events, l_{scatt}, is much larger than the characteristic size l_{syst} of the system, $l_{\text{scatt}} \gg l_{\text{syst}}$. On the other hand, if there are sufficiently many impurity atoms present, the electrons will be heavily scattered while travelling over a distance l_{syst}. The system is then said to be *diffusive*. Note that even the purest *macroscopic* samples will contain a large number of impurities so that the scattering length is of the order of $l_{\text{scatt}} \sim 10 \ldots 100\,\mu m$ in high-quality semiconductors. This is much smaller than the sample size of typically $l_{\text{syst}} \sim 1 \ldots 10\,mm$. Hence, macroscopic systems are diffusive in general.

To realize ballistic electron motion, one has to resort to system sizes on the nanometer scale, $l_{\text{syst}} < 1\,\mu m$, as for example in heterostructures formed in 2DEGs. These systems are called *mesoscopic* because on this scale the crossover between classical, macroscopic physics that dominates on large length scales, and quantum mechanics which is appropriate on small scales, occurs.

Motivated by the recent advances in the fabrication of semiconductor-heterostructures, the first part of this thesis will be devoted to the study of *ballistic* model systems. Since we are interested in geometric phases, we choose a *closed* ring-like structure (formed, e.g., in the plane of a 2DEG) with leads attached on either side. The *parameter* in the Hamiltonian that is *cycled* will be a non-uniform magnet field as shown in Fig. 3.1. Furthermore, we will investigate the limiting case in which the radial dimension of the ring is very thin such that the system becomes effectively one-dimensional (1d). Although this geometry is an idealization w.r.t. real samples used in experiments, it can be handled analytically and is expected to contain all the essential physics. In particular, an analytical description of the transition between adiabatic and non-adiabatic conditions is possible. Since we stated adiabaticity as prerequisit for the observation of Berry phases, we shall be able to single out geometric phase effects.

An important requirement for the observation of geometric phases is *phase coherence*: that is, the information about the phase of the electron wavefunction must be preserved during transport. Phase coherence is usually lost in inelastic scattering processes, e.g., with phonons, and hence low temperatures are important. In this context we refer to the debate about whether ballistic or diffusive systems are better suited to the detection of effects due to topological phases [32, 33]. Without going into the details, the crucial questions are in which system the condition of adiabaticity is easier to achieve, and whether sufficient phase coherence can be realized in the diffusive regime. However, there is agreement that ballistic systems should allow for identification of signatures of topological phases.

The first effect that was studied both theoretically [1] and subsequently in numerous experiments in such a ring structure with attached leads is the so-called *Aharonov-Bohm effect.* In general it is linked with the situation of a *uniform* magnetic field of any strength perpendicular to the ring and discussed in Section 3.1. At this point we just state that the essence of the Aharonov-Bohm effect are oscillations of period $\Phi_0 = hc/|e|$ in the conductance through the ring, where $\hbar = h/2\pi$ is Planck's constant, c is the velocity of light in vacuum, and e is the electric charge of the positron, resulting from the interference of electrons travelling in opposite arms of the ring. The system is well studied for rings with symmetrically attached leads (corresponding to arms of equal length) [27] as well as for asymmetric rings [26].

The phase that leads to the Aharonov-Bohm (interference) effect can be traced back to the electromagnetic vector potential $\vec{A}_{\text{em}}$ (see Appendix B), i.e., to a quantity that is a gauge potential and, therefore, is *not* observable in *classical* electrodynamics. The Aharonov-Bohm effect, however, states the physical significance of this quantity is accessible in quantum mechanics: even electrons that move in field-free space ($\vec{B} = 0$) are subject to the Aharonov-Bohm effect[2]!

The second effect that we can study in the model system mentioned above is based on topological phases. Their existence requires a *non-uniform* magnetic field. Accordingly, we study a ring with symmetrically attached leads and *inhomogeneous* configurations of the magnetic field (see Section 3.2). Concerning effects due to topological phases, the idea is to describe geometric phase effects in a way similar to the Aharonov-Bohm effect by introducing a *geometric* vector potential $\vec{A}_g$. We will apply this method [29] in Section 3.3.

---

[2] These ideas concerning an electric charge in a magnetic field were generalized in the Aharonov-Casher effect [31] that applies to a *magnetic* dipole in an *electric* field, constituting an effect "dual" to the Aharonov-Bohm effect.

When we consider the motion of electrons along the ring, it is important to distinguish two limiting cases. Their origin lies in the existence of two time scales that are defined for an electron with spin that moves along a 1d ring. On one hand, the characteristic time scale for the spin precession is given by the Larmor frequency ω_L,

$$\omega_L = \frac{-g^* e|\vec{B}|}{2m_e c}\,, \tag{2.1}$$

where the electric charge e of the electron is taken negative. $|\vec{B}|$ is the magnitude of the magnetic field that we assume to be constant, and ω_L describes the velocity of the spin's precession about the (local) magnetic field direction. On the other hand, the spatial motion of an electron with Fermi velocity v_F and (effective) mass M along a ring of radius a is characterized by its orbital frequency ω_{orb},

$$\omega_{\text{orb}} = \frac{v_F}{a} = \frac{\hbar k_F}{aM}. \tag{2.2}$$

The resulting angular velocity has to be compared with the spin precession velocity. If $\omega_L \gg \omega_{\text{orb}}$, then the magnetic field is strong and the electron moves slowly. Thus the spin follows the local direction of the magnetic field. We call this the *adiabatic* limit. In the other limit, if the magnetic field is weak or the electron moves sufficiently fast, the influence of the magnetic field on the spin is negligible. This situation is called *diabatic*. We will refer to the intermediate regime between the two limiting cases as the general non-adiabatic regime. The topological phase that occurs in this case we address as Aharonov-Anandan (or geometric) phase. In turn, we reserve the term Berry phase for the topological phase in the adiabatic situation; the Berry phase is the geometric phase in the adiabatic limit. We will see that there are no topological phases in the diabatic limit: the geometric (or Aharonov-Anandan) phase vanishes there.

We like to mention the similarity of the adiabatic limit introduced above to the Born-Oppenheimer approximation used in the context of atomic physics. There, the huge difference between the mass m_e of the electron and the proton m_p as component of the nucleus ($m_e/m_p \approx 10^{-3}$) is used to separate the motion of the electron and the nucleus. The equations of motion for the electron are solved while keeping the position of the nucleus *fixed* because the motion of the nucleus takes place on a much longer time scale. When we discuss the adiabatic limit, in analogy, now the evolution of the electron's spin is much faster than its orbital motion. Both degrees of freedom can be decoupled. We will make use of this in Section 3.4.

In this part of the thesis we will study spin-dependent transport through rings subject to non-uniform magnetic fields. The outline of Part I is as follows. In Chapter 3 we will specify the magnetic field textures under investigation and determine the corresponding eigenstates in the general non-adiabatic situation. In Chapter 4 we will calculate the magneto-conductance, that is transmission through the ring as a function of the applied magnetic field or the Fermi velocity of the electrons. To this end, we will introduce a transfer matrix method [27] for spin-dependent transport. In Chapter 5 we will consider two examples. First, we study a ring that is subject to an in-plane magnetic field. We give analytical evidence for a spinflip effect that can be controlled via an Aharonov-Bohm flux through the ring. This effect might find some application in future spintronic devices. As a second example, we discuss a ring with a central micromagnet, a setup that is motivated by recent experiments [35]. A joint summary with Part II on dielectric mesoscopic systems is given at the end of the work.

We will use units in which the Planck constant is $\hbar = 1$, as well as the speed of light in vacuum c=1. In Appendix C we describe the electric and magnetic fields involved in SI (or MKSA) units [53, 54].

3 Geometric phases in one-dimensional mesoscopic rings

In this chapter we introduce the model system of a one-dimensional ring subject to a non-uniform magnetic field with two possible textures and determine the eigenstates of electrons in these systems. After discussing the eigenstates of the adiabatic problem, we develop the concept of a geometric vector potential in order to treat the general non-adiabatic case. We demonstrate that the results have a clear geometrical interpretation. In the next chapter we will use the eigenstates found here to calculate the transmission probability through a one-dimensional ring.

3.1 Model system and Hamiltonian

We consider spin-dependent coherent transport of electrons in a one-dimensional (1d) ring of radius a, formed within a layer of a two-dimensional electron gas (2DEG). The electrons in the 2DEG are characterized by their electric charge $e < 0$, effective mass M rather than electron mass m_e, and their magnetic moment $\mu = s\, g^*\, \mu_B$ where $s = 1/2$ is the electronic spin, g^* the effective gyromagnetic ratio, and μ_B is Bohr's magneton, $\mu_B = |e|\hbar/(2m_e c)$ [36]. For free electrons in vacuum, the value of g is approximately 2. However, for electron-like quasi-particles in semiconductor heterostructures, there might be considerable deviations from this value depending on the material used. In the following, we consider a system in which the electrons are confined to a perfectly ballistic ring, i.e. the ring is assumed to contain no impurities. The electrons are exposed to a non-uniform magnetic field $\vec{B}(\vec{r})$ which couples to both spin and orbital degrees of freedom. The general Hamiltonian then reads (recall that we use units $\hbar = 1$, speed of light $c = 1$)

$$H^g = \frac{1}{2M}\left(\vec{p} - e\vec{A}_{\text{em}}(\vec{r})\right)^2 - \mu\, \vec{\sigma} \cdot \vec{B}(\vec{r})\,, \tag{3.1}$$

with $\vec{A}_{\text{em}}(\vec{r})$ being the vector potential of the (electro)magnetic field, $\vec{B}(\vec{r}) = \vec{\nabla} \times \vec{A}_{\text{em}}(\vec{r})$, and $\vec{\sigma}$ the vector of the Pauli spin matrices.

The first term describes the kinetic energy in terms of the generalized momentum $\vec{\Pi} = \vec{p} - e\vec{A}_{\text{em}}(\vec{r})$. The second term $-\mu\, \vec{\sigma} \cdot \vec{B}(\vec{r})$ corresponds to the Zeeman coupling of the electron spin $\vec{\sigma}$ to the magnetic field $\vec{B}(\vec{r})$. Spin-orbit interaction is assumed to be small, and will be neglected.

For a 1d ring of radius a in the $(z = 0)$-plane of a canonical cylindrical coordinate system, the momentum operator $\vec{p}$ is given by $\vec{p} = -\frac{i}{a}\frac{d}{d\phi}\vec{e_\phi}$. This means in particular that the polar angle ϕ is the only remaining coordinate that, therefore, determines the position of the electron along the ring, see also Fig. 4.2. Due to this spatial constraint, only the ϕ-component $\vec{A}^{\phi}_{\text{em}}$ of the electromagnetic vector potential is of importance for the orbital effect of the magnetic field, simplifying $\vec{\Pi}$ accordingly to

$$\vec{\Pi} = \left(-\frac{i}{a}\frac{d}{d\phi} - e\, A^{\phi}_{\text{em}}\right)\vec{e_\phi}\,. \tag{3.2}$$

Hence the Hamiltonian (3.1) takes the form

$$H = \frac{1}{2M}\left(-\frac{i}{a}\frac{d}{d\phi} - e\,A^{\phi}_{\mathrm{em}}\right)^2 - \mu\,\vec{\sigma}\cdot\vec{B}(\vec{r})\,. \tag{3.3}$$

For the following it is useful to introduce the magnetic flux through the ring. The flux Φ through an area S subject to a magnetic field $\vec{B}(\vec{r})$ is given as integral $\Phi = \int_S \vec{B}(\vec{r})\cdot d\vec{S}$ (with the directed area element $d\vec{S}$). Rewriting $\Phi = \int_S \left(\vec{\nabla}\times\vec{A}_{\mathrm{em}}(\vec{r})\right)\cdot d\vec{S}$, allows one to apply Stokes' formula $\int_S \left(\vec{\nabla}\times\vec{A}(\vec{r})\right)\cdot d\vec{S} = \oint_{\partial S}\vec{A}\cdot d\vec{l}$ where $\vec{l}$ is the (directed) element along the boundary of S. For the special case of a homogeneous magnetic field $\vec{B} = B_z\vec{e_z}$ the relation reads in symmetric gauge

$$\vec{A}_{\mathrm{em}}(\vec{r}) = \frac{1}{2}\vec{B}(\vec{r})\times\vec{r}\,; \tag{3.4}$$

such that at the position of the ring, $\vec{r} = a\vec{e_r}$, we find $\vec{A}_{\mathrm{em}} = \frac{1}{2}aB_z\vec{e_\phi} \overset{\mathrm{def}}{=} A^{\phi}_{\mathrm{em}}\vec{e_\phi}$. Hence we obtain the magnetic flux due to a magnetic field in z-direction through a ring of radius a as $\Phi = \oint A^{\phi}_{\mathrm{em}}d\phi = 2\pi a A^{\phi}_{\mathrm{em}}$. The electromagnetic vector potential $\vec{A}_{\mathrm{em}}$ can thus be expressed in terms of the magnetic flux as

$$\vec{A}_{\mathrm{em}} = A^{\phi}_{\mathrm{em}}\vec{e_\phi} = \frac{\Phi}{2\pi a}\vec{e_\phi}\,. \tag{3.5}$$

We note that the flux is not quantized as is the case in the context of superconductivity. Furthermore, we point out that the magnetic field can be confined to a solenoid such that the electrons in the ring are not subject to a magnetic field, as is assumed in the original Aharonov-Bohm effect [1]. We refer to this situation when we treat the Aharonov-Bohm flux (Φ or Φ^{AB}) through the ring as parameter that does not alter the magnetic field at the position of the electrons in the ring.

As is shown in Appendix B, the electromagnetic vector potential in Eq. (3.5) gives rise to a phase factor $\exp(-\frac{i}{\hbar}\frac{e}{c}\int A^{\phi}_{\mathrm{em}}\,ad\phi)$ (taken along the electron's path) in the electron wave function that leads to an interference effect – this is called Aharonov-Bohm effect [1]: oscillations of the period of the flux quantum $\Phi_0 = hc/|e|$ ($\equiv 2\pi/e$ in our units of $\hbar = c = 1$) in the transmission probability as a function of the applied Aharonov-Bohm flux $\Phi = \Phi^{AB}$ in a mesoscopic metal ring connected to current leads. This is evident when looking at the phase shift between the electrons travelling at opposite sides of the solenoid that is $\frac{e}{\hbar c}\oint A^{\phi}_{\mathrm{em}}\,ad\phi \equiv 2\pi\Phi^{AB}/\Phi_0$.

In inhomogeneous magnetic fields, besides Aharonov-Bohm-like effects due to the z-component of $\vec{B}(\vec{r})$, new phenomena can arise that are caused by topological phases of which Berry's phase [2] is the paradigm. Those effects are the subject of this first part of the thesis. The investigation is based on the concept of a geometric vector potential $\vec{A}_g$ [29] which originates from the coupling of the spin to a non-uniform magnetic field. The main idea is to exploit the analogies between Aharonov-Bohm phases (from $\vec{A}_{\mathrm{em}}$) and geometric phases (from $\vec{A}_g$).

3.2 Magnetic field configurations and corresponding eigenstates

The discussions in the following will be based on the adiabatic limit where the Larmor precession frequency ω_L defined in Eq. (2.1) of the spin is much larger than the orbital frequency ω_{orb} of the electron along the ring that is given in Eq. (2.2). Then the spin follows the (local) direction of the magnetic field $\vec{B}(\vec{r})$, and the Hamiltonian (3.3) is dominated by the spin-dependent part, i.e.,

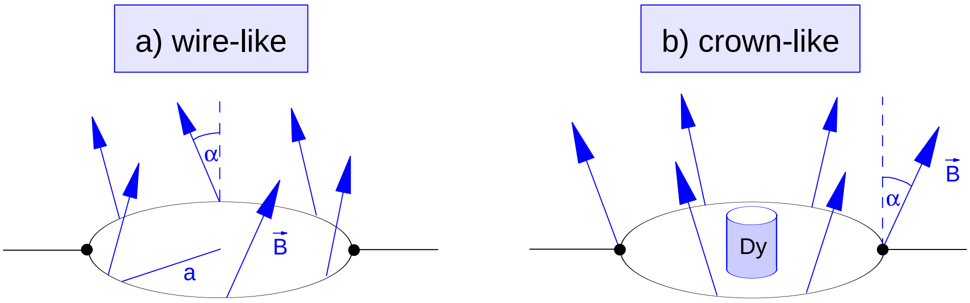

Figure 3.1: Magnetic field texture for a) a wire-like and b) a crown-like magnetic field. The angle α is defined as the angle of the magnetic field w.r.t. the z-axis. A possible way for creating a crown-like magnetic field in experiments is to place a micromagnet (here symbolized by Dy for Dysprosium) into the center of the ring.

the Zeeman term. Accordingly, we find the eigenstates of the *adiabatic* problem by diagonalizing the Zeeman term, $-\mu\vec{\sigma}\cdot\vec{B}(\vec{r})$. To this end, we first have to specify the magnetic fields that we will consider in the following. As a first example, we choose a wire-like magnetic field $\vec{B^w}$ [30] composed of a component $B_\phi\vec{e_\phi}$ that is tangent to the ring in all points, and a uniform part $B_z\vec{e_z}$ in z-direction, cf. Fig. 3.1a. In the other example, see Fig. 3.1b, we keep the uniform B_z-component, but add a radial magnetic field $B_r\vec{e_r}$ in order to obtain an inhomogeneous, crown-like magnetic field $\vec{B^c}$. We define B_ϕ to be positive in counter-clockwise direction and B_r pointing away from the centre of the ring. The magnitude of the fields is given by $B^w \stackrel{\text{def}}{=} \sqrt{B_\phi^2+B_z^2}$ and $B^c \stackrel{\text{def}}{=} \sqrt{B_r^2+B_z^2}$ for the wire-like and crown-like situation, respectively. In both cases, the direction of the resulting magnetic field is characterized by the angle α that is formed with the z-axis: $\tan\alpha^w = B_\phi/B_z$ (wire-like) or $\tan\alpha^c = B_r/B_z$ (crown-like). Experimentally, a wire-like magnetic field is generated by a central wire or appropriately aligned ferromagnetic atoms, whereas the crown-like type can, for example, be created using a central micromagnet.

Next, we determine the eigenvalues λ and spin eigenstates $|\widetilde{\Psi}\rangle$ of the Zeeman term $-\mu\,\vec{\sigma}\cdot\vec{B^w}(\vec{r})$ for the wire-like magnetic field. Using the Pauli spin matrices

$$\sigma_x = \begin{pmatrix} 0 & 1 \\ 1 & 0 \end{pmatrix}, \quad \sigma_y = \begin{pmatrix} 0 & -i \\ i & 0 \end{pmatrix}, \quad \sigma_z = \begin{pmatrix} 1 & 0 \\ 0 & -1 \end{pmatrix},$$

and the relation $\vec{e_\phi} = -\sin\phi\,\vec{e_x} + \cos\phi\,\vec{e_y}$ where ϕ is the polar angle of the position at the ring defined as usual (cf. Fig. 4.2), the eigenvalue equation for the eigenvector $\widetilde{\Psi} = (u_1, u_2)^T$ with the eigenvalue λ reads

$$-\mu \begin{pmatrix} B_z & -iB_\phi e^{-i\phi} \\ iB_\phi e^{i\phi} & -B_z \end{pmatrix} \begin{pmatrix} u_1 \\ u_2 \end{pmatrix} = \lambda \begin{pmatrix} u_1 \\ u_2 \end{pmatrix}. \tag{3.6}$$

The eigenvalues $\lambda_\mp = \mp\mu B^w$ correspond to electrons with spin parallel and antiparallel to the total magnetic field. To distinguish these states from spins pointing up and down in z-direction,

$|\uparrow\rangle$ and $|\downarrow\rangle$, the eigenstates with spin in field direction will be denoted by $|\nearrow(\phi)\rangle$ and $|\swarrow(\phi)\rangle$, respectively. Treating the polar angle ϕ as a parameter, the eigenstates for the wire-like magnetic field in S_z-basis are chosen as

$$|\nearrow(\phi)\rangle^w = \begin{pmatrix} \cos\frac{\alpha^w}{2} \\ i\, e^{i\phi}\, \sin\frac{\alpha^w}{2} \end{pmatrix}, \qquad |\swarrow(\phi)\rangle^w = \begin{pmatrix} \sin\frac{\alpha^w}{2} \\ -i\, e^{i\phi}\, \cos\frac{\alpha^w}{2} \end{pmatrix}. \tag{3.7}$$

The analogous procedure for the crown-like magnetic field leads to the eigenvalue problem

$$-\mu \begin{pmatrix} B_z & B_r e^{-i\phi} \\ B_r e^{i\phi} & -B_z \end{pmatrix} \begin{pmatrix} u_1 \\ u_2 \end{pmatrix} = \lambda \begin{pmatrix} u_1 \\ u_2 \end{pmatrix} \tag{3.8}$$

with the solution

$$|\nearrow(\phi)\rangle^c = \begin{pmatrix} \cos\frac{\alpha^c}{2} \\ e^{i\phi}\, \sin\frac{\alpha^c}{2} \end{pmatrix}, \qquad |\swarrow(\phi)\rangle^c = \begin{pmatrix} \sin\frac{\alpha^c}{2} \\ -\, e^{i\phi}\, \cos\frac{\alpha^c}{2} \end{pmatrix}. \tag{3.9}$$

To simplify further treatment of both cases, we introduce the unifying representation

$$|\nearrow(\phi)\rangle = \begin{pmatrix} \cos\frac{\alpha}{2} \\ e^{i(\phi+\phi_t)}\, \sin\frac{\alpha}{2} \end{pmatrix}, \qquad |\swarrow(\phi)\rangle = \begin{pmatrix} \sin\frac{\alpha}{2} \\ -\, e^{i(\phi+\phi_t)}\, \cos\frac{\alpha}{2} \end{pmatrix}, \tag{3.10}$$

with the field texture parameter ϕ_t taking the values

$$\phi_t = \begin{cases} 0 & \text{crown-like magnetic field} \\ \frac{\pi}{2} & \text{wire-like magnetic field.} \end{cases} \tag{3.11}$$

This also reveals the symmetry operation connecting the two textures of the magnetic field. To obtain an eigenstate for the wire-like field, one can start with the one for the crown-like field, and increase the angle ϕ by $\pi/2$.

So far, we have considered the spin part of the electron wave function. The orbital part can be written in terms of eigenstates $|\phi\rangle$ of the operator $e^{i\hat{\phi}}$. Then a basis of the Hamiltonian (3.3) is spanned by the product states $\{\nearrow\} \overset{\text{def}}{=} \{|\phi\rangle \otimes |\nearrow(\phi)\rangle\}$ and $\{\swarrow\} \overset{\text{def}}{=} |\phi\rangle \otimes |\swarrow(\phi)\rangle\}$ with $0 \leq \phi < \pi$.

In the adiabatic regime, i.e., for dominating Zeeman interaction, $\omega_L \ll \omega_{\text{orb}}$, the spins align either parallel or antiparallel to the magnetic field and never switch their direction, because the spin always follows the local direction of the magnetic field during its precession. This means that the $\{\nearrow\}$ and $\{\swarrow\}$ subspaces are completely decoupled. In the next section, we will use this property to write the Hamiltonian (3.3) as sum of two parts, namely the adiabatic part H_0 and the non-adiabatic part H_1. H_0 has non-zero matrix elements only within each subspace, whereas for H_1 the opposite is true. In a purely adiabatic situation, H_1 vanishes. To perform this decomposition, we shall apply the concept of a geometric vector potential $\vec{A}_g$ introduced by Aharonov et al. [29] that we introduce in Section 3.3.

Before we do so, we briefly consider the symmetries of our system. As known from Noether's theorem, there exists a conserved quantity for each continuous symmetry in a physical system. The one-dimensional ring we are dealing with here is characterized by symmetry with respect to rotations about the z-axis (i.e., perpendicular to the ring plane). Accordingly, we find that the operator L_z, that is the sum of the z-components of the orbital angular momentum and the spin,

$$L_z = -i\frac{d}{d\phi} + \frac{1}{2}\sigma_z, \tag{3.12}$$

is a conserved quantity. This can be easily checked by verifying its commutator with the Hamiltonian H from (3.3) as is performed in Appendix A.

3.3 Geometric vector potential $\vec{A}_g$

In this section we will employ the concept of a geometric vector potential $\vec{A}_g$ that contributes to the generalized mechanical momentum $\vec{\Pi}$ similar to the way the electromagnetic vector potential $\vec{A}_{\text{em}}$ does. Since due the constrictions caused by the 1d nature of the ring $\vec{\Pi}$ consists of a ϕ-component only [see Eq. (3.2)], we need only to consider the ϕ-components of all vector potentials; the other components do not play a role. We will use the following abbreviations:

$$\begin{aligned}
\vec{\Pi} &= \Pi \vec{e_\phi} = \left(-\frac{i}{a}\frac{d}{d\phi} - eA^{\phi}_{\text{em}} \right) \vec{e_\phi} \, , \\
\vec{A}_{\text{em}} &= A^{\phi}_{\text{em}} \vec{e_\phi} \, , \\
\vec{A}_g &= A^{\phi}_g \vec{e_\phi} \overset{\text{def}}{=} A_g \vec{e_\phi} \, .
\end{aligned} \tag{3.13}$$

Our starting point is the Hamiltonian (3.3) for the one-dimensional ring,

$$H = \frac{1}{2M}\,\Pi^2 - \mu\,\vec{\sigma} \cdot \vec{B}(\vec{r}) \, . \tag{3.14}$$

In the following we will decompose H into $H_0 + H_1$, where the adiabatic part H_0 contains no transitions between the $\{\nearrow\}$ and $\{\swarrow\}$ subspaces, whereas the non-adiabatic part H_1 exclusively describes such transitions. It is convenient to introduce *projection operators* onto the $\{\nearrow\}$ and $\{\swarrow\}$ subspaces, $\hat{P}^{\nearrow(\swarrow)} = \frac{1}{2}(1 + (-)\vec{n} \cdot \vec{\sigma})$, with $\vec{n} = \vec{B}/B$ the local direction of the magnetic field and $\vec{\sigma}$ the Pauli spin matrices as above. Then we have $\Pi = \hat{P}^{\nearrow}\Pi\hat{P}^{\nearrow} + \hat{P}^{\nearrow}\Pi\hat{P}^{\swarrow} + \hat{P}^{\swarrow}\Pi\hat{P}^{\nearrow} + \hat{P}^{\swarrow}\Pi\hat{P}^{\swarrow}$. The adiabatic part of Π^2 is obviously given by $(\hat{P}^{\nearrow}\Pi\hat{P}^{\nearrow} + \hat{P}^{\swarrow}\Pi\hat{P}^{\swarrow})^2 + (\hat{P}^{\nearrow}\Pi\hat{P}^{\swarrow} + \hat{P}^{\swarrow}\Pi\hat{P}^{\nearrow})^2$. Since we are heading for an expression of the form $(\Pi - A_g)^2$, we define[1] [29]

$$A_g = \Pi - \hat{P}^{\nearrow}\Pi\hat{P}^{\nearrow} - \hat{P}^{\swarrow}\Pi\hat{P}^{\swarrow} = \frac{1}{4}\,[\vec{n}\vec{\sigma},[\vec{n}\vec{\sigma},\Pi]] \, . \tag{3.15}$$

Using

$$\Pi^2 = (\Pi - A_g + A_g)^2 = \left[(\Pi - A_g)^2 + A_g^2\right] + \left[(\Pi - A_g)A_g + A_g(\Pi - A_g)\right] \tag{3.16}$$

and the fact that the Zeeman term is diagonal w.r.t. the subspaces $\{\nearrow\}$ and $\{\swarrow\}$, we find

$$\begin{aligned}
H_0 &= \frac{1}{2M}\left[(\Pi - A_g)^2 + A_g^2\right] - \mu\vec{\sigma} \cdot \vec{B} \, , \\
H_1 &= \frac{1}{2M}\left[(\Pi - A_g)A_g + A_g(\Pi - A_g)\right]
\end{aligned} \tag{3.17}$$

with the desired properties.

We now us Eq. (3.15) as defining equation for the geometric vector potentials of the two magnetic field configurations introduced in Section 3.2. Evaluating the commutator in Eq. (3.15) for the wire-like magnetic field (see Fig. 3.1a), $\vec{n} = \sin\alpha\vec{e_\phi} + \cos\alpha\vec{e_z}$, where $\vec{e_\phi} = -\sin\phi\vec{e_x} + \cos\phi\vec{e_y}$, leads via

---

[1] Note that the expression $\vec{A}_g = \vec{n} \times \vec{\sigma}/2a$ given in [29] is based on the special geometry used and, contrary to Eq. (3.15), not valid in general.

$$[\vec{n}\cdot\vec{\sigma}, \Pi] = \frac{i}{a}\begin{pmatrix} 0 & -e^{-i\phi}\sin\alpha \\ -e^{i\phi}\sin\alpha & 0 \end{pmatrix}$$

eventually to

$$A_g^w = \frac{\sin\alpha}{2a}\begin{pmatrix} -\sin\alpha & -i\ \cos\alpha\, e^{-i\phi} \\ i\ \cos\alpha\, e^{i\phi} & \sin\alpha \end{pmatrix}, \tag{3.18}$$

or, equivalently, this can be written as

$$A_g^w = \frac{\sin\alpha}{2a}\left(\cos\alpha\, \vec{\sigma}\cdot\vec{e_\phi} - \sin\alpha\, \sigma_z\right) . \tag{3.19}$$

Performing the same procedure for the crown-like field ($\vec{e_r} = \cos\phi\vec{e_x} + \sin\phi\vec{e_y}$) gives the same results except for the factors $-i$ and i, respectively, in the non-diagonal elements of (3.18). Correspondingly, the last equation is replaced by

$$A_g^c = \frac{\sin\alpha}{2a}\left(\cos\alpha\, \vec{\sigma}\cdot\vec{e_r} - \sin\alpha\, \sigma_z\right) . \tag{3.20}$$

Again, we can unify the representations as

$$A_g = \frac{\sin\alpha}{2a}\begin{pmatrix} -\sin\alpha & \cos\alpha\, e^{-i(\phi+\phi_t)} \\ \cos\alpha\, e^{i(\phi+\phi_t)} & \sin\alpha \end{pmatrix} \tag{3.21}$$

using the parameter ϕ_t introduced in Eq. (3.11). From this we find independent of ϕ_t

$$A_g^2 = \frac{\sin^2\alpha}{4a^2}\mathbb{I}_{2\times2}, \tag{3.22}$$

where $\mathbb{I}_{2\times2}$ denotes the unit matrix. Now we can use the decomposition of Eq. (3.17) and Eq. (3.22) to write

$$H_0 = \frac{(\Pi - A_g)^2}{2M} + \frac{\sin^2\alpha}{8Ma^2} - \mu\,\vec{\sigma}\cdot\vec{B}(\vec{r}) \tag{3.23}$$

and

$$H_1 = \frac{1}{2M}\left[(\Pi - A_g)A_g + A_g(\Pi - A_g)\right] . \tag{3.24}$$

In Section 3.4, we will discuss the *adiabatic* limit and the connection to the *Berry* phase. As discussed above, this requires the Hamiltonian H_0 only since by construction of H_0 and H_1 all matrix elements involving H_1 vanish. However, the general *non-adiabatic* case can be solved exactly as well, leading to nice analogues with the adiabatic case concerning, e.g., the structure of the eigenstates or the expression for the *geometric* (or *Aharonov-Anandan*) phase as shown in Section 3.5.

3.4 Adiabatic case

In the limit of a strong magnetic field, the Larmor frequency of the electron's spin dominates its orbital frequency, $\omega_L \gg \omega_{\mathrm{orb}}$, and we are in the adiabatic regime where the physics is completely comprised in H_0 since spin-flip processes between the subspaces $\{\nearrow\}$ and $\{\swarrow\}$ are forbidden.

3.4.1 Effective Hamiltonian for orbital motion

In the adiabatic limit ($H = H_0$) the spin dynamics upon orbital motion is completely contained in the two (local) eigenstates $|\nearrow(\phi)\rangle, |\swarrow(\phi)\rangle$ of the local Zeeman term. Therefore it is possible to trace out the spin degrees of freedom and to derive effective Hamiltonians ($H_0^{\nearrow\nearrow}$, $H_0^{\swarrow\swarrow}$) for the orbital motion only. Importantly, the $d/d\phi$ term in the Hamiltonian acts on *both* the spin and orbital component of the electron wave function $|\psi_n^\sigma\rangle \otimes |\sigma(\phi)\rangle$ with $\sigma = \nearrow, \swarrow$. Writing symbolically $H^{\sigma\sigma'} = \langle\sigma(\phi)|H|\sigma'(\phi)\rangle$ ($\sigma, \sigma' = \nearrow, \swarrow$), we are left with calculating the matrix elements $H^{\nearrow\nearrow} = H_0^{\nearrow\nearrow} = \langle\nearrow(\phi)|H_0|\nearrow(\phi)\rangle$ and $H^{\swarrow\swarrow} = H_0^{\swarrow\swarrow} = \langle\swarrow(\phi)|H_0|\swarrow(\phi)\rangle$.

We now briefly sketch the calculations necessary to obtain the Hamiltonian $H_0^{\nearrow\nearrow}$. First, we rewrite (3.23) as

$$H_0 = \frac{1}{2M}(\Pi^2 - A_g\Pi - \Pi A_g + A_g^2) + \frac{\sin^2\alpha}{8Ma^2} - \mu\,\vec{\sigma}\cdot\vec{B}(\vec{r})\,, \tag{3.25}$$

recalling that only the ϕ-components of the momentum and the vector potentials are of significance in the 1d ring, see Eq. (3.13). Since the ϕ-component A_{em}^ϕ of the electromagnetic vector potential originates from the z-component B_z of the magnetic field, it is the same for the wire-like and crown-like configuration. This holds for the ϕ-component Π of the generalized momentum, too, since $\Pi = -\frac{i}{a}\frac{d}{d\phi} - eA_{\mathrm{em}}^\phi$, and we can treat both cases simultaneously in terms of ϕ-component A_g of the unified geometric vector potential.

Using the substitution $\phi' \overset{\mathrm{def}}{=} \phi + \phi_t$, we find

$$(\Pi|\nearrow(\phi)\rangle)|\psi_n^\nearrow\rangle = \begin{pmatrix} 0 \\ \frac{1}{a}\sin\frac{\alpha}{2}e^{i\phi'} \end{pmatrix}|\psi_n^\nearrow\rangle + \begin{pmatrix} \cos\frac{\alpha}{2} \\ \sin\frac{\alpha}{2}e^{i\phi'} \end{pmatrix}\left(\Pi|\psi_n^\nearrow\rangle\right)\,, \tag{3.26}$$

and

$$A_g\Pi + \Pi A_g = 2A_g\Pi - \frac{i}{a}\frac{d}{d\phi}A_g\,. \tag{3.27}$$

Then the calculation is straightforward giving the constituting terms for the matrix element $\langle\nearrow|H_0|\nearrow\rangle$ as

$$\begin{aligned} \langle\nearrow(\phi)|\Pi^2|\nearrow(\phi)\rangle &= \Pi^2 + \sin^2\frac{\alpha}{2}\left(\frac{1}{a^2} + \frac{2}{a}\Pi\right)\,, \\ -\langle\nearrow(\phi)|A_g\Pi + \Pi A_g|\nearrow(\phi)\rangle &= -\frac{\sin\alpha\,\sin\frac{\alpha}{2}}{a^2}\left(\cos\alpha\,\cos\frac{\alpha}{2} + \sin\alpha\,\sin\frac{\alpha}{2}\right)\,, \\ \langle\nearrow(\phi)|A_g^2|\nearrow(\phi)\rangle &= \frac{\sin^2\alpha}{4a^2}\,. \end{aligned} \tag{3.28}$$

The sum of the Π-independent terms (multiplied by a^2) can be simplified and yields

$$\sin^2\frac{\alpha}{2} - \sin^2\alpha\,\sin^2\frac{\alpha}{2} + \frac{1}{4}\sin^2\alpha - \cos\alpha\,\sin\alpha\,\cos\frac{\alpha}{2}\,\sin\frac{\alpha}{2} = \sin^4\frac{\alpha}{2}\,.$$

Eventually, we obtain the effective Hamiltonians

$$\begin{aligned} H_0^{\nearrow\nearrow} &= \frac{1}{2M}\left(\Pi + \frac{1}{a}\sin^2\frac{\alpha}{2}\right)^2 + \frac{\sin^2\alpha}{8Ma^2} - \mu B\,,\,, \\ H_0^{\swarrow\swarrow} &= \frac{1}{2M}\left(\Pi + \frac{1}{a}\cos^2\frac{\alpha}{2}\right)^2 + \frac{\sin^2\alpha}{8Ma^2} + \mu B\,, \end{aligned} \tag{3.29}$$

where we have used $B = |\vec{B}| = \sqrt{(B^{w/c})^2 + B_z^2}$, that is the magnitude of the total magnetic field $\vec{B}$. Notice the additional term in the momentum in Eq. (3.29) which originates from the geometric vector potential A_g. We will see in the next section how it is related to the Berry phase.

3.4.2 Eigenstates and Berry phase

We will first specify the structure of the sets $\{\nearrow\}$ and $\{\swarrow\}$ and determine the eigenstates of the adiabatic problem $H = H_0$. Each eigenstate $|\Psi_n\rangle$ contains a spatial part $|\psi_n\rangle$ and a spin part, such that we have the two sets of eigenvectors $|\Psi_n^{\nearrow}\rangle = |\psi_n^{\nearrow}\rangle \otimes |\nearrow(\phi)\rangle$ and $\Psi_n^{\swarrow} = \psi_n^{\swarrow}(\phi) \otimes |\swarrow(\phi)\rangle$ in which the spin is parallel or antiparallel to the magnetic field as introduced in Section 3.2. The spatial functions $\psi_n^{\nearrow(\swarrow)}$ are, according to the structure of the Hamiltonian, plane waves $e^{in\phi}$, where n is the quantum number associated with the operator $-i\frac{d}{d\phi}$. For *spinless* electrons in an *isolated* ring eigenstates ψ_n are obtained for integer[2] values of n, manifesting the periodicity of the problem with respect to changes in the polar angle ϕ by 2π. This is illustrated in Appendix B using the analogy between electrons in a *closed* ring and electrons in an one-dimensional *periodic* potential.

We will call n' the quantum number of the generalized momentum Π that is related to the quantum number n by (note that e, the electric charge of the electron, was defined negative!)

$$n' = n - \frac{1}{2} e a^2 B_z \,. \tag{3.30}$$

Note the shift caused by a homogeneous magnetic field in z-direction. The n' are obtained from Eq. (3.29). However, we postpone their calculation to Section 3.5 when we consider the general non-adiabatic case that, of course, contains the adiabatic situation as a limiting case.

In Appendix B we demonstrate how additional terms in the momentum operator lead to additional phase factors in the wave function that can be observed in interference experiments. Although it is shown there for the example of the Aharonov-Bohm effect where the electromagnetic vector potential, $\vec{A}_{\text{em}}$, enters the generalized momentum, the same applies, of course, to the geometric vector potential that induces geometric phase factors. In the adiabatic regime, we refer to them as Berry phases.

We will now establish the relation between the additional contribution in the momentum term of Eq. (3.29) and the Berry phase. First of all, we find that these terms, $\sin^2\frac{\alpha}{2}$ and $\cos^2\frac{\alpha}{2}$, respectively, can be expressed through the *solid angle* subtended by the magnetic field vector $\vec{B}$ during one complete round trip (from $\phi = 0$ to $\phi = 2\pi$) along the ring in parameter space. In his seminal paper [2], M. V. Berry derived that the geometric phase Γ for electrons is given by half this solid angle Ω. The general expression for particles with spin s reads

$$\Gamma = -s\Omega \,. \tag{3.31}$$

This equation underlines the *geometrical* nature of the Berry phase and gives some intuitive meaning to it.

We shall now see that Eq. (3.31) is indeed equivalent to the expression that we derived using the geometric vector potential, cf. Eq. (3.29). For the $|\nearrow(\phi)\rangle$-eigenstate we obtain the solid angle $\Omega^{\nearrow}$ subtended by the magnetic field during one round trip as the part of the spherical surface $A^{\nearrow}$ that is sketched in Fig. 3.2 (using spherical coordinates and normalizing by the square of the magnitude B of the magnetic field) as

$$\Omega^{\nearrow} = \int_0^{2\pi}\int_0^{\alpha} \sin\alpha \, d\phi \, d\theta = 2\pi\,(1-\cos\alpha) = 4\pi\sin^2\frac{\alpha}{2} \,. \tag{3.32}$$

---

[2] We will see that for either including the spin into consideration or (and) opening the system as we will do in Chapter 4 by attaching leads to the ring, the quantum number n will not be an integer in general.

Replacing $\alpha \to \pi - \alpha$, we get the $|\swarrow(\phi)\rangle$-result,

$$\Omega^{\swarrow} = 2\pi(1+\cos\alpha) = 4\pi\cos^2\frac{\alpha}{2}\,. \tag{3.33}$$

Hence we can rewrite Eq. (3.29) as

$$H_0^{\nearrow\nearrow(\swarrow\swarrow)} = \frac{1}{2M}\left(\Pi + \frac{1}{2\pi a}\frac{\Omega^{\nearrow(\swarrow)}}{2}\right)^2 - \mu B + \frac{1}{2M}\frac{\sin^2\alpha}{4a^2}\,. \tag{3.34}$$

In Appendix B we demonstrate for the example of the Aharonov-Bohm effect how additional terms in the momentum (in that case given by the electromagnetic vector potential $\vec{A}_{\mathrm{em}}$) lead to additional phase factors in the wave function that can be observed in interference experiments. Here, the additional phase factor is a geometric phase $\Gamma^{\nearrow(\swarrow)}$, more precisely, a Berry phase since we deal with the adiabatic situation. According to Appendix B, we find

$$\begin{aligned}\Gamma^{\nearrow} &= -2\pi\sin^2\frac{\alpha}{2} = -\pi(1-\cos\alpha) &&= -\frac{\Omega^{\nearrow}}{2}\,,\\ \Gamma^{\swarrow} &= -2\pi\cos^2\frac{\alpha}{2} = -\pi(1+\cos\alpha) &&= -\frac{\Omega^{\swarrow}}{2}\,,\end{aligned} \tag{3.35}$$

as the additional phases arising during a closed cycle in parameter space. Unlike the Aharonov-Bohm phase that can take any value, geometric phases are constricted to the interval $[0, 2\pi]$.

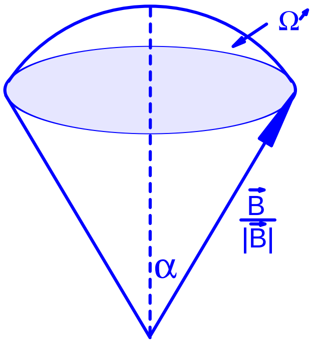

Figure 3.2: Solid angle $\Omega^{\nearrow}$ subtended by the magnetic field $\vec{B}$ during one round trip in parameter space.

Finally, we state that Eq. (3.35) for the Berry phase (i.e., the geometric phase in the adiabatic limes) can alternatively be obtained directly from [2]

$$\Gamma^{\nearrow(\swarrow)} = i\int_0^{2\pi} \langle\nearrow(\swarrow)|\,\frac{1}{a}\frac{d}{d\phi}\,|\nearrow(\swarrow)\rangle\, a\,d\phi$$

without applying the concept of the geometric vector potential. However, generalization to the non-adiabatic case is no longer straightforward. Furthermore, in Eq. (3.23), the geometric vector potential does not only *appear* as a vector potential in the Hamiltonian H_0 but also possesses all the properties that one expects for such a quantity [8].

At this point a remark on the significance of the induced geometric vector potential appearing in the generalized momentum is in order. To this end, we consider space translation transformations, generated by the momentum operator. Concerning the operator $e^{i\hat{\phi}}$, it describes the spatial translation of electrons where the direction of the spin is kept constant. On the contrary, the generalized momentum in the adiabatic Hamiltonian $H_0^{\nearrow\nearrow}, H_0^{\swarrow\swarrow}$, Eq. (3.34), is the generator of a transformation where the electron is translated spatially and the *spin follows* the direction of the magnetic field.

To summarize the *adiabatic case*, we state:

- The system is decomposed into two independent electron gases in which the spin is parallel or antiparallel to the magnetic field.

- The spin eigenstates are given in (3.10). The spin-independent part of the system is described by the Hamiltonians (3.29).
- The movement in an inhomogeneous magnetic field with tilt angle α results in the accumulation of a Berry phase that is given as $\Gamma^{\nearrow(\swarrow)} = -\pi(1-(+)\cos\alpha)$.

3.5 Non-adiabatic case

So far, we were only interested in the Hamiltonian H_0 given in Eq. (3.23) which was sufficient in the adiabatic regime. However, the decomposition (3.17) of the full Hamiltonian H involves the part H_1, Eq. (3.24), as well, and in the diabatic case it plays an important role as we shall see in this section.

We start by considering the non-diagonal matrix elements $H^{\nearrow\swarrow} = H_1^{\nearrow\swarrow} = \langle\nearrow(\phi)|H_1|\swarrow(\phi)\rangle$ and $H^{\swarrow\nearrow} = H_1^{\swarrow\nearrow} = \langle\swarrow(\phi)|H_1|\nearrow(\phi)\rangle$ of H_1. By construction, the diagonal matrix elements of H_1 vanish. We give a brief survey of the calculation of $H_1^{\swarrow\nearrow}$ which is very similar to what was done in evaluating $H_0^{\nearrow\nearrow}$ in the previous section. We note that

$$2M\,H_1 = [(\Pi - A_g)A_g + A_g(\Pi - A_g)] = \Pi A_g + A_g\Pi - A_g^2\,,$$

where the A_g^2-term will vanish upon calculating the matrix element, and we use Eq. (3.27) to evaluate the remaining terms. Then we find

$$\begin{aligned}\left(2A_g\Pi - \frac{i}{a}\frac{d}{d\phi}\right)|\nearrow(\phi)\rangle \quad &= \quad \frac{\sin\alpha}{2a^2}\begin{pmatrix} 2\cos\alpha\sin\frac{\alpha}{2} - \cos\alpha\sin\frac{\alpha}{2} \\ (2\sin\alpha\sin\frac{\alpha}{2} + \cos\alpha\cos\frac{\alpha}{2})e^{i\phi'}\end{pmatrix} + \\ &\quad\; 2\frac{\sin\alpha}{2a^2}\begin{pmatrix} -\sin\alpha\cos\frac{\alpha}{2} + \cos\alpha\sin\frac{\alpha}{2} \\ (\cos\alpha\cos\frac{\alpha}{2} + \sin\alpha\sin\frac{\alpha}{2})e^{i\phi'}\end{pmatrix}\Pi\,,\end{aligned}$$

and projection on $\langle\swarrow(\phi)|$ finally yields

$$H_1^{\swarrow\nearrow} = -\frac{\sin\alpha}{4Ma^2} - \frac{\sin\alpha}{2Ma}\Pi\,. \tag{3.36}$$

Now we have all the ingredients to determine the exact eigenstates $|\Psi_n\rangle$ of the non-adiabatic problem. They will contain a spin part which is now a *linear combination* of $|\nearrow(\phi)\rangle$- and $|\swarrow(\phi)\rangle$-states, and a spatial part $|\psi_n\rangle$ as in the adiabatic case considered in Section 3.4. Therefore we write

$$|\Psi_n\rangle = |\psi_n\rangle \otimes \left[C_1|\nearrow(\phi)\rangle + C_2|\swarrow(\phi)\rangle\right]\,. \tag{3.37}$$

The spatial part $|\psi\rangle$ can be chosen as "plane wave", $\psi_n(\phi) = e^{in\phi}$, where n can be considered as orbital quantum number.

The equations that determine C_1, C_2, and n are given in terms of the eigenvalue problem $H|\Psi_n\rangle = E_n|\Psi_n\rangle$, where E_n is the eigenenergy to the eigenstate $|\Psi_n\rangle$. Using Eq. (3.37) we obtain

$$(C_1 H|\nearrow(\phi)\rangle + C_2 H|\swarrow(\phi)\rangle)|\psi_n\rangle = E_n(C_1|\nearrow(\phi)\rangle + C_2|\swarrow(\phi)\rangle)|\psi_n\rangle\,. \tag{3.38}$$

Now we project $\langle\nearrow(\phi)|$ from the left and make use of the special decomposition (3.17) of the Hamiltonian H to obtain

$$(C_1 H_0^{\nearrow\nearrow} + C_2 H_1^{\nearrow\swarrow})|\psi_n\rangle = E_n C_1|\psi_n\rangle\,.$$

Correspondingly the projection with $\langle\swarrow(\phi)|$ yields

$$(C_1 H_1^{\swarrow\nearrow} + C_2 H_0^{\swarrow\swarrow})|\psi_n\rangle = E_n C_2 |\psi_n\rangle \,,$$

which can be combined to give

$$\begin{pmatrix} H_0^{\nearrow\nearrow} & H_1^{\nearrow\swarrow} \\ H_1^{\swarrow\nearrow} & H_0^{\swarrow\swarrow} \end{pmatrix} \begin{pmatrix} C_1 \\ C_2 \end{pmatrix} |\psi_n\rangle = E_n \begin{pmatrix} C_1 \\ C_2 \end{pmatrix} |\psi_n\rangle \,. \tag{3.39}$$

As expected, the diagonal elements describe the adiabatic part of the problem, whereas the non-diagonal entries contain the modifications necessary for treating the general non-adiabatic situation. They vanish in the adiabatic regime.

Using Eq. (3.28) for the matrix elements above and employing

$$\Pi|\psi_n\rangle = \frac{1}{a}\left(n - \frac{1}{2}ea^2 B_z\right)|\psi_n\rangle = \frac{1}{a}n'|\psi_n\rangle \,,$$

we obtain, for example,

$$\begin{aligned} \langle\nearrow(\phi)|H_0|\nearrow(\phi)\rangle &= \frac{1}{2Ma^2}\left(n'^2 + 2n'\sin^2\frac{\alpha}{2} + \sin^4\frac{\alpha}{2} + \frac{1}{4}\sin^2\alpha\right) - \mu B \\ &= \frac{1}{2Ma^2}\left(n'^2 + (2n'+1)\sin^2\frac{\alpha}{2}\right) - \mu B \,. \end{aligned} \tag{3.40}$$

Hence, we find (after multiplication by $2Ma^2$, $\widetilde{\mu} \overset{\text{def}}{=} 2Ma^2\mu$) that $\binom{C_1}{C_2}$ has to be an eigenvector of the matrix [30]

$$\mathcal{M} = \begin{pmatrix} n'^2 + (2n'+1)\sin^2\frac{\alpha}{2} - \widetilde{\mu}B & -\frac{2n'+1}{2}\sin\alpha \\ -\frac{2n'+1}{2}\sin\alpha & n'^2 + (2n'+1)\cos^2\frac{\alpha}{2} + \widetilde{\mu}B \end{pmatrix} . \tag{3.41}$$

According to the scaling factor $2Ma^2$, we will use scaled energies

$$\widetilde{E} \overset{\text{def}}{=} 2Ma^2\, E \tag{3.42}$$

in the following and also mark scaled quantities analogously.

To proceed further towards the exact eigenstates of the non-adiabatic problem, we first of all need the energy eigenvalues $\widetilde{\lambda}$ of $\mathcal{M}$. We obtain them from the usual condition for non-trivial solutions of this eigenvalue problem,

$$\det(\mathcal{M} - \lambda\mathbb{I}) = 0 \,,$$

to fulfill the equation

$$\widetilde{\lambda}_{1/2} = n'^2 + \frac{2n'+1}{2} \pm \sqrt{\left(\frac{2n'+1}{2}\right)^2 + (2n'+1)\widetilde{\mu}B\cos\alpha + (\widetilde{\mu}B)^2} \,. \tag{3.43}$$

Let us first consider the case without magnetic field, $B = 0$, where we have

$$\widetilde{\lambda}_1 = (n'+1)^2 = (n+1)^2 \quad \text{and} \quad \widetilde{\lambda}_2 = n'^2 = n^2 \,.$$

Requiring all electrons in the ring to possess the same energy, namely the (scaled) Fermi energy $\widetilde{E}_F = 2Ma^2\, E_F$, leads to $\widetilde{\lambda}_1 = \widetilde{\lambda}_2 \equiv \widetilde{E}_F$ or

$$\widetilde{E}_F = (n_1 + 1)^2 = n_2^2\,. \tag{3.44}$$

In other words, choosing $n_1 = \pm\sqrt{\widetilde{E}_F} - 1$ and $n_2 = \pm\sqrt{\widetilde{E}_F}$ yields the same eigenvalue $\widetilde{E}_F$. The sign of n determines the direction in which the electron moves along the ring: positive n corresponds to counter-clockwise propagation as is clear from the spatial part $e^{in\phi}$ of the wave function. Correspondingly, negative n describe clockwise travelling waves.

In the following, we will be interested in the situation just outlined: We look for eigenstates $|\Psi_n\rangle$ that are degenerate with respect to the eigenenergy $\widetilde{E}_F$ which will play the role of a Fermi energy $E_F = \widetilde{E}_F/2Ma^2$. As we have just learned, the corresponding n_1 and n_2 are shifted by 1 (when choosing the same sign in the $\sqrt{\widetilde{E}_F}$-term). The origin of this shift lies in the $e^{i\phi}$-dependence of the second spinor component and will become clearer when we now consider the case with non-zero magnetic field.

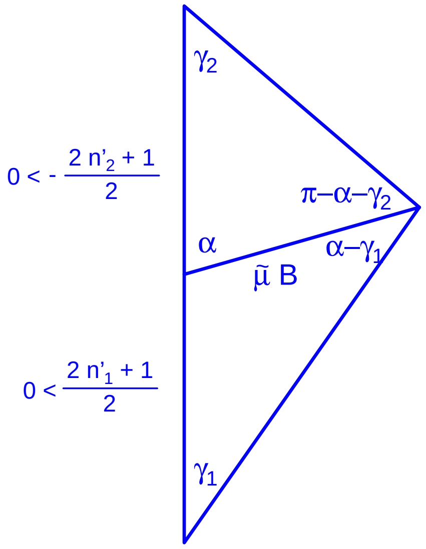

Figure 3.3: Interpretation of the square root term in Eq. (3.43) using the cosine theorem. If $\alpha > \pi/2$, n'_1 and n'_2 have to be assigned the other way round.

To this end, we note that the structure of the square root term in Eq. (3.43) resembles that of the theorem for the cosine in a triangle. This allows us to evaluate the square root by introducing an angle γ and applying the projection theorem, see Figs. 3.3 and 3.4. Since the cosine theorem requires the central term to be negative, we have to distinguish two cases (discussing $0 < \alpha < \pi/2$): For $2n' + 1 < 0$ (clockwise propagation) we can employ a triangle with α, whereas for $2n' + 1 > 0$ (counter-clockwise propagation) we have to substitute $\alpha \to \pi - \alpha$. This gives rise to the geometrical interpretation illustrated in Fig. 3.3, where we introduce the angles γ_1, γ_2 with $0 \leq \gamma_1, \gamma_2 \leq \pi$. The analytical expressions that define γ_1 and γ_2 read[3]

$$2n'_1 + 1 > 0 : \cot\gamma_1 = \cot\alpha + \frac{(2n'_1 + 1)}{2}\,\frac{1}{\tilde{\mu}B\sin\alpha}\,, \tag{3.45}$$

$$2n'_2 + 1 < 0 : \cot\gamma_2 = -\cot\alpha - \frac{(2n'_2 + 1)}{2}\,\frac{1}{\tilde{\mu}B\sin\alpha}\,. \tag{3.46}$$

In the adiabatic limit, $\tilde{\mu}B \gg n'$, the γ take the values $\gamma_1 = \alpha$ and $\gamma_2 = \pi - \alpha$, respectively, whereas in the diabatic limit $\gamma_1 = \gamma_2 = 0$.

---

[3] We use the so-called tangent formula [55] that relates the angles and sides in a triangle by the formulae (adopting the common notation for sides and angles)

$$\cot\alpha = -\cot\beta + \frac{c}{a\sin\beta} = -\cot\gamma + \frac{b}{a\sin\gamma}\,.$$

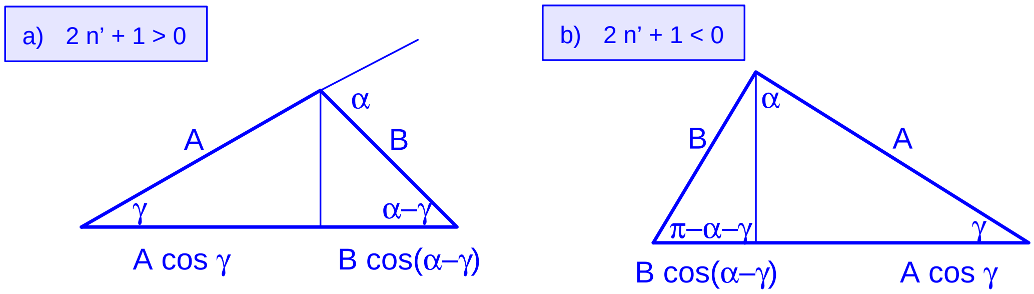

Figure 3.4: Tangent formula. a) Geometry in the case of counter-clockwise travelling waves, $2n' + 1 > 0$. b) The same for clockwise propagation, $2n' + 1 < 0$.

For counter-clockwise travelling waves and at a given (scaled) Fermi energy $\widetilde{E}_F$, Eq. (3.43), takes the form (see Fig. 3.4a)

$$\widetilde{E}_F = {n'}_1^2 + \frac{2{n'}_1 + 1}{2}(1 \mp \cos\gamma_1) \mp \widetilde{\mu}B\cos(\gamma_1 - \alpha) \;,$$

where the two signs stand for the spin directions parallel or antiparallel to an axis forming an angle γ_1 with the z-axis[4]. The resulting two solutions for positive $n' = n'_1$ read

$$ {n'}_1^{\nearrow(\swarrow)} = -\frac{1 - (+)\cos\gamma_1^{\nearrow(\swarrow)}}{2} + \sqrt{\widetilde{E}_F - \frac{\sin^2\gamma_1^{\nearrow(\swarrow)}}{4} + (-)\widetilde{\mu}B\cos(\gamma_1^{\nearrow(\swarrow)} - \alpha)} \;, \tag{3.47}$$

where, according to the slight difference in ${n'}_1^{\nearrow}$ and ${n'}_1^{\swarrow}$, also $\gamma_1^{\nearrow}$ and $\gamma_1^{\swarrow}$ are not exactly equal. In particular, we find

$$ {n'}_1^{\nearrow} > {n'}_1^{\swarrow} \quad \longrightarrow \quad \gamma_1^{\nearrow} < \gamma_1^{\swarrow} \tag{3.48}$$

in general as is most easily seen using the geometrical interpretation, cf. the lower triangle in Fig. 3.3.

A similar discussion is necessary for the eigenstates to negative $n' = n'_2$ in the re-adjusted geometry, cf. the upper triangle in Fig. 3.3. This leads via

$$\widetilde{E}_F = {n'}_2^2 + \frac{2{n'}_2 + 1}{2}(1 \mp \cos\gamma_2) \mp \widetilde{\mu}B\cos(\gamma_2 + \alpha) \;,$$

to the equation

$$ {n'}_2^{\nearrow(\swarrow)} = -\frac{1 - (+)\cos\gamma_2^{\nearrow(\swarrow)}}{2} - \sqrt{\widetilde{E}_F - \frac{\sin^2\gamma_2^{\nearrow(\swarrow)}}{4} + (-)\widetilde{\mu}B\cos(\gamma_2^{\nearrow(\swarrow)} + \alpha)} \;, \tag{3.49}$$

eventually resulting in the relationship

$$ 0 > {n'}_2^{\nearrow} > {n'}_2^{\swarrow} \quad \longrightarrow \quad \gamma_2^{\nearrow} > \gamma_2^{\swarrow} \,. \tag{3.50}$$

We mention that the non-diagonal terms in Eq. (3.41) only vanish in the adiabatic case, leading to avoided level crossing in the general non-adiabatic situation. Therefore, ${n'}_1^{\nearrow} > {n'}_1^{\swarrow}$ and ${n'}_2^{\nearrow} > {n'}_2^{\swarrow}$ always hold as is illustrated in Fig. 3.5. If ${n'}_1^{\nearrow}$ and ${n'}_1^{\swarrow}$ (and, correspondingly, $\gamma_1^{\nearrow}$

---

[4] We will use indices $\nearrow$ and $\swarrow$ to distinguish the spin eigenstates in γ-direction. To simplify the labelling, the index $\nearrow$ is always used for the state with larger quantum number n', regardless of its Zeeman energy, see Fig. 3.5.

and $\gamma_1^{\swarrow}$) do not differ too much, the smallest gap occurs for $\gamma_1^{\nearrow} \approx \gamma_1^{\swarrow} = \pi/2$ which, in turn, can be translated into an angle $\alpha = \alpha_1$ and the corresponding magnetic field configuration. Similar relations are valid for $n'^{\nearrow}_2$ and $n'^{\swarrow}_2$, however, we find the smallest gap now for $\alpha_2 \neq \alpha_1$. More precisely, the two regions of closest approach are symmetric w.r.t. $\alpha = 0$, cf. Fig. 3.5.

For practical calculations, it has to be noted that Eqs. (3.48, 3.50) are implicit relations involving both n' and γ. The four possible n' appear as solutions of the forth order equation

$$0 = n'^4 + 2n'^3 + (1 - 2\widetilde{E}_F)n'^2 - 2(\widetilde{E}_F + \widetilde{\mu}B\cos\alpha)n' + \widetilde{E}_F^2 - \widetilde{E}_F - \widetilde{\mu}B\cos\alpha - (\widetilde{\mu}B)^2 \qquad (3.51)$$

and Eqs. (3.45, 3.46) provide the relation to the four corresponding angles γ.

Next we address the eigenvectors of the matrix $\mathcal{M}$ (3.41), i.e., we look for the constants C_1, C_2 in Eq. (3.39). We do not give the full calculation but rather the results for the four cases introduced above:

- $2n_1' + 1 > 0$:

$\lvert\nearrow(\phi)\rangle$	$\lvert\swarrow(\phi)\rangle$
$C_1 = \cos\frac{\alpha-\gamma_1^{\nearrow}}{2}$ $C_2 = \sin\frac{\alpha-\gamma_1^{\nearrow}}{2}$	$C_1 = \sin\frac{\gamma_1^{\swarrow}-\alpha}{2}$ $C_2 = \cos\frac{\gamma_1^{\swarrow}-\alpha}{2}$
$\Psi_{n_1^{\nearrow}}(\phi) = e^{in_1^{\nearrow}\phi}\begin{pmatrix}\cos\frac{\gamma_1^{\nearrow}}{2}\\ e^{i\phi'}\sin\frac{\gamma_1^{\nearrow}}{2}\end{pmatrix}$	$\Psi_{n_1^{\swarrow}}(\phi) = e^{in_1^{\swarrow}\phi}\begin{pmatrix}\sin\frac{\gamma_1^{\swarrow}}{2}\\ -e^{i\phi'}\cos\frac{\gamma_1^{\swarrow}}{2}\end{pmatrix}$

(3.52)

- $2n_2' + 1 < 0$:

$\lvert\nearrow(\phi)\rangle$	$\lvert\swarrow(\phi)\rangle$
$C_1 = \cos\frac{\alpha+\gamma_2^{\nearrow}}{2}$ $C_2 = \sin\frac{\alpha+\gamma_2^{\nearrow}}{2}$	$C_1 = \sin\frac{\gamma_2^{\swarrow}+\alpha}{2}$ $C_2 = -\cos\frac{\gamma_2^{\swarrow}+\alpha}{2}$
$\Psi_{n_2^{\nearrow}}(\phi) = e^{in_2^{\nearrow}\phi}\begin{pmatrix}\cos\frac{\gamma_2^{\nearrow}}{2}\\ -e^{i\phi'}\sin\frac{\gamma_2^{\nearrow}}{2}\end{pmatrix}$	$\Psi_{n_2^{\swarrow}}(\phi) = e^{in_2^{\swarrow}\phi}\begin{pmatrix}\sin\frac{\gamma_2^{\swarrow}}{2}\\ e^{i\phi'}\cos\frac{\gamma_2^{\swarrow}}{2}\end{pmatrix}$

(3.53)

This representation reveals the physical meaning of γ: In the generalized non-adiabatic problem it replaces α. On the other hand, in the adiabatic case (by definition) the magnetic field is strong enough to force the spin to align parallel to the magnetic field corresponding to an angle α with respect to the z-axis. In the diabatic situation the spin appears to be aligned with an angle γ. The analogy extends even further, in particular to the generalized geometric (or Aharonov-Anandan) phase that replaces the Berry phase in the non-adiabatic situation: there, γ replaces α in the interpretation in terms of the solid angle enclosed during one round trip in parameter space. For the state $\Psi_{n_1^{\nearrow}}$, where $0 < \gamma_1^{\nearrow} < \alpha$ holds, this nicely follows the intuitive interpretation that in the non-adiabatic case the magnetic field is not strong enough to force

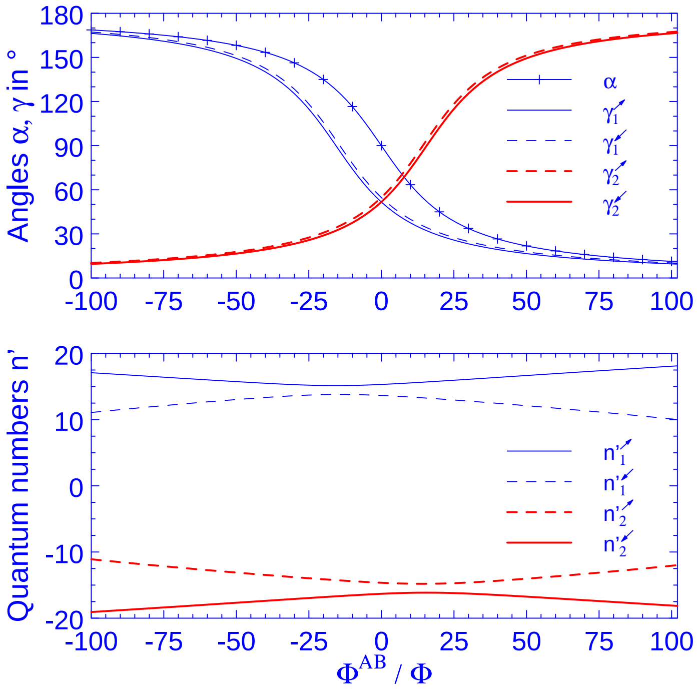

Figure 3.5: Avoided level crossing in an isolated ring subject to a wire-like magnetic field with fixed $\widetilde{E}_F = 225$, $B_\phi = 20\,\Phi_0/(\pi a^2)$ and $B_z = \Phi^{AB}/(\pi a^2)$ varied $(g^* = 1, M = m_e)$. The evolution of the angles involved is shown in the top graph. Avoided crossing occurs at $\gamma_1^{\nearrow} \approx \gamma_1^{\swarrow} = \pi/2$ for $n'^{\nearrow}_1 > n'^{\swarrow}_1$ and at $\gamma_2^{\nearrow} \approx \gamma_2^{\swarrow} = \pi/2$ for $0 > n'^{\nearrow}_2 > n'^{\swarrow}_2$.

the spin into the direction of α but to a smaller angle γ. In this sense $\left|\frac{\gamma-\alpha}{\alpha}\right|$ can be thought of as a qualitative measure for the deviation from the adiabatic case: Starting with $\gamma = \alpha$ in the adiabatic situation, γ decreases to eventually reach $\gamma = 0$ in the diabatic limit. In the context of the examples in Chapter 5 we will give an analytical expression for this, cf. Eq. (5.34) and the discussion there.

With this discussion we finish the problem of the closed one-dimensional ring, keeping it as a limiting case in the subsequent considerations. In the next chapter we will open the system by attaching leads. This will affect the quantum number n that is not an integer any more.

4 Ballistic quantum transport

In this chapter we briefly introduce the transfer matrix approach introduced by Büttiker et al. [27] to describe elastic scattering for spinless particles in one-dimensional structures. We extend this method using and improving ideas by Yi et al. [34] to describe *spin-dependent* transport in an one-dimensional ring coupled to leads. We calculate and discuss the transmission properties of this system, and find the special case of a homogeneous magnetic field that is discussed in [27] as a limiting case of the generalized result.

4.1 Spinless transport

We first consider spinless transport in order to introduce the transfer matrix method [27] in a straightforward example. We will find Aharonov-Bohm-like signatures in the transmission probability of the one-dimensional (1d) ring coupled to leads. Moreover, the results can easily be generalized to account for spin-dependent transport. We will make use of this when we calculate the transmission probability for electrons *with* spin in Section 4.2.

Although we will talk about *transmission probabilities* T_{mn} throughout this chapter, we have in mind the *(magneto-) conductance* G that is accessible in experiments. Both quantities are related in the framework of the Landauer formalism by

$$G = \frac{e^2}{h} \sum_{m,n}^{N} T_{mn} \, , \tag{4.1}$$

where the sum runs over all (partial) transmission probabilities occurring between the channels m and n of the system and N is the total number of open channels. This sum is sometimes called dimensionless conductance g and equivalent to the total transmission probability T. We will use the latter term in the following discussions. The maximum value that T (or g, respectively) can take is that of the number of open channels, N. Correspondingly, we will find T to be bounded by 1 when we discuss spinless transport in this section. However, in the case of spin-dependent transport (Section 4.2) there are two open channels corresponding to the two different spin states the electron can take and, accordingly, we have $0 \leq T \leq 2$.

4.1.1 Transfer and scattering matrices

Before we begin our investigation of transport through an 1d ring, we briefly consider transport through a linear 1d system that is divided into a left and a right part by a potential barrier $V(x)$, see Fig. 4.1. If $V(x)$ is explicitly known, we can use the 1d Schrödinger equation to find the transmission and reflection amplitudes $\beta_1, \beta_1', \beta_2, \beta_2'$ on either side. However, a compact notation for describing the elastic scattering in the ring is given by the transfer matrix $\underline{t}$ that directly relates the amplitudes on the left and the right of the scatterer, i.e.,

$$\begin{pmatrix} \beta_2 \\ \beta_2' \end{pmatrix} = \underline{t} \begin{pmatrix} \beta_1 \\ \beta_1' \end{pmatrix} . \tag{4.2}$$

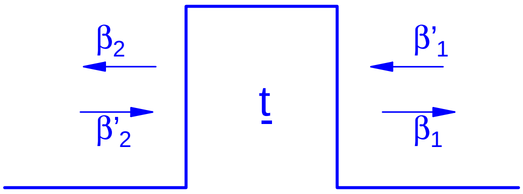

Figure 4.1: Transmission and reflection amplitudes for a scattering potential described by a transfer matrix $\underline{t}$.

Next, we apply the concept of transfer matrices to the situation illustrated in Fig. 4.2. We consider a 1d ring with two leads attached to it, dividing the ring into an upper and lower arm. Eventually we will be interested in the relation between the incoming and outgoing amplitudes in the leads, $\alpha_{1(2)}, \alpha'_{1(2)}$. It is, however, useful to split the scattering problem into (i) scattering at each junction and (ii) the transport through the arms of the ring. Correspondingly, we will introduce (i) a matrix $\underline{S}$, relating the three outgoing wave amplitudes $(\alpha', \beta', \gamma')^T$ to the three incoming waves $(\alpha, \beta, \gamma)^T$ at each of the (identical) junctions,

$$\vec{\alpha}' = \underline{S}\vec{\alpha}\,, \tag{4.3}$$

and (ii) transfer matrices $\underline{t}_1$ and $\underline{t}_2$ describing the transport through the upper and lower arm of the ring (see next subsection).

The algebraic properties of $\underline{S}$ are of physical nature:

- Current conservation $\longrightarrow$ $\underline{S}$ unitary,
- Time reversal symmetry at each junction $\longrightarrow$ $\underline{S}$ symmetric.

This reduces the number of independent parameters from nine to five. We further assume that $\underline{S}$ is symmetric w.r.t. the two branches of the ring (→ three parameters) and presume that $\underline{S}$ is real (→ one independent parameter). The latter is motivated by the intention to make $\underline{S}$ as simple as possible retaining the complexity of the scatterers into the transfer matrices $\underline{t}_1, \underline{t}_2$. One could also imagine the opposite viewpoint of two general scattering matrices while omitting the transfer matrices $\underline{t}_1, \underline{t}_2$ completely.

We write $\underline{S}$ in the form [27]

$$\underline{S} = \begin{pmatrix} -(a+b) & \sqrt{\epsilon} & \sqrt{\epsilon} \\ \sqrt{\epsilon} & a & b \\ \sqrt{\epsilon} & b & a \end{pmatrix} \tag{4.4}$$

together with the requirement of current conservation leading to[1]

$$\begin{aligned} a &= \frac{1}{2}\left(\sqrt{1-2\epsilon} - 1\right)\,, \\ b &= \frac{1}{2}\left(\sqrt{1-2\epsilon} + 1\right)\,. \end{aligned} \tag{4.5}$$

---

[1] The equations allow also for other solutions, e.g., $a_- = -a, b_- = -b$, which are of no interest here [27].

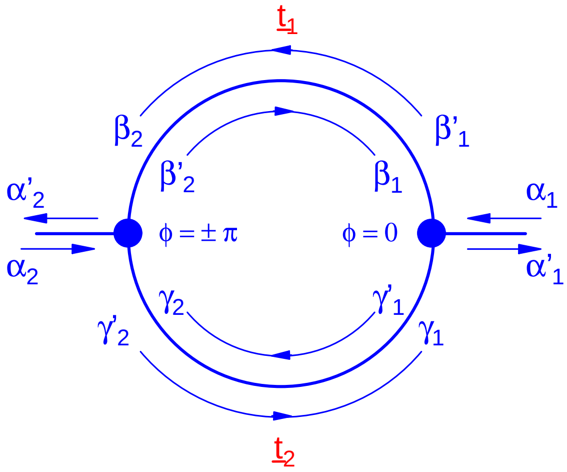

Figure 4.2: Definition of transmission and reflection amplitudes in the one-dimensional ring coupled to current leads.

The only remaining parameter, ϵ, characterizes the coupling strength between the leads and the ring: A wave is transmitted into each of the two branches of the ring with equal probability ϵ, whereas the reflection occurs with probability $(a+b)^2 = 1-2\epsilon$. In particular, for $\epsilon = 0$, all particles are reflected so that there is no coupling into the ring (zero coupling limit corresponding to the isolated ring). Note also that $b - a = 1$.

4.1.2 Transmission probability

Let us consider a wave of unit amplitude $\alpha_1 = 1$ incident from the right ($\alpha_2 = 0$). The transmission probability T of the ring is then given by $T = |\alpha_2'|^2$ so that we have to determine α_2' as a function of the coupling parameter ϵ and the flux Φ through the ring.

At the left junction we find from (4.3, 4.4) that

$$\begin{aligned} \alpha_2' &= \sqrt{\epsilon}\,(\beta_2+\gamma_2)\,, \\ \beta_2' &= a\beta_2 + b\gamma_2\,, \\ \gamma_2' &= b\beta_2 + a\gamma_2\,. \end{aligned} \tag{4.6}$$

The first two relations yield

$$\alpha_2' = \frac{\sqrt{\epsilon}}{b}\left[(b-a)\beta_2 + \beta_2'\right]\,. \tag{4.7}$$

Now we use the last two equations to relate the amplitudes γ_2', γ_2 and β_2, β_2' (see Fig. 4.2) by a matrix $\underline{S}_{\mathrm{lr}}$,

$$\begin{pmatrix}\gamma_2'\\ \gamma_2\end{pmatrix} = \underline{S}_{\mathrm{lr}}\begin{pmatrix}\beta_2\\ \beta_2'\end{pmatrix} \quad \text{with} \quad \underline{S}_{\mathrm{lr}} = \frac{1}{b}\left(\begin{array}{cc} (b^2-a^2) & a \\ -a & 1 \end{array}\right)\,. \tag{4.8}$$

Although $\det \underline{S}_{\mathrm{lr}} = 1$, $\underline{S}_{\mathrm{lr}}$ is unitary only in the zero coupling limit $\epsilon = 0$.

At the right junction we find analogously from (4.3, 4.4) that

$$\alpha_1' = -(a+b) + \sqrt{\epsilon}(\beta_1+\gamma_1)\,,$$

$$\begin{aligned} \beta_1' &= \sqrt{\epsilon} + a\beta_1 + b\gamma_1 \ , \\ \gamma_1' &= \sqrt{\epsilon} + b\beta_1 + a\gamma_1 \ , \end{aligned} \tag{4.9}$$

so that we can write

$$\begin{pmatrix} \beta_1' \\ \beta_1 \end{pmatrix} = \frac{\sqrt{\epsilon}}{b} \begin{pmatrix} b-a \\ -1 \end{pmatrix} + \underline{S}_{\mathrm{lr}} \begin{pmatrix} \gamma_1 \\ \gamma_1' \end{pmatrix} . \tag{4.10}$$

This formula describes the coupling of the wave amplitudes when passing the right junction.

In the next step, we relate the amplitude changes within each of the arms to the transfer matrices $\underline{t}_1, \underline{t}_2$:

$$\begin{pmatrix} \beta_2 \\ \beta_2' \end{pmatrix} = \underline{t}_1 \begin{pmatrix} \beta_1' \\ \beta_1 \end{pmatrix} , \tag{4.11}$$

$$\begin{pmatrix} \gamma_1 \\ \gamma_1' \end{pmatrix} = \underline{t}_2 \begin{pmatrix} \gamma_2' \\ \gamma_2 \end{pmatrix} . \tag{4.12}$$

We use Eqs. (4.11, 4.12) and (4.8, 4.10) to find a formula for the amplitudes β_1, β_1' alone,

$$\underline{\Pi} \begin{pmatrix} \beta_1' \\ \beta_1 \end{pmatrix} = -\frac{\sqrt{\epsilon}}{b} \begin{pmatrix} b-a \\ -1 \end{pmatrix} , \tag{4.13}$$

with the abbreviation

$$\underline{\Pi} = (\underline{S}_{\mathrm{lr}}\, \underline{t}_2\, \underline{S}_{\mathrm{lr}}\, \underline{t}_1 - \mathbb{I}_{2\times 2}) \ . \tag{4.14}$$

Finally, we put this into Eq. (4.7) to find

$$\begin{aligned} T &= |\alpha_2'|^2 \ , \\ \alpha_2' &= -\frac{\epsilon}{b^2} (b-a, 1)\, \underline{t}_1\, \underline{\Pi}^{-1} \begin{pmatrix} b-a \\ -1 \end{pmatrix} . \end{aligned} \tag{4.15}$$

For completeness, we mention that the reflection probability R is obtained as $R = |\alpha_1'|^2$, and, of course, $R + T = 1$ holds since we consider here only one spin channel. When we investigate spin dependent transport in Section 4.2, we have to take into account two possible spin channels (for incoming $|\uparrow\rangle$ and $|\downarrow\rangle$ electrons) such that then $R + T = 2$ is valid.

The transfer matrices $\underline{t}_1, \underline{t}_2$ comprise two phase factors each, namely the dynamic phase θ_d associated with the (pure, not generalized) kinetic energy $\widetilde{E}_F \overset{\mathrm{def}}{=} (k_{\mathrm{eff}} a)^2$, $\theta_d = \pi k_{\mathrm{eff}} a$, and an Aharonov-Bohm phase arising from the applied flux Φ^{AB} through the ring (cf. Appendix B). In the following, we will be interested in a perfectly symmetric ring. Then the Aharonov-Bohm phase for each of the arms is given by

$$\theta_{AB} \overset{\mathrm{def}}{=} \pi \frac{\Phi^{AB}}{\Phi_0} . \tag{4.16}$$

For ballistically moving particles we end up with

$$\underline{t}_1 = \underline{t}_2 = e^{-i\theta_{AB}} \begin{pmatrix} e^{i\theta_d} & 0 \\ 0 & e^{-i\theta_d} \end{pmatrix} . \tag{4.17}$$

The final result is the transmission probability T as a function of the coupling ϵ, the scaled Fermi (kinetic) energy $\widetilde{E}_F$ that enters via $\theta_d = \pi\sqrt{\widetilde{E}_F}$ and the applied flux $\Phi^{AB} = \pi a^2 B_z$ (via $\theta_{AB} = \pi\Phi/\Phi_0$) that reads [27]

$$T(\epsilon, \widetilde{E}_F, \Phi) = \frac{4\epsilon^2 \sin^2\theta_d \cos^2\theta_{AB}}{\left[a^2 + b^2\cos 2\theta_{AB} - (1-\epsilon)\cos 2\theta_d\right]^2 + \epsilon^2 \sin^2 2\theta_d} \tag{4.18}$$

and is discussed in the next paragraph.

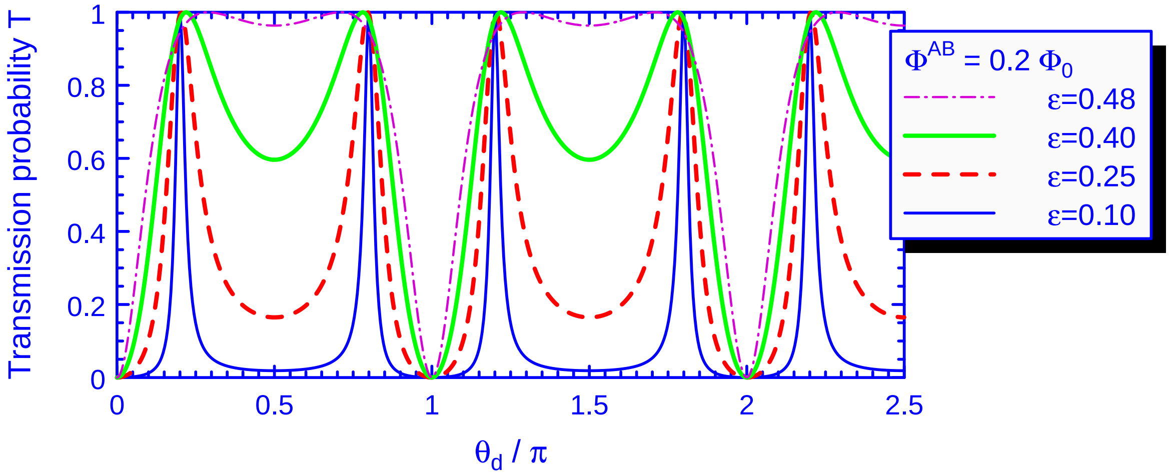

Figure 4.3: Transmission probability vs. incident momentum for an Aharonov–Bohm flux of $0.2\,\Phi_0$ through the ring. The coupling strength ϵ is varied and determines the depth of the minima, and, in particular for ϵ near the maximal coupling strength of 0.5, the position of the maxima. In the other limit of weak coupling ($\epsilon \approx 0$), the maxima become sharp resonance peaks at the eigenenergies of the closed system. The transmission probability is periodic in $\sqrt{\widetilde{E}_F} = \theta_d/\pi$ with minima occurring whenever θ_d/π is integer. Changing the Aharonov-Bohm flux shifts the position of the maxima: Decreasing θ_{AB} causes clustering of every two maxima around θ_d/π integer such that the minimum becomes ever narrower, eventually leading to the merging of the maxima at $\theta_{AB} = 0$, cf. Eq. (4.18). In the opposite direction, increasing θ_{AB} broadens the minimum until the maxima form now pairs at half-integer values of θ_d/π.

4.1.3 Aharonov-Bohm oscillations in a 1d ring

Let us first consider electrons in a *closed* ring subject to an Aharonov-Bohm flux ϕ^{AB} as discussed in Appendix B. There we employed the analogy with electrons in a 1d periodic potential and found how the *eigenenergies* of the closed system are affected by Φ^{AB}, see Eq. (B.1). Accordingly, in the zero coupling limit, ϵ =0, we expect transmission to occur only if the Fermi energy $\widetilde{E}_F = (k_{\text{eff}}a)^2$ of the incident electrons coincides with the eigenenergies, which happens if [in generalization of Eq. (B.1)]

$$k_{\text{eff}}a = n' \pm \frac{\Phi^{AB}}{\Phi_0} \equiv n\,, \quad n \in \mathbb{Z}\,. \tag{4.19}$$

Then we find a sharp peak in the transmission.

If we now increase the coupling, we find that these peaks become broader, see Fig. 4.3. They are referred to as resonance peaks, because we now deal with an open system where the eigenstates are replaced by resonances. The broadest peaks correspond to the highest coupling $\epsilon = 0.5$, and neighbouring resonance peaks might merge with increasing coupling, cf. Fig. 4.3.

In Fig. 4.4 we investigate the dependence of the transmission probability on the Aharonov-Bohm flux Φ^{AB} through the ring for finite coupling strength, i.e., the Aharonov-Bohm effect

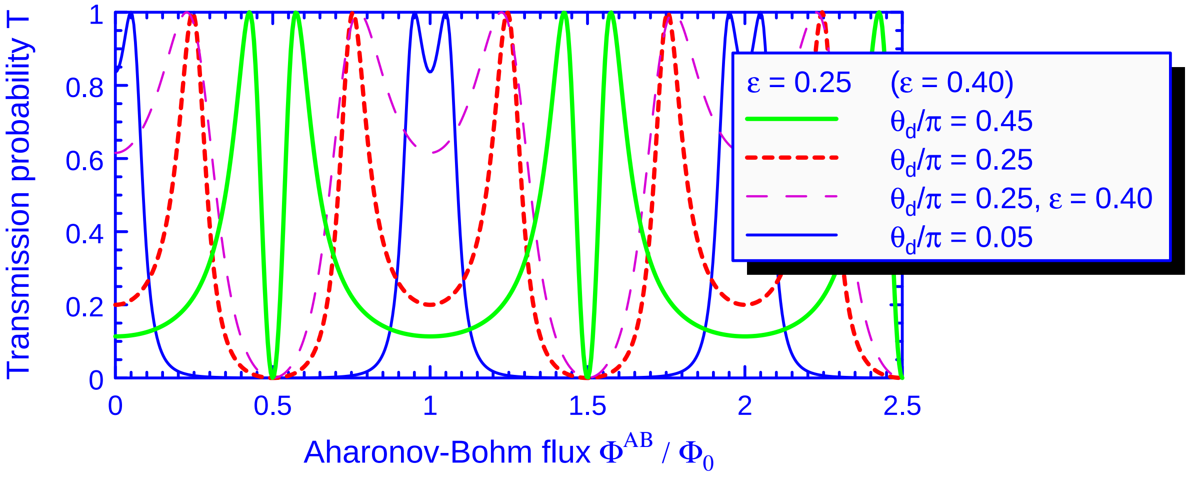

Figure 4.4: Transmission probability vs. Aharonov-Bohm flux through the ring for various incident momenta θ_d. The period is given by the flux quantum Φ_0. The data was obtained choosing a coupling strength $\epsilon = 0.25$, except for the thin dashed line where $\theta_d/\pi = 0.25$ (as for the other dashed line) and $\epsilon = 0.4$. A change in ϵ thus causes a change in the shape and the depth of the (local) minima. Note that the curves remain unchanged under the addition of integers to θ_d/π and under the reflection-like operation $\theta_d/\pi \to 1 - \theta_d/\pi$.

in an open system. One immediately realizes that, according to Eq. (4.18), T vanishes for $\cos\theta_{AB} = 0$ independent of the coupling strength, i.e., for Φ^{AB} equal to a half integer number of flux quanta penetrating the ring. Also, the transmission probability T drops to zero if θ_d is an integer multiple[2] of π for any value of the Aharonov-Bohm phase θ_{AB} and ϵ.

In Fig. 4.3 we saw that the concrete form of the oscillations, e.g., the depth of the minima, depends on the coupling parameter ϵ. This feature becomes clearer if we look at the energy-averaged transmission probability $\langle T\rangle$, that in turn depends on the (fixed) Aharonov-Bohm flux Φ^{AB} through the ring. Averaging the expression (4.18) for the transmission probability $T(\epsilon, \theta_d, \theta_{AB})$ at zero magnetic field ($\theta_{AB} = 0$) over one period in θ_d gives

$$\begin{aligned} \langle T\rangle &= \frac{1}{\pi}\int_0^\pi \frac{4\epsilon^2 \sin^2\theta_d}{\left[a^2 + b^2 - (1-\epsilon)\cos 2\theta_d\right]^2 + \epsilon^2 \sin^2 2\theta_d} \\ &= \frac{\epsilon^2}{(1-2\epsilon)\sin^2\theta_d + \epsilon^2}\,, \end{aligned}$$

that leads to the final relation

$$\langle T(\epsilon)\rangle = \frac{\epsilon}{1-\epsilon}\,. \qquad (4.20)$$

This reveals that (as expected) the averaged transmission probability increases as the coupling ϵ is increased, i.e., the ring becomes more transparent.

We use the analogy between electrons in a 1d ring and (Bloch-) electrons in a 1d periodic potential once more in order to discuss the boundary conditions. For Bloch eigenstates, the periodic boundary conditions (for $\Phi^{AB} = 0$) require $k_{\text{eff}}a$ to be an *integer* given by the kinetic energy quantum number n. This means for the closed ring that, whenever the (varied) Fermi energy allows $k_{\text{eff}}a = n$ to be an eigenvalue, the transmission shows *resonant* behaviour. Now, when we open the system and pass over to resonances, this means in particular that the values of the quantum number n are not restricted to integer values any more.

---

[2] Care must be taken if $\Phi^{AB} = 0$: The minimum then appears (singularly) sharp as the two maxima to its left and right merge as Φ^{AB} approaches zero (see Fig. 4.3).

Anticipating discussions in the subsequent sections, we would like to mention that Eq. (4.18) can be extended to describe electrons with spin in the (adiabatic) situation. This regime is characterized by the presence of two completely decoupled electron gases as described in Section 3.4. Then the Aharonov-Bohm phase θ_{AB} has to be corrected by the geometric phase, namely

$$\theta_{AB} = \frac{\pi}{\Phi_0}\Phi^{AB} \quad \longrightarrow \quad \theta_{AB}^{\nearrow(\swarrow)} = \frac{\pi}{\Phi_0}\left(\Phi^{AB} - \Phi_0\frac{\Gamma^{\nearrow(\swarrow)}}{2\pi}\right) , \tag{4.21}$$

and the kinetic energy has now a contribution due to the Zeeman interaction energy,

$$\theta_d = \pi\sqrt{\widetilde{E}_F} \quad \longrightarrow \quad \theta_d^{\nearrow(\swarrow)} = \pi\sqrt{\widetilde{E}_F + (-)\widetilde{\mu}B} \, . \tag{4.22}$$

This splitting implies an interference and beating effect due to the slightly different oscillation frequencies of the two electron species and destroys the Φ_0-periodicity related to the Aharonov-Bohm effect that is seen in Fig. 4.4. A detailed discussion is given in Section 4.3.

4.2 Spin-dependent transport

4.2.1 Transmission probability

In this part, we extend the results of the previous Section 4.1.3 to the case of electrons with spin, or, more generally, spin-$\frac{1}{2}$ particles [34]. The generalization requires essentially two changes, one of formal and one of physical nature:

1. The wave functions acquire a spin dependence at each spatial position (cf. Chapter 3) and all equations are to be formulated in the resulting product space (orbital motion $\otimes$ spin state).

   Practically, this is done by applying the direct product ($\otimes$) to the expressions derived for spinless transport, e.g., $\underline{S}_{\text{lr}} \to \underline{S}_{\text{lr}} \otimes \sigma_0$ where σ_0 is the 2×2 unit matrix in spin space. For the transfer matrices $\underline{t}_1, \underline{t}_2$ this means that they are now 4×4 matrices since they couple 2×2 spinor components.

2. Assuming electrons entering the ring with a Fermi energy E_F, the kinetic energy of the electrons will depend on their spin due to the Zeeman-interaction. Therefore, also the velocity depends on the spin direction. Since *transmission* is defined as the ratio of (transmitted and incident) *fluxes*, and

   $$\text{flux} \overset{\text{def}}{=} \sqrt{\text{velocity}} \cdot \text{amplitude} \ , \tag{4.23}$$

   the transmission coefficient is no longer equivalent to the ratio of probabilities alone but has to be corrected by the corresponding velocity factors.

According to the first point, all amplitudes α, β, γ now each consist of two components, namely $\alpha^{\uparrow}, \alpha^{\downarrow}, \beta^{\uparrow}, \beta^{\downarrow}, \gamma^{\uparrow}, \gamma^{\downarrow}$, where ↑ (↓) denotes the spin state in z-direction. Together with the second point, Eq. (4.23), this requires Eqs. (4.11, 4.12) to be replaced by

$$\begin{pmatrix} \sqrt{v_1^{\uparrow}}\beta_2^{\uparrow} \\ \sqrt{v_1^{\downarrow}}\beta_2^{\downarrow} \\ \sqrt{v_2^{\uparrow}}\beta'^{\uparrow}_2 \\ \sqrt{v_2^{\downarrow}}\beta'^{\downarrow}_2 \end{pmatrix} = \underline{t}_I \begin{pmatrix} \sqrt{v_1^{\uparrow}}\beta'^{\uparrow}_1 \\ \sqrt{v_1^{\downarrow}}\beta'^{\downarrow}_1 \\ \sqrt{v_2^{\uparrow}}\beta_1^{\uparrow} \\ \sqrt{v_2^{\downarrow}}\beta_1^{\downarrow} \end{pmatrix}, \tag{4.24}$$

$$\begin{pmatrix} \sqrt{v_1^{\uparrow}}\gamma_1^{\uparrow} \\ \sqrt{v_1^{\downarrow}}\gamma_1^{\downarrow} \\ \sqrt{v_2^{\uparrow}}\gamma'^{\uparrow}_1 \\ \sqrt{v_2^{\downarrow}}\gamma'^{\downarrow}_1 \end{pmatrix} = \underline{t}_{II} \begin{pmatrix} \sqrt{v_1^{\uparrow}}\gamma'^{\uparrow}_2 \\ \sqrt{v_1^{\downarrow}}\gamma'^{\downarrow}_2 \\ \sqrt{v_2^{\uparrow}}\gamma_2^{\uparrow} \\ \sqrt{v_2^{\downarrow}}\gamma_2^{\downarrow} \end{pmatrix}, \tag{4.25}$$

in order to relate the fluxes. The transfer matrices $\underline{t}_I, \underline{t}_{II}$ are unitary and assure particle conservation, see below. The velocities $v_1^{\uparrow(\downarrow)} (v_2^{\uparrow(\downarrow)})$ characterize the transport of counter-clockwise (clockwise) travelling electrons with ↑ (↓) w.r.t. S_z-basis.

According to the remarks above, Eq. (4.15) for the transmitted amplitude is replaced by:

$$\begin{aligned} \underline{\alpha}'_2 &= -\frac{\epsilon}{b^2}\left([b-a,1]\otimes\sigma_0\right)\underline{t}_I\,\underline{\Pi}^{-1}\left(\begin{bmatrix} b-a \\ -1 \end{bmatrix}\otimes\sigma_0\right) \\ &\overset{\text{def}}{=} -\epsilon\, m_1\,\underline{t}_I\,\underline{\Pi}^{-1} m_2\,, \end{aligned} \tag{4.26}$$

with the abbreviation

$$\underline{\Pi} = (\underline{S}_{\mathrm{lr}}\otimes\sigma_0)\,\underline{t}_{II}\,(\underline{S}_{\mathrm{lr}}\otimes\sigma_0)\,\underline{t}_I - \mathbb{1}_{2\times 2}\otimes\sigma_0\,, \tag{4.27}$$

and the substitutions

$$\begin{aligned} m_1 &\overset{\text{def}}{=} \frac{1}{b}\left([b-a,1]\otimes\sigma_0\right)\,, \\ m_2 &\overset{\text{def}}{=} \frac{1}{b}\left(\begin{bmatrix} b-a \\ -1 \end{bmatrix}\otimes\sigma_0\right)\,; \end{aligned}$$

$\underline{S}_{\mathrm{lr}}$ is defined in (4.8). The result (4.26) is similar to the one obtained in [34], however, the transfer matrices in [34] are defined between probabilities rather than fluxes, more precisely in terms of the matrices $\underline{t}_1, \underline{t}_2$ that we will introduce below. Consequently, the transfer matrices used in [34] are *not unitary*. This would lead to a transmission probability T that can take values above two, in contradiction to particle number conservation.

The total transmission probability T is again obtained from $\underline{\alpha}'_2$ which appears as a 2×2 matrix. We call this transmission matrix $\underline{T}^z$, where z indicates that all spinors are expressed w.r.t. S_z-basis (i.e. in terms of the eigenstates of σ_z),

$$\underline{T}^z = \begin{pmatrix} t_{\uparrow\uparrow} & t_{\uparrow\downarrow} \\ t_{\downarrow\uparrow} & t_{\downarrow\downarrow} \end{pmatrix}. \tag{4.28}$$

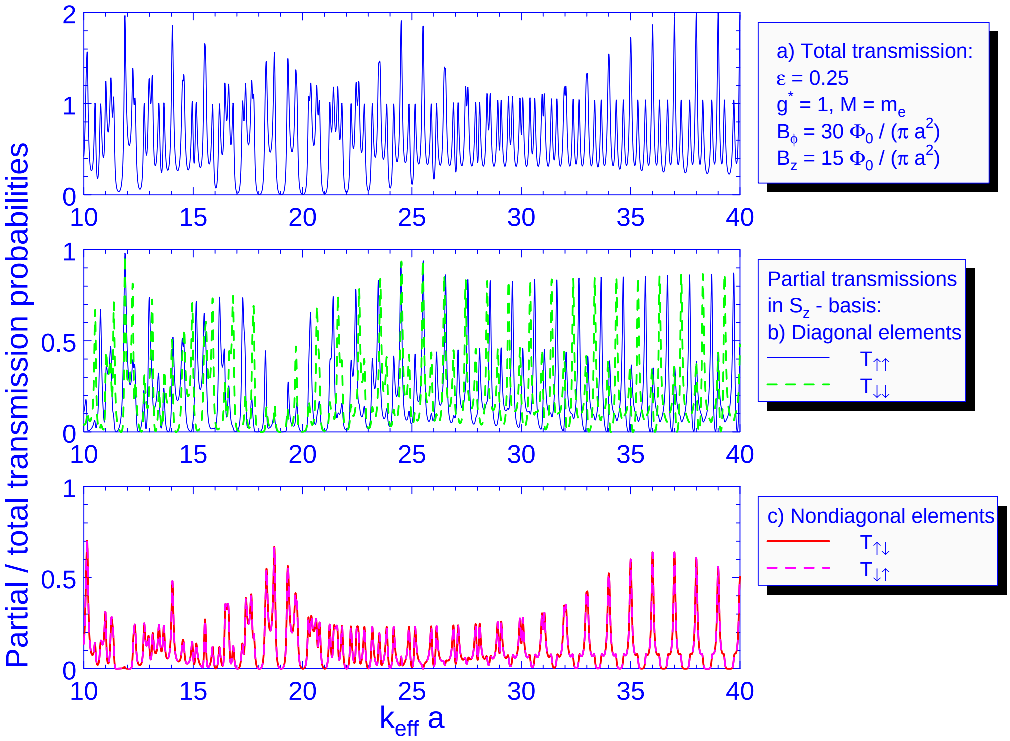

Figure 4.5: a) Total transmission probability and b), c) partial contributions vs. scaled Fermi energy $\sqrt{\widetilde{E}_F} = k_{\text{eff}} a$ of the incident electrons. The coupling strength to the current leads is set to $\epsilon = 0.25$. The magnetic field texture is chosen wire-like with the ϕ-component twice as large as the z-component corresponding to $\alpha = \arctan 2 \approx 63.4^o$. Note the coincidence of the non-diagonal elements in c), arising from the symmetry w.r.t. reflections about an axis perpendicular to the leads through the centre of the ring.

Its four entries measure the transmission amplitudes between all possible spin state combinations in S_z-basis. For unpolarized incident electrons, T is given by

$$T = |t_{\uparrow\uparrow}|^2 + |t_{\uparrow\downarrow}|^2 + |t_{\downarrow\uparrow}|^2 + |t_{\downarrow\downarrow}|^2 \overset{\text{def}}{=} T_{\uparrow\uparrow} + T_{\uparrow\downarrow} + T_{\downarrow\uparrow} + T_{\downarrow\downarrow}\,. \tag{4.29}$$

For practical calculations, the transmission probability for spin-dependent transport has to be evaluated numerically. In Fig. 4.5, we show an example for the full as well as the partial transmission probabilities, anticipating the results of Section 4.2.2.

It is worth analyzing the structure of $\underline{\alpha}'_2$ and $\underline{\Pi}$ (4.26, 4.27) where on first sight the symmetry that one expects when desribing a perfectly symmetric ring is not manifest. In fact, this can easily be overcome. We introduce the matrix

$$\underline{m}_3 = \frac{1}{b}\begin{pmatrix} b^2 - a^2 & 0 & a & 0 \\ 0 & b^2 - a^2 & 0 & a \\ -a & 0 & 1 & 0 \\ 0 & -a & 0 & 1 \end{pmatrix} \overset{\text{def}}{=} \underline{N}_1\,\underline{N}_2\,, \tag{4.30}$$

with the decomposition

$$\underline{N}_1 = \frac{1}{\sqrt{2b}} \begin{pmatrix} b+a & 0 & -(b-a) & 0 \\ 0 & b+a & 0 & -(b-a) \\ 1 & 0 & 1 & 0 \\ 0 & 1 & 0 & 1 \end{pmatrix} \tag{4.31}$$

and

$$\underline{N}_2 = \frac{1}{\sqrt{2b}} \begin{pmatrix} b-a & 0 & 1 & 0 \\ 0 & b-a & 0 & 1 \\ -(b+a) & 0 & 1 & 0 \\ 0 & -(b+a) & 0 & 1 \end{pmatrix} . \tag{4.32}$$

With this notation, we transform (4.26),

$$\begin{aligned} \underline{\alpha}'_2 &= -\epsilon\, m_1\, \underline{t}_I\, \underline{\Pi}^{-1}\, m_2 \\ &= -\epsilon\, m_1\, \underline{t}_I\, (\underline{m}_3 \underline{t}_{II} \underline{m}_3 \underline{t}_I - \mathbb{I}_{4\times 4})^{-1}\, m_2 \\ &= -\epsilon\, m_1\, \underline{t}_I\, \left[(\underline{N}_1 \underline{N}_2 \underline{t}_{II} \underline{N}_1 \underline{N}_2 - \underline{t}_I^{-1})\, \underline{t}_I \right]^{-1}\, m_2 \\ &= -\epsilon\, m_1\, \left[(\underline{N}_2 \underline{t}_{II} \underline{N}_1 - \underline{N}_1^{-1} \underline{t}_I^{-1} \underline{N}_2^{-1}) \underline{N}_2 \right]^{-1} \underline{N}_1^{-1}\, m_2 \, , \end{aligned}$$

ending up with the symmetric structure

$$\underline{\alpha}'_2 = -\epsilon\, m_1\, \underline{N}_2^{-1}\, \left[\underline{N}_2 \underline{t}_{II} \underline{N}_1 - \underline{N}_1^{-1} \underline{t}_I^{-1} \underline{N}_2^{-1} \right]^{-1} \underline{N}_1^{-1}\, m_2 \, . \tag{4.33}$$

We will see in the following sections that this expression allows for a much simpler handling of the transmission probability. In particular, if we introduce

$$\underline{a} \overset{\text{def}}{=} \left[\underline{N}_2 \underline{t}_{II} \underline{N}_1 - \underline{N}_1^{-1} \underline{t}_I^{-1} \underline{N}_2^{-1} \right]^{-1} \, , \tag{4.34}$$

we see from (4.33) that the term to the left and right of $\underline{a}$ projects out just the *upper right* corner of $\underline{a}$, so that we actually need to calculate the entries $a_{13}, a_{14}, a_{23}, a_{24}$ of the matrix $\underline{a}$:

$$\underline{\alpha}'_2 = -\epsilon\, \frac{2}{b} \begin{pmatrix} a_{13} & a_{14} \\ a_{23} & a_{24} \end{pmatrix} \equiv \begin{pmatrix} t_{\uparrow\uparrow} & t_{\uparrow\downarrow} \\ t_{\downarrow\uparrow} & t_{\downarrow\downarrow} \end{pmatrix} = \underline{T}^z \, . \tag{4.35}$$

4.2.2 Transfer matrices

In this section we will determine the transfer matrices $\underline{t}_I$ and $\underline{t}_{II}$ that we need in order to calculate the transmission probability T. We will do so by first finding the transfer matrices $\underline{t}_1, \underline{t}_2$ that relate the wave function amplitudes,

$$\begin{pmatrix} \beta_2^{\uparrow} \\ \beta_2^{\downarrow} \\ \beta'^{\uparrow}_2 \\ \beta'^{\downarrow}_2 \end{pmatrix} = \underline{t}_1 \begin{pmatrix} \beta'^{\uparrow}_1 \\ \beta'^{\downarrow}_1 \\ \beta_1^{\uparrow} \\ \beta_1^{\downarrow} \end{pmatrix} , \quad \begin{pmatrix} \gamma_1^{\uparrow} \\ \gamma_1^{\downarrow} \\ \gamma'^{\uparrow}_1 \\ \gamma'^{\downarrow}_1 \end{pmatrix} = \underline{t}_2 \begin{pmatrix} \gamma'^{\uparrow}_2 \\ \gamma'^{\downarrow}_2 \\ \gamma_2^{\uparrow} \\ \gamma_2^{\downarrow} \end{pmatrix} . \tag{4.36}$$

For convenience, we introduce the velocity matrices

$$\underline{v}_1 \overset{\text{def}}{=} \begin{pmatrix} \sqrt{v_1^{\uparrow}} & 0 \\ 0 & \sqrt{v_1^{\downarrow}} \end{pmatrix}, \quad \underline{v}_2 \overset{\text{def}}{=} \begin{pmatrix} \sqrt{v_2^{\uparrow}} & 0 \\ 0 & \sqrt{v_2^{\downarrow}} \end{pmatrix}. \tag{4.37}$$

The relation between the matrices $\underline{t}_1, \underline{t}_2$ above and $\underline{t}_I, \underline{t}_{II}$ in Eqs. (4.24, 4.25) is then given by

$$\begin{aligned} \underline{t}_I &= \underline{v}_1 \underline{t}_1 \underline{v}_1^{-1}, \\ \underline{t}_{II} &= \underline{v}_2' \underline{t}_2 \underline{v}_2^{-1}. \end{aligned} \tag{4.38}$$

In order to determine first of all the matrix $\underline{t}_1$ in Eq. (4.36), we consider the electrons in the open ballistic ring, see Chapter 3. All electrons are transported at fixed Fermi energy $\widetilde{E}_F = 2Ma^2E_F$, see Eq. (3.42). Each state is a superposition of the four wave functions at energy E_F that were derived in Chapter 3. The four basis states for the open ring are given in (3.52, 3.53). In terms of these functions, we can express the amplitude of the wave propagating counter-clockwise (i.e., $n' \overset{\text{def}}{=} n_1'$, $2n_1'+1 > 0$, $n_1 = n_1' + ea^2B_z/2$) by means of the two components $\Psi_{n_1^{\prime\nearrow}}(\phi)$ and $\Psi_{n_1^{\prime\swarrow}}(\phi)$, substituting $\zeta \overset{\text{def}}{=} \gamma/2$,

$$\Psi_{n_1^{\prime\nearrow}}(\phi) = e^{in_1^{\prime\nearrow}\phi} \begin{pmatrix} \cos\zeta_1^{\nearrow} \\ e^{i\phi'}\sin\zeta_1^{\nearrow} \end{pmatrix} \quad \text{and} \quad \Psi_{n_1^{\prime\swarrow}}(\phi) = e^{in_1^{\prime\swarrow}\phi} \begin{pmatrix} \sin\zeta_1^{\swarrow} \\ -e^{i\phi'}\cos\zeta_1^{\swarrow} \end{pmatrix} \tag{4.39}$$

We hence obtain the amplitude β_1' at $\phi = 0$ as a superposition with appropriate coefficients c_1, c_2,

$$\beta_1' \overset{\text{def}}{=} \begin{pmatrix} \beta'^{\uparrow}_1 \\ \beta'^{\downarrow}_1 \end{pmatrix} = c_1 \Psi_{n_1^{\prime\nearrow}}(0) + c_2 \Psi_{n_1^{\prime\swarrow}}(0). \tag{4.40}$$

Since we exclude scattering processes within the arms of the ring, the amplitude β_2 at $\phi = \pi$ is

$$\beta_2 \overset{\text{def}}{=} \begin{pmatrix} \beta_2^{\uparrow} \\ \beta_2^{\downarrow} \end{pmatrix} = c_1 \Psi_{n_1^{\prime\nearrow}}(\pi) + c_2 \Psi_{n_1^{\prime\swarrow}}(\pi). \tag{4.41}$$

To complete the set of amplitudes that is connected by the transfer matrix $\underline{t}_1$, we have to take into account the clockwise propagation (now with coefficients d_1, d_2) as well:

$$\beta_1 \overset{\text{def}}{=} \begin{pmatrix} \beta_1^{\uparrow} \\ \beta_1^{\downarrow} \end{pmatrix} = d_1 \Psi_{n_2^{\prime\nearrow}}(0) + d_2 \Psi_{n_2^{\prime\swarrow}}(0), \tag{4.42}$$

and

$$\beta_2' \overset{\text{def}}{=} \begin{pmatrix} \beta'^{\uparrow}_2 \\ \beta'^{\downarrow}_2 \end{pmatrix} = d_1 \Psi_{n_2^{\prime\nearrow}}(\pi) + d_2 \Psi_{n_2^{\prime\swarrow}}(\pi). \tag{4.43}$$

Now we can determine the transfer matrix $\underline{t}_1$ in (4.11). There are several possibilities to do so; we will adopt an approach that makes the meaning of the transfer matrices more transparent. We start by considering the amplitudes of counter-clockwise travelling waves,

$$\begin{pmatrix} \beta_2^{\uparrow} \\ \beta_2^{\downarrow} \end{pmatrix} = \begin{pmatrix} g_1 & g_2 \\ g_3 & g_4 \end{pmatrix} \begin{pmatrix} \beta'^{\uparrow}_1 \\ \beta'^{\downarrow}_1 \end{pmatrix}, \tag{4.44}$$

which is the upper left 2×2 matrix of $\underline{t}_1$. Now we make use of the freedom in the choice of the coefficients c_1, c_2 in (4.40) and choose them as

$$\begin{aligned} c_1 \overset{\text{def}}{=} c_1^{\uparrow} &= \frac{\cos\zeta_1^{\swarrow}}{\cos\zeta_1^{\nearrow}\cos\zeta_1^{\swarrow} + \sin\zeta_1^{\nearrow}\sin\zeta_1^{\swarrow}}\,, \\ c_2 \overset{\text{def}}{=} c_2^{\uparrow} &= \frac{\sin\zeta_1^{\nearrow}}{\cos\zeta_1^{\nearrow}\cos\zeta_1^{\swarrow} + \sin\zeta_1^{\nearrow}\sin\zeta_1^{\swarrow}}\,, \end{aligned} \tag{4.45}$$

which is motivated by the result

$$\beta_1'(c_1^{\uparrow}, c_2^{\uparrow}) = \begin{pmatrix} 1 \\ 0 \end{pmatrix}. \tag{4.46}$$

This just means that the special choice (4.45) for c_1, c_2 constitutes a $\binom{1}{0} \overset{\text{def}}{=} \uparrow$-state in S_z-basis. Evaluating (4.44) with this special choice, we find immediately

$$\begin{aligned} \beta_2^{\uparrow}(c_1^{\uparrow}, c_2^{\uparrow}) &= g_1\,, \\ \beta_2^{\downarrow}(c_1^{\uparrow}, c_2^{\uparrow}) &= g_3\,, \end{aligned} \tag{4.47}$$

which illuminates the meaning of g_1 and g_3: for a $\uparrow$-state of unit amplitude entering the ring, g_1 gives the amplitude that it remains in this state, whereas g_3 accounts for spin-flip processes. This interpretation applies to the other entries accordingly.

We analyze Eq. (4.47) with the help of (4.41), applying the well-known relations between trigonometric functions [55] to yield

$$\begin{aligned} g_1 &= \frac{1}{\cos(\zeta_1^{\nearrow} - \zeta_1^{\swarrow})}\left(e^{in_1^{\nearrow}\pi}\cos\zeta_1^{\nearrow}\cos\zeta_1^{\swarrow} + e^{in_1^{\swarrow}\pi}\sin\zeta_1^{\nearrow}\sin\zeta_1^{\swarrow}\right)\,, \\ g_3 &= \frac{-e^{i\phi_t}}{\cos(\zeta_1^{\nearrow} - \zeta_1^{\swarrow})}\left(e^{in_1^{\nearrow}\pi} - e^{in_1^{\swarrow}\pi}\right)\sin\zeta_1^{\nearrow}\cos\zeta_1^{\swarrow}\,, \end{aligned} \tag{4.48}$$

where ϕ_t is the field texture parameter introduced in Eq. (3.11).

The analogous procedure, performed with

$$\begin{aligned} c_1 \overset{\text{def}}{=} c_1^{\downarrow} &= \frac{e^{-i\phi_t}\sin\zeta_1^{\swarrow}}{\cos\zeta_1^{\nearrow}\cos\zeta_1^{\swarrow} + \sin\zeta_1^{\nearrow}\sin\zeta_1^{\swarrow}}\,, \\ c_2 \overset{\text{def}}{=} c_2^{\downarrow} &= \frac{-e^{-i\phi_t}\cos\zeta_1^{\nearrow}}{\cos\zeta_1^{\nearrow}\cos\zeta_1^{\swarrow} + \sin\zeta_1^{\nearrow}\sin\zeta_1^{\swarrow}}\,, \end{aligned} \tag{4.49}$$

now, of course, guided by the resulting $\binom{0}{1} \overset{\text{def}}{=} \downarrow$-state in S_z-basis, allows us to determine g_2 and g_4:

$$\begin{aligned} g_2 &= \frac{e^{-i\phi_t}}{\cos(\zeta_1^{\nearrow} - \zeta_1^{\swarrow})}\left(e^{in_1^{\nearrow}\pi} - e^{in_1^{\swarrow}\pi}\right)\cos\zeta_1^{\nearrow}\sin\zeta_1^{\swarrow}\,, \\ g_4 &= \frac{-1}{\cos(\zeta_1^{\nearrow} - \zeta_1^{\swarrow})}\left(e^{in_1^{\nearrow}\pi}\sin\zeta_1^{\nearrow}\sin\zeta_1^{\swarrow} + e^{in_1^{\swarrow}\pi}\cos\zeta_1^{\nearrow}\cos\zeta_1^{\swarrow}\right)\,. \end{aligned} \tag{4.50}$$

To complete the procedure necessary to determine the transfer matrix $\underline{t}_1$, we now turn towards the clockwise propagating waves given in Eqs. (4.42, 4.43). The basis states, cf. Eq. (3.53),

$$\Psi_{n_2^{\nearrow}}(\phi) = e^{in_2^{\nearrow}\phi}\begin{pmatrix} \cos\zeta_2^{\nearrow} \\ -e^{i\phi'}\sin\zeta_2^{\nearrow} \end{pmatrix} \quad \text{and} \quad \Psi_{n_2^{\swarrow}} = e^{in_2^{\swarrow}\phi}\begin{pmatrix} \sin\zeta_2^{\swarrow} \\ e^{i\phi'}\cos\zeta_2^{\swarrow} \end{pmatrix}\,, \tag{4.51}$$

differ slightly from the clockwise propagating basis states (4.39). Therefore the calculation now yields (switching from $c_i \to d_i$ and $g_i \to h_i$ in the notation)

$$\begin{aligned} d_1^{\uparrow} &= \frac{\cos\zeta_2^{\swarrow}}{\cos\zeta_2^{\nearrow}\cos\zeta_2^{\swarrow} + \sin\zeta_2^{\nearrow}\sin\zeta_2^{\swarrow}}\,, \\ d_2^{\uparrow} &= \frac{\sin\zeta_2^{\nearrow}}{\cos\zeta_2^{\nearrow}\cos\zeta_2^{\swarrow} + \sin\zeta_2^{\nearrow}\sin\zeta_2^{\swarrow}}\,, \end{aligned} \tag{4.52}$$

for constructing an incident ↑-state, and

$$\begin{aligned} d_1^{\downarrow} &= \frac{-e^{-i\phi_t}\sin\zeta_2^{\swarrow}}{\cos\zeta_2^{\nearrow}\cos\zeta_2^{\swarrow} + \sin\zeta_2^{\nearrow}\sin\zeta_2^{\swarrow}}\,, \\ d_2^{\downarrow} &= \frac{e^{-i\phi_t}\cos\zeta_2^{\nearrow}}{\cos\zeta_2^{\nearrow}\cos\zeta_2^{\swarrow} + \sin\zeta_2^{\nearrow}\sin\zeta_2^{\swarrow}}\,, \end{aligned} \tag{4.53}$$

for the ↓-state. Eventually, we obtain the matrix elements that connect the amplitudes β at the entrance and the exit of the ring, namely,

$$\begin{pmatrix} \beta'^{\uparrow}_2 \\ \beta'^{\downarrow}_2 \end{pmatrix} = \begin{pmatrix} h_1 & h_2 \\ h_3 & h_4 \end{pmatrix} \begin{pmatrix} \beta^{\uparrow}_1 \\ \beta^{\downarrow}_1 \end{pmatrix}, \tag{4.54}$$

which is the lower right 2 × 2 matrix of $\underline{t}_1$, i.e.

$$\begin{aligned} h_1 &= \frac{1}{\cos(\zeta_2^{\nearrow} - \zeta_2^{\swarrow})}\left(e^{in_2^{\nearrow}\pi}\cos\zeta_2^{\nearrow}\cos\zeta_2^{\swarrow} + e^{in_2^{\swarrow}\pi}\sin\zeta_2^{\nearrow}\sin\zeta_2^{\swarrow}\right)\,, \\ h_3 &= \frac{e^{i\phi_t}}{\cos(\zeta_2^{\nearrow} - \zeta_2^{\swarrow})}\left(e^{in_2^{\nearrow}\pi} - e^{in_2^{\swarrow}\pi}\right)\sin\zeta_2^{\nearrow}\cos\zeta_2^{\swarrow}\,, \\ h_2 &= \frac{-e^{-i\phi_t}}{\cos(\zeta_2^{\nearrow} - \zeta_2^{\swarrow})}\left(e^{in_2^{\nearrow}\pi} - e^{in_2^{\swarrow}\pi}\right)\cos\zeta_2^{\nearrow}\sin\zeta_2^{\swarrow}\,, \\ h_4 &= \frac{-1}{\cos(\zeta_2^{\nearrow} - \zeta_2^{\swarrow})}\left(e^{in_2^{\nearrow}\pi}\sin\zeta_2^{\nearrow}\sin\zeta_2^{\swarrow} + e^{in_2^{\swarrow}\pi}\cos\zeta_2^{\nearrow}\cos\zeta_2^{\swarrow}\right)\,. \end{aligned} \tag{4.55}$$

Now we can specify the first transfer matrix $\underline{t}_1$: We have determined the two diagonal 2 × 2 matrices that constitute $\underline{t}_1$ since the off-diagonal 2 × 2 matrices, that would describe waves that change their sense of rotation, are zero. (This is forbidden due to the conservation of the angular momentum $L_z = -id/d\phi + 1/2\sigma_z$ in z-direction.) Any propagating wave with fixed energy possesses a well defined momentum that excludes reflection processes. Hence we find

$$\underline{t}_1 = \begin{pmatrix} g_1 & g_2 & 0 & 0 \\ g_3 & g_4 & 0 & 0 \\ 0 & 0 & h_1 & h_2 \\ 0 & 0 & h_3 & h_4 \end{pmatrix}. \tag{4.56}$$

Using relation (4.38), we obtain

$$\underline{t}_I = \begin{pmatrix} g_1 & \sqrt{v_1^{\uparrow}/v_1^{\downarrow}}\, g_2 & 0 & 0 \\ \sqrt{v_1^{\downarrow}/v_1^{\uparrow}}\, g_3 & g_4 & 0 & 0 \\ 0 & 0 & h_1 & \sqrt{v_2^{\uparrow}/v_2^{\downarrow}}\, h_2 \\ 0 & 0 & \sqrt{v_2^{\downarrow}/v_2^{\uparrow}}\, h_3 & h_4 \end{pmatrix} \overset{\text{def}}{=} \begin{pmatrix} g_1 & \widetilde{g}_2 & 0 & 0 \\ \widetilde{g}_3 & g_4 & 0 & 0 \\ 0 & 0 & h_1 & \widetilde{h}_2 \\ 0 & 0 & \widetilde{h}_3 & h_4 \end{pmatrix} . \quad (4.57)$$

Next, we have to find the velocity ratios occurring in $\underline{t}_I$. The origin of the different velocities lies in the different spin directions w.r.t. the magnetic field for fixed Fermi energy. They are characterized by different Zeeman energies necessary for the alignment of the spins leaving a different amount for the kinetic energy along the ring.

We start by noting that the Hamiltonian H in (3.3) is Hermitian. This implies the conservation of particles or of the global integrated quantum mechanical probability density, respectively, which translates into a (local) continuity equation. In our system, the propagation takes place along the ring and no additional particle sources or drains are present. Hence we finally arrive at the conservation of the quantum mechanical current density, which leads to the requirement of unitarity of the transfer matrix $\underline{t}_I$ (and, of course, also of $\underline{t}_{II}$). As a consequence of this, the following equations expressing the orthonormality of the eigenvectors (which are just the columns of $\underline{t}_I$) result:

$$\begin{aligned} g_1^* g_1 + \widetilde{g}_3^* \widetilde{g}_3 &= 1\,, \\ \widetilde{g}_2^* \widetilde{g}_2 + g_4^* g_4 &= 1\,, \\ g_1^* \widetilde{g}_2 + \widetilde{g}_3^* g_4 &= 0\,, \\ g_1^* \widetilde{g}_3 + \widetilde{g}_2^* g_4 &= 0\,, \end{aligned}$$

(and a similar set of equations for the h_i). g_1 and g_4 obviously fulfill the relation

$$\begin{aligned} g_1^* g_1 = g_4^* g_4 \;=\; & \frac{1}{\cos^2(\zeta_1^{\nearrow} - \zeta_1^{\swarrow})} \times \\ & \Big[\cos^2 \zeta_1^{\nearrow} \cos^2 \zeta_1^{\swarrow} + \sin^2 \zeta_1^{\nearrow} \sin^2 \zeta_1^{\swarrow} + \\ & \left(e^{i(n_1^{\nearrow} - n_1^{\swarrow})\pi} - e^{-i(n_1^{\nearrow} - n_1^{\swarrow})\pi} \right) \cos \zeta_1^{\nearrow} \cos \zeta_1^{\swarrow} \sin \zeta_1^{\nearrow} \sin \zeta_1^{\swarrow} \Big] \,, \end{aligned}$$

which leads to

$$\widetilde{g}_2^* \widetilde{g}_2 = \widetilde{g}_3^* \widetilde{g}_3 = 1 - g_1^* g_1 \,. \quad (4.58)$$

After evaluation we find

$$\widetilde{g}_2^* \widetilde{g}_2 = \widetilde{g}_3^* \widetilde{g}_3 = \frac{1}{\cos^2(\zeta_1^{\nearrow} - \zeta_1^{\swarrow})} \left[2 - e^{i(n_1^{\nearrow} - n_1^{\swarrow})\pi} - e^{-i(n_1^{\nearrow} - n_1^{\swarrow})\pi} \right] \cos \zeta_1^{\nearrow} \cos \zeta_1^{\swarrow} \sin \zeta_1^{\nearrow} \sin \zeta_1^{\swarrow} \,. \quad (4.59)$$

Note the closer similarity between $\widetilde{g}_2$ and $\widetilde{g}_3$ than between the matrix elements g_2 and g_3 in $\underline{t}_1$.

Comparing the last equation with the expressions (4.48, 4.50), we read off the velocity ratio

$$\frac{v_1^{\uparrow}}{v_1^{\downarrow}} = \frac{\cos \zeta_1^{\swarrow} \sin \zeta_1^{\nearrow}}{\cos \zeta_1^{\nearrow} \sin \zeta_1^{\swarrow}} = \frac{\tan \zeta_1^{\nearrow}}{\tan \zeta_1^{\swarrow}} \,. \quad (4.60)$$

Repetition of the calculation replacing $g_i \to h_i$ is straightforward and the velocity ratio for clockwise propagating waves becomes

$$\frac{v_2^{\uparrow}}{v_2^{\downarrow}} = \frac{\cos\zeta_2^{\swarrow}\sin\zeta_2^{\nearrow}}{\cos\zeta_2^{\nearrow}\sin\zeta_2^{\swarrow}} = \frac{\tan\zeta_2^{\nearrow}}{\tan\zeta_2^{\swarrow}}\,, \tag{4.61}$$

completing the ingredients required to compute transmission probabilities. Eqs. (4.60, 4.61) can be easily checked by actually calculating the velocity expectation values.

The calculation for the transfer matrix $\underline{t}_{II}$ relating the amplitudes in the lower branch of the ring is very similar. The only difference is that we now have to look at amplitudes at angles $\phi = -\pi$ evolving to angles $\phi = 0$! We refrain from giving the details and just state the results. We keep the notations essentially as before but switch to capital letters for the coefficients (i.e., $c \to C, g \to G$, etc.). To illustrate the procedure, we consider counter-clockwise travelling waves in the lower branch of the ring, i.e.,

$$\begin{pmatrix}\gamma_1^{\uparrow}\\ \gamma_1^{\downarrow}\end{pmatrix} = \begin{pmatrix} G_1 & G_2 \\ G_3 & G_4 \end{pmatrix}\begin{pmatrix}\gamma'^{\uparrow}_2\\ \gamma'^{\downarrow}_2\end{pmatrix}, \tag{4.62}$$

which is the upper left 2×2 matrix of $\underline{t}_2$. We first look at a $\uparrow$-state w.r.t. S_z-basis at the position $\phi = 0$ which in analogy to Eqs. (4.45, 4.46) is provided choosing the coefficients

$$\begin{aligned} C_1^{\uparrow} &= \frac{\cos\zeta_1^{\swarrow} e^{in_1^{\nearrow}\pi}}{\cos\zeta_1^{\nearrow}\cos\zeta_1^{\swarrow} + \sin\zeta_1^{\nearrow}\sin\zeta_1^{\swarrow}}\,, \\ C_2^{\uparrow} &= \frac{\sin\zeta_1^{\nearrow} e^{in_1^{\swarrow}\pi}}{\cos\zeta_1^{\nearrow}\cos\zeta_1^{\swarrow} + \sin\zeta_1^{\nearrow}\sin\zeta_1^{\swarrow}}\,. \end{aligned} \tag{4.63}$$

Note the additional exponential term in comparison to Eq. (4.45). These equations yield eventually

$$\begin{aligned} G_1 &= \frac{1}{\cos(\zeta_1^{\nearrow} - \zeta_1^{\swarrow})}\left(e^{in_1^{\nearrow}\pi}\cos\zeta_1^{\nearrow}\cos\zeta_1^{\swarrow} + e^{in_1^{\swarrow}\pi}\sin\zeta_1^{\nearrow}\sin\zeta_1^{\swarrow}\right) = g_1\,, \\ G_3 &= \frac{e^{i\phi_t}}{\cos(\zeta_1^{\nearrow} - \zeta_1^{\swarrow})}\left(e^{in_1^{\nearrow}\pi} - e^{in_1^{\swarrow}\pi}\right)\sin\zeta_1^{\nearrow}\cos\zeta_1^{\swarrow} = -g_3\,. \end{aligned} \tag{4.64}$$

The analogous procedure, performed with

$$\begin{aligned} C_1^{\downarrow} &= \frac{-e^{-i\phi_t} e^{in_1^{\nearrow}\pi}\sin\zeta_1^{\swarrow}}{\cos\zeta_1^{\nearrow}\cos\zeta_1^{\swarrow} + \sin\zeta_1^{\nearrow}\sin\zeta_1^{\swarrow}}\,, \\ C_2^{\downarrow} &= \frac{e^{-i\phi_t} e^{in_1^{\swarrow}\pi}\cos\zeta_1^{\nearrow}}{\cos\zeta_1^{\nearrow}\cos\zeta_1^{\swarrow} + \sin\zeta_1^{\nearrow}\sin\zeta_1^{\swarrow}}\,, \end{aligned} \tag{4.65}$$

in order to obtain a $\downarrow$-state in S_z-basis, leads to

$$\begin{aligned} G_2 &= \frac{-e^{-i\phi_t}}{\cos(\zeta_1^{\nearrow} - \zeta_1^{\swarrow})}\left(e^{in_1^{\nearrow}\pi} - e^{in_1^{\swarrow}\pi}\right)\cos\zeta_1^{\nearrow}\sin\zeta_1^{\swarrow} = -g_2\,, \\ G_4 &= \frac{-1}{\cos(\zeta_1^{\nearrow} - \zeta_1^{\swarrow})}\left(e^{in_1^{\nearrow}\pi}\sin\zeta_1^{\nearrow}\sin\zeta_1^{\swarrow} + e^{in_1^{\swarrow}\pi}\cos\zeta_1^{\nearrow}\cos\zeta_1^{\swarrow}\right) = g_4\,. \end{aligned} \tag{4.66}$$

The evaluation of the matrix elements H_1, H_2, H_3, H_4 that relate the clockwise propagating amplitudes can be done in the same spirit – in principle the subscript 1 has to be replaced by the subscript 2 indicating clockwise movement together with the appropriate changes in the notation. Accordingly, we obtain the relations

$$\begin{aligned} H_1 &= h_1\,, \qquad & H_2 &= -h_2\,, \\ H_4 &= h_4\,, \qquad & H_3 &= -h_3\,, \end{aligned} \tag{4.67}$$

so that finally we find

$$\underline{t}_2 = \begin{pmatrix} g_1 & -g_2 & 0 & 0 \\ -g_3 & g_4 & 0 & 0 \\ 0 & 0 & h_1 & -h_2 \\ 0 & 0 & -h_3 & h_4 \end{pmatrix} . \tag{4.68}$$

Again, from Eq. (4.38) we find

$$\underline{t}_{II} = \begin{pmatrix} g_1 & -\sqrt{v_1^{\uparrow}/v_1^{\downarrow}}\, g_2 & 0 & 0 \\ -\sqrt{v_1^{\downarrow}/v_1^{\uparrow}}\, g_3 & g_4 & 0 & 0 \\ 0 & 0 & h_1 & -\sqrt{v_2^{\downarrow}/v_2^{\uparrow}}\, h_2 \\ 0 & 0 & -\sqrt{v_2^{\uparrow}/v_2^{\downarrow}}\, h_3 & h_4\,, \end{pmatrix} \tag{4.69}$$

which is a unitary matrix (in contrast to the matrix $\underline{t}_2$ used in [34]).

Now we have provided all ingredients to calculate transmission amplitudes and probabilities according to Eqs. (4.35, 4.29) for any[3] desired field configuration that respects rotational symmetry. One example is shown in Fig. 4.5, a part of which is zoomed in Fig. 4.7b.

4.3 Uniform field perpendicular to the ring as limiting case

The situation of a homogeneous magnetic field in z-direction, $\vec{B} = B_z \vec{e_z}$, was already studied in Section 4.1.3. The effect of the magnetic field is then just an Aharonov-Bohm flux $\Phi^{AB} = \pi a^2 B_z$ through the ring of radius a leading to huge simplifications. Formally, the reason for this lies in the fact that $\alpha = 0$ for $\vec{B} = B_z \vec{e_z}$. In particular, S_z- and S_α-basis coincide and the eigenstates of the Zeeman term are $\binom{1}{0}$ and $\binom{0}{1}$. The physical reason is, of course, the simple texture of the magnetic field. This takes away the possibility of observing Berry phase interference effects as is also clear from the solid angle argument, cf. Eqs. (3.32, 3.33).

We already know the result for the transmission through a 1d ring in a homogeneous magnetic field, namely formula (4.18). However, we have to correct the Fermi energy by $\pm\widetilde{\mu}B$, according to the Zeeman interaction energy for the spin states $\binom{1}{0}$ and $\binom{0}{1}$. To assure consistency of the results, we now show that Eq. (4.18) from [27] coincides with the outcome of the algorithm introduced in the previous sections.

---

[3] Due to the Zeeman interaction, a minimal Fermi energy of $\widetilde{E}_F^{\min} \approx \widetilde{\mu}B$ is required so that the spin can align antiparallel to the magnetic field.

For a homogeneous magnetic field $\vec{B} = B_z \vec{e_z}$ with $B_z > 0$ such that $\alpha = 0$, we find either from (3.45), or, more illustratively, in terms of the geometrical interpretation of Fig. 3.4

$$\gamma_1^{\nearrow} = \gamma_1^{\swarrow} = 0 \,. \tag{4.70}$$

Concerning γ_2, we have to distinguish[4]

$$1. \quad \left| n'^{\nearrow}_2 + \frac{1}{2} \right| > \widetilde{\mu} B_z \quad : \quad \gamma_2^{\nearrow} = \gamma_2^{\swarrow} = 0 \,, \; n'^{\nearrow}_1 = -n'^{\nearrow}_2 \,, \; n'^{\swarrow}_1 = -n'^{\swarrow}_2 - 2 \tag{4.71}$$

$$2. \quad \left| n'^{\swarrow}_2 + \frac{1}{2} \right| < \widetilde{\mu} B_z \quad : \quad \gamma_2^{\nearrow} = \gamma_2^{\swarrow} = \pi \,, \; n'^{\nearrow}_1 = -n'^{\swarrow}_2 \,, \; n'^{\swarrow}_1 = -n'^{\nearrow}_2 - 2 \,. \tag{4.72}$$

$$\tag{4.73}$$

Since the relations

$$g_2 = g_3 = 0 \,, \quad h_2 = h_3 = 0 \,,$$

and

$$\begin{aligned} g_1 &= e^{i n_1^{\nearrow} \pi} \,, & g_4 &= -e^{i n_1^{\swarrow} \pi} \,, \\ h_1 &= e^{i n_2^{\nearrow} \pi} \,, & h_4 &= -e^{i n_2^{\swarrow} \pi} \,, \end{aligned}$$

hold in any case, we find the expected diagonal structure of the transfer matrices $\underline{t}_I, \underline{t}_{II}$. The other matrix entries fulfill in the first case the relations (substituting $n' = n - \frac{1}{2} e a^2 B_z = n - \frac{e}{2\pi} \Phi^{AB}$)

$$\begin{aligned} g_1 &= e^{i n_1^{\nearrow} \pi} = e^{-i n_2^{\nearrow} \pi} e^{ie\Phi^{AB})} = h_1^* e^{iea^2 B_z \pi} \,, \\ g_4 &= -e^{i n_1^{\swarrow} \pi} = -e^{-i n_2^{\swarrow} \pi} e^{-2i\pi} e^{ie\Phi^{AB}} = h_4^* e^{iea^2 B_z \pi} \,, \end{aligned}$$

resulting in

$$\begin{aligned} \underline{t}_I &= \mathrm{diag} \left(e^{i n_1^{\nearrow} \pi}, -e^{i n_1^{\swarrow} \pi}, e^{-i n_1^{\nearrow} \pi + ie\Phi^{AB}}, -e^{-i n_1^{\swarrow} \pi + ie\Phi^{AB}} \right) \\ &= e^{\frac{ie}{2} \Phi^{AB}} \mathrm{diag} \left(e^{i \left(n_1^{\nearrow} \pi - \frac{e}{2} \Phi^{AB} \right)}, -e^{i \left(n_1^{\swarrow} \pi - \frac{e}{2} \Phi^{AB} \right)}, e^{-i \left(n_1^{\nearrow} \pi - \frac{e}{2} \Phi^{AB} \right)}, -e^{-i \left(n_1^{\swarrow} \pi - \frac{e}{2} \Phi^{AB} \right)} \right) \\ &\equiv e^{\frac{ie}{2} \Phi^{AB}} \mathrm{diag} \left(e^{i n'^{\nearrow}_1 \pi}, -e^{i n'^{\swarrow}_1 \pi}, e^{-i n'^{\nearrow}_1 \pi}, -e^{-i n'^{\swarrow}_1 \pi} \right) \\ &= \underline{t}_{II} \,. \end{aligned}$$

In the other case, the relations

$$\begin{aligned} g_1 &= e^{i n_1^{\nearrow} \pi} = e^{-i n_2^{\swarrow} \pi} e^{ie\Phi^{AB}} = -h_4^* e^{ie\Phi^{AB}} \,, \\ g_4 &= -e^{i n_1^{\swarrow} \pi} = -e^{-i n_2^{\nearrow} \pi} e^{-2i\pi} e^{ie\Phi^{AB}} = -h_1^* e^{ie\Phi^{AB}} \,, \end{aligned}$$

hold instead, giving rise to

$$\begin{aligned} \underline{t}_I &= \mathrm{diag} \left(e^{i n_1^{\nearrow} \pi}, -e^{i n_1^{\swarrow} \pi}, e^{-i n_1^{\swarrow} \pi + ie\Phi^{AB}}, -e^{-i n_1^{\nearrow} \pi + ie\Phi^{AB}} \right) \\ &= e^{\frac{ie}{2} \Phi^{AB}} \mathrm{diag} \left(e^{i \left(n_1^{\nearrow} \pi - \frac{e}{2} \Phi^{AB} \right)}, -e^{i \left(n_1^{\swarrow} \pi - \frac{e}{2} \Phi^{AB} \right)}, e^{-i \left(n_1^{\swarrow} \pi - \frac{e}{2} \Phi^{AB} \right)}, -e^{-i \left(n_1^{\nearrow} \pi - \frac{e}{2} \Phi^{AB} \right)} \right) \\ &\equiv e^{\frac{ie}{2} \Phi^{AB}} \mathrm{diag} \left(e^{i n'^{\nearrow}_1 \pi}, -e^{i n'^{\swarrow}_1 \pi}, e^{-i n'^{\swarrow}_1 \pi}, -e^{-i n'^{\nearrow}_1 \pi} \right) \\ &= \underline{t}_{II} \,. \end{aligned}$$

---

[4] The very special case of $\left| n'^{\nearrow}_2 + \frac{1}{2} \right| < \widetilde{\mu} B_z < \left| n'^{\swarrow}_2 + \frac{1}{2} \right|$ leading to $\gamma_2^{\nearrow} = \pi, \gamma_2^{\swarrow} = 0$ is not further considered here.

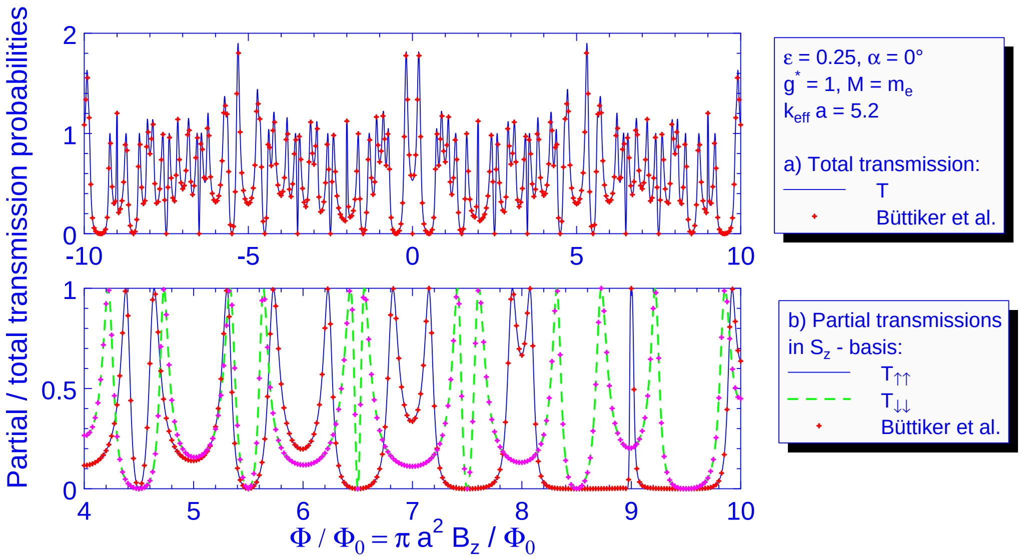

Figure 4.6: a) Total and b) partial transmission probabilities for the situation of a varying homogeneous magnetic field perpendicular to the ring ($\vec{B} = B_z \vec{e_z}$). In this situation, the electron gases of ↑- and ↓-electrons are decoupled and no spin flips occur, $T_{\uparrow\downarrow} = T_{\downarrow\uparrow} = 0$. The (numerical) results of the calculation described above are compared with the (analytical) results of Büttiker et al. [27], see Eq. (4.18), where we have corrected the energy of the electrons by the Zeeman interaction energy, see Eq. (4.77), for $|\uparrow\rangle$- and $|\downarrow\rangle$-electrons respectively, summing up both contributions. As expected, the results are the same.

Now, this has to be put into the matrix (4.34) to obtain the transmission. There, in one of the summands, the *inverse* of the matrix $\underline{t}_I$ occurs whereas the other product contains the matrix $\underline{t}_{II}$ itself giving rise to different prefactors $\exp(-\frac{ie}{2}\Phi^{AB})$ and $\exp(\frac{ie}{2}\Phi^{AB})$ demanding for numerical evaluation in the general case $e\Phi/2\pi \equiv \Phi/\Phi_0 \neq 0, \pm 1, \pm 2, \ldots$. The result is shown in Fig. 4.6.

However, for the situation where the flux Φ^{AB} equals an integer of the flux quantum Φ_0, we can proceed further in the analytical calculation. Doing so for the case $|n_2'^{\nearrow} + 1/2| > \tilde{\mu} B_z$, cf. Eq. (4.71), and using the relations given prior to (4.34), we evaluate the terms in (4.34) under utilization of

$$g_1 = e^{in_1'^{\nearrow}\pi} \,, \quad g_4 = -e^{in_1'^{\swarrow}\pi} \,, \quad \underline{t}_I = \underline{t}_{II} = \mathrm{diag}(g_1, g_4, g_1^*, g_4^*) \,,$$

and make use of the unitarity of $\underline{t}_I$, $\underline{t}_I^{-1} = \underline{t}_I^{+} = \underline{t}_I^{*}$, we find

$$\underline{N}_2 \underline{t}_{II} \underline{N}_1 = \frac{1}{2b} \begin{pmatrix} g_1(b+a) + g_1^* & 0 & g_1^* - g_1 & 0 \\ 0 & g_4(b+a) + g_4^* & 0 & g_4^* - g_4 \\ g_1^* - g_1(a+b)^2 & 0 & g_1(b+a) + g_1^* & 0 \\ 0 & g_4^* - g_4(a+b)^2 & 0 & g_4(b+a) + g_4^* \end{pmatrix} ,$$

$$\underline{N}_1^{-1}\underline{t}_I^{-1}\underline{N}_2^{-1} = \frac{1}{2b}\begin{pmatrix} g_1(b+a)+g_1^* & 0 & -g_1^*+g_1 & 0 \\ 0 & g_4(b+a)+g_4^* & 0 & -g_4^*+g_4 \\ -g_1^*+g_1(a+b)^2 & 0 & g_1(b+a)+g_1^* & 0 \\ 0 & -g_4^*+g_4(a+b)^2 & 0 & g_4(b+a)+g_4^* \end{pmatrix}.$$

Subtracting these expressions, we arrive at the matrix $\underline{a}^{\mathrm{BI}} \overset{\mathrm{def}}{=} \underline{a}(\frac{\Phi}{\Phi_0} \in \mathbb{Z})$ that we expect to coincide with the result [27] of Büttiker et al. ("BI"). We obtain

$$\left(\underline{a}^{\mathrm{BI}}\right)^{-1} = \frac{1}{b}\begin{pmatrix} 0 & 0 & g_1^*-g_1 & 0 \\ 0 & 0 & 0 & g_4^*-g_4 \\ g_1^*-g_1(a+b)^2 & 0 & 0 & 0 \\ 0 & g_4^*-g_4(a+b)^2 & 0 & 0 \end{pmatrix}, \tag{4.74}$$

the inversion of which eventually gives

$$\begin{aligned} a_{13}^{\mathrm{BI}} &= \frac{b}{g_1^*-g_1(a+b)^2}, \\ a_{24}^{\mathrm{BI}} &= \frac{b}{g_4^*-g_4(a+b)^2}, \\ a_{14}=a_{23} &= 0\,. \end{aligned} \tag{4.75}$$

Using that $g_1^*\,g_1 = g_4^*\,g_4 = 1$, we find for the transmission amplitudes

$$\begin{aligned} T_{\uparrow\uparrow}^{\mathrm{BI}} = \frac{4\epsilon^2}{b^2}\left(a_{13}^{\mathrm{BI}}\right)^* a_{13}^{\mathrm{BI}} &= \frac{4\epsilon^2}{1-2\cos\left(2\theta_d^{\uparrow}+2\theta_{AB}\right)(a+b)^2+(a+b)^4}, \\ T_{\downarrow\downarrow}^{\mathrm{BI}} = \frac{4\epsilon^2}{b^2}\left(a_{24}^{\mathrm{BI}}\right)^* a_{24}^{\mathrm{BI}} &= \frac{4\epsilon^2}{1-2\cos\left(2\theta_d^{\downarrow}+2\theta_{AB}\right)(a+b)^2+(a+b)^4}, \end{aligned} \tag{4.76}$$

with

$$\theta_d^{\uparrow(\downarrow)} = \pi\sqrt{\widetilde{E}_F+(-)\tilde{\mu}B_z}\,, \tag{4.77}$$

$$\theta_{AB} = \pi\frac{\Phi^{AB}}{\Phi_0} \equiv 0, \pm\pi, \pm 2\pi, \pm 3\pi, \dots\,, \tag{4.78}$$

cf. also Eqs. (4.21, 4.22). We convince ourselves that this expression is equivalent to Eq. (4.18) in the limit $B_z = 0, \Phi^{AB} = 0$ by first rewriting (using $a+b = \sqrt{1-2\epsilon}\,, a^2+b^2 = 1-\epsilon$)

$$T^{\mathrm{BI}}(\Phi^{AB}=0) = \frac{4\epsilon^2}{1-2(1-2\epsilon)\cos 2\theta_d+(1-2\epsilon)^2}\,.$$

Evaluating the result of Büttiker et al. for the transmission probability $T(\epsilon, \widetilde{E}_F, \Phi^{AB})$, cf. Eq. (4.18), indeed yields

$$\begin{aligned} T(\epsilon, \widetilde{E}_F, \Phi^{AB}=0) &= \frac{4\epsilon^2(1-\cos 2\theta_d)}{2\left[(1-\epsilon)^2(1-\cos 2\theta_d)^2+\epsilon^2(1-\cos^2 2\theta_d)\right]} \\ &= \frac{4\epsilon^2}{1-2(1-2\epsilon)\cos 2\theta_d+1-4\epsilon+4\epsilon^2} \\ &\equiv T^{\mathrm{BI}}(\Phi^{AB}=0)\,, \quad \textit{q.e.d.} \end{aligned} \tag{4.79}$$

Hence, we have shown numerically (cf.Fig. 4.6) and analytically [for certain parameters, see Eq. (4.79)], respectively, that our general approach to spin-dependent transport in non-uniform magnetic fields (Section 4.2) contains the well-known result (4.18) (cf. Section 4.1.3, [27]) as limiting case of a uniform magnetic field $\vec{B} = B_z \vec{e}_z$.

4.4 Transformations in spin space and symmetries of the transmission matrix

So far, we always used the S_z-basis to express the spin states needed to calculate the transfer matrices. Here, the transmission probability for spin-flip processes, $t_{\uparrow\downarrow}, t_{\downarrow\uparrow}$ is non-zero for a tilted magnetic field even in the adiabatic limit. We recall that there are no transitions between the propagating $|\nearrow(\phi)\rangle$-, $|\swarrow(\phi)\rangle$-states in this case. This is, of course, no contradiction since the $|\nearrow(\phi)\rangle$-, $|\swarrow(\phi)\rangle$-states represent spins aligned with the magnetic field, given in S_z-basis as [cf. Eq. (3.10), ϕ_t is the field texture parameter, see Eq. (3.11)]

$$|\nearrow(\phi)\rangle = \begin{pmatrix} \cos\frac{\alpha}{2} \\ e^{i(\phi+\phi_t)}\,\sin\frac{\alpha}{2} \end{pmatrix}, \qquad |\swarrow(\phi)\rangle = \begin{pmatrix} \sin\frac{\alpha}{2} \\ -\,e^{i(\phi+\phi_t)}\,\cos\frac{\alpha}{2} \end{pmatrix}. \tag{4.80}$$

Alternatively, one can consider transmission amplitudes in the (local) S_α-basis, where the $\nearrow$- and $\swarrow$-states are rotated by an angle α w.r.t. z-axis. The new transmission amplitudes $t^\alpha_{\nearrow\nearrow}, t^\alpha_{\nearrow\swarrow}, t^\alpha_{\swarrow\nearrow}, t^\alpha_{\swarrow\swarrow}$ that replace the ones w.r.t. S_z-basis, given in the matrix $\underline{T}^z$ in (4.28), $t_{\uparrow\uparrow}, t_{\uparrow\downarrow}, t_{\downarrow\uparrow}, t_{\downarrow\downarrow}$, are obtained by performing the appropriate projections. For example,

$$t^\alpha_{\nearrow\nearrow} = \langle\nearrow(\phi=\pi)|\underline{T}^z|\nearrow(\phi=0)\rangle\;, \tag{4.81}$$

with the physical interpretation that a spin aligned in the direction of the magnetic field, expressed in S_z-basis, enters the ring at the position $\phi = 0$. Finally we are interested in the amplitude that the spin is still oriented with the magnetic field at the end of the ring ($\phi = \pi$) – this is precisely what we $t^\alpha_{\nearrow\nearrow}$ expect to describe. In the adiabatic limit, we will find $t^\alpha_{\nearrow\swarrow}, t^\alpha_{\swarrow\nearrow}$ to vanish as expected, cf. for example Fig. 4.7c.

For completeness, we give the evaluated quantities,

$$\begin{aligned}
t^\alpha_{\nearrow\nearrow} &= t_{\uparrow\uparrow}\cos^2\frac{\alpha}{2} + t_{\uparrow\downarrow}\cos\frac{\alpha}{2}\sin\frac{\alpha}{2}e^{i\phi_t} - t_{\downarrow\uparrow}\cos\frac{\alpha}{2}\sin\frac{\alpha}{2}e^{-i\phi_t} - t_{\downarrow\downarrow}\sin^2\frac{\alpha}{2}\;, \\
t^\alpha_{\nearrow\swarrow} &= t_{\uparrow\uparrow}\cos\frac{\alpha}{2}\sin\frac{\alpha}{2} - t_{\uparrow\downarrow}\cos^2\frac{\alpha}{2}e^{i\phi_t} - t_{\downarrow\uparrow}\sin^2\frac{\alpha}{2}e^{-i\phi_t} + t_{\downarrow\downarrow}\cos\frac{\alpha}{2}\sin\frac{\alpha}{2}\;, \\
t^\alpha_{\swarrow\nearrow} &= t_{\uparrow\uparrow}\cos\frac{\alpha}{2}\sin\frac{\alpha}{2} + t_{\uparrow\downarrow}\sin^2\frac{\alpha}{2}e^{i\phi_t} + t_{\downarrow\uparrow}\cos^2\frac{\alpha}{2}e^{-i\phi_t} + t_{\downarrow\downarrow}\cos\frac{\alpha}{2}\sin\frac{\alpha}{2}\;, \\
t^\alpha_{\swarrow\swarrow} &= t_{\uparrow\uparrow}\sin^2\frac{\alpha}{2} - t_{\uparrow\downarrow}\cos\frac{\alpha}{2}\sin\frac{\alpha}{2}e^{i\phi_t} + t_{\downarrow\uparrow}\cos\frac{\alpha}{2}\sin\frac{\alpha}{2}e^{-i\phi_t} - t_{\downarrow\downarrow}\cos^2\frac{\alpha}{2}\;.
\end{aligned} \tag{4.82}$$

The total transmission probability T is certainly conserved as can be easily checked keeping in mind that sandwiching $\underline{T}^z$ with the different spin states can be represented by unitary transformation matrices $\underline{U}^1$ and $\underline{U}^2$, respectively. In S_z-basis,

$$T^{(z)} = \sum_{i,j=\uparrow,\downarrow} t_{ij} t^*_{ij}\;; \tag{4.83}$$

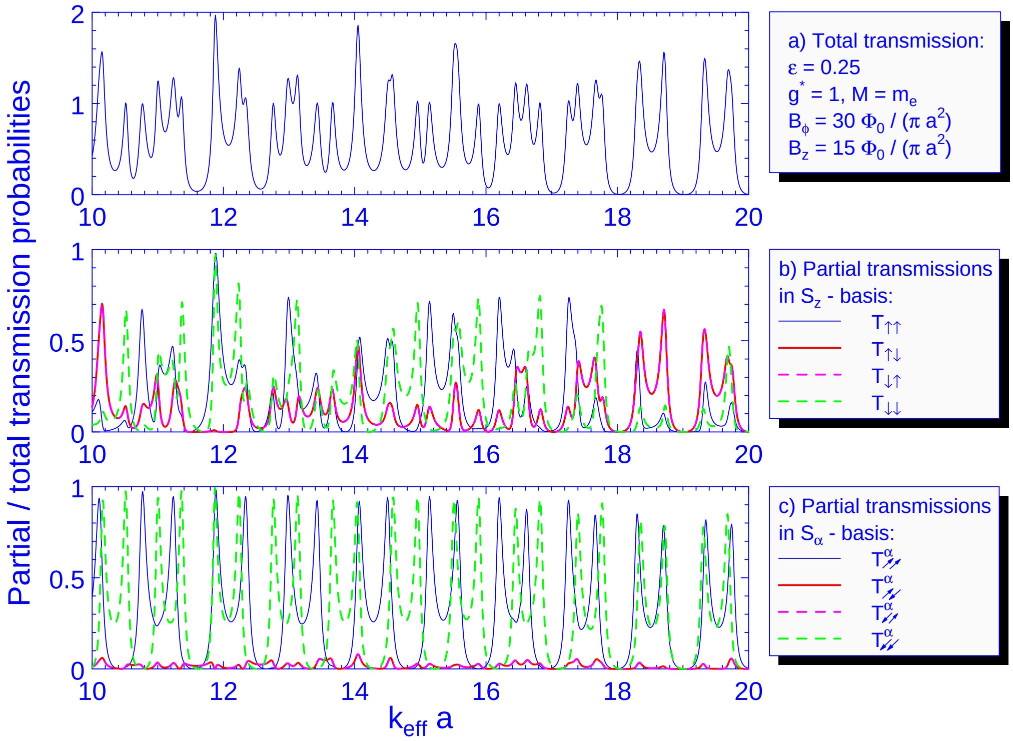

Figure 4.7: a) Total transmission probability and partial contributions in b) S_z-basis and c) S_α-basis vs. the Fermi energy $\sqrt{\widetilde{E}_F} = k_{\rm eff}a$ of the incident electrons, for the same parameters as in Fig. 4.5. Note that the spin switching (non-diagonal) partial transmissions *coincide* in both S_z- and S_α-basis. For all Fermi energies $k_{\rm eff}a$ we are in an (almost) adiabatic situation as confirmed by the small spin-flip probabilities in S_α-basis in c).

while we find in S_α-basis

$$\begin{aligned}
T^{(\alpha)} &= \sum_{i,j=\nearrow,\swarrow} t^{\alpha}_{ij} t^{\alpha *}_{ij} = \sum_{i,j,k,l,m,n=\uparrow,\downarrow} \left(\underline{U}^2_{ik} t_{kl} \underline{U}^1_{lj}\right) \left(\underline{U}^2_{im} t_{mn} \underline{U}^1_{nj}\right)^* \\
&= \sum_{i,j,k,l,m,n=\uparrow,\downarrow} \underline{U}^2_{ik} t_{kl} \underline{U}^1_{lj} \left(\underline{U}^1\right)^*_{nj} t^*_{mn} \left(\underline{U}^2\right)^*_{im} \\
&= \sum_{i,k,l,m,n=\uparrow,\downarrow} \underline{U}^2_{ik} t_{kl} \delta_{ln} t^*_{mn} \left(\underline{U}^2\right)^{-1}_{mi} = \sum_{i,k,l,m=\uparrow,\downarrow} \left(\underline{U}^2\right)^{-1}_{mi} \underline{U}^2_{ik} t_{kl} t^*_{ml} = \sum_{k,l=\uparrow,\downarrow} t_{kl} t^*_{kl} \,,
\end{aligned}$$

so that indeed

$$T^{(z)} = T^{(\alpha)} \equiv T \,. \tag{4.84}$$

We point out the coincidence of the *non-diagonal* partial transmission amplitudes in S_z-basis *as well as* in S_α-basis, see Figs. 4.5, 4.7,

$$t_{\uparrow\downarrow} = t_{\downarrow\uparrow} \quad \text{and} \quad t^{\alpha}_{\nearrow\swarrow} = t^{\alpha}_{\swarrow\nearrow} \,. \tag{4.85}$$

The reason for this is the symmetry of the ring w.r.t. reflections about a central axis that is perpendicular to the axis formed by the leads.

The individual contributions to the total transmission probability in S_z- and S_α-basis are illustrated in Fig. 4.7. In the following chapter, we will preferentially discuss transmission amplitudes t_{ij}^{α} and probabilities $\left|t_{ij}^{\alpha}\right|^2 \overset{\text{def}}{=} T_{ij}$, respectively, in S_α-basis, except when we perform calculations revealing a spin-flip effect in the Section 5.1.

5 Transmission in non-uniform magnetic fields: Examples

In this chapter we will consider two special magnetic field geometries. In the first one, the magnetic field is constricted to the plane of the ring ($\alpha = \pi/2$). This has remarkable implications on the partial transmission amplitudes that are independent of the degree of adiabaticity. Applying a magnetic flux of half a flux quantum through the ring will invert the properties of the transmissions amplitudes. We provide an analytical proof for this effect and compare our results with those obtained in a two-dimensional tight-binding model. The second example refers to a situation that was already studied in experiments [35] and consists in placing a micromagnet in the centre of the ring. We discuss implications for magneto-conductance measurements.

5.1 In-plane magnetic field

5.1.1 Aharonov-Bohm ring as a spin switch

Throughout this section we shall consider a ring that is subject to an in-plane magnetic field, that can be either tangent, radial, or a combination of the two that is rotationally invariant. In experiments, such a field might be generated by, e.g., a current through the ring as reported in the context of Oerstedt switching [51].

In this geometry we find an interesting *spin-flip effect* [40] that allows one to change the spin polarization of an electron transmitted through an one-dimensional[1] ring by adding Aharonov-Bohm flux through the ring. The spin-dependent transmission is periodic in the applied flux with a period of one flux quantum, Φ_0. In particular, the polarization state of polarized electrons can be changed by altering the flux by $\Phi_0/2$. Before we discuss possible applications that might become interesting in future spintronic devices, we compute the transmission amplitudes for the case of an in-plane magnetic field. Firstly, we investigate the case where no additional flux through the ring is present, in the next step we incorporate half a flux quantum.

In this case of an in-plane magnetic field, $\alpha = \pi/2$, we find a high symmetry between the clockwise and counter-clockwise propagating wave. This becomes manifest in the relationships between the angles γ entering the (general non-adiabatic) spin states and the orbital quantum numbers n [cf. Eqs. (3.52, 3.53) and before]

$$\begin{aligned} \gamma_1^{\nearrow} &= \gamma_2^{\swarrow}\,, \qquad & n_1^{\nearrow} &= -n_2^{\swarrow} - 1\,, \\ \gamma_1^{\swarrow} &= \gamma_2^{\nearrow}\,, \qquad & n_1^{\swarrow} &= -n_2^{\nearrow} - 1\,; \end{aligned} \tag{5.1}$$

$$\tag{5.2}$$

enormously simplifying the structure of the transfer matrices $\underline{t}_I, \underline{t}_{II}$, see Eqs. (4.57, 4.69), since they reduce the number of independent entries by means of the identities [cf. Eqs. (4.48, 4.50,

---

[1] This effect does not require a 1d ring and was also found in (more realistic) two-dimensional geometries, see [40].

4.55)]

$$
\begin{aligned}
g_1 &= h_4^* & g_2 &= h_3^* \,, \\
g_4 &= h_1^* & g_3 &= h_2^* \,.
\end{aligned}
\tag{5.3}
$$

The number of variables can be reduced further if we specify the field texture parameter ϕ_t [see Eq. (3.11)] in order to relate g_2 and g_3, see Eqs. (4.48, 4.50). In the case of a radial magnetic field, $\phi_t = 0$,

$$
\sqrt{\frac{v_1^{\uparrow}}{v_1^{\downarrow}}}\, g_2 = -\sqrt{\frac{v_1^{\downarrow}}{v_1^{\uparrow}}}\, g_3 \,; \tag{5.4}
$$

and for a tangent magnetic field, $\phi_t = \pi/2$,

$$
\sqrt{\frac{v_1^{\uparrow}}{v_1^{\downarrow}}}\, g_2 = \sqrt{\frac{v_1^{\downarrow}}{v_1^{\uparrow}}}\, g_3 \,. \tag{5.5}
$$

These relations hold even when an integer number of flux quanta penetrate the ring as can be seen from Eqs. (4.48, 4.50, 4.55) because this corresponds to changes of n by an integer and an overall sign change, where applicable, does not change the transmission amplitude.

We shall now study the implications of these relationships on the transmission amplitudes, see Eq. (4.35). We will find that in S_α-basis the spin-preserving transmissions (also called diagonal contributions subsequently) vanish ($t^\alpha_{\nearrow\nearrow} = t^\alpha_{\swarrow\swarrow} = 0$), whereas the spin-flipping, or non-diagonal, transmission amplitudes are non-zero and equal ($t^\alpha_{\nearrow\swarrow} = t^\alpha_{\swarrow\nearrow}$). In the following, all spin directions are related *to the direction of the magnetic field that is not fixed in real space!* We give now analytical evidence for this at first sight surprising behaviour, using the definitions (4.57, 4.69, 4.30-4.32) and the relations (5.3) and the unitarity of the matrices $\underline{t}_I, \underline{t}_{II}$, especially that $\underline{t}_I^{-1} = \underline{t}_I^*$.

Evaluating the matrix $\underline{a}^{-1}$ given by Eq. (4.34) in a straightforward computation we obtain for a tangent magnetic field, $\widetilde{g}_2 = \widetilde{g}_3$,

$$
\underline{a}^{-1} = \frac{1}{2b}
\begin{pmatrix}
\delta_1 & \delta_2 & \delta_3 & 0 \\
\delta_2 & -\delta_1 & 0 & \delta_3 \\
\delta_9 & 0 & \delta_1 & \delta_2 \\
0 & \delta_9 & \delta_2 & -\delta_1
\end{pmatrix} ,
\tag{5.6}
$$

with

$$
\begin{aligned}
\delta_1 &= (g_1 - g_4)(a+b) - (g_1^* - g_4^*) \,, \\
\delta_2 &= -2\left(\widetilde{g}_2(a+b) + \widetilde{g}_3^*\right) \,, \\
\delta_3 &= -(g_1 + g_4) + (g_1^* + g_4^*) \,, \\
\delta_9 &= -(g_1 + g_4)(a+b)^2 + (g_1^* + g_4^*) \,.
\end{aligned}
\tag{5.7}
$$

The inversion of this matrix yields

$$
a_{13} = a_{24} = 2b \frac{\delta_3}{\delta_3\delta_9 - \left(\delta_1^2 + \delta_2^2\right)} \,, \tag{5.8}
$$

$$
a_{14} = a_{23} = 0 \,, \tag{5.9}
$$

and these results are passed on into the transmission amplitudes in S_z-basis,

$$t_{\uparrow\uparrow} = t_{\downarrow\downarrow} \quad \text{and} \quad t_{\uparrow\downarrow} = t_{\downarrow\uparrow} = 0\,. \tag{5.10}$$

In terms of transmission probabilities w.r.t. S_α-basis this reads according to Eqs. (4.82) for $\phi_t = \pi/2, \alpha = \pi/2$

$$\begin{aligned} t^\alpha_{\nearrow\nearrow} &= \frac{1}{2}\left(t_{\uparrow\uparrow} + it_{\uparrow\downarrow} + it_{\downarrow\uparrow} - t_{\downarrow\downarrow}\right)\,, \\ t^\alpha_{\nearrow\swarrow} &= \frac{1}{2}\left(t_{\uparrow\uparrow} + it_{\uparrow\downarrow} - it_{\downarrow\uparrow} + t_{\downarrow\downarrow}\right)\,, \\ t^\alpha_{\swarrow\nearrow} &= \frac{1}{2}\left(t_{\uparrow\uparrow} - it_{\uparrow\downarrow} + it_{\downarrow\uparrow} + t_{\downarrow\downarrow}\right)\,, \\ t^\alpha_{\swarrow\swarrow} &= \frac{1}{2}\left(t_{\uparrow\uparrow} - it_{\uparrow\downarrow} - it_{\downarrow\uparrow} - t_{\downarrow\downarrow}\right)\,; \end{aligned} \tag{5.11}$$

therefore,

$$t^\alpha_{\nearrow\nearrow} = t^\alpha_{\swarrow\swarrow} = 0 \quad \text{and} \quad t^\alpha_{\nearrow\swarrow} = t^\alpha_{\swarrow\nearrow} \equiv t_{\uparrow\uparrow} = t_{\downarrow\downarrow}\,, \tag{5.12}$$

that is, the role of the diagonal (↑↑ and ↓↓) and non-diagonal elements (↑↓ and ↓↑) is just interchanged when switching between S_z- and S_α-basis.

The result (5.12) is rather surprising since it states that only electrons that *change*[2] their spin are transmitted through the ring and this holds in particular *also* in the *adiabatic* limit! As a consequence the transmission probability tends to zero.

Although we have proven the properties (5.12) of the transmission amplitudes (and probabilities, respectively) for the special case of a tangent magnetic field, they remain valid for a purely radial magnetic field and therefore for any in-plane magnetic field. Furthermore, this effect was also found in two-dimensional rings as we shall discuss below.

We turn now to the case where half a flux quantum penetrates the ring, such that there is an Aharonov-Bohm flux $\Phi^{AB} = \Phi_0/2$. However, we assume the magnetic field at the position of the ring to remain unchanged, i.e., the AB flux to be generated by a solenoid (rather than by a homogeneous B_z-component). The quantum number n is then reduced by half an integer, cf. Eq. (3.30), and Eq. (5.3) has to be replaced by

$$\begin{aligned} g_1 &= -h_4^* \qquad & g_2 &= -h_3^*\,, \\ g_4 &= -h_1^* \qquad & g_3 &= -h_2^*\,, \end{aligned} \tag{5.13}$$

resulting in a minus-sign in front of the lower-right diagonal 2×2 matrix. However, alternatively we can use Eqs. (4.48, 4.50, 4.55) for the g_i, h_i directly and realize that they are just rotated by $e^{-i\pi/2}$ w.r.t. the $\Phi^{AB} = 0$ values. Hence, we can write

$$\underline{t}^{\Phi_0/2}_{I(II)} = -i\underline{t}^0_{I(II)}\,, \tag{5.14}$$

where $\underline{t}^0_{I(II)}$ are the transfer matrices in the zero-flux situation. Accordingly, we find the matrix $\underline{a}$ as

$$\begin{aligned} \underline{a}^{\Phi_0/2} &\overset{\text{def}}{=} \left[-i\underline{N}_2\underline{t}^0_{II}\underline{N}_1 - \frac{1}{-i}\underline{N}_1^{-1}{\underline{t}^0_I}^{-1}\underline{N}_2^{-1}\right]^{-1}\,, \\ &= -\frac{1}{i}\left[\underline{N}_2\underline{t}^0_{II}\underline{N}_1 + \underline{N}_1^{-1}{\underline{t}^0_I}^{-1}\underline{N}_2^{-1}\right]^{-1}\,. \end{aligned} \tag{5.15}$$

---

[2] Concerning the direction of the spin it has to be noted and carefully kept in mind that $|\nearrow\rangle$ always means a spin *in direction* of the magnetic field. For a tangent magnetic field, consequently, the spin of an $|\nearrow\rangle$-electron points into *opposite* directions at the entrance and the exit of the ring, respectively.

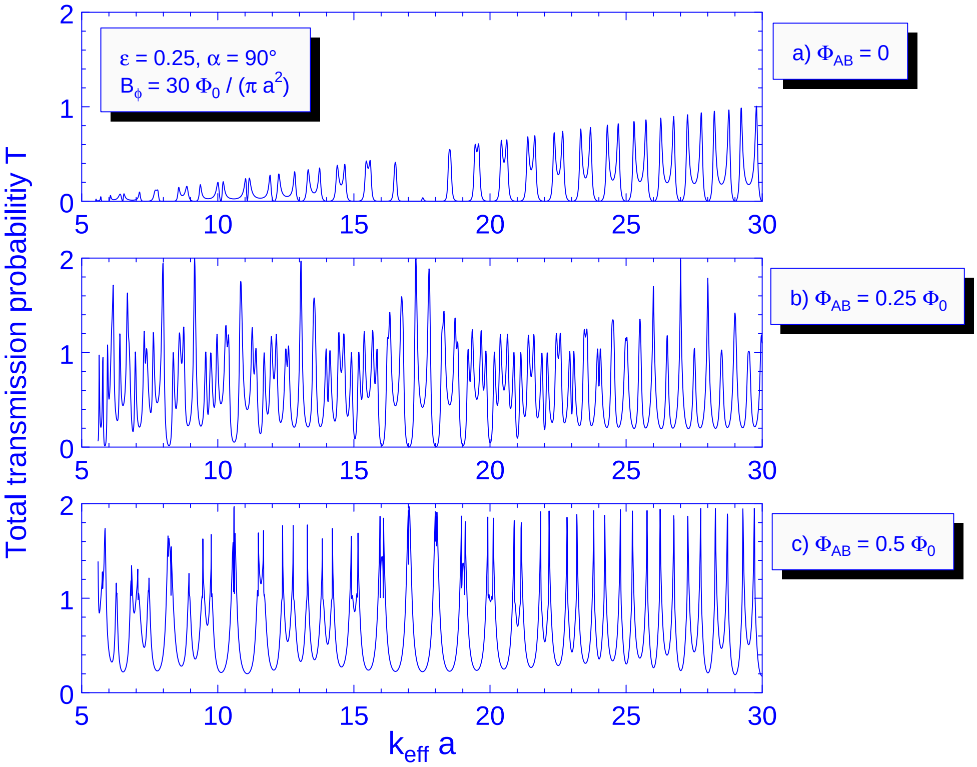

Figure 5.1: Total transmission probability in a model system with $g^* = 1$ and $M = m_e$ at fixed strength of the tangent magnetic field B_ϕ vs. energy of the incident electrons. In the upper picture, no Aharonov-Bohm flux is penetrating the ring. For small $k_{\text{eff}}a$, we are in the adiabatic limit with zero transmission, see text. Clearly visible is the minimum in the transmission at $k_{\text{eff}}a = \widetilde{\mu}B/\sqrt{3}$. For non-zero flux through the ring, the structure is less characteristic.

The inverse takes then the form (again, for the special case of a tangent magnetic field, $\widetilde{g}_2 = \widetilde{g}_3$

$$\left(\underline{a}^{\Phi_0/2}\right)^{-1} = \frac{1}{2b}\begin{pmatrix} \rho_1 & 0 & \rho_3 & \rho_4 \\ 0 & -\rho_1 & \rho_4 & -\rho_3 \\ \rho_9 & \rho_{10} & \rho_1 & 0 \\ \rho_{10} & -\rho_9 & 0 & -\rho_1 \end{pmatrix} , \tag{5.16}$$

with

$$\begin{aligned} \rho_1 &= (g_1 + g_4)(a+b) + (g_1^* + g_4^*) , \\ \rho_3 &= -(g_1 - g_4) - (g_1^* - g_4^*) , \\ \rho_4 &= 2\left(\widetilde{g}_2 - \widetilde{g}_3^*\right) , \\ \rho_9 &= -(g_1 - g_4)(a+b)^2 - (g_1^* - g_4^*) , \\ \rho_{10} &= 2\left(\widetilde{g}_2(a+b)^2 - \widetilde{g}_3^*\right) , \end{aligned} \tag{5.17}$$

where the g_i are the *same* as in the case without Aharonov-Bohm flux. Inverting this matrix one obtains

$$\begin{aligned} a_{13}^{\Phi_0/2} = -a_{24}^{\Phi_0/2} &= 2b\frac{-\rho_1^2\rho_3 + \left(\rho_3^2+\rho_4^2\right)\rho_9}{\mathcal{N}} \\ a_{14}^{\Phi_0/2} = a_{23}^{\Phi_0/2} &= 2b\frac{-\rho_1^2\rho_4 + \left(\rho_3^2+\rho_4^2\right)\rho_{10}}{\mathcal{N}}\,, \end{aligned} \tag{5.18}$$

with the common denominator

$$\mathcal{N} = \rho_1^4 + \left(\rho_3^2+\rho_4^2\right)\left(\rho_9^2+\rho_{10}^2\right) - 2\rho_1^2(\rho_3\rho_9+\rho_4\rho_{10})\,. \tag{5.19}$$

Again, this is transmitted to the transmission amplitudes, and the result in S_z-basis reads

$$t_{\uparrow\uparrow}^{\Phi_0/2} = -t_{\downarrow\downarrow}^{\Phi_0/2} \quad \text{and} \quad t_{\uparrow\downarrow}^{\Phi_0/2} = t_{\downarrow\uparrow}^{\Phi_0/2}\,, \tag{5.20}$$

where all quantities are non-zero contrasting the result for the non-diagonal transmission amplitudes in the case without flux. Transformation to S_α-basis yields according to Eq. (5.11) that

$$\begin{aligned} t_{\nearrow\nearrow}^{\alpha\;\Phi_0/2} &= t_{\uparrow\uparrow}^{\Phi_0/2} + i t_{\uparrow\downarrow}^{\Phi_0/2} \neq 0\,, \\ t_{\swarrow\swarrow}^{\alpha\;\Phi_0/2} &= t_{\uparrow\uparrow}^{\Phi_0/2} - i t_{\uparrow\downarrow}^{\Phi_0/2} \neq 0\,, \\ t_{\nearrow\swarrow}^{\alpha\;\Phi_0/2} &= t_{\swarrow\nearrow}^{\alpha\;\Phi_0/2} = 0\,. \end{aligned} \tag{5.21}$$

This result applies whenever the Aharonov-Bohm flux equals half an integer number of flux quanta Φ_0, i.e. $\Phi^{AB} = \pm\Phi_0/2, \pm3\Phi_0/2, \ldots$. Remember that we have assumed the Aharonov-Bohm flux to cause no change in the angle α of the magnetic field $\vec{B}$ with the z-axis! Therefore, in realistic situations where the flux might originate from a (homogeneous) magnetic field B_z in z-direction, we expect deviations from the result (5.21) depending on the effect of B_z on α. However, for large in-plane magnetic fields the influence of $B_z \equiv \Phi_0/2\pi a^2$ will be negligible.

The physical meaning of this result is that in the presence of half a quantum flux only electrons that *keep* their spin direction during transport are transmitted – precisely the opposite of what we found for zero quantum flux (see Figs. 5.1, 5.2 and the discussion of averaged transmission probabilities in the following section). This opens the possibility of controlling the transmission of (polarized) electrons by varying the number of flux quanta penetrating the ring: If their number is integer, only spin-flipping electrons are transmitted; for a flux constituted by a half-integer number of flux quanta solely electrons keeping their spin can be found in the exiting lead. For magnetic fluxes in between, the situation is intermediate with transport in all channels see Fig. 5.2b.

We summarize this novel *spin-flip effect* as follows [40]: For in-plane field geometries and symmetric ballistic microstructures we have demonstrated how an additional small Aharonov-Bohm flux Φ^{AB} can be used to control spin flips and to tune the polarization of transmitted electrons. This quantum interference mechanism does not require adiabaticity. In combination with a spin detector such a device may be used to control spin polarized current, similar to the spin field-effect transistor proposed in [46].

One question arising is whether such an effect prevails when considering *diffusive* devices and disorder-averaged quantities. This remains as an interesting problem so far. Another question is related to possible measurements or applications of this effect. Recent experimental progress

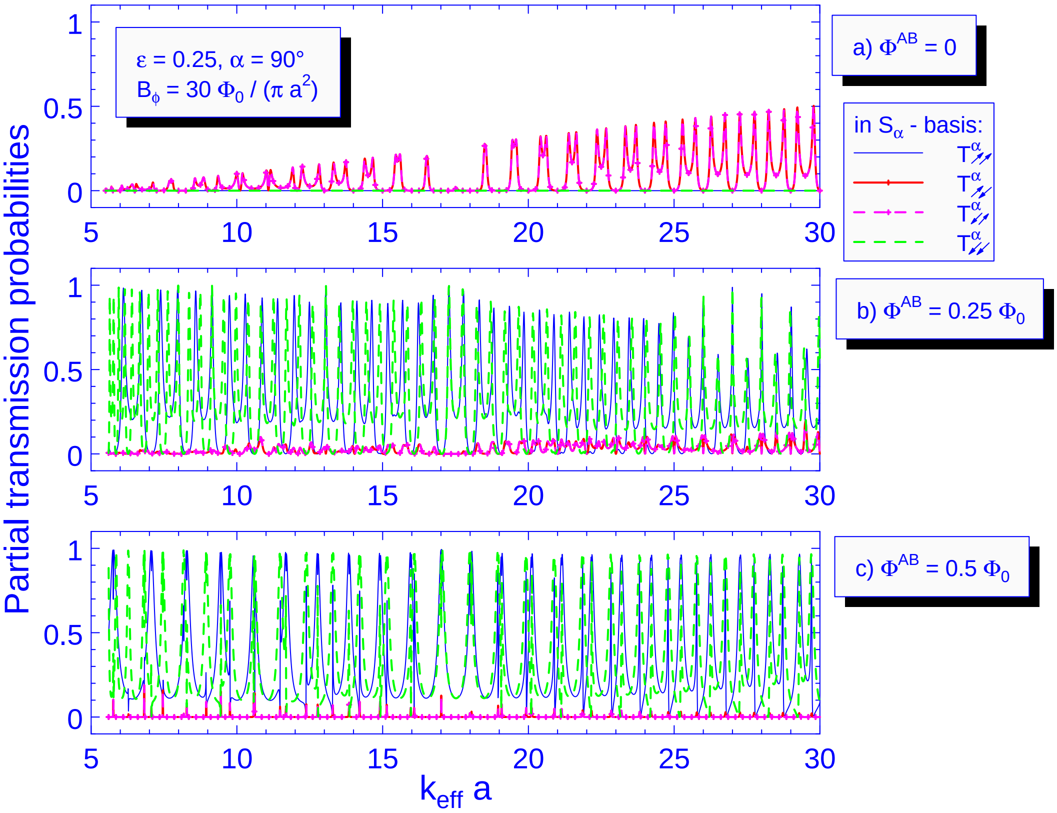

Figure 5.2: Partial transmission probabilities vs. momentum $k_{\text{eff}}a$ of the incident electrons in the same model system as for Fig. 5.1 ($g^* = 1, M = m_e$), again at fixed strength of the tangent magnetic field B_ϕ. a) No Aharonov-Bohm flux penetrating the ring: besides zero transmission for small $k_{\text{eff}}a$ and the $\sqrt{3}$-feature, we see that the transmission is provided *only* by the spin-flipping channels, i.e., only $T^\alpha_{\nearrow\swarrow}$ and $T^\alpha_{\swarrow\nearrow}$ are *non-zero.* c) Half a quantum flux through the ring: opposite situation such that now $T^\alpha_{\nearrow\nearrow}$ and $T_{\swarrow\swarrow}$ are non-zero. The deviations visible in the diagram arise from the fact that the flux was created by a homogeneous field B_z, therefore affecting the angle α. b) For other values of the Aharonov-Bohm flux, transport occurs in all channels. Hence, for polarized incident electrons, the spin can be switched by applying an Aharonov-Bohm flux of half a flux quantum.

in creating spin-polarized electrons in semiconductors is reported, e.g., in [42]. It is important to note that the interference-based spin-flip effect discussed above requires phase coherence over the whole sample. Experimentally, it was indeed found that coherence of spin-states can be maintained up to scales of more than 100 μm [44] at *temperatures of a few Kelvin.*

Generally, coherent control and quantum transport of spin states in semiconductor heterojunctions or quantum dots is attracting increasing interest [45]. Applications proposed so far include spin transistors [46], filters [47], and scalable devices for quantum information processing [48, 49]. Advances in the injection of spin-polarized charge carries [42] indicates the principle ability to perform spin electronics [43] based on nonmagnetic semiconductor devices. This widens the field of usual magneto-electronics in metals and opens up the program of combining

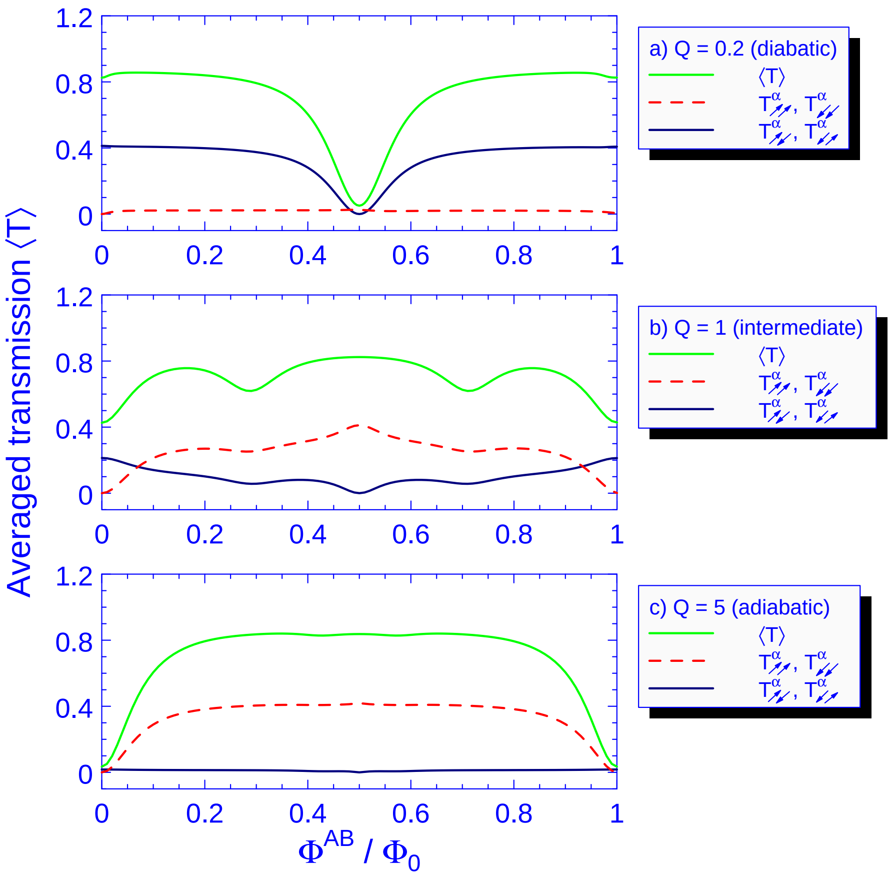

Figure 5.3: Partial and full transmission probabilities in S_α-basis, averaged over energy, vs. the Aharonov-Bohm flux through the ring. The coupling parameter is ϵ=0.3. The strength of the tangent magnetic field is increased from a) to c), corresponding to different degrees of adiabaticity, indicated by the adiabaticity parameter Q. Note the change in the polarization of transmitted electrons upon tuning the flux $\Phi^{\mathrm{AB}}/\Phi_0$ through the ring, resulting in a spin-flip mechansim at $\Phi^{\mathrm{AB}}/\Phi_0 = 0.5$. The shift of the global minimum by half a flux quantum in c) w.r.t. a) is an effect of the Berry phase that is present in the adiabatic situation c).

the rich physics of spin-polarized particles with all the advantages of semiconductor fabrication and technology, e.g., precise design of nanoelectronic devices with controllable charge carrier densities and optoelectronical applications. In this context, the theoretically predicted spin-flip effect discussed above might become an interesting control mechanism at sufficiently low temperatures.

5.1.2 Averaged transmission probabilities

So far we discussed the spin-flip effect found in the previous section in terms of (total and partial) transmission probabilities that are fastly oscillating. Averaging these quantities cancels out the fast oscillations and reveals the inherent features of the transmission probability. In this section, we will demonstrate the spin-flip effect in terms of averaged transmissions, see Fig. 5.3.

To this end, we consider the energy (E_F, or $\widetilde{E}_F$, respectively) averaged total transmission in the case of no additional flux, keeping the degree of adiabaticity constant. We introduce the *adiabaticity parameter* Q as the ratio of the spin precession (or Larmor) frequency ω_L given in Eq. (2.1) to the orbital angular frequency ω_{orb} defined in Eq. (2.2) and obtain (with $c = 1$ and negative charge e of the electron)

$$Q = \frac{\omega_L}{\omega_{\mathrm{orb}}} = \frac{-\frac{2Ma^2}{\hbar^2}\frac{g^* e\hbar}{4m_e}|\vec{B}|}{k_F a} \equiv \frac{\widetilde{\mu}B}{\sqrt{\widetilde{E}_F}}\,. \tag{5.22}$$

The adiabaticity parameter Q is the higher the more adiabatic the situation is.

The averaged transmission in the absence of an additional Aharonov-Bohm flux through the ring is shown in Fig. 5.4. In the adiabatic limit ($Q \to \infty$), the transmission approaches zero due to the effect of the Berry phase. In the other, diabatic, limit ($Q \to 0$), the numerical data agree with the analytical result (4.20), namely $\langle T\rangle = 2\epsilon/(1-\epsilon)$, obtained by averaging the expression (4.18) for the transmission probability $T(\epsilon, \theta_d, \theta_{AB} = 0)$ and by multiplying by two to account for two open channels.

Most interestingly, there are regions where $\langle T\rangle$ drops to zero that are not caused by geometric phase effects. In order to investigate what happens there, we look at the non-vanishing transmission amplitudes (5.9), in particular at the numerator $\delta_3 = g_1^* - g_1 + g_4^* - g_4 = -2\,i\,\mathrm{Im}(g_1 + g_4)$. With the expressions for g_1, g_4 put in, cf. Eqs. (4.48, 4.50), we find

$$\delta_3 = -2\,i\,(\sin n_1^{\nearrow}\pi - \sin n_1^{\swarrow}\pi)\,\frac{\cos(\zeta_1^{\nearrow} + \zeta_1^{\swarrow})}{\cos(\zeta_1^{\nearrow} - \zeta_1^{\swarrow})}\,, \tag{5.23}$$

meaning that δ_3 goes to zero whenever the difference in the second factor vanishes. Obviously, this occurs when $n_1^{\nearrow}$ and $n_1^{\swarrow}$ differ by an even integer number. Expanding the difference $n_1^{\nearrow} - n_1^{\swarrow} \overset{\mathrm{def}}{=} \Delta n$ using (3.47) for $\widetilde{\mu}B/\widetilde{E}_F$ small, and $\gamma_1^{\nearrow} \approx \gamma_1^{\swarrow}$, we have to solve the (Diophantic-like) equation

$$\Delta n = \cos\frac{\gamma_1^{\nearrow} + \gamma_1^{\swarrow}}{2} + \frac{\widetilde{\mu}B}{\sqrt{\widetilde{E}_F}}\sin\frac{\gamma_1^{\nearrow} + \gamma_1^{\swarrow}}{2} \tag{5.24}$$

to yield Δn as an even integer – keeping in mind that the γ themselves depend on the n. The first zero is related to $\Delta n = 2$ with $(\gamma_1^{\nearrow} + \gamma_1^{\swarrow})/2 = \pi/3$, giving rise to a ratio[3]

$$\frac{\widetilde{\mu}B}{\sqrt{\widetilde{E}_F}} = \sqrt{3} \tag{5.25}$$

in accordance with the observation. The following zeros in the averaged transmission belong to $\Delta n = 4, 6, \ldots$ and occur at ratios $\widetilde{\mu}B/\sqrt{\widetilde{E}_F} \equiv 1/q$ of $\sqrt{15}, \sqrt{35}, \ldots$, see Fig. 5.4 for illustration. For completeness, we state that the last factor of (5.23) contributes to the general slope of $\langle T\rangle$, whereas the factor discussed above is responsible for the oscillations, the fine structure of which in turn is determined by the denominator.

We also point out that the symmetry properties of the oscillations of $\langle T\rangle$ (between the zeros) strongly depend on the coupling parameter ϵ between the ring and the leads, see Fig. 5.4. For maximal coupling strength ($\epsilon = 0.5$), an approximate analytical expression for the averaged transmission $\bar{T}$ can be obtained.

---

[3] Note that the result is indeed consistent with the imposed condition $\widetilde{\mu}B/\widetilde{E}_F$ to be small as long as $\sqrt{E_F} \gg \sqrt{3}$.

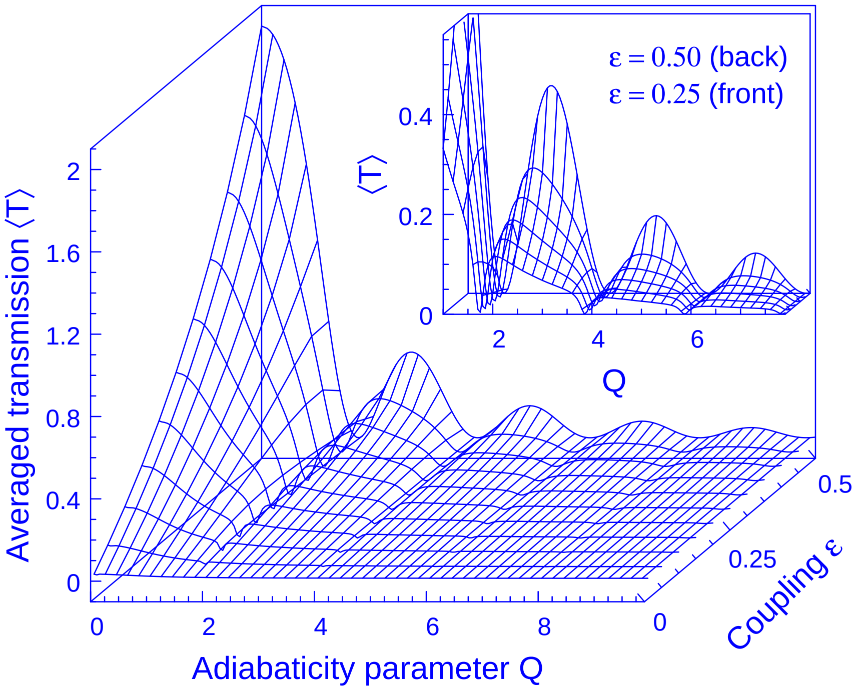

Figure 5.4: Transmission probability averaged over the Fermi energy E_F ($\widetilde{E}_F$, respectively) as a function of the adiabaticity parameter Q for an in-plane (tangent) magnetic field and no Aharonov-Bohm flux penetrating the ring. The tilted axis is the coupling parameter ϵ. The material specific parameters g^* for the gyromagnetic ratio and the effective mass M are chosen here and in the following figures as $g^* = 15$ and $M = 0.023 m_e$ corresponding to InAs. The maximum $\langle T\rangle_{\max}$ of $\langle T\rangle$ is observed at $Q = 0$, i.e., in the diabatic limit. It only depends on ϵ and obeys the law $\langle T\rangle_{\max} = 2\,\epsilon/(1-\epsilon)$ where $0 \leq \epsilon \leq 0.5$. The minima in $\langle T\rangle$ at $Q = \sqrt{3}, \sqrt{15}, \sqrt{35}, \sqrt{63}, \sqrt{99}$ are clearly visible and described in the text. The overall decay of $\langle T\rangle$ to zero as adiabaticity is reached ($Q \to \infty$) is an effect of the Berry phase that contributes strongest in the adiabatic limit. In the inset, the most interesting properties are enlarged.

We start evaluating Eq. (5.7) for $\epsilon = 0.5$ (hence, $a + b = \sqrt{1-2\epsilon} \equiv 0$) resulting in

$$\begin{aligned} \delta_1 &= -(g_1^* - g_4^*)\,, \\ \delta_2 &= -2\widetilde{g}_3^*\,, \\ \delta_3 &= g_1^* - g_1 + g_4^* - g_4\,, \\ \delta_9 &= g_1^* + g_4^*\,. \end{aligned} \tag{5.26}$$

For the denominator $\mathcal{N} \equiv \delta_3\delta_9 - \left(\delta_1^2 + \delta_2^2\right)$ in Eq. (5.9), we obtain thus

$$\begin{aligned} \mathcal{N} &= -(g_1 + g_4)(g_1^* + g_4^*) + (g_1^* + g_4^*)^2 - (g_1^* - g_4^*)^2 - 4\,(\widetilde{g}_3^*)^2 \\ &= -(g_1 + g_4)(g_1^* + g_4^*) + 4\det{}^*\,, \end{aligned} \tag{5.27}$$

with det $\overset{\text{def}}{=} g_1 g_4 - \tilde{g}_3^2$. Inserting Eqs. (4.48, 4.50) and substituting $\Delta n = n_1^{\nearrow} - n_1^{\swarrow}$, we arrive at

$$\begin{aligned} (g_1+g_4)(g_1^*+g_4^*) = |g_1+g_4|^2 &= 2\frac{\cos^2(\zeta_1^{\nearrow}+\zeta_1^{\swarrow})}{\cos^2(\zeta_1^{\nearrow}-\zeta_1^{\swarrow})}\,(1-\cos\Delta n\pi)\ , \\ \det &= -e^{i(n_1^{\nearrow}+n_1^{\swarrow})\pi}\ . \end{aligned} \tag{5.28}$$

This finally leads to the following analytical expression for the transmission *probability* (4.29) for $\epsilon = 1/2$ $(a=-1/2, b=1/2)$:

$$T_{1/2}^{\text{ana}} = T_{\uparrow\uparrow} + T_{\downarrow\downarrow} = \frac{8\epsilon^2}{b^2}\,a_{13}a_{13}^* = \frac{8\,\delta_3\delta_3^*}{(|g_1+g_4|^2+4\det^*)\,(|g_1+g_4|^2+4\det)}\ . \tag{5.29}$$

In Eq. (5.23) we already evaluated part of the numerator that finally yields

$$\begin{aligned} \delta_3\delta_3^* &= 4\,\frac{\cos^2(\zeta_1^{\nearrow}+\zeta_1^{\swarrow})}{\cos^2(\zeta_1^{\nearrow}-\zeta_1^{\swarrow})}\,(\sin n_1^{\nearrow}\pi - \sin n_1^{\swarrow}\pi)^2 \\ &= 16\,\frac{\cos^2(\zeta_1^{\nearrow}+\zeta_1^{\swarrow})}{\cos^2(\zeta_1^{\nearrow}-\zeta_1^{\swarrow})}\,\sin^2\frac{\Delta n\pi}{2}\,\cos^2\frac{(n_1^{\nearrow}+n_1^{\swarrow})\pi}{2}\ . \end{aligned} \tag{5.30}$$

Furthermore, the denominator evaluates to

$$\begin{aligned} \mathcal{N}_T &= |g_1+g_4|^4 + 8\,|g_1+g_4|^2\,\text{Re}(\det) + 16 \\ &= 4\,\frac{\cos^4(\zeta_1^{\nearrow}+\zeta_1^{\swarrow})}{\cos^4(\zeta_1^{\nearrow}-\zeta_1^{\swarrow})}\,(1-\cos\Delta n\pi)^2 \\ &\quad -16\,\frac{\cos^2(\zeta_1^{\nearrow}+\zeta_1^{\swarrow})}{\cos^2(\zeta_1^{\nearrow}-\zeta_1^{\swarrow})}\,(1-\cos\Delta n\pi)\cos(n_1^{\nearrow}+n_1^{\swarrow})\pi + 16\ , \end{aligned} \tag{5.31}$$

where we have used the unitarity ($\det\det^* = 1$) of $\underline{t}_I, \underline{t}_{II}$.

The next step is to perform the averaging. Here, we are only interested in the qualitative behaviour and not in all the quantitative details. Therefore, we perform the averaging procedure for Eqs. (5.30, 5.31) by neglecting all terms bearing fast oscillations, in particular we put a factor 1/2 for the last $\cos^2$-term in the numerator (5.30) and neglect the second term in the denominator (5.31). This yields for the averaged transmission probability

$$\langle T_{1/2}^{\text{ana}}\rangle = \frac{8\times 16\,\frac{\cos^2(\zeta_1^{\nearrow}+\zeta_1^{\swarrow})}{\cos^2(\zeta_1^{\nearrow}-\zeta_1^{\swarrow})}\,\sin^2\frac{\Delta n\pi}{2}\times\frac{1}{2}}{4\left(4+\frac{\cos^4(\zeta_1^{\nearrow}+\zeta_1^{\swarrow})}{\cos^4(\zeta_1^{\nearrow}-\zeta_1^{\swarrow})}(1-\cos\Delta n\pi)^2\right)} \approx \frac{16\,\cos^2(\zeta_1^{\nearrow}+\zeta_1^{\swarrow})\,\sin^2\frac{\Delta n\pi}{2}}{4+\cos^4(\zeta_1^{\nearrow}+\zeta_1^{\swarrow})\,(1-\cos\Delta n\pi)^2}\ , \tag{5.32}$$

using $\zeta_1^{\nearrow} \approx \zeta_1^{\swarrow}$ in the last step. It is worth to introduce the mean angle $\bar\gamma$ (or $\bar\zeta = \bar\gamma/2$, respectively), namely $\bar\gamma \overset{\text{def}}{=} \frac{1}{2}(\gamma_1^{\nearrow}+\gamma_1^{\swarrow})$. For completeness, we also define the mean kinetic energy quantum number $\bar n = \frac{1}{2}(n_1^{\nearrow}+n_1^{\swarrow})$, and the difference angle $\Delta\gamma = \gamma_1^{\nearrow}-\gamma_1^{\swarrow}$, generalizing Eq. (3.45) to

$$\cot\bar\gamma = \frac{\bar n + \frac{1}{2}}{\tilde\mu B}\ , \tag{5.33}$$

and giving rise to the relations

$$\begin{aligned} \bar n &= \sqrt{\widetilde{E}_F} - \frac{1}{2} + \sin\frac{\Delta\gamma}{2}\sin\bar\gamma \approx \sqrt{\widetilde{E}_F} - \frac{1}{2}\ , \\ \Delta n &= \cos\bar\gamma + \frac{\tilde\mu B}{\sqrt{\widetilde{E}_F}}\sin\bar\gamma\ , \\ \tan\Delta\gamma &= -\frac{\Delta n}{\tilde\mu B + \frac{\bar n(\bar n-1)}{\tilde\mu B}}\ . \end{aligned}$$

Furthermore, we can easily express $\bar{\gamma}$ and Δn in terms of the adiabaticity parameter Q defined in Eq. (5.22):

$$\begin{aligned} \cot\bar{\gamma} &= \frac{1}{Q} \longrightarrow \cos\bar{\gamma} = \frac{1}{\sqrt{1+Q^2}}\,, \\ \Delta n &= = \sqrt{1+Q^2}\,. \end{aligned} \tag{5.34}$$

This relation between the adiabaticity parameter Q and $\bar{\gamma}$ elucidates the role of the geometric phase as a measure of adiabaticity.

Inserting the last relations into Eq. (5.32), we obtain after straightforward algebra the following approximate result for the averaged transmission in the case of maximal coupling strength ($\epsilon = 0.5$) and no Aharonov-Bohm flux penetrating the ring:

$$\begin{aligned} \langle T^{\mathrm{ana}}_{1/2}\rangle &= \frac{16\cos^2\bar{\gamma}\sin^2\Delta n\frac{\pi}{2}}{4+\cos^4\bar{\gamma}\,(1-\cos\Delta n\pi)^2} \\ &= \frac{16}{1+Q^2}\frac{\sin^2\left(\frac{\pi}{2}\sqrt{1+Q^2}\right)}{4+(1+Q^2)^{-2}\left(1-\cos\left(\pi\sqrt{1+Q^2}\right)\right)^2}\,. \end{aligned} \tag{5.35}$$

From this equation we immediately read off the zeros of $\langle T^{\mathrm{ana}}_{1/2}\rangle$ to occur whenever $\sqrt{1+Q^2}$ evaluates to an even integer. As already described above (see Fig. 5.4), this happens at $Q^2 \equiv \widetilde{\mu}^2 B^2/\widetilde{E}_F = 3, 15, 35, \ldots$. In Fig. 5.5, the result of Eq. (5.35) is shown in comparison with the numerical data, pointing out a good agreement of the two curves. In addition, we clearly observe deviations of the local maxima from the values given by the Lorentzian prefactor $1/(1+Q^2)$. Interestingly, the prefactor *dominates* the fall-off for coupling strengths ϵ below ≈ 0.4 as illustrated in Fig. 5.6 and can also be confirmed in Fig. 5.4 (inset)[4].

We state that the behaviour of the *envelope* $\langle T\rangle_{\mathrm{env}}$ of the averaged transmission $\langle T\rangle$ for $\epsilon \to 0$ is rather well described by

$$\langle T\rangle_{\mathrm{env}} = 2\,\frac{\epsilon}{1-\epsilon}\,\frac{1}{1+Q^2}\,, \tag{5.36}$$

as demonstrated in Fig. 5.6 for $\epsilon \leq 0.4$. For small values of ϵ, deviations from Eq. (5.36) occur merely at the positions where $\langle T\rangle$ drops to zero (i.e., $Q = \sqrt{3}, \sqrt{15}, \sqrt{35}, \ldots$), and the dips become the narrower the smaller ϵ.

So far, we investigated the situation where no Aharonov-Bohm flux was penetrating the ring. The result in the presence of a (weak) homogeneous magnetic field B_z corresponding to half a flux quantum is shown in Fig. 5.7. The dominant structure is the (global) minimum where the curve starts from, i.e., we find zero (averaged) transmission in the diabatic limit $Q = 0$. One might call this effect in a sense dual to the asymptotic value of zero for the transmission in the case without additional flux and in the adiabatic limit: The condition for

---

[4] At this point we briefly refer to a possible interpretation of the results in terms of path integrals [41]. Without going into details, the curve for $\epsilon = 0.5$ resembles closely that of one-loop contributions (electrons performing half a round trip in each arm). For lower couplings, $\epsilon < 0.5$, we find deviations from this result as the influence of multi-loop paths increases. This can be understood as resulting from better confinement of the electrons in the ring for decreased coupling to the leads.

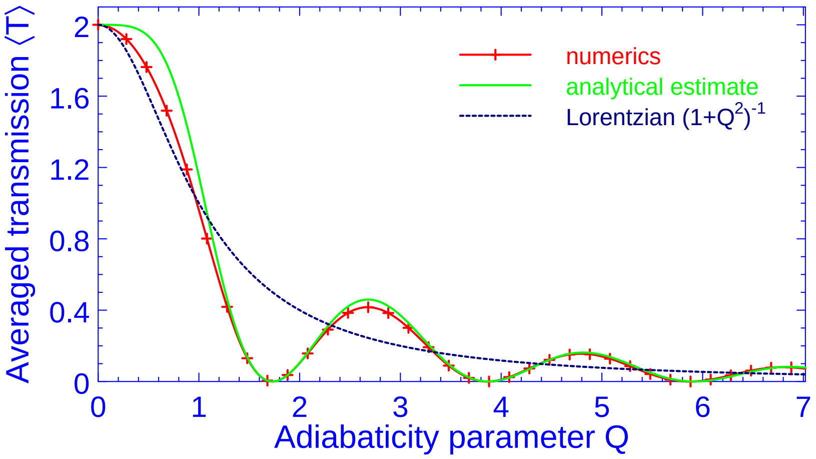

Figure 5.5: Averaged transmission probability for maximal coupling strength, $\epsilon = 0.5$, in an in-plane (tangent) magnetic field, and again without additional Aharonov-Bohm fluxes. The numerical data (crosses) are well described by the analytical expression (5.35). For comparison, a Lorentzian decay that describes the overall behaviour for smaller couplings (see Fig. 5.6) is shown.

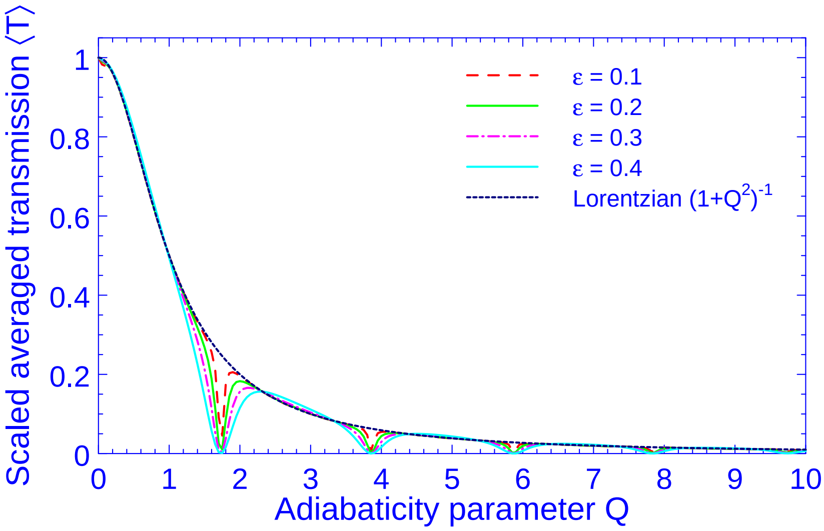

Figure 5.6: Averaged transmission probability scaled by a factor $(1-\epsilon)/\epsilon$ for various coupling strengths. Though the concrete shape of the minima depends strongly on the value of ϵ (in particular, it becomes singular for $\epsilon \to 0$), the overall decay away from the minima is very well described by a Lorentzian for $\epsilon \lesssim 0.4$. A major change in the shape of the maxima as $\epsilon \to 0.5$, see Fig. 5.5.

zero averaged transmission is an effective flux of half a flux quantum (with a Φ_0-periodicity as investigated in Section 4.1.3). When no Aharonov-Bohm flux exists, the flux can be provided as geometric flux via the geometric phase, cf. Eq. (4.21). Note, however, that $\Phi_0/2$ is the maximal possible geometric flux that is achieved in the adiabatic limit and that geometric phase effects are reduced in non-adiabatic situations, see also Fig. 5.4. In turn, when already half a flux

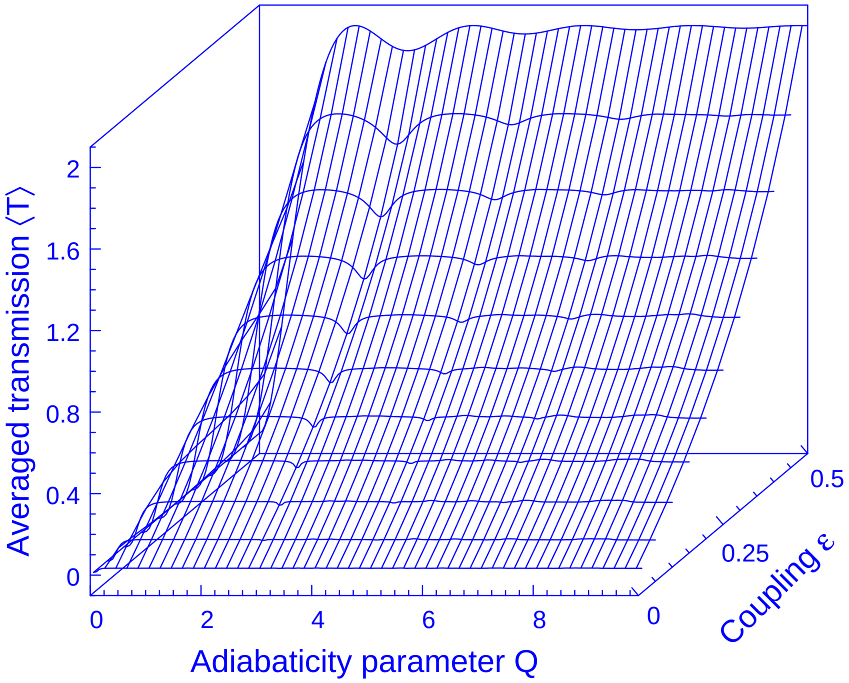

Figure 5.7: Transmission probability averaged over the Fermi energy E_F as a function of the adiabaticity parameter Q for an in-plane magnetic field and half a flux quantum penetrating the ring. The material specific parameters g^* and M are again for InAs (see Fig. 5.4). For $Q = 0$, there is no transmission, see text. On the other hand, for $Q \to \infty$, the oscillations are lost and $\langle T \rangle$ depends only on the coupling ϵ, saturating at $\langle T \rangle = 2\,\epsilon/(1-\epsilon)$ rather than going to zero as in Fig. 5.4 since now the effect of the Berry phase in this adiabatic limit is compensated by the Aharonov-Bohm flux through the ring. The minima of $\langle T \rangle$ occur now at $Q = \sqrt{8}, \sqrt{24}, \sqrt{48}, \sqrt{80}$.

quantum due to an additional Aharonov-Bohm flux is present, an additional geometric flux of $\Phi_0/2$ in the adiabatic limit destroys the situation, see Fig. 5.7. However, then we expect zero transmission in the diabatic limit and indeed find it there[5]. Furthermore, in the situation with half a flux quantum penetrating the ring, we find the same $\epsilon/(1-\epsilon)$-dependence of the averaged transmission[6] in the *adiabatic* limit that we know from the zero-flux case in the diabatic limit. This can be understood by realizing that the geometric flux carries a negative sign and therefore compensates the Aharonov-Bohm flux.

Note that *local* minima occur at the positions $Q = \sqrt{8}, \sqrt{24}, \sqrt{48}, \sqrt{80}$, these are precisely the numbers $\sqrt{n^2 - 1}$ with n an *odd* integer. In contrast, in the zero-flux case the minima occur

---

[5] In further generalizing these ideas one might expect that for any Aharonov-Bohm flux through the ring there exists a degree of adiabaticity where the corresponding geometric flux completes half the flux quantum such that the transmission becomes zero. However, though this is true for the non-averaged transmissions, cf. ,e.g., Fig. 5.1b, this effect is lost during the averaging procedure because in order to keep Q fixed upon varying $\widetilde{E}_F$, different magnetic field strength enter the calculation, see Fig. 5.8.

[6] As can already be seen in Fig. 5.7, the oscillations are washed out as Q increases leading asymptotically to the above mentioned value.

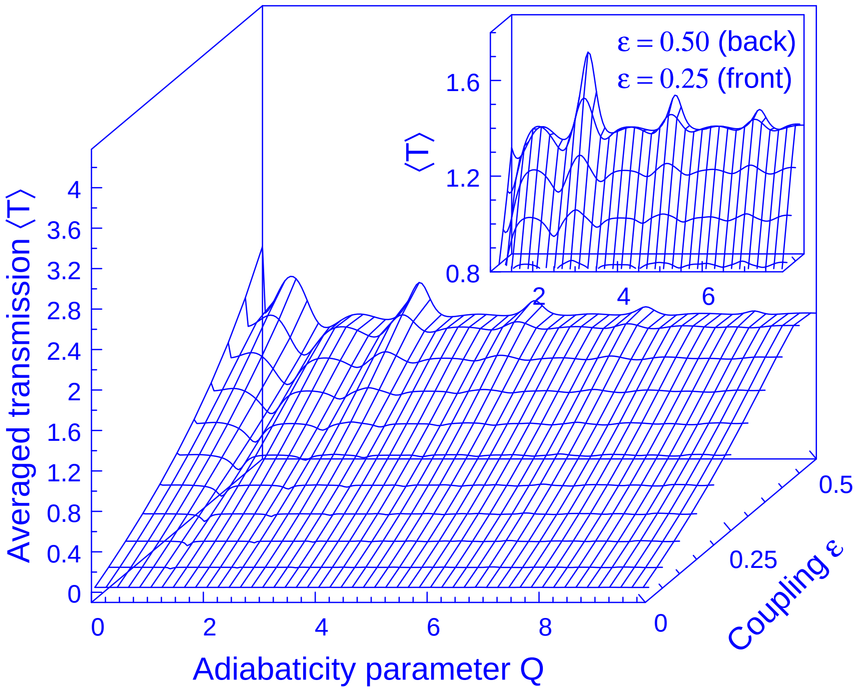

Figure 5.8: Transmission probability averaged over the Fermi energy E_F as a function of the adiabaticity parameter Q for an in-plane magnetic field and a quarter of a flux quantum penetrating the ring for InAs (see also Figs. 5.4 and 5.7). Although there is some structure in the curve, it is far less characteristic than in the special situations discussed above.

at $\sqrt{n^2 - 1}$ with n an *even* integer. However, here the transmission is only diminished and does *not* drop to zero, in fact the oscillations vanish in the adiabatic limit as discussed above.

In the general situation where the Aharonov-Bohm flux is neither an integer nor half an integer multiple of the flux quantum Φ_0, there are no signatures of special interest in the averaged transmission probability. One typical example is shown in Fig. 5.8 for a flux $\Phi^{AB} = 0.25\,\Phi_0$.

5.1.3 Comparison with a two-dimensional model

So far, we discussed transmission amplitudes in an one-dimensional model system. Concerning experimental realisation where rings of *finite width* are used, a two-dimensional (2d) system, is, of course, more realistic. The effect of the non-vanishing radial extension of the ring is the possibility of having several *transverse* modes, or, open channels, arising from the confining potential in radial direction. In the limit of one open channel, i.e., one transverse mode, we find the closest similarity to a 1d ring[7]. In Fig. 5.9 we compare results for the 1d ring with data from [41] for a 2d ring model with just one open channel. The latter are obtained within a 2d tight-binding model in a Green function formalism [52].

We point out that the 2d model of [41] has no adjustable parameter controlling the coupling between the ring and the leads, as is given in terms of ϵ for the 1d model. To compare the data, ϵ was adjusted using the value of $\langle T\rangle$ at $Q = 0$, where we can apply the analytical result

---

[7] In experiments with semiconductor heterostructures this can be achieved by tuning additional gate voltages.

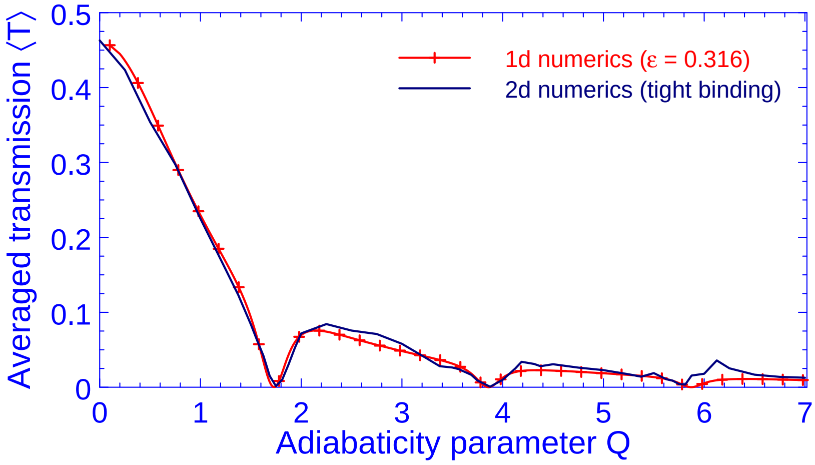

Figure 5.9: Averaged transmission probability for $\epsilon = 0.316$ compared with the results of a 2d model [41]. The results were adjusted by choosing ϵ to give coincidence at $Q = 0$. The two curves agree well.

$\langle T\rangle(Q = 0) = 2\,\epsilon/(1 - \epsilon)$. Accordingly, $\epsilon = 0.316$ was chosen. The agreement of the two curves is satisfying, in particular when noticing that the shape of the curve is determined by ϵ, see Figs. 5.5, 5.6!

5.1.4 Limiting situations: Adiabatic and diabatic regime

Finally, we briefly investigate the transmission probabilities in the *adiabatic* and the *diabatic* limit for the in-plane magnetic field geometry. Adiabaticity is characterized by the dominance of the magnetic field over the orbital motion, manifesting itself in $\gamma_1^{\nearrow} = \gamma_1^{\swarrow} = \gamma_2^{\nearrow} = \gamma_2^{\swarrow} = \pi/2$ which is evident when thinking in the geometric interpretation of the angles γ, cf. Fig. 3.3. Inserting the corresponding values for the angles $\zeta \overset{\text{def}}{=} \gamma/2$,

$$\zeta_1^{\nearrow} = \zeta_1^{\swarrow} = \zeta_2^{\nearrow} = \zeta_2^{\swarrow} = \frac{\pi}{4}\,, \tag{5.37}$$

into Eqs. (4.48, 4.50) leads to a relation between the matrix elements of the transfer matrices $\underline{t}_I, \underline{t}_{II}$, namely $g_1 = -g_4$. When no additional Aharonov-Bohm flux is present, we obtain from Eq. (5.7) $\delta_3 = 0$, giving via Eq. (5.9) immediately

$$T = 0 \tag{5.38}$$

for the transmission probability in the adiabatic limit with $\Phi^{AB} = 0$. This is a clear and well known [39] sign of a Berry phase that effectively acts like an Aharonov-Bohm flux on the transmission probability and, accordingly, contributes to the interference effects. Whereas in the usual Aharonov-Bohm experiment zero transmission is achieved with *half* a quantum flux penetrating the ring, we find this situation in the *presence of a Berry phase* equivalent to half a flux quantum[8] for zero Aharonov-Bohm flux. Consequently, if we apply an additional

---

[8] Indeed, for $\alpha = \pi/2$ the Berry phase takes the value $\Gamma = -\pi$ and the effective flux associated reads $\Phi_\Gamma = \Gamma\,\Phi_0/2\pi$, see, e.g., [39].

Aharonov-Bohm flux, the interference effects are, of course, changed and we now observe non-zero transmission since the negative interference effect of the Berry phase is canceled upon adding up all phases, cf. the discussion at the end of Section 5.1.2.

In the opposite case, i.e., for diabatic conditions, the magnetic field does not play a role, and we are in the situation of

$$\zeta_1^{\nearrow} = \zeta_1^{\swarrow} = \zeta_2^{\nearrow} = \zeta_2^{\swarrow} = 0\,, \tag{5.39}$$

as again is clear from the geometric picture. This last equation still holds in the case of a (not too strong) homogeneous magnetic field perpendicular to the ring. After straightforward manipulation, we recover an equation for the transmission probability similar to Eq. (4.76), namely

$$T_{\uparrow\uparrow}^{\mathrm{diab}} = T_{\downarrow\downarrow}^{\mathrm{diab}} = \frac{4\epsilon^2}{1 - 2\cos\left(2\theta_d + 2\theta_{AB}\right)(a+b)^2 + (a+b)^4}\,, \tag{5.40}$$

with

$$\theta_d = \pi\sqrt{\widetilde{E}_F}\,, \quad \theta_{AB} = \pi\frac{\Phi^{AB}}{\Phi_0}\,,$$

where Φ^{AB} is again the Aharonov-Bohm flux through the ring. This expression is equivalent to Eq. (4.18) obtained by Büttiker et al. [27], which not surprisingly reveals the close vicinity of a 1d ring subject to an external Aharonov-Bohm flux analyzed there and the diabatic limit (with flux Φ^{AB}) considered here, cf. also the discussion in Section 4.1.3.

5.2 Central micromagnet

One possibility to achieve a crown-like magnetic field (cf. Fig. 3.1b) consists in placing a micromagnet in the centre of the ring in which the electrons move. In experiments, this can be done by superimposing ferromagnetic microstructures at the appropriate position in an Aharonov-Bohm device [35]. The experimental realization used in Ref. [35] is a dysprosium[9] (Dy) micromagnet in the centre of a micron-sized loop located in the high mobility two-dimensional electron gas (2DEG) of a GaAs-AlGaAs heterojunction. The electrons then see a ring-like geometry as illustrated in Fig. 3.1b, and they are subject to the non-uniform magnetic field created by the micromagnet. The tilt angle α of the magnetic field w.r.t. z-axis varies on mesoscopic length scales and therefore allows to observe signatures of geometric phases in magneto-conductance measurements. In the experiment [35] clear signs of the non-uniform magnetic field were seen, e.g., beating patterns in the Aharonov-Bohm oscillation. Berry phase effects have been proposed as one possible mechanism to describe these features.

We now present calculations of the magneto-conductance (or transmission probability, respectively) through a 1d ring with a central micromagnet under variation of an external magnetic field perpendicular to the ring in order to address the experiment in Ref. [35].

The magnetic field of a cylinder-shaped micromagnet is computed in Appendix C. In the far-field, in particular at the position of the ring, the magnetic field is rather well treated by the

---

[9] Dysprosium is a rare earth metal with a magnetic polarization as high as 3.8 Tesla in the crystalline state. Its Curie temperature of $T_C \approx 89$ K guarantees ferromagnetic ordering at experimental relevant temperatures of $T \leq 0.3$ K.

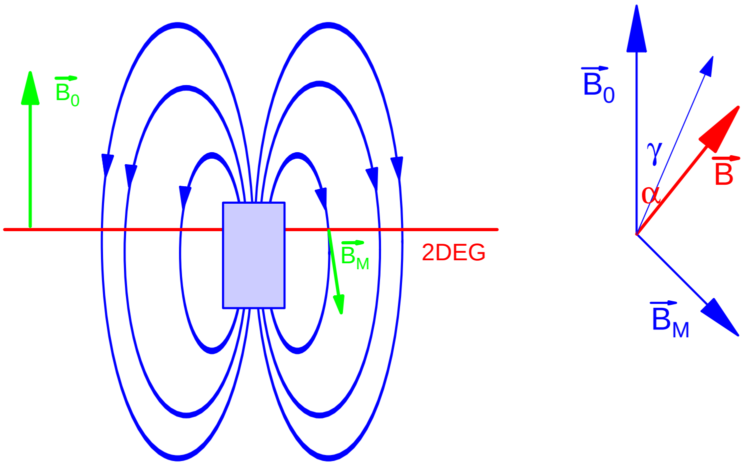

Figure 5.10: Electrons in a 1d ring subject to an inhomogeneous magnetic field created by a central Dysprosium micromagnet. Superimposed is a homogeneous magnetic field B_0 perpendicular to the ring that can be varied.

dipole approximation and we have according to Eq. (C.10)

$$\vec{H}(\vec{r}) = -\frac{M}{2} H R'^2 \left(r^2 + z^2\right)^{-\frac{5}{2}} \left[-3rz\vec{e_r} + (r^2 - 2z^2)\vec{e_z}\right] \; ; \tag{5.41}$$

where the bar magnet has a height $2H$ and a radius R', see Fig. C.2. The magnetic field $\vec{H}$ is illustrated in Fig. 5.11. The magnetization of the bar magnet is assumed to be longitudinal, $\vec{M} = M\vec{e_z}$. In the experiment mentioned above, it is created by initially applying a strong magnetic field in z (or $-z$) direction.

Motivated by the kind of measurements carried out in [35], we incorporate an external homogoneous magnetic field B_0 in z-direction in our considerations and study magneto-conductance as a function of this external field B_0 that gives rise to an *external* Aharonov-Bohm flux $\Phi^{AB} \overset{\text{def}}{=} \pi a^2 B_0$. The total magnetic field[10] is then the sum of the magnetic field $\vec{B}_M(a)$ due to the micromagnet and the variable homogeneous magnetic field $B_0\vec{e_z}$, see Fig. 5.10.

In this geometry, the electrons in the ring are exposed to an *inhomogeneous* field (except if the plane of the 2DEG coincides with the central plane of the micromagnet) of fixed modulus $|\vec{B}(a)| = |\vec{B}_M(a) + B_0\vec{e_z}|$. This opens the possibility of observing signs of geometric phases, in particular signs of Berry phases in the adiabatic limit where the effects are expected to be strongest. The reason for this is discussed in Chapter 3 and can be easiest understood when thinking of the Berry phase as the solid angle in parameter space that is traced during one round trip. Whereas in the adiabatic situation, this solid angle is determined by the angle α of the total magnetic field $\vec{B}$ to the z-axis, in the non–adiabatic case α has to be replaced by the smaller angle γ [see Eqs. (3.45, 3.46)] that goes to zero in the diabatic limit, reducing the solid angle accordingly.

When discussing properties of the magneto-conductance in dependence of B_0 it has to be taken into account that both the external magnetic field $B_0\vec{e_z}$ and the field $\vec{B}_M$ of the magnet

---

[10] We use the notions magnetic field ($\vec{H}$) and magnetic induction ($\vec{B}$) synonymously in this chapter, because we exclusively consider points outside the micromagnet where $\vec{B} = \mu_0\vec{H}$ holds.

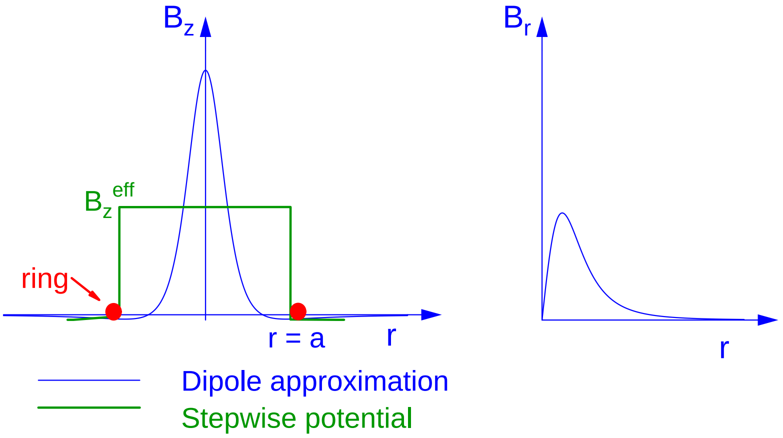

Figure 5.11: Vertical and radial magnetic field B_z and B_r in dipole approximation (C.10) in the same arbitrary units for a micromagnet with $H = R' = 1$ for $z = 0.6$. Whereas the magnetic field B_z is *negative* at the position of the ring, $r = a$, it is positive for small r. Therefore, the *total* flux through the ring can be modelled by a stepwise potential with a *positive* maximal value $B_z^{\rm eff}$.

contribute to the Aharonov-Bohm flux through the ring. For simplicity, we describe the micromagnet as a dipole *everywhere* in space[11]. Within this approximation, the z-component B_z of $\vec{B}_M$ gives rise to an Aharonov-Bohm flux Φ^M through the ring with z-coordinate $z \overset{\rm def}{=} z_R$ that is

$$\begin{aligned} \Phi^M &= \int_0^{2\pi} d\phi \int_0^a dr r B_z \\ &= -\frac{\mu_0 M}{2} 2\pi H R'^2 \int_0^a \frac{r(r^2 - 2z_R^2)}{(r^2 + z_R^2)^{\frac{5}{2}}} dr \\ &= \frac{\mu_0 M V}{2} \frac{a^2}{(a^2 + z_R^2)^{\frac{3}{2}}} , \end{aligned} \tag{5.42}$$

where we have defined $V = 2H\pi R'^2$, the volume of the micromagnet. The total Aharonov-Bohm flux through the ring is then given by

$$\Phi_{\rm tot}^{AB} = \pi a^2 \left(B_0 + \frac{\mu_0 M V}{2\pi (a^2 + z_R^2)^{\frac{3}{2}}} \right) \overset{\rm def}{=} \pi a^2 \left(B_0 + B_z^{\rm eff} \right) , \tag{5.43}$$

where $B_z^{\rm eff}$ is a *constant* magnetic field that creates the same Aharonov-Bohm flux Φ^M through the ring as the varying B_z-component of the magnetic field $\vec{B}_M$ of the micromagnet[12].

Since the magnetization of the micromagnet is not exactly known in the underlying experiment, it is characterized by the parameter M^{AB},

$$\pi a^2 B_z \overset{\rm def}{=} -M^{AB} \Phi_0 \quad (\neq \Phi^M) \tag{5.44}$$

---

[11] As shown in Appendix C this is an approximation in the vicinity of the micromagnet. However, the difference between the exact Aharonov-Bohm flux due to the magnet and the one obtained in dipole approximation corresponds to a shift along the Φ^{AB}-axis and does not affect the principle results.

[12] These two fields are related by $B_z^{\rm eff} = -2\frac{a^2+z_R^2}{a^2-2z_R^2} B_z$. Note the opposite direction of B_z and $B_z^{\rm eff}$, cf. also in Fig. 5.11.

in the calculations. From this definition and Eq. (5.43) it is immediately clear that the z-component of the total magnetic field vanishes for $\Phi^{AB} = M^{AB}\Phi_0$, implying an in-plane magnetic field[13], $\vec{B} = B_r\vec{e_r}, \alpha = \pi/2$. Although the (total) magnetic field is symmetric w.r.t. this point, the (total) Aharonov-Bohm flux through the ring is *not!* The reason for this is the "extra" flux caused by the non-uniform magnetic field of the micromagnet, cf. Eq. (5.43). Consequently, we cannot expect the transmission probability to be symmetric w.r.t. an external flux $\Phi^{AB} = M^{AB}\Phi_0$, see Fig. 5.12. We also mention that at given external magnetic field $B_0 = \Phi^{AB}/\pi a^2$ the angle α of the total magnetic field $\vec{B}$ at the ring position w.r.t. z-axis depends, of course, on the strength of the micromagnet, and is provided by ($\tilde{z} \overset{\text{def}}{=} z_R/a$)

$$\cos\alpha = \frac{B_0 + B_z}{\sqrt{(B_0+B_z)^2 + B_r^2}} = \frac{1 - \frac{\Phi^{AB}}{M^{AB}\Phi_0}}{\sqrt{(1 - \frac{\Phi^{AB}}{M^{AB}\Phi_0})^2 + \frac{3\tilde{z}}{1-2\tilde{z}^2}}} . \tag{5.45}$$

Furthermore, we introduce an adiabaticity parameter Q_M for the micromagnet in analogy to Eq. (5.22),

$$Q_M = \frac{\tilde{\mu}|\vec{B}_M|}{\sqrt{E_F}} = \frac{\tilde{\mu}\frac{B_z}{\cos\alpha(\Phi^{AB}=0)}}{k_{\text{eff}}a} ,$$

that is zero in the diabatic limit and increases when approaching adiabaticity. With the conventions of Chapter 3, it can be expressed in terms of M^{AB} and the effective gyromagnetic ratio g^* as

$$Q_M = \frac{g^*\frac{M}{m_e}M^{AB}\frac{3\tilde{z}}{1-2\tilde{z}^2}}{\sqrt{E_F}} . \tag{5.46}$$

The results for the calculated magneto-conductance are shown in Figs. 5.12, 5.14 for three different degrees of adiabaticity, $Q_M = 0.4, 1, 10$. This parameter is adjusted by the proper choice of the effective gyromagnetic ratio g^* and the effective mass M, leaving the strength of the micromagnet constant at $M^{AB} = 5$. (The connection to a specific material system is provided by choosing Q_M according to the product g^*M.) We follow the geometry described in [35] and choose the radius as $a = 500\,nm$. The 2DEG is placed in a plane lying $150\,nm$ above the central plane of the Dysprosium. Eventually, we assume maximal coupling, $\epsilon = 0.5$.

The total transmission is shown in Fig. 5.12. For comparison, we show in Fig. 5.12a the result of Büttiker et al. [27], Eq. (4.18), that applies to a situation *without* micromagnet. The external flux leads to the well-known Aharonov-Bohm oscillations. However, here we have taken into account the Zeeman splitting of the energy and the influence of the Berry phase (assuming an adiabatic situation). The geometric flux according to the Berry phase is included in the (effective) Aharonov-Bohm flux, cf. Eq. (4.21), removing the degeneracy of the two electron gases $\{\nearrow\}$ ($\{\swarrow\}$) where the spin is (anti)aligned with the total magnetic field $\vec{B}$ (cf. Chapter 3). In the adiabatic limit, Fig. 5.12d, the sum of the two corresponding curves should give the exact result as indeed is found, see the discussion below.

In Fig. 5.12b-d the strongest deviations from Aharonov-Bohm-like oscillations are seen around $\Phi^{AB}/\Phi_0 = M^{AB} = 5$, indicating the importance of geometric phases there. In fact,

---

[13] This situation was studied in detail in Section 5.1 and we found a characteristic dependence of the (averaged) transmission probability on the Aharonov-Bohm flux through the ring. However, in the present situation we can *not control* the (residue) flux due to the non-uniform magnetic field of the micromagnet and the in-plane magnetic field appears as transient regime when varying the external Aharonov-Bohm flux.

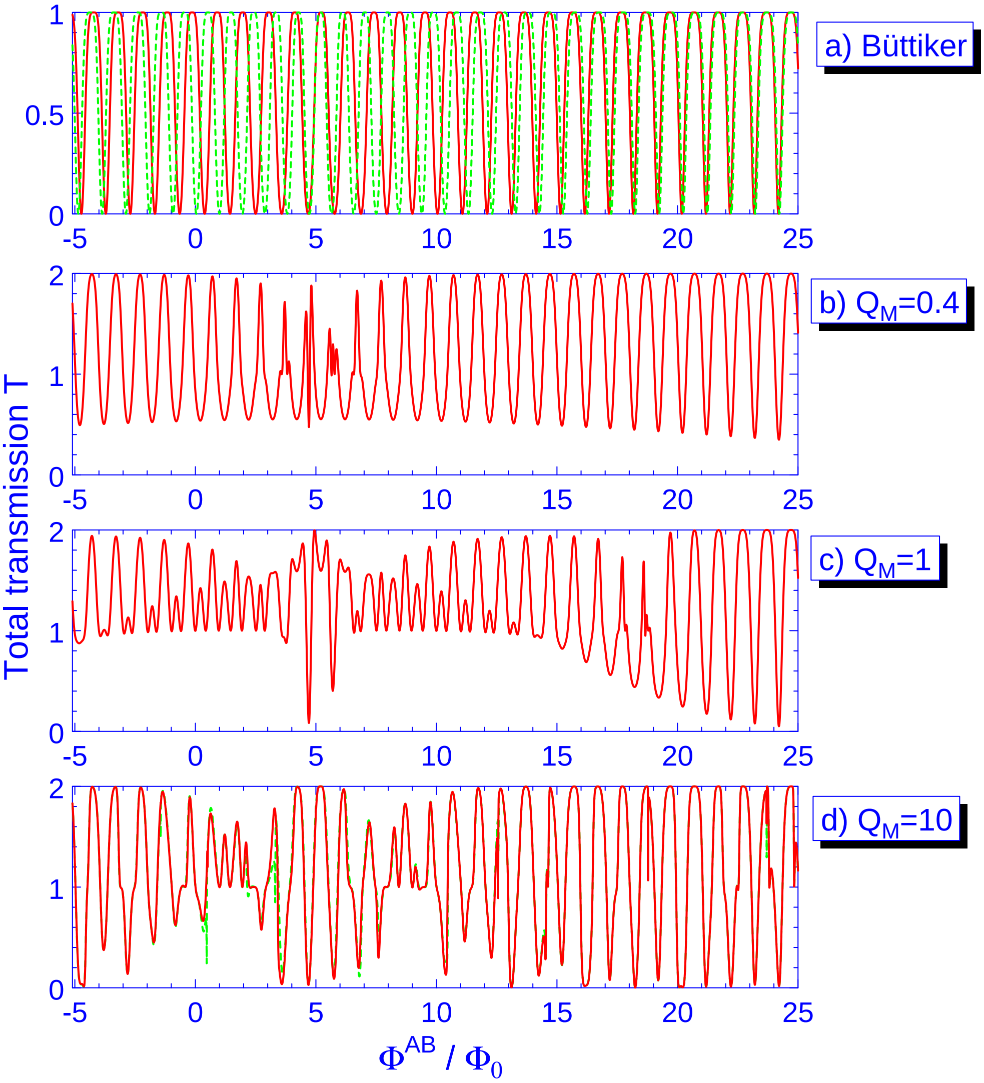

Figure 5.12: Magneto-conductance for an Aharonov-Bohm device with a central micromagnet ($M^{AB} = 5$) under variation of the external flux Φ^{AB}. a) Transmission probability without micromagnet according to Eq. (4.18) (Büttiker et al., cf. [27]) adapted to electrons with spin subject to a Berry phase. The solid and dashed line correspond to the two emerging electron gases $\{\nearrow\}, \{\swarrow\}$. In d), the sum of the two contributions is shown as dashed line. b)-d) Total transmission probability for spinful electrons; b) diabatic regime in which transmission is similar to that described in [27], c) intermediate case where effects due to geometrical phases become visible, d) adiabatic limit d) that is dominated by interference effects due to different Berry phases for the $|\nearrow\rangle$- and $|\swarrow\rangle$-electron gases. In all cases, the effect of geometric phases is lost for dominating external field, $\Phi^{AB} \ll M^{AB}\Phi_0$.

this corresponds to the situation where the external flux Φ^{AB} cancels the flux due to the micromagnet such that the non-uniform field of the micromagnet becomes maximally important. The strong interference effects around $\Phi^{AB}/\Phi_0 = M^{AB}$ stem from the slightly different oscillation frequencies of the $|\nearrow\rangle$- and $|\swarrow\rangle$-electrons due to the effect of the Berry phase. Regular Aharonov-Bohm-like oscillations are recovered as the external magnetic field $B_0 = \Phi^{AB}/\pi a^2$ becomes

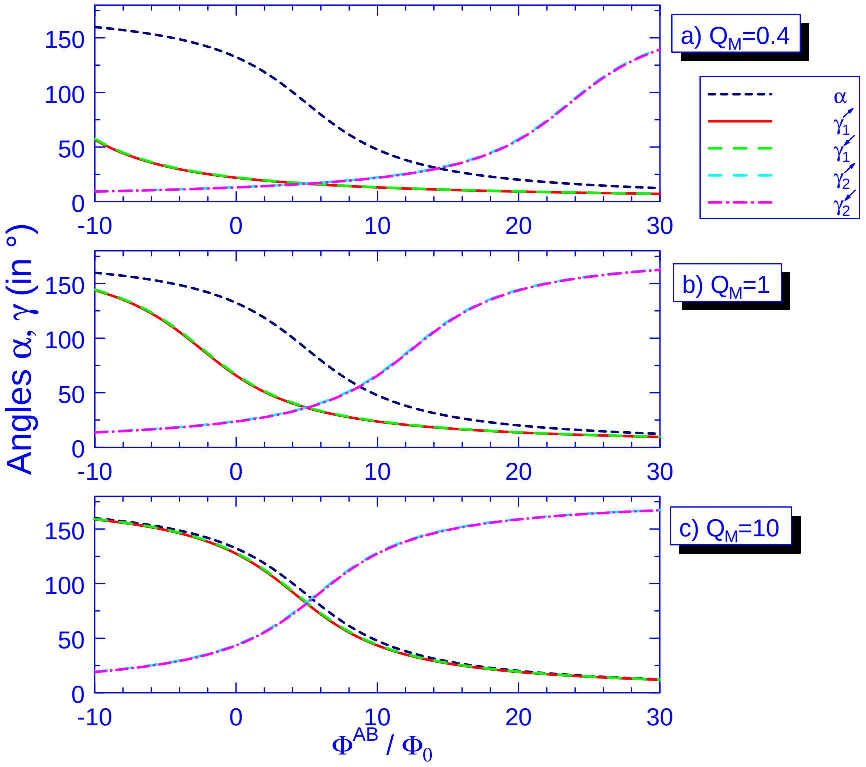

Figure 5.13: Evolution of the angles α and γ under the change of the external field B_0. In the adiabatic situation c), $\gamma_1^{\nearrow}, \gamma_1^{\swarrow}$ follow the angle α respecting $\gamma_1^{\nearrow}, \gamma_1^{\swarrow} < \alpha$ always. The more diabatic the regime is, the larger is the difference between $\gamma_1^{\nearrow}, \gamma_1^{\swarrow}$ and α. The other pair of angles, $\gamma_2^{\nearrow}, \gamma_2^{\swarrow}$, is related to $\gamma_1^{\nearrow}, \gamma_1^{\swarrow}$ by the symmetry line through $\alpha = 0$.

dominating. This takes place faster in diabatic situations (Fig. 5.12b) than in intermediate (Fig. 5.12c) or adiabatic (Fig. 5.12d) cases.

We point out that there are two adiabatic limits possible: one for dominating field of the *micromagnet*, the other one for dominating external field B_0. Here, we describe the strength of the micromagnet in terms of Q_M that is defined at the point $\Phi^{AB}/\Phi_0 = M^{AB}$. In Fig. 5.12b-d, the adiabaticity *at this point* is increased. On the other hand, adiabaticity can be reached independent of the strength of the micromagnet for strong external magnetic fields B_0, i.e. for $|\Phi^{AB}| \gg M^{AB}\Phi_0$. Accordingly, we find the sum of the two curves for the $\{\nearrow\}$ and $\{\swarrow\}$ electron gases in Fig. 5.12a to coincide with the exact magneto-conductance for large external fluxes Φ^{AB} *as well as* for high adiabaticity parameter Q_M (indicated by the dashed curve in Fig. 5.12d).

In Fig. 5.13 we illustrate the variation of the external field B_0 and the corresponding (external) flux $\Phi^{AB} = \pi a^2 B_0$ in terms of the tilt angle α of the resulting total magnetic field $\vec{B}$. The curve for α is independent of adiabaticity and the same in all three pictures. Major differences arise, however, when looking at the angle γ, introduced in Eqs. (3.45, 3.46). Clearly visible is the complementary behaviour of $\gamma_1^{\nearrow}, \gamma_1^{\swarrow}$ on one hand, and $\gamma_2^{\nearrow}, \gamma_2^{\swarrow}$ on the other hand as suggested by the geometrical interpretation, see Fig. 3.3. The angles $\gamma_1^{\nearrow}, \gamma_1^{\swarrow}$ are close to α in the adiabatic limit, Fig. 5.13c, whereas they tend to lower values in Fig. 5.13a,b and eventually to zero in

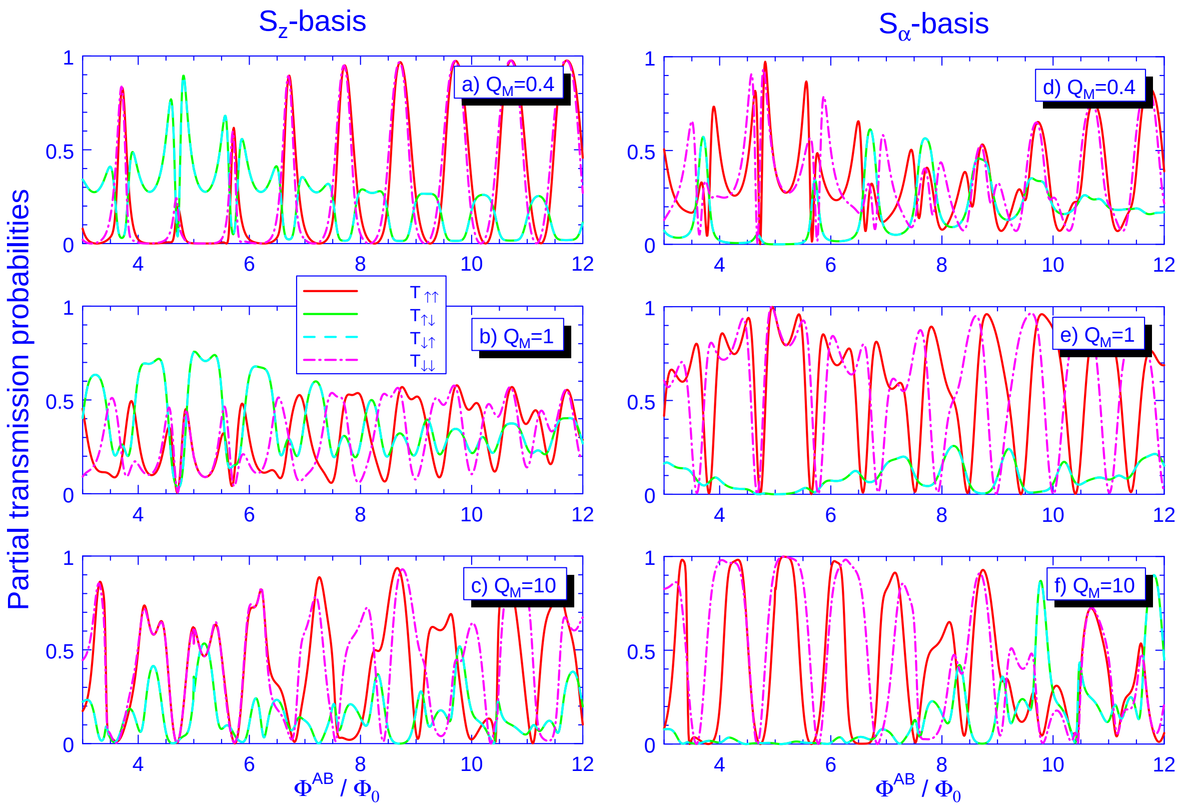

Figure 5.14: Same as Fig. 5.12 but for the partial transmission amplitudes in S_z-basis [see a)-c)], and S_α-basis [see d)-f)], respectively.

the (deep) diabatic limit. Note the symmetry of the curves for $\gamma_1^{\nearrow}, \gamma_1^{\swarrow}$ and $\gamma_2^{\nearrow}, \gamma_2^{\swarrow}$ w.r.t. $\alpha = 0$ at $\Phi^{AB}/\Phi_0 = M^{AB}$.

Eventually, we briefly discuss the partial transmission amplitudes, what can be done either in S_z- or S_α-basis, see Section 4.4. In Fig. 5.14 we compare both representations, again for three different degrees of adiabaticity (cf. Fig. 5.14a-c). Whereas on a first sight the partial transmission probabilities in *both* representations look strongly oscillating, a closer look at $\Phi^{AB}/\Phi_0 = M^{AB} = 5$ reveals the difference: Around this point, the off-diagonal terms $T_{\uparrow\downarrow}, T_{\downarrow\uparrow}$ vanish in S_α- but not in S_z-basis. The effect is the stronger the deeper we are in the adiabatic regime, i.e., increases from Fig. 5.14a to c. In this sense the S_α-basis is the appropriate choice as it shows the expected diagonality in the transmission coefficients in the adiabatic limit where the electron spin follows the direction of the magnetic field.

To summarize, we have identified clear signatures of geometric phases in the calculated magneto-conductance of 1d rings with central micromagnet[14], see Fig. 5.12. They appear as interference effects that destroy the regular Aharonov-Bohm oscillations in a certain range of external fluxes Φ^{AB}. The size of this interval depends on the strength of the micromagnet and is smaller in diabatic regimes. Concerning the above-mentioned experiment [35], it was performed under rather diabatic conditions (similar to those of Fig. 5.12b) that are not favorable for the observation of geometric phase effects. Accordingly, it was found that the experimental observations could not be accounted for by geometric phases. However, the observation of geometric phase effects in electronic ring structures appears to be possible in more adiabatic regimes, that can, e.g., be achieved with stronger micromagnets. Other possibilities are the fabrication of appropriately arranged ferromagnetic particles [50] above or into the plane of the 2DEG, or to use metallic (rather than semiconducting) rings. In view of the increasing strengths of non-uniform magnetic fields achieved in experiments, magneto-conductance calculations for rings remain an interesting subject.

---

[14] Not included in the present considerations is the influence of the smooth change in the magnetic field from purely homogeneous in z-direction far outside in the leads to more and more crown-like as the electrons approach the micromagnet.

Part II:

Chaos and regularity in optical systems: Correspondence of the ray and wave picture

6 Introduction

The field of quantum chaos, i.e., quantum mechanics of classically chaotic systems, has attracted a lot of interest in the last years. Quantum chaotic behaviour can be realized in quantum dots and quantum wells [58], where the electrons are modelled by a Schrödinger equation with certain boundary conditions. Interestingly, similar phenomena can be found in optical or microwave cavities. There, the description by geometrical optics corresponds to classical mechanics, whereas "quantum" aspects arise from Maxwell's equations. Although there are physical as well as formal differences between the Schrödinger and Maxwell equations, we shall see below that it does make sense to study quantum chaos in optical, or dielectric, systems. Before we do so, let us briefly discuss quantum chaos and optical cavities separately.

6.1 Quantum chaos

A system is said to be (classically) chaotic if the distance between two trajectories started with nearly the same initial conditions grows exponentially. This divergence is described by the Lyapunov exponent [75]. In contrast, if nearby started trajectories remain close together, the system is called regular. Many systems contain both chaotic and regular orbits: these are termed mixed. Billiards are the paradigmatic example of chaotic as well as regular and mixed systems, both in experiment and theory. Experiments have been performed, e.g., with differently shaped mesoscopic quantum dot billiards [58] and (closed) microwave cavities [57] of normal and superconducting material.

In microwave cavity experiments, the eigenfrequency spectrum is determined by measuring the absorption of microwaves fed in via an antenna and is found to show strong fluctuations. However, the statistical properties of the spectra are universal and depend only on the dynamics of the underlying classical system. For example, in the case of chaotic cavities, like the stadium or the Sinai billiard, the nearest-neighbour spacing follows the so-called Wigner distribution that favours *finite* spacing between adjacent eigenenergies. Integrable systems like a rectangular billiard obey, in contrast, the Poisson distribution that does not support level repulsion. Most real systems are, however, *mixed*, and show a level statistics in between the two. A powerful tool in this context is the Random Matrix Theory (RMT) [60, 61]. Originally it was designed by Wigner to deal with the statistics of eigenvalues and eigenfunctions in many-body systems, and was successfully applied in the description of atomic nuclei, complex atoms and molecules. More recently, RMT became an important technique also in other fields, namely for example [62] the chiral phase transition in quantum chromodynamics, conductance fluctuations in mesoscopic wires, equilibrium transport properties of disordered quantum systems [73] and classically chaotic systems. Properties of these systems are well-described by ensembles of random matrices. For example, the Wigner-Dyson ensemble of Hermitian square matrices was found to apply generically to chaotic systems, resulting, e.g., in Wigner-distributed nearest-neighbour energy level spacing.

This distinction between regular or chaotic underlying classical dynamics persists when we turn to semiclassics, i.e., the trace formulas [76]. They provide a semiclassical approximation for the oscillatory part of the density of states of a quantum system in terms classical periodic orbits[1] If the classical system is integrable, the Berry-Tabor formula applies, whereas Gutzwiller's trace formula is valid for non-integrable systems. For mixed systems, a generalized trace formula was derived [77] and successfully tested in microwave experiments [78]. We will use the relation between the density of states and the length of periodic orbits when we *Fourier transform* the (delay time) spectra to extract information on the periodic orbits involved. However, in the *dielectric* system, we have to distinguish between the optical and the geometric length of a trajectory, in particular if the orbit goes through regions of different refractive index. The Fourier transformed spectra possess peaks at the *optical* length of contributing paths. The details of this problem are discussed in Chapter 9.

In quantum systems, interesting phenomena were found that were not expected when coming from the classical physics side. One prominent example is the observation of so-called scars [81], i.e., modes that are localized on (short) *classically unstable* periodic orbits. They are observed in experiments with billiards and quantum dots (see e.g. [57, 5, 82, 83]) as well as in numerical calculations (see e.g. [102]). Another well-studied phenomenon is *chaos-assisted tunnelling* that was studied in various systems [79, 100, 101, 80]. It occurs in quantum systems with discrete symmetry that leads to distinct, but symmetry related, regions in the corresponding classical phase space. Assuming two regular layers separated by a chaotic area, quantum-mechanically the coupling between the regular regions is enhanced by dynamical tunnelling. It results in a doublet splitting of the regular states that depends on the coupling strength to the irregular eigenstates associated with the chaotic sea. A well-investigated system in this context is the *annular billiard* where waves are confined in an annular region, see Fig. 9.1. The phase space has the structure described above, and the tunnel splitting was investigated in detail [100, 101].

In Chapter 9 we will consider a system similar to the annular billiard that, however, is generalized to a *dielectric* system in which the light waves are allowed to penetrate into the inner disk and the surroundings according to the optical properties of the neighbouring materials. If we use *light rays* to describe the corresponding processes, we have to apply the laws for reflection and refraction of rays at planar interfaces (curvature is irrelevant in the classical limit) in order to determine the behaviour of the system. Besides being an interesting model system for microresonators, the dielectric annular billiard also appears in everyday life and can be used as a model for melting ice particles in clouds [106] or cladded optical fibres that are commonly used in optical communication networks.

6.2 Optics

Classical or geometrical optics ideas have been known since Galileo's time (around 1600, see [72] for details). Propagation of light following straight lines and the laws of reflection and refraction were known. The observation of Fresnel diffraction and double refraction (both before 1700) were the first puzzling elements in a process that lead to the wave-corpuscle controversy. Huygens' construction and the derivation of Fermat's principle assume the wave nature of light

---

[1] The other contribution to the density of states, the smooth part, is semiclassically expressed by the Weyl formula, see e.g. [57, 99].

[72]. A new stage was initiated with Maxwell's equations that established a unifying basis for the description of electromagnetic waves, including light. They also brought certainty about the transverse nature of electromagnetic waves in isotropic materials with the electric and magnetic field vectors $\vec{E}$ and $\vec{H}$ being *normal* to the propagation direction $\vec{k}$, giving rise to two possible polarization directions w.r.t. $\vec{E}$. This becomes important if a certain plane in space is specified, as will be the case when we consider two-dimensional microcavities. Accordingly, we have to distinguish two polarization directions, one in which $\vec{E}$ is perpendicular to the plane of the system (called TM – the magnetic field is transverse to the boundary), and another one where $\vec{E}$ lies in the cavity plane (TE for "transverse electric"). Details are given in Section 7.2. Tying up with the first part of this work, we mention that the polarizability of light was used in the detection of geometric phases (Section 2.1) in curled optical fibres [14]. Also, recall the Gouy phase shift [12] of a focussed beam that we discussed in this context.

Nowadays, quantum optics has joined geometrical, wave, and nonlinear optics; and cavity quantum electrodynamics receives an increasing interest. Properties of light rays have now even been observed in reaction-diffusion systems, for example the refraction of chemical waves obeys Snell's law for refraction [71]. Ray optics is still the first method employed when explaining for example the phenomenon of caustics (see Fig. 6.1), of which the rainbow is a particular example. At caustics the ray picture predicts an infinite brightness [70]; an unphysical singularity that is softened by wave physics. This becomes clear when recalling that the ray picture is the zero-wavelength limit of wave optics.

6.3 Fusion: Chaotic light

Besides the recent experimental and theoretical advances concerning *electronic* mesoscopic structures that we discussed in the first part, there is a vivid field of studying the properties of light (or, more general, electromagnetic waves) in systems where the wave nature of light overwhelms the simple ray-based description. These optical microcavities have attracted much interest in the last years, both in the field of classical and quantum optics and as model systems for classical and quantum chaos [63]. On the theoretical side, a plethora of phenomena related to the interplay of classical and quantum chaos is found [57, 75, 76, 61]. On the experimental side, optical cavities are used either as (passive) optical filters which are of great technological interest for planar integrated filter applications, or as microlasers, that is, active elements. Many investigations are motivated by the high potential of future applications in the field of optical communication, information technologies, and microlasers.

Rich phenomena are found in compound dielectric systems with different refractive indices. In optical systems with refractive index n larger than the one of the surroundings, *whispering gallery*[2] modes (WG modes or WGMs) can form when the light is confined by total internal reflection, that is, the angle of incidence χ (see Fig. 6.1) is bigger than the critical angle $\chi_c = \arcsin(1/n)$. An example of such a WGM is shown in Fig. 6.1a. However, the confinement by total internal reflection is not complete and there is *evanescent leakage* marked by dashed arrows

---

[2] Lord Rayleigh named and explained the phenomenon that was first observed when *whispers* could be heard all along the *gallery* of St. Pauls's Cathedral, London.

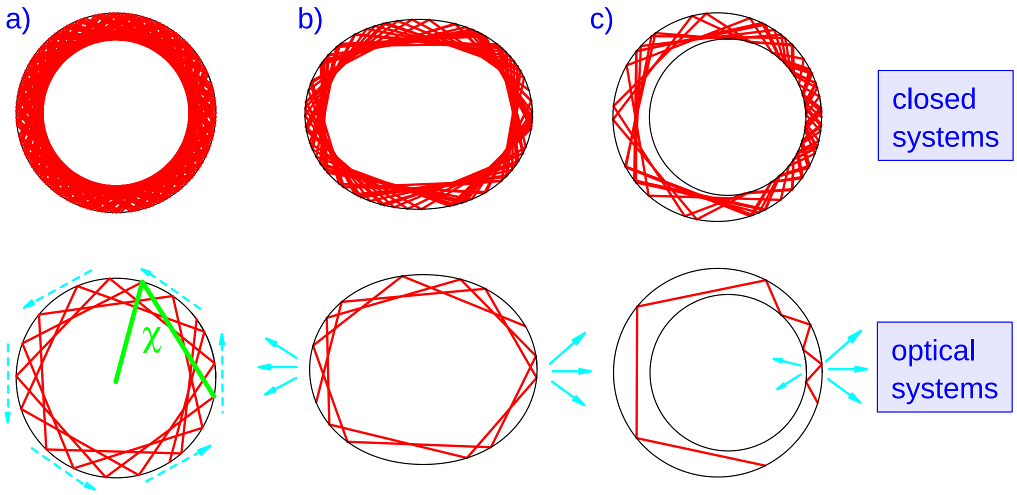

Figure 6.1: Optical microresonators as described in the ray picture, each with a single ray traced for a number of round-trips. Top row: closed systems with hard walls. Bottom row: open systems with different refractive indices. Confinement is provided by total internal reflection, refractive escape is possible. Solid (dashed) arrows denote refractive (tunnelling) escape. a) Circular cavity. The angle of incidence χ, measured between the ray and the boundary normal, is the same at each reflection point and positive (negative) for counter-clockwise (clockwise) propagating waves. Note the formation of a *caustic* that marks the border to a region that is not accessible for rays of this angle of incidence; the intensity becomes infinite there. Local violation of the condition for total internal reflection for WG modes can be controlled by breaking the rotational symmetry. b) Deformation of the disk resulting in lower angles of incidence in the regions of heighest curvature, c) eccentrical placing of another dielectric favours refractive escape in the constricted region.

in Fig. 6.1. This effect is caused by quantum tunnelling and is exponentially small as we shall see in Chapter 7. Consequently, WGMs are characterized by very long storage times corresponding to very high *Q-factors* of up to 10^{10}. The Q-factor is used in optics to characterize the quality of a cavity, or, resonator mode. It is proportional to the product of the mode frequency ν and its lifetime τ (that, in turn, is related to the *line width* $\Delta\nu$ of the mode, $\tau \sim 1/\Delta\nu$) and defined as

$$Q = 2\pi\nu\tau\ . \tag{6.1}$$

The range of application of whispering gallery modes is broad and includes spectroscopy, optical communication, photon rather than electron based future information technologies, and microlasers [135]. However, it is technologically desirable to couple to regions where *higher* and *directed* output rather than evanescent leakage occurs. In this context it is important to note that emission can be directional for deformed (oval-shaped) disks. Refractive escape takes place preferentially at the surfaces of highest curvature, see Fig. 6.1, because there the condition for total internal reflection tends to be violated first [132]. Whereas the WGMs of circular shaped cavities show isotropic power output upon lasing, a direction-dependent increase in output power of up to three orders of magnitude was observed in resonators with deformed cross section, i.e., for a bow-tie shaped lasing mode [135]. Using *ray-tracing* simulations, i.e., following the subsequent specular reflections of a model ray in resonators of several shapes, one can easily interpret the behaviour found in experiment [69], or formulate theoretical predictions [108, 132].

Besides the forcing of violation of total internal reflection by *deformation* of the disk, there is the alternative mechanism of placing an obstacle (e.g., an airy inclusion) eccentrically within the disk, see Fig. 6.1c. The correspondence between ray and wave properties of light in the resulting *dielectric annular billiard* has not been addressed in literature to date. It will be a major topic of this second part and is discussed in detail in Chapter 9. Our focus will be on the special properties of the *open optical* system, in contrast to the studies, e.g., on chaos assisted tunnelling, in the closed system in Refs. [57, 79, 100, 101]. One great advantage is that the "openness" of the system can be controlled by varying the refractive indices of the optical system components, and the whole range from closed cavities (complete confinement by total internal reflection for $n = \infty$) to a transparent system (same index of refraction for system and environment) is accessible. Optical systems such as dielectric billiards or gradient refractive index fibres [74] might, therefore, well enrich the series of quantum chaotic model systems. In a gradient-index-fibre billiard , the light rays follow regular or chaotic *curved* paths analogous to those of an electron in a resonant tunnelling diode [74]. Recent experiments [130] using a quadrupolar-shaped microcavity illuminated by a laser beam have shown periodic filter characteristics in the far-field output. Besides interesting applications in optical filtering or fibre diagnostics, this might be considered as a probe of fibre trajectory properties (the experiment was performed in the ray limit), and might be used as a very sensitive tool to study system characteristics. More details are given in Section 10.1 where we present an analysis of the experimental data and numerical ray-tracing simulations which provide an excellent theoretical description of the experimental findings.

Though the ray picture often provides an easy understanding of the optical system and mostly yields qualitatively correct results, a more sophisticated description is required when the wavelength becomes of the order of the device size. First steps towards a more advanced apparatus were undertaken in [108, 132] and revealed the interesting physics of those mesoscopic optical systems. There are many open questions to be answered before broad technical applications are possible. For example, simple expressions for the reflection coefficients at *curved* interfaces are desirable in order to figure out the influence of a curved rather than a planar boundary for which the result in terms of Fresnel's laws is well-known. So far, a clear interpretation of the arising corrections based on the ray picture is missing. A joint analytical treatment of the two possible polarization directions has not been given as well, neither in ray-based nor in wave-based pictures. We shall fill both gaps with the discussions in Chapter 8, where on one hand we derive generalized Fresnel formulas that can be used over a wide parameter range. On the other hand and for the first time, the ray picture at a curved interface is extended by incorporating the Goos-Hänchen effect. The Goos-Hänchen shift is a lateral shift of the reflected beam upon total internal reflection. We show, both qualitatively and quantitatively, how the wavelength dependent deviations of reflection coefficients arise at curved interfaces from Fresnel's result for the planar interface.

An important technical issue is the description of scattering properties of optical systems.

So far, the optical system was probed by plane-waves of varying energy, and the intensity change at a single point, e.g., on the boundary, was used to identify resonance signatures. Depending on the choice of this reference point, they appear as peaks or dips in the local cross section, but might also be missed [108]. We suggest usage of the S-matrix method for optical systems and demonstrate it for the example of the annular billiard mentioned above. We find *all* resonances to be principally accessible, and they are of the characteristic Breit-Wigner type.

The outline of Part II of this work is as follows: In Chapter 7 we study the example of the dielectric disk in order to introduce the methods that we subsequently use to describe optical systems. Firstly, this is the ray picture together with instruments of classical mechanics. Secondly, we present the wave approach to optical resonators, based on one hand on complex wave vectors for quasibound or resonant states, and on the other hand on a scattering picture on the real energy axis. As mentioned above, the application of an S-matrix formalism to optical systems is novel and allows for a consistent description of families of resonances as we shall demonstrate. Chapter 8 is devoted to the generalization of Fresnel's laws to curved interfaces. The wave picture naturally results in a slight discrepancy between Fresnel coefficients for planar and curved interfaces, and we give a joint analytical description of both possible polarisation directions, considerably improving results that have been reported so far. Adopting the concept of the Goos-Hänchen effect, we provide the first (to our knowledge) ray-picture based explanation of deviations from Fresnel's law due to curvature effects. The ray-wave correspondence in the dielectric annular billiard is the subject of Chapter 9. We will show how ray and wave picture based ideas can be used to interpret and classify the plethora of resonance phenomena peculiar to this system, that for the first time is used in this respect. The freedom in tuning the openness of the system by means of the refractive indices will play an important role. In Chapter 10 we return to the ray picture, that we find to deliver an excellent description of a recent passive optical fibre experiment, and outline its application in the design of microlaser cavities. A joint summary and outlook to both parts closes the work.

The notation "classical" will be used in the following synonymously with "ray picture" or geometrical optics. Similarly, "quantum mechanical" stands for "wave mechanical" whenever wave properties are of importance.

7 Ray and wave description of the open dielectric disk

In this chapter we introduce the methods used in this second part of the thesis to describe open dielectric resonators, employing a two-dimensional disk as example. There are three possible approaches. The first one is classical ray optics. We describe the nature of this approach in Section 7.1 and refer to these ideas in the following by the notion *ray picture*. More accurate approaches in the sense that they account for the *wave* nature of light are based on Maxwell's equations. The resulting wave equation describes the *resonances* of the *open* system (or eigenstates in the case of a closed systems). One way is to directly solve these exact equations for the complex energies of resonances. We will refer to this with the term *wave picture* introduced in Section 7.2. However, especially for more complicated systems, it turns out that it is hard to solve the exact equations in the complex energy plane. Leaving a more detailed discussion to Section 7.3, one way out of this problem is to study the signatures of resonances on the *real energy* axis. This is done not by investigating the decaying states of the system alone, but by probing the resonant properties of the system from *outside*. One possibility is to add an external light source and investigate the *scattering* properties of the disk. Changing the (real) energy of the probing wave allows us to study the properties of the system, in particular the cross section or the Wigner delay time which show characteristic fingerprints of resonances. One typical signature of resonances are so-called Breit-Wigner peaks in the cross section [93]. Their energy and width correspond, respectively, to the real and imaginary parts of the resonance energy. In Section 7.3 we will apply the S-matrix method to the dielectric disk and use the characteristic peaks in the (generalized) Wigner delay time to identify resonances.

All approaches incorporate the openness (resonant nature) of the problem in a different way. In the ray picture, the system becomes open when the condition for total internal reflection is violated and *refractive escape* of rays is possible. In the wave picture, we deal with resonances of a certain *width* rather than eigenstates that provide the appropriate description for closed systems. Finally, in the scattering picture, we directly use that the system is not closed by probing its properties from outside.

7.1 Ray picture: Classical billiards with total internal reflection

Here, we introduce both the methods used in the investigation of classical dynamical systems like Poincaré sections and the principles of geometric optics. We outline how both concepts merge in the description of dielectric billiards. Finally, we introduce Fresnel coefficients.

7.1.1 Billiards in terms of Poincaré's surface of section

The classical ray picture of a closed cavity is equivalent to the model of a point particle moving in a classical billiard of the same shape. The point-particle trajectory consists of straight line segments with specular reflection events whenever the boundary is hit. This is the well-studied

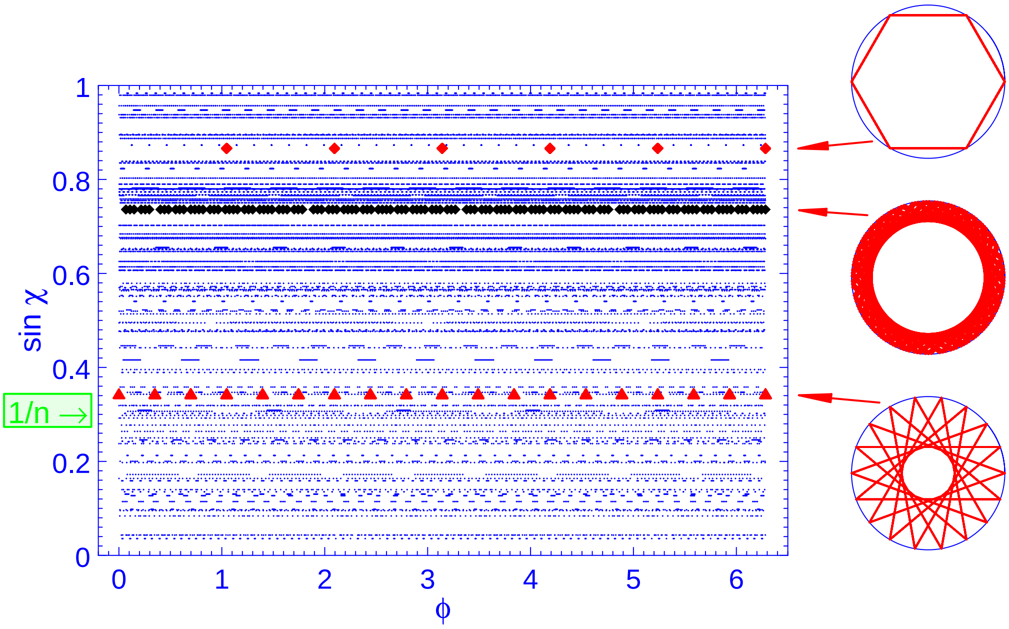

Figure 7.1: Poincaré surface of section for the closed disk. This plot was obtained by starting 150 clockwise-travelling trajectories with otherwise random initial conditions. Counter-clockwise travelling rays yield a similar picture with $0 > \sin\chi > -1$. Each ray was traced over 500 reflections. The trajectories on the right correspond to a period-six orbit ($\chi_0 = 60^o$), a quasi-periodic state (χ_0 nearly irrational), and a high-order periodic orbit ($\chi_0 = 20^o$). The corresponding SOS points are shown with symbols. On the vertical axis, the value $\sin\chi = 1/n \equiv \sin\chi_c$ is shown (assuming a refractive index $n \approx 3$). It marks the line under which the condition for total internal reflection is violated, see Section 7.1.2, Eq. (7.3).

planar billiard problem. Any trajectory in the billiard can be completely specified by the sequence of points where collision with the outer boundary occurs. For a convex shaped billiard, each boundary point is uniquely specified by the polar angle in a coordinate system centred within the billiard. The trajectory is thus reconstructed by simply connecting the sequence of reflection points P_j given in terms of their polar angle ϕ_j by straight lines. Periodic orbits are characterized by the continued repetition of a finite series of N points $\{\phi_j | j = 1 \ldots N\}$ where N is the number of reflection points that closes the orbit. This method of characterizing ray trajectories in *real space* is called *ray tracing*.

A way to record more information about the ray trajectory is provided by the *Poincaré section method* that is well-established in nonlinear dynamics. It stores *phase space* information rather than real space data alone and therefore allows one to address the *ray dynamics*. The additional quantity is the angle of incidence χ, or more precisely, $\sin\chi$, that is proportional to the tangent *momentum* of the ray or the point particle at the reflection point. A Poincaré section is obtained by plotting the pair of conjugate variables (tangent momentum $\sim \sin\chi$, polar angle ϕ) at each boundary reflection point[1]. A first simple example is the Poincaré surface of

---

[1] This constitutes one particular choice of the surface where the Poincaré section is taken. Other choices as a

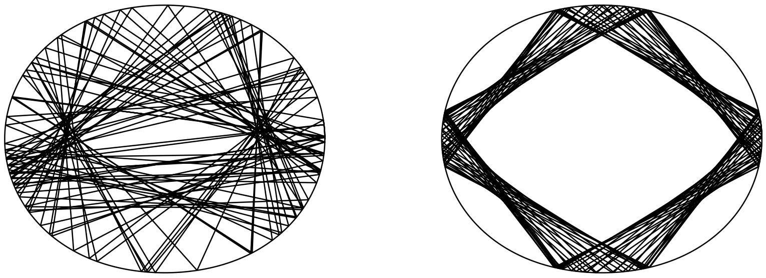

Figure 7.2: Typical trajectories in the quadrupolar billiard defined by the boundary $r_b(\phi) = R_0(1+\epsilon\cos 2\phi)$ where R_0 is the mean radius, and $\epsilon = 0.09$ in both examples. Besides chaotic trajectories (left) there is a variety of stable periodic orbits like the "diamond" (right). The phase space of the quadrupolar billiard is mixed.

section (SOS) for the closed disk shown in Fig. 7.1. It consists of sequences of points that all possess the same $\sin\chi = \text{const.}$, given by the initial angle of incidence χ_0 of the trajectory. This directly results from the rotational symmetry of the disk, implying conservation of the angular momentum, in addition to conservation of energy. Systems where the number of constants of motion equals the number of degrees of freedom are called *integrable*. Their phase space is *regular*. The phase space motion takes place on *invariant tori* [75]. Depending on the ratio between the two winding numbers that characterize the torus, the regular trajectories are either closed (rational ratio, periodic orbits) or quasi-periodic (irrational ratio, closing after an infinite number of round-trips).

In the example of the disk the phase space is composed of a dense set of straight lines $\sin\chi_{\text{irr}} = \text{const.}$, where χ_{irr} is an *irrational* multiple of π, that correspond to quasiperiodic orbits. If the motion of the ray is *periodic*, i.e., it encounters after a certain number N of reflections the same sequence of reflections points, the angle χ is required to be a *rational* multiple of π. Then the orbit is represented by N points in the Poincaré section.

Starting with the spherical billiard, there are two possibilities to arrive at more interesting Poincaré sections:

1. Deformation of the disk ($\longrightarrow$ elliptic, quadrupolar, ...)
2. Placing an obstacle within the disk ($\longrightarrow$ annular geometry)

In both cases the *rotational invariance* of the system is *broken* so that we arrive at non-integrable systems with *mixed* phase space. The first scenario was studied in [108], and an example of a quadrupolar deformation is shown in Fig. 7.2. We will be more interested in the second possibility throughout the second part of this work. Now what happens if we place an opaque obstacle of radius R_2 in a disk of radius $R_1 = 1$? Since rotational invariance is assured, each trajectory is represented by a series of points or lines of constant $\sin\chi$ in the Poincaré section as before. However, another type of trajectory arises due to the possibility of the ray hitting the inner disk. The two types of trajectories are separated by the line $\sin\chi_s = R_2$. Now, in addition, we can shift the inner disk off the centre of the outer disk by an amount δ, removing

---

circle with smaller radius are possible.

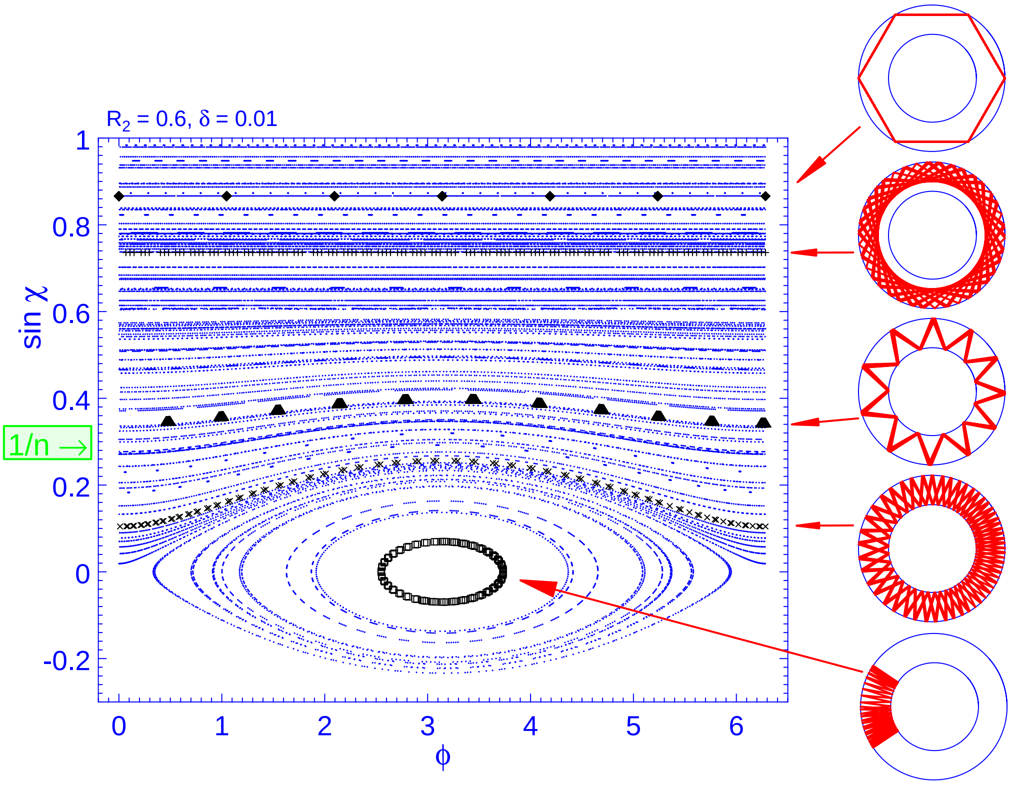

Figure 7.3: Poincaré section for the annular billiard with $R_1 = 1, R_2 = 0.6$ and $\delta = 0.01$ (see Fig. 9.1 for notations). Although the displacement of the inner disk is rather small, it has major impact on trajectories that explore the region $\sin\chi < R_2 - \delta$. Other trajectories are not influenced, see the two upper-most examples on the right. For this and the following phase space plots 200 trajectories were started randomly at the *outer* boundary with $\phi' \in [0, \pi/2]$ and $\sin\chi \in [0, 1 - \epsilon_{\mathrm{WG}}]$ and followed 500 reflections each. ϵ_{WG} is chosen slightly above the border for the existence of whispering gallery orbits, in particular in the Poincaré sections in Chapter 9. Positive $\sin\chi$ implies that only counter-clockwise propagating trajectories were started. Nonetheless regions $\sin\chi < 0$ are explored implying a *change in the sense of rotation*, see e.g. the lower-most trajectory on the right.

the rotational invariance of the system. The result is a *deformation* of trajectories with small angles of incidence whereas orbits close enough to the outer boundary are not affected by the inner disk, similar to what occured in the concentric case. The separation line is now given by $\sin\chi_s = R_2 - \delta$. Sample trajectories are shown in Fig. 7.3 where $\delta = R_1/100$. We will further investigate this situation of the *annular billiard* in Chapter 9.

We end this section by stating the theoretical basis on which the influence of deformations on the phase-space structure can be understood. For intermediate time scales[2] and small deformations we can use *adiabatic invariant curves* [86] to predict the motion in phase space. This means that orbits will follow a curve $\sin\chi = \sin\chi(\phi)$ in the two-dimensional phase space $(\phi, \sin\chi)$ corresponding to the existence of an (almost) conserved quantity which can be associated with a curvature-corrected effective momentum. Fig. 7.3 is a nice example of this behaviour: Although the rotational invariance of the system is slightly perturbed, all trajectories remain regular up to a displacement of $0.03R_1$. Another important principle is formulated in the KAM-theorem [87] and states that invariant tori in phase space are not immediately destroyed under a perturbation of the integrable system. Rather, the evolution (that will in general end in a chaotic phase space for sufficiently high deformations) takes place via a KAM scenario [88].

---

[2] The round-trip time of the orbit is required to be much smaller than its diffusion time in space. This gives rise to the term “adiabatic” in close relation to what is said in the first part of this work.

If we proceed to perturbations resulting in partial chaotic behaviour, the phase space is called mixed. One example is shown in Fig. 9.2. The chaotic trajectories fill the chaotic part of the phase space such that these parts are recognized by a cloud of dots in the Poincaré section. However, there are some regular regions (called "stable islands") where the motion is regular as indicated by the one-dimensional curves orbits started there trace. This is due to the existence of an additional (adiabatic) constant of motion in these regions [75]. However, to identify the responsible integral is not a simple question. Rather, the Poincaré section is used as a handy instrument to *find* regions of regular motion. In Fig. 9.2 some regular orbits are shown in the top and bottom row.

7.1.2 Total internal reflection and Fresnel's law

Consider a light ray incident on a *planar* interface between two dielectric media of different refractive indices n_1 and n_2 (see Fig. 7.4). In terms of classical ray optics, it is charactrized by an *angle of incidence*, χ_1, measured w.r.t. the *normal* of the interface. When the light ray hits the interface coming from the first medium (n_1), it can either be *reflected* or *refracted*. In the first case, the light ray is scattered off the other medium with an angle of reflection χ_2 according to the

$$\text{Law of reflection:} \quad \chi_1 = \chi_2 \,. \tag{7.1}$$

In the case of refraction, the light ray is transmitted into the other medium (n_2). The direction of the light ray is changed to an angle η_1 obeying

$$\text{Snell's law:} \quad n_1 \, \sin\chi_1 = n_2 \sin\eta_1 \tag{7.2}$$

which also follows from the principle of minimum action as the law for reflection. In the situation $n_1 > n_2$, Eq. (7.2) cannot be fulfilled to yield real η_1 for any angle of incidence χ_1. This effect is called *total internal reflection* (TIR) because then light can *only be reflected* under $\chi_2 = \chi_1$. We state the condition for

$$\text{Total internal reflection:} \quad \sin\chi_1 \geq \sin\chi_c \overset{\text{def}}{=} \frac{n_2}{n_1} \,, \tag{7.3}$$

where we have introduced the *critical* angle χ_c. We can easily implement the information of total internal reflection into the Poincaré map by marking the line $\sin\chi_c = 1/n$ ($n_2 = 1, n_1 = n$) as is done in Figs. 7.1, 7.3. If $\sin\chi$ falls below this value at a certain reflection point, the ray may escape refractively. In other words, rays with $\sin\chi > 1/n$ are always *confined by total internal reflection.* In the disk, either all or none of the reflection points of a given trajectory obey total internal reflection. However, in an annular geometry the condition for total internal reflection might hold for a certain range of polar angles ϕ (namely those in the wide region of the annulus)

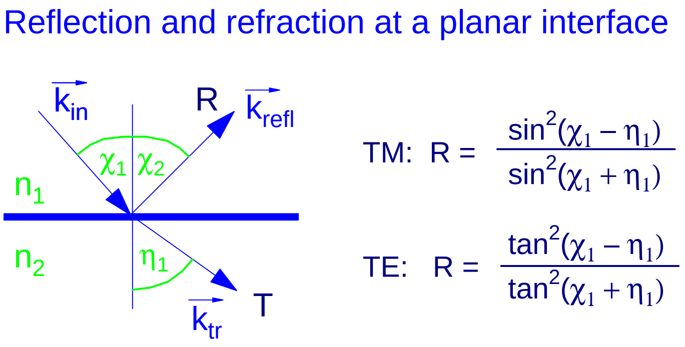
Reflection and refraction at a planar interface
$\vec{k}_{in}$
R
$\vec{k}_{refl}$
χ_1
χ_2
n_1
n_2
η_1
$\vec{k}_{tr}$
T
TM: $R = \frac{\sin^2(\chi_1 - \eta_1)}{\sin^2(\chi_1 + \eta_1)}$
TE: $R = \frac{\tan^2(\chi_1 - \eta_1)}{\tan^2(\chi_1 + \eta_1)}$

Figure 7.4: Ray incident on a planar interface as described in classical ray optics.

whereas it is violated for others (namely those in the constriction where, indeed, we find the smaller χ), see the examples in Fig. 7.3.

Snell's law and the law of reflection at a planar interface, Eqs. (7.1, 7.2), also hold for *plane waves* described by the exponential $e^{i\vec{k}\cdot\vec{r}}$ involving both the wave vector $\vec{k}$ and the spatial position $\vec{r}$. In this language, an incident plane wave with $\vec{k}_{\rm in}$ is reflected into a plane wave of wave vector $\vec{k}_{\rm refl}$ and refracted into a plane wave of wave vector $\vec{k}_{\rm tr}$. The laws for reflection and refraction arise then a consequence of momentum conservation.

Whereas classical ray optics does not allow for any statement concerning the amount of reflected and transmitted light intensities, the wave picture does! Applying Maxwell's equations [72] to the case of an incident plane wave of amplitude A=1, the reflected intensities $R^{\rm TM}$, $R^{\rm TE}$ for TM and TE polarization[3], respectively

$$R^{\rm TM} = \frac{\sin^2(\chi_1 - \eta_1)}{\sin^2(\chi_1 + \eta_1)}\,, \tag{7.4}$$

$$R^{\rm TE} = \frac{\tan^2(\chi_1 - \eta_1)}{\tan^2(\chi_1 + \eta_1)}\,. \tag{7.5}$$

The transmitted intensity T is obtained via $R + T = 1$. For details and a discussion of the reflected *amplitudes*, see e.g. [72, 90].

The result for the reflected intensities is shown in Fig. 7.5 for both TM and TE polarisation. Note the special feature of zero reflection at the so-called *Brewster* angle $\chi_{\rm Br} = \arctan(n_2/n_1)$ for TE polarized light. This implies that light reflected under this angle, $\chi_2 = \chi_{\rm Br}$, is completely TM polarized. If $\chi_1 = \chi_{\rm Br}$, transmitted and reflected light rays form a right angle as one easily verifies. This can be formulated as an argument for an atomistic explanation of the effect [90].

Although Fresnel's laws result from Maxwell's theory for electromagnetic *waves* (applied to plane waves), we state the result in this ray optics section in order to distinguish it from the wave picture that we will develop in Section 7.2. More than once, however, we will run into the essentially wave-like nature of Fresnel's laws.

We will see in the following that corrections to Fresnel's laws are necessary in order to account for curved interfaces. However, as a first approximation, we use the reflection coefficients given in Eqs. (7.4, 7.5) and justify this approach by realizing that a *ray* incident on any interface

---

[3] For the definition of TM and TE polarization see Section 7.2.

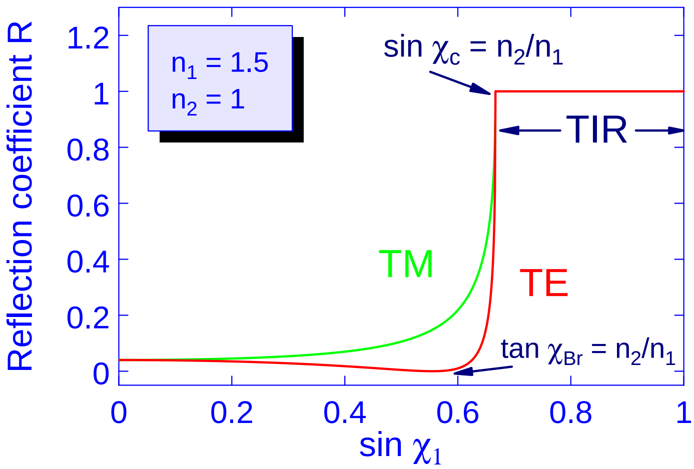

Figure 7.5: Fresnel laws for reflection at a planar interface. The region of total internal reflection and the Brewster angle in case of TE polarization are marked.

only sees *one point* of the interface which, of course, cannot carry any curvature information. Remembering the *waves* involved in the derivation of Fresnel's formulas [72], it is immediately clear that this statement can hold only in the case that the wavelength λ is much smaller than the local radius R of curvature. This is because one expects a wave to probe (at least) a region of typical size λ *around the point* of incidence. In Section 7.4 we will find these ideas to be correct.

Finally, we state that a phase change occurs upon each reflection at the optically denser medium ($n_1/n_2 < 1$). The amount of this shift is given by [89]

$$\Phi(\chi) = -2 \arctan \left(\mathcal{T} \frac{\sqrt{\cos^2 \chi_c - \cos^2 \chi}}{\cos \chi} \right) , \tag{7.6}$$

with the parameter $\mathcal{T} = 1$ ($\mathcal{T} = n_1^2/n_2^2$) for TM (TE) polarized light.

7.2 Wave picture: From Maxwell to Schrödinger

In this section, we introduce the description of dielectric resonators by the example of a (infinite) dielectric cylinder the cross section of which is the two dimensional dielectric disk. We start from Maxwell's equations that we solve for the two possible polarisation directions, i.e., transverse electric and transverse magnetic field. The different types of solutions find an illustrative interpretation in terms of an effective potential. In a further section, we introduce the scattering matrix of the dielectric disk and discuss the resulting scattering properties.

7.2.1 Maxwell's equations for the dielectric disk

The system we study first is an infinite dielectric cylinder of radius R and refractive index n that is embedded in vacuum or air with refractive index $n_0 = 1$. Of course, both refractive indices can be multiplied by the same number to yield another combination of refractive indices for which the same results hold. We will call k the wave number outside the cylinder and, analogously, nk

is the wave number inside. We assume a harmonic time dependence $e^{-i\omega t}$ with the dispersion relation $\omega = kc$, where c is the speed of light.

Maxwell's equations for the vortices of the electro-magnetic field then read in SI units [72]

$$\begin{aligned} \vec{\nabla} \times \vec{E} &= -\dot{\vec{B}} = ikc\mu\mu_0\vec{H} \,, && (7.7) \\ \vec{\nabla} \times \vec{H} &= \dot{\vec{D}} = -ikc\epsilon\epsilon_0\vec{E} \,, && (7.8) \end{aligned}$$

where $\vec{E}(\vec{r}, t)$ and $\vec{H}(\vec{r}, t)$ are the vectors of the electric and magnetic field, $\vec{D}(\vec{r}, t) = \epsilon\epsilon_0\vec{E}(\vec{r}, t)$ is the dielectric polarization, and $\vec{B}(\vec{r}, t) = \mu\mu_0\vec{B}(\vec{r}, t)$ is the magnetic induction with ϵ the dielectric constant and μ the permeability of the medium which we assume to be one for frequencies of light [72]. ϵ is related to the refractive index by $\epsilon = n^2$, and for the vacuum light velocity the relation $c = 1/\sqrt{\epsilon_0\mu_0}$ holds.

Inserting (7.7) into (7.8) and vice versa, we obtain equations for $\vec{E}$ and $\vec{H}$ only,

$$\begin{aligned} \vec{\nabla} \times \vec{\nabla} \times \vec{E} &= n^2k^2\vec{E} \,, && (7.9) \\ \vec{\nabla} \times \vec{\nabla} \times \vec{H} &= n^2k^2\vec{H} \,. && (7.10) \end{aligned}$$

Recalling that charge density ρ can only appear at the surface of the dielectric, we find from Maxwell's equations for the sources of the electro-magnetic field that $\vec{\nabla} \times \vec{E} = 0$ in each domain of constant n.

Let us first consider the case where the electric field $\vec{E}$ is parallel to the z-axis that is perpendicular to the disk plane. Then the magnetic field lies in the cavity plane and is transverse to both the z-axis and the field propagation direction and we refer to this situation as transverse magnetic, or TM, polarization. Since we will impose boundary conditions for the electric field $\vec{E}$ below, we express Maxwell's equations in terms of $\vec{E}$. Applying $\vec{a} \times \vec{b} \times \vec{c} = \vec{b}\,(\vec{a} \cdot \vec{c}) - \vec{c}\,(\vec{a} \cdot \vec{b})$, (7.9) becomes in each region of constant n

$$-\vec{\nabla}^2\vec{E} = (n\,k)^2\,\vec{E} \,. \qquad (7.11)$$

This equation can be rewritten [91] in a form that is *similar* to the conventional *Schrödinger equation*,

$$-\vec{\nabla}^2\vec{E} + k^2\,(1 - n^2)\vec{E} = k^2\,\vec{E} \,. \qquad (7.12)$$

However, one important difference is the character of the fields: the wave function in the quantum mechanical Schrödinger equation is a complex scalar, whereas $\vec{E}, \vec{H}$ are vector fields[4], implying in particular a polarization dependence of the boundary conditions (TM vs. TE, see Section 7.2.3). A second far-reaching difference is that the *potential* term in Eq. (7.12) (the second term on the lhs) appears with a factor k^2, i.e., it is multiplied by the energy eigenvalue k^2 and is, therefore, *energy dependent*. Furthermore, Eq. (7.12) reveals immediately that dielectric regions with $n > 1$ correspond (for any energy k^2) to an attractive well in the quantum analogy and that a potential-like structure requires different refractive indices for different regions.

The same manipulations as above are possible for transverse electric field, or TE polarization, as well. Then the magnetic field is parallel to the z-axis, and apart from different boundary conditions (see below), the desired equations are obtained by replacing $\vec{E}$ in Eq. (7.12) by the magnetic field $\vec{H}$. So we obtain from Maxwell's equations for TE polarized light

---

[4] In a two-dimensional system, Eq. (7.12) can be reduced to a scalar equation [54].

$$-\vec{\nabla}^2\vec{H} + k^2(1-n^2)\vec{H} = k^2\vec{H}\,. \tag{7.13}$$

For the moment, we stick to the case of TM polarization, $\vec{E} = E\vec{e_z}$. To proceed further with (7.12) we make use of the rotational symmetry of our system, and apply $\vec{\nabla}^2$ in cylindrical coordinates r, ϕ, z as

$$\vec{\nabla}^2 U = \frac{1}{r}(rU_r)_r + \frac{1}{r^2}U_{\phi\phi} + U_{zz}\,. \tag{7.14}$$

Assuming a ϕ-dependence according to $e^{im\phi}$, and a z-dependence $e^{ik_z z}$, separation of variables leads to the radial equation

$$-\left[\frac{d^2}{dr^2} + \frac{1}{r}\frac{d}{dr}\right]E(r) + V_{\text{eff}}(r)E(r) = k^2E(r) \tag{7.15}$$

with the effective potential

$$V_{\text{eff}}(r) = k^2(1-n^2) + m^2/r^2 + k_z^2\,. \tag{7.16}$$

In comparison to Eq. (7.12), the effective potential contains now two additional terms. On one hand, m^2/r^2 is due to the conservation of the z-component of the angular momentum in our rotational invariant system that is characterized by the good quantum number m. On the other hand, k_z^2 expresses the conservation of the linear momentum in z-direction, i.e., along the cylinder axis, and acts as an offset in energy. From now on we deal with the case of a dielectric disk (that is, we choose a particular cross sectional plane of the cylinder to obtain an effectively two-dimensional (2d) system)[5] – then we can set k_z to zero corresponding to an incident wave in the x-y plane.

In this 2d problem of a dielectric disk, the effective potential thus results as the sum of the attractive well due to the presence of the dielectric with $n \neq 0$ and the repulsive angular momentum barrier m^2/r^2. It is illustrated in Fig. 7.6. Approaching the disk from $r = \infty$, outside the disk ($r > R, n = 1$) there is only the angular momentum (for $m \neq 0$) contribution to the effective potential V_{eff}. At the position of the disk ($r = R$), there is a discontinuity in the effective potential V_{eff} that is proportional to $1 - n^2$. It corresponds to the non-continuous change in the refractive index. The absolute size of the jump is obtained after multiplication by k^2 and, hence, is *energy dependent!* The jump at $r = R$ reaches from $k^2_{\text{max}} = m^2/R^2$ to $k^2_{\text{min}} = m^2/(n\,R)^2$ as we will motivate in the following paragraph. Inside the disk, the angular momentum contribution, now shifted by $k^2_{\text{max}} - k^2_{\text{min}}$, again determines the behaviour, see Fig. 7.6.

The form of the potential suggests an interpretation in the spirit of quantum mechanics with metastable (or resonant) states in the potential well that decay by tunnelling escape. The decay rate will depend on their energy, that is, their position in the potential well. Note, however, that the particular shape and the depth of the well depend themselves on the energy of the metastable state under consideration!

Apart from this, there is a more formal difference between the radial equation (7.15) and the 1d Schrödinger equation: The first term contains not only the second derivative of $E(r)$,

---

[5] Although taking into consideration $k_z \neq 0$ changes the matching conditions explained below, it does not add any essential physics.

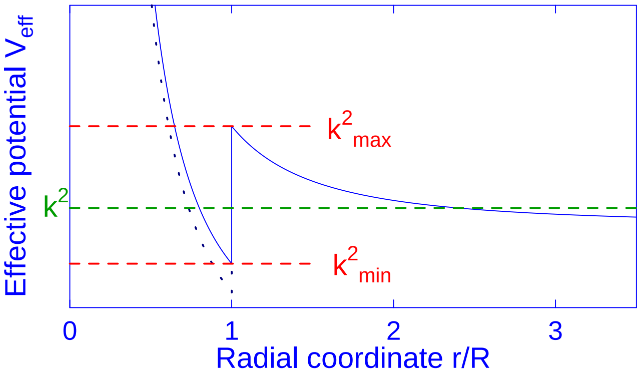

Figure 7.6: Effective potential for a dielectric disk for the value k^2 indicated by the horizontal dashed line; $k_{\text{max}} = m/R$ and $k_{\text{min}} = m/(n\,R)$. The dotted line indicates the form of the potential for a wave vector $k' = 1.1k$.

but also a first derivative contribution. This can be eliminated by introducing the new variable ξ and substituting $\xi \overset{\text{def}}{=} \ln(kr)$, that by straightforward manipulation transforms into

$$\left[\frac{d^2}{d\xi^2} + \widetilde{k}^2(\xi)\right] E(\xi) = 0\,, \tag{7.17}$$

where

$$\widetilde{k}(\xi) = \sqrt{e^{2\xi}\,n^2 - m^2} \equiv \sqrt{(kr)^2\,n^2 - m^2}$$

is the effective wave vector of the rescaled problem.

For resonant solutions of the electric field $E(\xi)$ to exist, the (effective) wave vector $\widetilde{k}(\xi)$ has to be real inside the dielectric disk and imaginary outside (corresponding to evanescent escape only). The minimal possible value k_{min} that allows this condition to be fulfilled is

$$k_{\text{min}} = \frac{m}{n\,R}\,,$$

by guaranteeing $\widetilde{k}$ to be real for $k > k_{\text{min}}$. The highest possible value k_{max} is given by

$$k_{\text{max}} = \frac{m}{R}\,.$$

Summarizing, we expect narrow resonances of angular momentum m that are broadened by tunnelling decay (*evanescent leakage*), in the interval

$$\frac{m}{n\,R} \leq k \leq \frac{m}{R}\,, \tag{7.18}$$

which corresponds to the extension of the well in the effective potential. Note, however, that there need not to be solutions that actually take the boundary values!

Eq. (7.18) is equivalent to

$$\frac{1}{n} \leq \frac{m}{nkR} \leq 1\,,$$

and within the ray-wave correspondence discussed in Section 7.4 we will see that this relation corresponds to total internal reflection where indeed evanescent escape is the only decay mechanism. In particular we will see that $m/(nkR)$ can be identified with the sine of the angle of incidence of the according family of rays.

7.2.2 Eigenvalues of the closed disk

We begin our discussion of Eq. (7.15) with a system consisting of a *closed* disk with radius R – this means that the wave function is confined inside the disk and cannot leak outside. This can be achieved by choosing the refractive index n of the disk to be infinity keeping the index of the surrounding (air or vacuum) fixed at one. Then the effective potential V_{eff} is equivalent to that of an infinite well, and the wavefunction outside the disk vanishes. Later we will use this limiting situation of large n to compare the results for the *fully dielectric* system with the results for the closed disk. Although in the case of the closed system the refractive index of the disk could be completely absorbed in the wave vector, we keep n as parameter to be consistent with later considerations.

We already know the ϕ-dependence that we assumed to be $e^{im\phi}$. m is the angular momentum quantum number which is conserved due to rotational invariance in the dielectric disk. Hence the separation ansatz for the electric ($E \equiv \Psi^m(\vec{r})$, TM polarization) or magnetic ($H \equiv \Psi^m(\vec{r})$, TE polarization) field, respectively, reads

$$\Psi^m(\vec{r}) = \begin{cases} A^m\, \psi^m(r)\, e^{im\phi} & \text{if } r < R \\ 0 & \text{if } r \geq R \end{cases} . \tag{7.19}$$

The radial wave function $\psi^m(r)$ is obtained as solution of the radial Schrödinger equation (7.15) for the electromagnetic field. This equation is of the type of Bessel's differential equation [55] as becomes clear immediately when we rewrite Eq. (7.15) in terms of the dimensionless scaled radial coordinate $\bar{r} \overset{\text{def}}{=} kr$, where k is the wave vector in the medium of refractive index one,

$$\left[\bar{r}^2 \frac{d^2}{d\bar{r}^2} + \bar{r}\frac{d}{d\bar{r}}\right] \psi(\bar{r}) + \left(n^2\bar{r}^2 - m^2\right) \psi(\bar{r}) = 0\,. \tag{7.20}$$

This scaling also reveals the close connection between k and r, in the sense that only the product is important. We will make use of this freedom in scaling by subsequently fixing the radius R of the disk at $R \equiv 1$. The general solutions of Eq. (7.20) are Bessel and Neumann functions, $J_m(n\bar{r}) = J_m(nkr)$ and $Y_m(n\bar{r}) = Y_m(nkr)$, of order m. Here, nk is the wave vector inside the disk, and we have $n = 1$, $nk = k$ outside.

Since the Neumann functions diverge at the origin, but physics requires a finite value of $\psi^m(r = 0)$, the solution inside the disk can only consist of Bessel functions,

$$\psi^m(r) = J_m(nkr)\,, \tag{7.21}$$

where we have assumed all amplitudes to be contained in A^m, see Eq. (7.19).

The eigenvalues of the closed disk follow from the ansatz in Eq. (7.19) according to the boundary condition

$$J_m(nkR) = 0\,. \tag{7.22}$$

In other words, all zeros of Bessel functions J_m, m arbitrary, are solutions of the closed system. We will classify them by two quantum numbers,

1. the angular momentum quantum number m that corresponds to the order of the Bessel function,

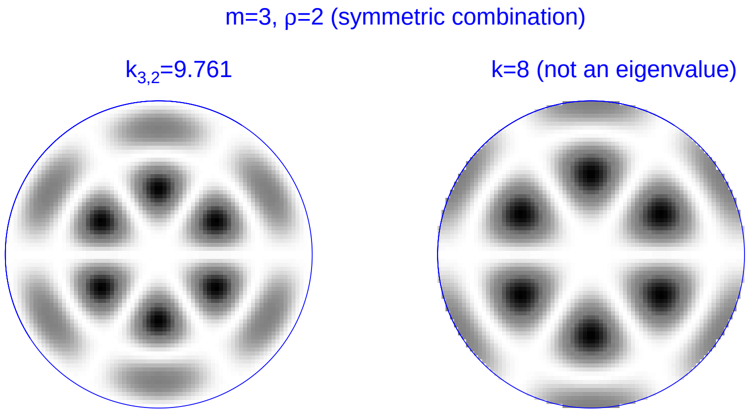

Figure 7.7: Probability density (black means high intensity) of the wave functions for the closed dielectric disk (symmetric combination Ψ_s^m). On the left, an *eigenfunction* classified by the quantum numbers m=3, ρ=2 is shown. On the right, we kept m=3 but k was chosen in between two eigenvalues, $k_{3,1} < k < k_{3,2}$; then the boundary condition, $\psi^m(r = R) = 0$, is violated.

2. the radial quantum number ρ that counts the zeros of the corresponding Bessel function J_m for a given m,

and label the eigenvalues as $k_{m,\rho}$.

Hence, the eigenfunctions of the closed disk are of the form (see Eq. (7.19), assuming A^m=1)

$$\Psi^m(\vec{r}) = \begin{cases} J_m(nk_{m,\rho}r)\, e^{im\phi} & \text{if } r < R \\ 0 & \text{if } r \geq R \end{cases} . \tag{7.23}$$

The solutions to angular momentum m and $-m$ can be combined to symmetric and antisymmetric solutions (or, even and odd parity states),

$$\begin{aligned} \Psi_s^m(\vec{r}) &\overset{\text{def}}{=} \frac{1}{2}\left(\Psi^m(\vec{r}) + \Psi^{-m}(\vec{r})\right) , \\ \Psi_{as}^m(\vec{r}) &\overset{\text{def}}{=} \frac{1}{2}\left(\Psi^m(\vec{r}) - \Psi^{-m}(\vec{r})\right) . \end{aligned} \tag{7.24}$$

Both correspond to standing wave patterns[6], the symmetric wave function obeys $\Psi_s^m(\phi) = \Psi_s^m(-\phi)$, for the antisymmetric $\Psi_{as}^m(\phi) = -\Psi_{as}^m(-\phi)$ applies.

The angular momentum quantum number m multiplied by two determines the number of azimuthal nodes of the wave function. Accordingly, the radial quantum number ρ measures the radial nodes away from the origin. To this end we arrange the counting in such a way that the zero of $J_m(nkr)$ at $r = 0$ ($m > 0$) corresponds to $\rho = 0$. By means of the two quantum numbers m, ρ the eigenfunctions of the closed system can be uniquely classified. We illustrate their meaning Fig. 7.7 for the eigenfunction $m = 3, \rho = 2, nk_{3,2} = 9.761$. We will use this classification scheme as the starting point when we study the open system and in particular when we turn towards the *eccentric* annular billiard where, strictly speaking, due to the lost rotational symmetry, no good quantum numbers exist.

---

[6] In contrast to this, $\exp(im\phi)$ describes rotating waves where the characteristic azimuthal node pattern is lost. The symmetric and antisymmetric combination will gain physical importance when we discuss the *eccentric* annular billiard in Chapter 9.

7.2.3 Quasibound states of the dielectric disk

We now know the solutions, namely eigenvalues and eigenfunctions, of the closed disk that was characterized by an infinite potential well. Next we consider the question what happens if we approach the more realistic situation of a *dielectric* disk with *finite* index of refraction. This system is described by the effective potential given in Eq. (7.16) rather than an infinite well. Hence, tunnelling escape is possible, and we do not ask for eigenfunctions but for resonant solutions or quasibound states with no incoming wave, i.e., decaying states that obey Sommerfeld's radiation condition. These are characterized by a *complex* wave vector, where the imaginary part accounts for tunnelling (or evanescent leakage). Accordingly, we have to extend the ansatz made in Eq. (7.19) by allowing a non-zero wave function outside the disk,

$$\Psi^m(\vec{r}) = \begin{cases} A^m \, \psi^m(r) \, e^{im\phi} & \text{if } r < R \\ A_0^m \, \psi_0^m(r) \, e^{im\phi} & \text{if } r \geq R \end{cases} . \tag{7.25}$$

Concerning $\psi^m(r)$, the same arguments as in Section 7.2.2 apply, and we find $\psi^m(r) = J_m(nkr)$ for the radial wave function inside the disk. The radial wave function $\psi_0(r)$ *outside* the disk is an outgoing wave. Also, it has to be a linear combination of Bessel and Neumann functions $J_m(kr)$ and $Y_m(kr)$ that are the solutions of the differential equation (7.15) for ψ_0. The function with the desired properties is a *Hankel function of the first kind*,

$$H_m^{(1)}(kr) = H_m^{(+)}(kr) \overset{\text{def}}{=} J_m(kr) + iY_m(kr) \, . \tag{7.26}$$

For completeness we introduce the *Hankel functions of the second kind*,

$$H_m^{(2)}(kr) = H_m^{(-)}(kr) \overset{\text{def}}{=} J_m(kr) - iY_m(kr) \, , \tag{7.27}$$

that we will use in the discussion of the scattering approach. Studying the current associated with $H_m^{(2)}$, one easily checks that $H_m^{(2)}$ corresponds to an *incident* wave in contrast to the outward directed current associated with $H_m^{(1)}$.

Thus we arrive at the ansatz for quasibound states where we have used the freedom in setting the amplitude scale by choosing $A_0^m \overset{\text{def}}{=} 1$,

$$\Psi^m(\vec{r}) = \begin{cases} A^m \, J_m(nkr) \, e^{im\phi} & \text{if } r < R \\ H_m^{(1)}(kr) \, e^{im\phi} & \text{if } r \geq R \end{cases} , \tag{7.28}$$

Now we solve the eigenvalue problem using the *matching conditions* that we know from Maxwell's equations [54]:

1. The tangential components of the electric and magnetic fields, $\vec{E}, \vec{H}$ at the interface boundary have to be continuous.

2. The *normal* components of the dielectric polarization and the magnetic induction, $\vec{D}, \vec{B}$ have to be continuous as well.

Let us consider the implications for TM polarized light first. Here, the electric field $\vec{E} = E(r)\vec{e_z}$ is parallel to the interface and, therefore, has to be continuous, $E(r_>) = E(r_<)$. There is no electric field component normal to the interface. The magnetic field $\vec{H}$ is related to the electric field via Eq. (7.7). In particular we find the ϕ-component of $\vec{H}$ (that is parallel to the interface) to be proportional to the radial derivative of the electric field, so that the boundary condition for the derivatives therefore reads $\partial E/\partial r|_{r_>} = \partial E/\partial r|_{r_<}$. Continuity of the wave function (the electric field, respectively) means that for TM polarized the boundary conditions are the same as for the Schrödinger equation. The only difference between the two situations is the energy dependence of the effective potential for electromagnetic waves.

In analogy, we find for TE polarized light ($\vec{H} = H(r)\vec{e_z}$) that the wave function has to satisfy $H(r_>) = H(r_<)$. We now use Eq. (7.8) to relate the electric field component $\vec{E}_\phi$ that is parallel to the interface to the derivative of the magnetic field. This implies a jump of n^2 in the derivative of the magnetic field when going outwards, namely $\partial H/\partial r|_{r_<} = n^2\, \partial H/\partial r|_{r_>}$. This means that for TE polarized light the boundary conditions are different to those of quantum mechanics. The analogy to the Schrödinger equation is re-established when we complement the effective potential $V_{\text{eff}}(r)$ by a δ-like correction at the boundary position. Apart from this, the shape and energy dependence of V_{eff} is not affected. Furthermore, we will see that the required jump in the derivative leads to more complex equations when we discuss the case of TE polarization.

Let us first consider the TM situation. Since the Bessel (Neumann) functions form a set of linearly independent functions, the matching conditions have to be fulfilled *for each m* individually. Hence, the matching conditions lead to the requirement

$$\begin{aligned} A^m\, J_m(nkR) &= H_m^{(1)}(kr)\,, & (7.29)\\ A^m\, \frac{d}{dr} J_m(nkR) &= \frac{d}{dr} H_m^{(1)}(kr)\,. & (7.30) \end{aligned}$$

We rewrite the last equation denoting the derivative w.r.t. the *argument* of the according function by the symbol $()'$,

$$A^m\, nk J_m'(nkR) = k {H_m^{(1)}}'(kr)\,. \tag{7.31}$$

Eqs. (7.29, 7.31) have to be fulfilled simultaneously and their non-trivial solutions for complex k define the quasibound states. Both equations can be combined to yield

$$J_m(nkR)\, {H_m^{(1)}}'(kR) = n\, J_m'(nkR)\, H_m^{(1)}(kR)\,; \tag{7.32}$$

in other words, the determinant $\mathcal{D}$ of the homogeneous system,

$$\mathcal{D} = \begin{vmatrix} J_m(nkR) & -H_m^{(1)}(kR) \\ nJ_m'(nkR) & -{H_m^{(1)}}'(kR) \end{vmatrix}\,, \tag{7.33}$$

has to vanish.

By means of the recursion formulas for Bessel functions $Z_m \in \{J_m, Y_m, H_m^{(1)}, H_m^{(2)}\}$ of argument x [56],

$$\begin{aligned} Z_m'(x) &= Z_{m-1}(x) - \frac{m}{x} Z_m(x)\,, \\ Z_{m-1}'(x) &= \frac{m-1}{x} Z_{m-1}(x) - Z_m(x)\,, & (7.34) \end{aligned}$$

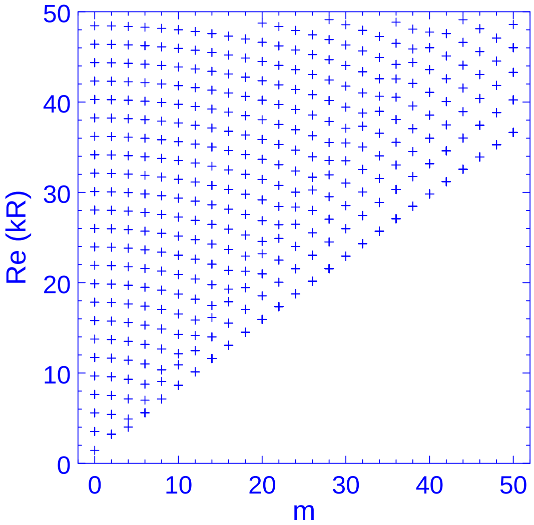

Figure 7.8: Resonances of TE polarized light in a dielectric disk of refractive index n= 1.54 with real part $\mathrm{Re}(kR) \leq 50$. The resonance below the line $\mathrm{Re}(kR) = m$ correspond to broad so-called above-barrier resonances, that is, their $\mathrm{Re}(kR)$ lies above the well in the effective potential, see Fig. 7.6.

Eq. (7.32) can be rewritten in terms of Bessel functions of neighbouring order rather than derivatives, namely

$$nJ_{m-1}(nkR)H_m^{(1)}(kR) - J_m(nkR)H_{m-1}^{(1)}(kR) = 0\,. \tag{7.35}$$

From this equation all wave vectors corresponding to TM polarized quasibound states can be obtained. It is a complex equation for complex (nontrivial) solutions for kR. These solutions are discrete points in the complex kR-plane, i.e., for a given $\mathrm{Re}(kR)$ *does not necessarily exist* a $\mathrm{Im}(kR)$ such that kR is a solution of Eq. (7.35).

We now turn to the case of TE polarization. Then the wave function Ψ plays the role of the *magnetic* field. The relevant boundary conditions are then i) continuity of $H(r)$ at $r = R$, and ii) a jump in the derivative dH/dr that is proportional to n^2 as discussed above. This leads to the equation

$$nJ_m(nkR)H_m^{(1)'}(kR) = J_m'(nkR)H_m^{(1)}(kR)\,, \tag{7.36}$$

which again is a complex equation for complex kR defining a quasibound state. Using the recursion formulas (7.34) we obtain

$$\begin{aligned} nJ_m(nkR)H_{m-1}^{(1)}(kR) - J_{m-1}(nkR)H_m^{(1)}(kR) \quad &= \\ \frac{m}{kR}\left(n - \frac{1}{n}\right) J_m(nkR)H_m^{(1)}(kR)\,. \end{aligned} \tag{7.37}$$

Note that in contrast to the TM case, now the rhs does *not* vanish, and on the lhs the subscripts m and $m-1$ are interchanged.

Eqs. (7.35, 7.37) can be solved numerically to give the exact complex resonance positions $kR \overset{\mathrm{def}}{=} x + \mathrm{i}y$. An example of solutions of Eq. (7.37) is given in Fig. 7.8 where we have indicated

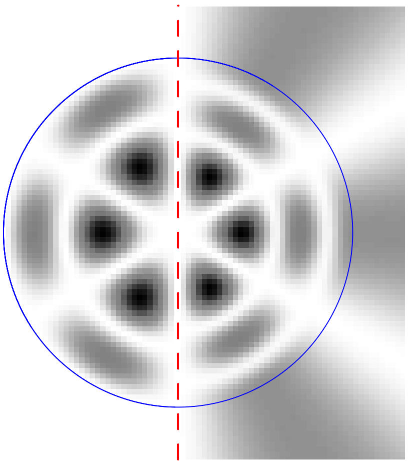

Figure 7.9: Probability densities (arbitrary units, higher intensity in darker regions) for an eigenstate of the closed disk (left half, $nkR = 9.761$ as in Fig. 7.7) and a quasibound state of similar energy (right half, $nkR = 11.428 - 0.254i$), both for TM polarization. Note the non-vanishing intensity outside the disk for the quasibound state!

the real part $\mathrm{Re}(kR)$ of all the resonances found versus the corresponding angular momentum quantum number.

In Fig. 7.9 we compare an eigenstate of the closed system with a corresponding state of the open system. The differences in the wave patterns inside and, especially, outside the disk are clearly visible.

The real (imaginary) part $x(y)$ of kR determines the energy and the width of the quasibound state, respectively. The width of the state is related to its lifetime. We will see in Section 7.4 that there is a ray optical interpretation of y in terms of a relation to reflection and transmission coefficients. Therefore it would be nice to have an analytical estimate for y. For small width y, that is narrow resonances, this can be achieved in principle by an expansion of Eqs. (7.37, 7.35) for small y. We will discuss this approach, its difficulties and alternatives in Chapter 8.

We now introduce another approach for the investigation of the dielectric disk, namely the scattering approach. We will compare the exact numerical results obtained from Eqs. (7.35, 7.37) with the results obtained within the S-matrix approach.

7.3 Scattering approach to the dielectric disk

7.3.1 Scattering matrix

The main idea of any scattering problem is to probe the response to incoming test waves. We expect that the *scattered* wave can be used to extract system properties like resonance position and width. Technically, this method is formulated for purely *real* wave vectors. This implies that the resonance width cannot arise as imaginary part of the wave vector! We will see below that the scattering approach nonetheless provides information on the resonance width.

We want to investigate the scattering properties of the dielectric disk for electromagnetic waves in the framework of scattering matrix (S-matrix) theory [93, 57, 92]. One possible choice for the testing wave are, of course, plane waves as incident waves. For our rotational invariant disk of finite dimension, however, incident waves that allow for angular momentum classification are much more convenient: Then we need to take into consideration only waves with impact parameter of the order of the system dimension or smaller. The Hankel functions of the second kind introduced in Eq. (7.27) possess the desired properties.

Again, we consider a dielectric disk of radius R and refractive index n and denote the vacuum wave vector by k. According to Maxwell's equations and the discussion in Section 7.2 we start from the ansatz

$$\Psi^m(\vec{r}) = \begin{cases} A^m\, \psi^m(r)\, e^{im\phi} & \text{if } r < R \\ A_0^m\, \psi_0^m(r)\, e^{im\phi} & \text{if } r \geq R \end{cases}, \tag{7.38}$$

for the wave function. We already know (see Section 7.2.2) that $\psi^m(r)$ has to be identified with the Bessel function $J_m(nkr)$. The radial wave function $\psi_0^m(r)$ outside will contain a contribution due to an incoming Hankel function $H_m^{(2)}$ of appropriate angular momentum m. Besides this, there are now scattered waves in terms of outgoing Hankel functions $H_l^{(1)}$ of order l. Assuming an incoming Hankel function $H_m^{(2)}$ with azimuthal dependence $\exp(im\phi)$, it will give rise to a scattered wave containing contributions from all angular momenta l, $-\infty < l < \infty$, described by Hankel functions $H_l^{(1)}$ times the corresponding azimuthal function $\exp(il\phi)$. The corresponding scattering amplitudes are S_{ml}, where the first subscript characterizes the incident, the latter the scattered wave. Hence we write the outside wave function Ψ_m^{scatt} that is excited by an incident wave of angular momentum m as

$$\Psi_m^{\text{scatt}}(kr) = H_m^{(2)}(kr)e^{im\phi} + \sum_{l=-\infty}^{\infty} S_{ml} H_l^{(1)}(kr) e^{il\phi}\,. \tag{7.39}$$

In order to find the radial wave function $\psi_0^m(kr)$ in the ansatz (7.38) we have to re-arrange the angular momentum contributions such that $\psi_0^M(kr)$ comprises all terms that contain a factor $\exp(iM\phi)$. Eventually, we arrive at

$$\psi_0^M(kr) = H_M^{(2)}(kr) + \sum_{m=-\infty}^{\infty} S_{mM} H_M^{(1)}(kr)\,. \tag{7.40}$$

The scattering amplitudes S_{ml} are comprised in the S-matrix. It follows from current conservation that S has to be unitary, a property that we will use subsequently. Starting with a general situation in which S can have entries everywhere, symmetry requirements will reduce the number of independent matrix elements. For the dielectric disk, the scattered wave has to obey angular momentum conservation and will, therefore, be a Hankel function of the same order m as the incoming Hankel function, such that the scattering matrix is diagonal. In the general case where angular momentum is not conserved (as, for example, for a deformed disk or the annular geometry of Chapter 9), scattering will occur to *all* possible angular momenta l.

For the case of an dielectric disk we will now sketch the main steps of the calculation of the scattering amplitudes S_{mm}. We start by rewriting Eq. (7.40) as

$$\psi_0^m(kr) = H_m^{(2)}(kr) + S_{mm} H_m^{(1)}(kr)\,, \tag{7.41}$$

which yields the ansatz (7.38) in the specified form

$$\Psi^m(\vec{r}) = \begin{cases} A^m \, J_m(nkr) \, e^{im\phi} & \text{if } r < R \\ \left[H_m^{(2)}(kr) + S_{mm} H_m^{(1)}(kr) \right] \, e^{im\phi} & \text{if } r \geq R \end{cases} . \tag{7.42}$$

Employing the matching conditions (cf. Section 7.2) for TM polarization, we obtain from the requirement of continuity of the wave function[7] and their derivative

$$\begin{aligned} A^m J_m(nkr) &= H_m^{(2)}(kr) + S_{mm} H_m^{(1)}(kr) \, , & (7.43) \\ A^m n J_m'(nkr) &= H_m^{(2)\prime}(kr) + S_{mm} H_m^{(1)\prime}(kr) \, , & (7.44) \end{aligned}$$

where the angular dependence $e^{im\phi}$ is the same on both sides and the prime stands for the derivative w.r.t. the full argument nkr and kr, respectively. Solving this system of equations for the amplitudes A and the matrix elements $S_{mm'}$ gives the result

$$\begin{aligned} A^m &= \frac{H_m^{(2)}(kr) + S_{mm} H_m^{(1)}(kr)}{J_m(nkr)} \, , & (7.45) \\ S_{mm'} &= - \frac{H_m^{(2)\prime}(kr) - n \frac{J_m'(nkr)}{J_m(nkr)} H_m^{(2)}(kr)}{H_m^{(1)\prime}(kr) - n \frac{J_m'(nkr)}{J_m(nkr)} H_m^{(1)}(kr)} \, \delta_{mm'} \, , & (7.46) \end{aligned}$$

which allows us to calculate the wave function for any given $k \in \mathbb{R}$. However, so far we do not know anything about the resonances that we are interested in! We will approach this issue in the following Section 7.3.2.

7.3.2 Wigner delay time

The general idea for identifying resonances of the system under consideration is that a probing wave with resonance energy will interact *longer* with the system than a wave with "non-fitting" energy. In this section we will introduce the *Wigner delay time* τ as the corresponding physical quantity. For unitary S-matrix, with eigenphases θ_l and determinant

$$\det S = e^{i \sum_l \theta_l} \overset{\text{def}}{=} e^{i\theta} \, , \tag{7.47}$$

the Wigner delay time is defined [94, 95] as

$$\tau^W(E) \overset{\text{def}}{=} \operatorname{Im} \operatorname{tr} \left(S^+ \frac{dS}{dE} \right) .$$

In an eigenbasis of S this is easily evaluated and we end up with the Wigner delay time τ^W as derivative of the total phase,

$$\tau^W(E) = \frac{d\theta(E)}{dE} \, . \tag{7.48}$$

Using the relation $E = k^2$, this can be expressed as a function of momentum,

$$\tau^W = \frac{d\theta}{dk} \frac{dk}{dE} = \frac{1}{2k} \frac{d\theta}{dk} \, .$$

---

[7] As before, we use the expressions electric field and wave function synonymously.

For the numerical calculations, this expression was scaled by a factor $2k$ and the phase θ was normalized to lie in the interval $[0,1)$, $\theta \to \widetilde{\theta} \stackrel{\mathrm{def}}{=} \theta/2\pi$. In the following graphs we will investigate the *delay time*

$$\tau(k) \stackrel{\mathrm{def}}{=} \frac{d\widetilde{\theta}(k)}{dk} \equiv 4\pi\, k\, \tau^{W}(k^2) \tag{7.49}$$

in order to find signatures of resonances.

Note that there is a relation between the (total) phase $\theta(E)$ of the S-matrix and the so-called resonance counting function $N(E) = \theta(E)/2\pi$, cf. [92]. The idea is that a resonance is encountered whenever the phase θ of $\det S$ increases by 2π upon increasing energy E or momentum k.

In the following we will use the function $\tau(k)$ to determine the resonances. They appear as peaks in $\tau(k)$, see Fig. 7.10, above a background. The area under the curve $\tau(k)$ is proportional to the number of states with wave vectors smaller than k [92, 97]. In the case of *stepwise* potentials such as realized in ray-splitting billiards, simple Weyl formulas for the smooth part of the density of states were derived for a number of geometries [99]. The application of these results to optical systems where ray splitting is realized by refraction and transmission at refractive index boundaries is tempting. However, here we work with an *energy dependent* effective potential, in contrast to the situation studied in [99] where only (stepwise) spatial dependence of the potential was assumed. Consequently, a generalization of the formulas derived in [99] would be required if one is interested in an analytical expression for the smooth part of the density of states, which is, however, not the subject of this work.

The form of a resonance peak in the delay time τ is related to the imaginary part of the wave vector in Section 7.2. To see this, we consider a single, isolated resonance for which the S-matrix is just an energy-dependent complex number $s(E)$ with $E \in \mathbb{R}$. We *continue* this function to *complex energies* and make use of the fact that the S-matrix is a meromorphic function [96] that we can expand around its *pole* E_0 in the *complex* energy plane into a Laurent series, $s(E) = \mathcal{N}/(E - E_0)$, where $\mathcal{N}$ is a constant. The poles are precisely the positions of resonances in the imaginary energy plane, and we write $E_0 = E_1 - i\Gamma_1$, where $\Gamma_1 > 0$ is the width of the resonance in the sense of Section 7.2 (note, however, that so far we work with energies rather than momenta).

Since we know that $s(E)$ has to be unitary on the real axis, it can be expressed as

$$s(E) = \frac{E - E_0^*}{E - E_0} = \frac{E - E_1 - i\Gamma_1}{E - E_1 + i\Gamma_1} = e^{i\theta_1}\,, \tag{7.50}$$

with

$$\theta_1 \stackrel{\mathrm{def}}{=} 2\arctan\frac{-\Gamma_1}{E - E_1}\,. \tag{7.51}$$

The angle $\theta_1/2$ can be given an illustrative meaning: if we approach the resonance $E_1 - i\Gamma_1$ on the *real* axis from the left, $\theta_1/2$ appears to be the angle between the real (positive) axis and the direction towards the pole $(E_1, -i\Gamma_1)$ of the S-matrix [93]. Upon passing the resonance, θ_1 changes from zero to the value of 2π. Since this happens at each resonance, following the value of θ_1 reveals the connection to the resonance counting function above.

As we approach the resonance, θ_1 changes in a characteristic way, resulting in the typical

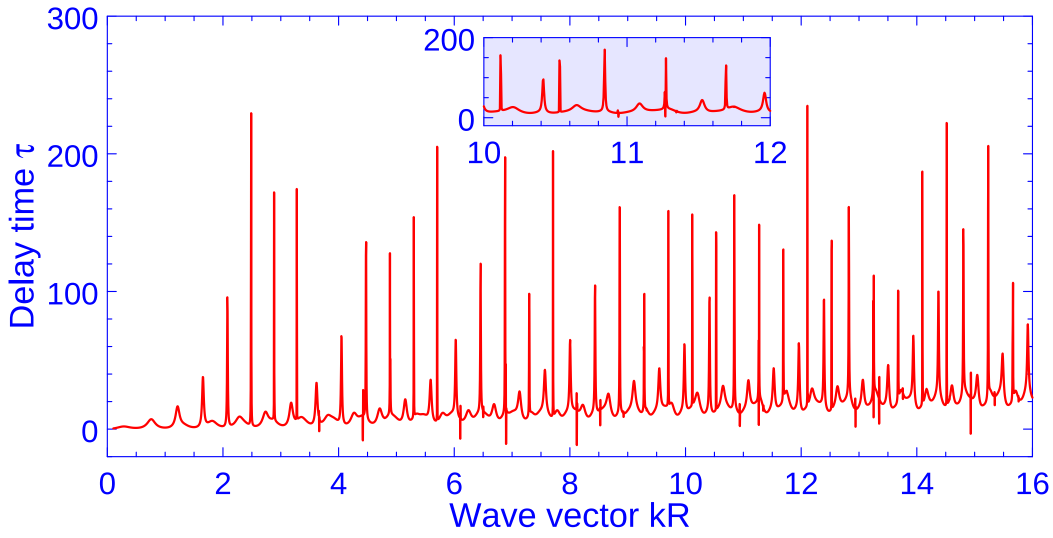

Figure 7.10: Resonances probed in terms of the delay time $\tau(k)$ for the dielectric disk of refractive index n =3. The wave number tested ranges from zero to k =16, with the interval $[10, 12]$ enlarged in the inset. Peaks on scales smaller than Δk (here, $\Delta k = 0.004$) cannot be (properly) resolved as is clearly visible in the first family of resonances (see text for detailed explanation) starting with $k \approx 0$. One observes peaks of decreasing width and increasing height until k =2.5; the following peaks of height $\tau \approx 170$ are not completely resolved and bear some artefacts, see text.

Lorentzian line shape for $\sin\theta_1/2$,

$$\sin\frac{\theta_1(E)}{2} = \frac{\Gamma_1}{\sqrt{(E-E_1)^2+\Gamma_1^2}} . \tag{7.52}$$

Such resonances are called *Breit-Wigner resonances* [93, 94]. The width of the corresponding peak in $\sin\theta_1(E)/2$ when passing a resonance at $E = E_1$, measured at half the peak height, is given by $2\Gamma_1$. That is, the imaginary part of the resonance energy gives the half width of the peak.

Using the definition (7.48) of the Wigner delay time together with Eq. (7.51) we obtain

$$\tau^W = \frac{d\theta_1}{dE} = \frac{2\Gamma_1}{(E-E_1)^2+\Gamma_1^2} , \tag{7.53}$$

giving again peaks of half-width Γ_1.

The same holds if we work with momenta rather than energies. If we assume the resonance at $k_0 \overset{\text{def}}{=} x + iy$, $y < 0$, we find from $E_0 = k_0^2$ the relationship $E_1 = x^2 - y^2$, $\Gamma_1 = 2x|y|$ and the Breit-Wigner resonance-type behaviour expressed as a function of $k = \sqrt{E}$ in the form

$$\sin\frac{\theta_1}{2} = \frac{-2x|y|}{\sqrt{(k^2-x^2+y^2)^2+4x^2y^2}} , \tag{7.54}$$

where now the imaginary part of the *momentum* defines the peak width at half peak height.

Finally, for the delay time τ this implies

$$\tau = \frac{d\theta_1}{dk} = 4k \frac{2x|y|}{(k^2 - x^2 + y^2)^2 + 4x^2y^2}\,, \tag{7.55}$$

which indeed has the expected width of $2|y|$. Furthermore, at the resonance position ($k^2 = x^2 - y^2$) the value of τ is proportional to $1/|y|$, i.e., the height of the resonance peak may serve as a further measure of the resonance width.

At this point some remarks concerning the numerical evaluation of $\tau(k)$ are necessary. The function $\theta(k)$ is determined by scanning the k-axis in steps (grid points) separated by an amount Δk, where computing time sets a lower bound on Δk. The differentiation operation to obtain $\tau(k)$ is performed as a quotient of differences. Therefore resonances that show signatures on a smaller k-scale than Δk *cannot be resolved properly* by this method as illustrated in Fig. 7.10. However, we point out that with some probability resonances whose widths are up to one or two orders of magnitude smaller than Δk will be *seen* (though not properly resolved). This happens whenever the corresponding resonance peak lies close to a grid point. The reason for this is the algebraic decay in the tails of the Lorentzian line shape: although the width of the resonance measured at half the peak height might be much smaller than Δk, there might be some resonance-like signals or spikes when one of the scanning values hits the shoulder of the resonance. However, there is at most information concerning the real part of the resonance contained, but no values for the imaginary part can be deduced.

Besides this limitation towards extremely narrow resonances, the resolution to the broad-resonance end is limited, too. The limiting situation is defined by two (broad) resonances that overlap in such a way that they cannot be resolved.

It is useful to compare this S-matrix method to another approach used in [108] that identifies resonance signatures in the plane-wave response of the system. There, the energy of a incident plane wave is varied and the change in the wave intensity at a certain (boundary) point is traced. Resonances appear as peaks or dips; however, for systems with discrete symmetry the direction of incidence matters, and it is likely that not all resonances are excited, and consequently, are not found. Furthermore, the peaks (dips) are not necessarily of Lorentzian line shape making it difficult to identify families of resonances. The resolution problem is similar to that described above. Using the S-matrix method and the delay time τ to search for resonances has the advantage of being able to identify *families* of resonances, i.e., to gain information about the angular momenta of the resonant states, simply by (carefully) counting the peaks. The series may even be continued to narrow resonances that are only poorly resolved. Furthermore, *all* resonances are of the generic Lorentzian line shape and its width is proportional to the resonance width. We will use this S-matrix method in particular when dealing with the annular billiard in Chapter 9.

7.3.3 Comparison of wave-based methods

In Section 7.3.2 we already described the relation between the shape of a resonance peak in the delay time $\tau(k)$ and the imaginary part y of the complex resonance $kR \overset{\text{def}}{=} x + iy$. In Fig. 7.11 we quantify this comparison and give both the resonance width, as calculated with the exact formula Eq. (7.32), and a plot of the delay time $\tau(k)$ for the resonances labelled by the arrows

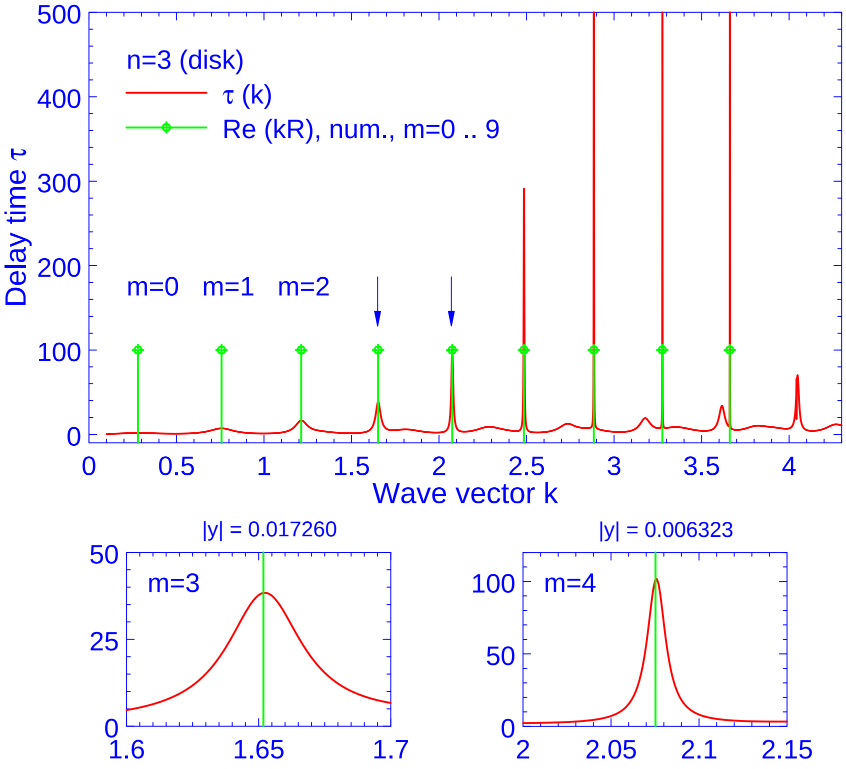

Figure 7.11: Signatures of the first resonances (ρ =1, first family) of the dielectric disk (n=3), labelled by their angular momentum quantum number m in terms of the delay time $\tau(k)$. The vertical lines (arbitrary height) indicate the real part of the corresponding solutions of Eq. (7.32). For the resonances m =3 and m =4 (arrows), we compare the numerical width (imaginary part y) from Eq. (7.32) with the peak width, see the two lower panels. The peak half width (estimated to be 0.017 and 0.006 at half peak height) is a very good estimate for y. The resonances for m >6 are not shown in full height. Note the emerging of the *second family* starting at k >2 with a rather pronounced peak at $k \approx 4$.

in Fig. 7.11. Indeed, we find a good quantitative agreement. Alternatively, one could relate the *height* of the resonance peak to the imaginary part of the wave vector, see the discussion in Section 7.3.2,

Another crucial point is whether we can classify the resonances obtained within the scattering formalism in a way similar to the classification by angular momentum and radial quantum numbers as in Section 7.2. The answer is yes! Investigation of the function $\tau(k)$ reveals *families* of resonances characterized by decreasing width and increasing height with similar distances between neighbouring peaks. Comparison with the exact solutions of Eq. (7.32) shows that the *radial* quantum number ρ within such a family is the same and that the *angular* quantum number m increases by one from resonance to resonance. This is illustrated in Fig. 7.11. Note that the assignment of the correct m might become tricky in higher families when one just counts the peaks, since the first and broadest peaks might be not resolved and, thus, are not visible. Then comparison with the exact numerical results from Eq. (7.32) is required. When we investigate

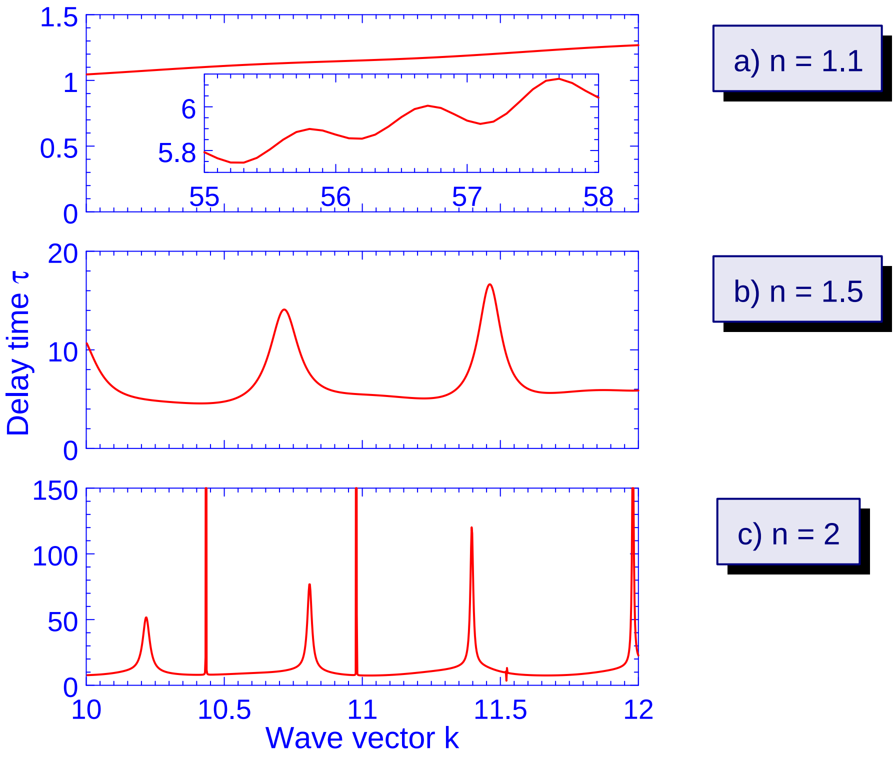

Figure 7.12: Emergence of resonances for increasing refractive index n for a certain range of the wave vector k outside the disk. In c), an artefact of a not properly resolved narrow resonance is visible at $k \approx 11.5$.

the *annular billiard* in Chapter 9 we will use this correspondence to label our modes even in the eccentric case when m and ρ are no good quantum numbers. The idea is then to start with a *disk* by choosing[8] $n_1 = n_2$ where labeling is unique, and follow the resonances while changing the value of n_1 (or n_2).

At this point it is useful to discuss the families of resonances in terms of the effective potential, cf. Eq. (7.16). Within each family, m increases and the form of the potential changes accordingly [*besides* the overall k-stretching due to $V_{\rm eff}(k)$]. Alternatively, we can consider resonances of the same m in different families where the relative *shape* of the potential is the same and only the stretching factors change.

We finish this section by briefly studying the implications of a variation of n from $n = 1$ to $n = \infty$. For intermediate values of n we already found the resonances characteristic for an open system. First, we ask the question of how they *appear* when we increase the refractive index of the disk from $n = 1$ (airy disk in air) to finite values of n. The result is shown in Fig. 7.12 – it indicates that for fixed vacuum wave vector, the resonances become increasingly sharp for higher n. This can immediately be understood within the picture of the effective potential with a well height proportional to $(1 - n^2)$, cf. Eq. (7.16). Since the effective potential well is, on the other hand, energy dependent (proportional to k^2), we expect more pronounced resonances for higher k. As can be seen in the inset for n =1.1, this indeed is the case. In terms of the ray picture, higher n means better confinement according to Fresnel's law. This aspect is further

---

[8] For notations, see the beginning of Chapter 9.

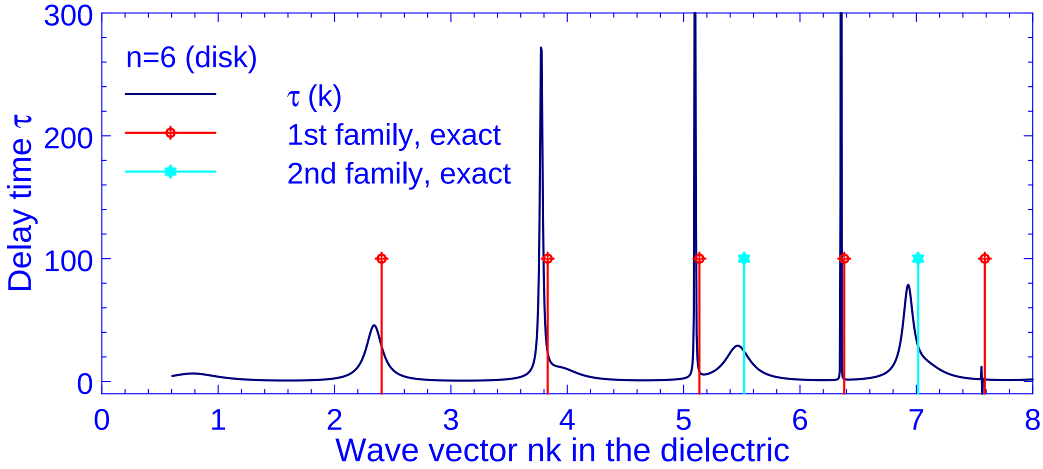

Figure 7.13: Comparison of the eigenvalues for the closed system with resonances of dielectric disk of refractive index $n = 6$. The agreement improves for narrower resonances that lie deeper in the potential well and, therefore, experience a confinement that better resembles the closed system.

developed in Section 7.4.

We just learned that resonances become narrower with increasing refractive index n due to the deeper well of the effective potential. In this context, the interesting question of the relation to the closed system arises. We study this issue by comparing the resonance positions of a disk of refractive index n =6 with the exact eigensolutions of the closed system given in Eq. (7.22). The result is shown in Fig. 7.13 and reveals that already a refractive index of n =6 indicates a "fairly closed" system. In terms of Fresnel's law (7.4) we find a reflectivity of 70% even for perpendicular incidence.

7.4 Quantum – classical correspondence: Ray versus wave picture

In this section we want to connect the ray picture (Section 7.1) and the wave picture (Sections 7.2, 7.3). On one hand, we will find a connection between the angle of incidence χ, and the angular momentum quantum number m comparing the classical and quantum expressions for the angular momentum perpendicular (i.e., in z-direction) to the ring. On the other hand, we will develop a model that allows us to relate the reflection coefficients obtained from Fresnel formulas (7.4, 7.5) to the resonance width, that is, the imaginary part of the complex solutions of Eqs. (7.32, 7.36) for the wave vector.

In the ray picture, the reflection or transmission of a light ray at a given interface is fully characterized by the angle of incidence χ, even in the case of a curved interface. The reason is that the ray picture corresponds to the limit of zero wavelength, such that all radii of curvature are large and any interface appears *locally planar*. The wave picture characterizes each wave by a wave number k and the quantum number m for the z-component of angular momentum. In a classical picture, the z-component L_z of the angular momentum is given by

$$L_z = Rnp \sin\chi \,, \tag{7.56}$$

where R is the radius of the disk and np the (classical) momentum of a ray inside. Using $p = \hbar k$ and the (semiclassical) quantization condition $L_z = \hbar m$ we obtain

$$\hbar m = nR\hbar k \sin\chi\,, \tag{7.57}$$

or

$$\sin\chi = \frac{m}{nkR}\,. \tag{7.58}$$

The physical content of this equation is that each wave solution can be uniquely assigned to an angle of incidence, that is, a classical angular momentum, that is, a ray! However, in general this angle χ will *not* correspond to a closed (whispering gallery) orbit within the disk in the sense that $2\pi/\chi$ is an integer number as one might expect. This can be easily checked by computing $\sin\chi$ from Eq. (7.58) for a few values, see Table 7.4. For increasing m the solutions for the wave vector k fixed radial quantum number ρ are such that χ increases as well – that means that the whispering gallery modes are increasingly localized at the disk boundary. The largest value of χ is, of course, $\pi/2$, and in this limit the naive picture of a corresponding orbit works and yields a polygon with infinitely many corners – a circle! In Table 7.4 we give the values for $\sin\chi$ and other characteristics for the resonances in Fig. 7.11.

Another argument that illustrates that a resonance with, e.g., angular momentum quantum number $m = 3$ (as in Fig. 9.11) and, consequently, $2m = 6$ intensity maxima cannot correspond to a regular whispering gallery orbit in the form of hexagon is provided by the phase space plot. Periodic whispering gallery orbits, of which the hexagon is one example, fill an area of zero measure in the Poincaré section! Since there is no reason why wave solutions should not fill the *whole* phase space, deviations in $\sin\chi$ are unavoidable.

We will now explain the effect of the narrowing of the resonance peak with increasing χ in terms of a model of sequential reflections. For a linear resonator with parallel mirrors of reflection probability R_m on both ends, it is well-known that the leakage loss γ can be obtained by applying R_m sequentially to rays travelling back and forth between the mirrors. We are in a situation where we have information about the loss in terms of the imaginary part y of the wave vector, $kR \overset{\text{def}}{=} x + iy, y < 0,\ R \equiv 1$. From this knowledge we want to calculate the reflection probability or *reflection coefficient* R_s of an individual reflection in the dielectric disk.

We begin by rewriting the time dependence $\exp(-i\omega t)$ of the wave function using the dispersion relation $\omega = ck$ of light, with c the wave velocity in the dielectric disk. The imaginary part of k causes an exponential decay $\exp(cyt/R) \overset{\text{def}}{=} \exp(-t/t_0)$ that is characterized by the time scale $t_0 \overset{\text{def}}{=} R/c|y|$. If we ask for the time dependence $P(t)$ of the *intensity*[9], we have to square the decay factor of the wave function,

$$P(t) = e^{-\frac{2t}{t_0}}\,. \tag{7.59}$$

Otherwise, we can think of this decay as caused by s sequential reflections at the disk boundary, each with a probability R_s,

$$P(t) = (R_s)^s\,. \tag{7.60}$$

The optical distance d_s between two of these reflections is given in terms of the ray model as $d_s = 2nR\cos\chi$, the time taken is $t_s = d_s/c$. This provides us with the number s of reflections after time t, $s = t/t_s = ct/(2nR\cos\chi)$ and we can relate

---

[9] We are interested in a relation to (Fresnel's) reflection coefficients that are defined for intensities.

$$\ln P(t) = -\frac{2tc|y|}{R} = \frac{ct}{2nR\cos\chi}\ln R_s\,, \tag{7.61}$$

which eventually yields

$$R_s = e^{-4n|y|\cos\chi} \tag{7.62}$$

as the desired relation between the resonance width $y = \mathrm{Im}(kR) < 0$ and a corresponding reflection coefficient.

Eq. (7.62) enables a *comparison* between the wave-picture results, see Eqs. (7.32, 7.36), where the curved interface of the disk is fully taken into account and those of the ray picture that assumes a planar interface in terms of *reflection coefficients*[10]. The results are shown in Figs. 7.14 and 7.15. The planar interface (Fresnel) result is clearly verified as the zero-wavelength limit of the wave approach. For smaller kR, deviations occur mainly in the region around the critical angle. The exponentially small corrections due to tunnelling escape of light upon total internal reflection are discussed in [108] and not subject of this work. In Fig. 7.16 we eventually illustrate the situation of a disk with lower refractive index than the surroundings, i.e., $n < 1$. Then *no* total internal reflection *inside* the disk is possible and the mechanism that confines the light in the microcavity is lost. In terms of the effective potential the well is replaced by a monotonically increasing potential with a jump at $r = R$. As for the solutions of Eqs. (7.32, 7.36) we find the corresponding reflection coefficients well described by Fresnel's law for a planar interface, see Fig. 7.16. In the following we will mainly be interested in microcavities that allow for the confinement of light by total internal reflection.

Another comment is necessary on the sign of the angular momentum quantum number m of the whispering gallery modes. Although we only addressed positive m so far, it is straightforward to extend the picture to negative m giving rise to resonances with the same properties in the same effective potential but the opposite sense of rotation when translated into an angle of incidence via Eq. (7.58). Since the system is rotational invariant and angular momentum is conserved, the states are paired in doublets composed of angular momentum components m and $-m$ that are degenerate in energy. This degeneracy will be lifted in the *eccentric* annular billiard [101] when rotational symmetry is reduced to reflection symmetry about the x-axis.

Finally, we develop a relation between the *length* of an orbit and the resonance *spacing dk*. The semiclassical interpretation of a closed orbit states that the optical length $n\,L$ is an integer multiple q of the (vacuum) wavelength λ, $nL = q\lambda$. If we ask for which wavelengths this relation holds, we find a neighbouring $\lambda_1 = \lambda - d\lambda$ fulfilling $nL = (q+1)\lambda_1$. Using $\lambda = 2\pi/k$ and $\lambda_1 = 2\pi/(k+dk)$, we obtain the orbit length as

$$L = \frac{2\pi}{ndk}\,. \tag{7.63}$$

On the other hand, we can deduce a length L_χ for a given angle χ by generalizing the concept of closed polygonal orbits. For a polygon of $q \in \mathbb{N}$ corners, $\chi \overset{\text{def}}{=} (q-2)\pi/(2q)$ in order to have a closed orbit. Its length is then $L_\chi = 2q\cos\chi$. If we allow $q \to \tilde{q} \notin \mathbb{N}$, we find for a given χ a generalized polynomial with

$$\tilde{q} = \frac{2\pi}{\pi - 2\chi}\,, \quad L_\chi = 2\tilde{q}\cos\chi\,. \tag{7.64}$$

---

[10] Alternatively, one could, of course, translate Fresnel's reflection coefficients into resonance widths.

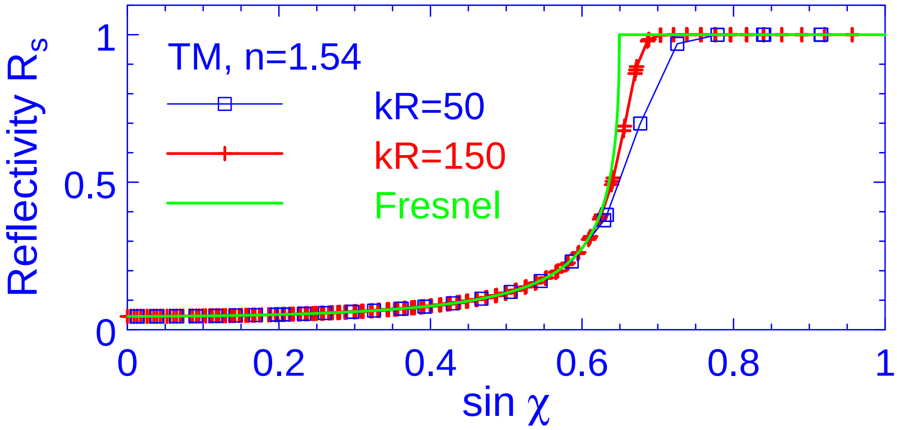

Figure 7.14: Reflection coefficient versus sine of the angle of incidence χ for transverse magnetic (TM) polarized light reflected at dielectric of $n = 1.54$ (typical value for glass). The result of Fresnel's law (7.4) describes reflection at a planar interface. The symbols mark numerical solutions of Eq. (7.32) with real part $\text{Re}(kR)$ close to 50 (squares) or 150 (crosses), respectively. The imaginary part of the solution is expressed as reflection coefficient via the sequential reflection model, Eq. (7.62). Note that the Fresnel result (full line) is approached in the limit $\text{Re}(kR) \to \infty$, that is, zero wavelength.

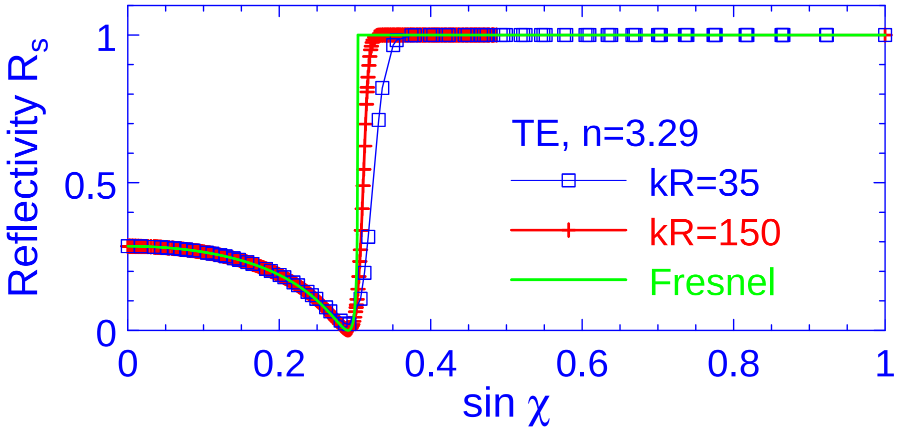

Figure 7.15: Same as Fig. 7.14 but for refractive index $n = 3.29$ as is typical for semiconductor material and TE polarized light. The symbols stand now for numerical solutions of Eq. (7.36). Note the feature of the Brewster angle for this polarization that is also respected by the wave solutions. Again, ray optics is approached as $\text{Re}(kR) \to \infty$.

In the following table we give $m, k, dk, L, \sin\chi, \widetilde{q}$ and L_χ for the first resonances of Fig. 7.11:

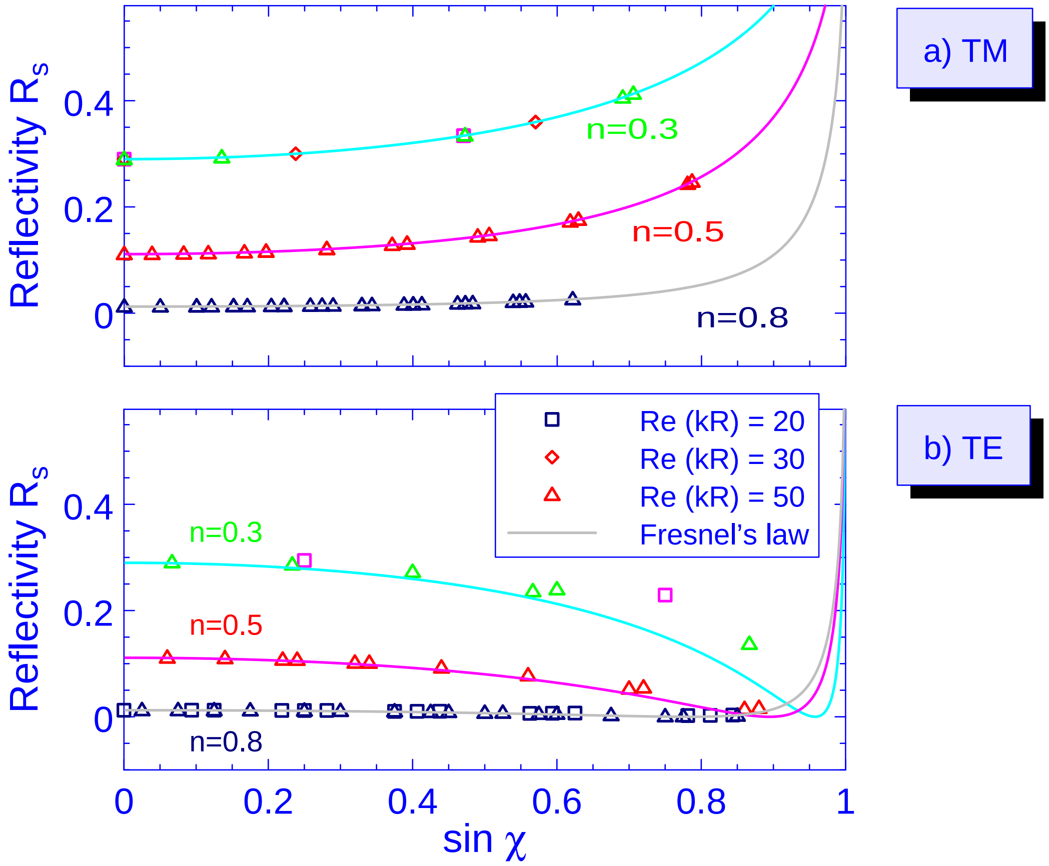

Figure 7.16: Reflection coefficients for a) TM and b) TE polarized light, obtained in the sequential reflection model for disks with index of refraction $n < 1$ ($n = 1$ outside). The full lines indicate Fresnel's law for a planar interface. It provides a good description of the curved interface even for moderate wave vectors kR – here the ray limit is applicable for a wider range of kR than in the case of $n > 1$.

m	k	$dk = k_{m+1} - k_m$	$L = \frac{2\pi}{ndk}$	$\sin\chi = \frac{m}{nkR}$	$\tilde{q} = \frac{2\pi}{\pi - 2\chi}$	$L_\chi = 2\tilde{q}\cos\chi$
1	0.7577	0.4549	4.60	0.440	2.82	5.06
2	1.2126	0.4392	4.77	0.550	3.18	5.31
3	1.6518	0.4235	4.95	0.605	3.41	5.43
4	2.0753	0.4098	5.11	0.642	3.60	5.51
5	2.4851	0.3992	5.25	0.671	3.76	5.58

Note the increase in χ accompanying the narrowing of the resonances. Note also that both the length L_χ and L increase, too, meaning that the resonances become more whispering-gallery like. Correspondingly, the resonance spacing dk decreases. There is a discrepancy in the lengths, $L_\chi > L$, which indicates that the *true* waves do not follow generalized polygons but *shorter* (optimal) circle-like orbits as also suggested by the wave function plots. – In this context we point out that the contribution of whispering gallery orbits to the trace formula is not fully understood [102].

Before we conclude this chapter with some general remarks concerning *practical aspects* of the complementary relation between ray and wave concepts, let us refer to some experimental findings and applications first.

In experiments with easily produced and manipulated silica microspheres [64] whispering gallery modes were found to be sustained if the sphere circumference is larger than a few wavelengths. Storage times of the order of one microsecond are reported, corresponding to Q-factors of up to 10^{10}. Slight variations in the shape of the microsphere cause WGMs to exist mainly in one (equatorial) plane. The well-defined frequency of WGMs renders them ideal subsystems in the investigation of their interaction with two-level atoms [65], or their coupling to nanocrystals and quantum dots, respectively [66].

The frequency of the equatorial WGMs in silica microspheres can be *tuned* by a change in temperature or strain[11], both keeping the circular shape but affecting the diameter of the sphere. After the discussions of this chapter, this behaviour is easily understood recalling that only the *product* kR is fixed at a resonance. However, this finding cannot be explained if we have in mind the *ray* that travels along the cavity boundary possessing a fixed angle of incidence. Other properties can be well understood in terms of geometrical optics. This applies, for example, to the shape-dependent emission that was found in GaAs whispering gallery microdisk lasers [69, 132].

The concept of the ray picture is easily applied to any optical system and gives immediately rough ideas of what is going on in a closed cavity. Adding the concept of total internal reflection allows qualitative understanding of the open system. However, deviations due to curved boundary interfaces (see Figs. 7.14, 7.15) limit the quantitative predictions. In Chapter 8 we will extend the ray picture by the Goos-Hänchen effect as an ingredient that originates from properties of *waves*. We will see that we can use it to improve the predictions for circular-shaped interfaces. The application to interfaces of any shape is then straightforward by assuming locally a circle. Employing the ray picture a successful explanation of a recent cavity fibre experiment [130] could be found, see Section 10.1.

Wave concepts give the exact solutions at the price of much more complicated equations. For the dielectric disk, it is not too hard to find numerical solutions. For more complicated shapes, however, the equations will increase in complexity making the numerical treatment demanding. In symmetric systems, the solutions can be labelled by quantum numbers like m (azimuthal nodal lines) and ρ (radial nodal lines) in the example of the dielectric disk. Complications arise in the case when there are no good quantum numbers, as is the case in most non-circular (oval) resonators, where ray concepts, however, are not at all affected and may allow for a classification of solutions by the ray-wave correspondence.

Another type of corrections to the ray picture arises in the presence of classical chaos in the system under investigation. For the integrable disk that we studied so far this is not the case. In Chapter 9 we will consider the *annular billiard* as a system that shows classical chaos. The impact of this fact onto the properties of wave solutions (and vice versa) is the subject of *quantum*

---

[11] Strain can be applied strechting a *two stem* sphere.

chaos. In optical systems, this aspect is combined with the *openness* of the system caused by the always leaky confinement of the modes for finite refractive indices and the *vectorial nature of light* that requires a distinction between TM and TE polarization. This turns the subject into a rich and challenging problem in which ray and wave methods complement each other. Hereby ray methods are in particular useful because they provide a first classification of the classical phase space associated with the *closed* system in terms of a Poincaré surface of section. This is commonly used as a classification scheme for wave solutions. In Chapter 9 examples for this can be found. Once the principle difference between rays and waves is identified and known, one might return to the simpler ray picture in order to study other system and *subsequently add the modifications that waves require for*. We will use these ideas in Section 10.2 when we discuss resonators of various shapes and their possible applications as microresonators.

We want to point out once more that the (effective) quantum-mechanical description of electromagnetic waves is well possible but requires some care. For example, Maxwell's equations do *not* depend on anything similar to Planck's constant $\hbar$. However, in quantum mechanics, $\hbar$ is of importance for example in the uncertainty relation between conjugate variables, that also determines the resolution of classical phase space features that can be achieved. According to the knowledge we gained up to this point we would expect $\hbar$ to be related to the reciprocal wave vector, $\hbar \sim 1/k$, because we expect $\hbar \to 0$ in the ray limit $k \to \infty$. We can improve this picture by considering the pair of conjugate variables ϕ, $m = nkR \sin\chi$. If we plot the Poincaré section w.r.t. these variables, we see that the phase space is the more stretched the higher k. If we furthermore take Eq. (7.15) to read off $\hbar \equiv 1$, we find indeed that a certain phase space feature is the better resolved the larger k, which can be equivalently interpreted as $\hbar \to 0$. Alternatively, we could have divided Eq. (7.15) by k^2, thereby removing the k^2-dependence of the effective potential, and identify $1/k$ with $\hbar$.

8 Fresnel laws at curved interfaces

This chapter is devoted to approximate analytical expressions for Fresnel coefficients at *curved* interfaces – these describe the enhanced escape of quasibound states at curved interfaces. First, we base our investigation on the ray picture. By means of the Goos-Hänchen effect we find a qualitative and quantitative explanation of the modification of Fresnel's laws at curved interfaces. In the second part of this chapter, we start from the wave picture. Expanding the exact equations for small resonance widths causes problems in general. Therefore, we employ the Debye approximation for Bessel functions as an alternative in order to derive an analytical expression for the resonance width (or the reflectivity, respectively) appropriate for not too small refractive indices. This allows a convenient computation of corrected Fresnel coefficients for (convex) interfaces that can be locally approximated by a sphere.

8.1 Extending the ray picture: Goos-Hänchen shift

In Section 7.4 we compared Fresnel coefficients for planar interfaces (Fresnel's laws) with those for spherical interfaces obtained via the sequential reflection model, cf. Figs. 7.14, 7.15. The latter were obtained by numerically solving the implicit Eqs. (7.32, 7.36). For quantitative predictions of the reflections properties of microcavities in *practical applications* it is desirable to have direct analytical expressions for curvature-corrected Fresnel coefficients available. This problem has been addressed by applying various techniques. For example, in [109] the Fresnel result for a planar interface was corrected by multiplication with a polarization-independent curvature factor. However, the results obtained there were not fully conclusive under closer investigation. The *complex ray method* in a paraxial approximation was used in [110] to describe light rays approaching the disk from outside. In [111] *conformal mapping* was used to access the eigenvalue of an open optical cavity. One might also think of adopting methods that were established in the context of planar interface, like the introduction of an interface transfer matrix that allows to describe the Fresnel coefficients as hyperbolic rotations of this matrix [112]. However, although the problem of Fresnel coefficients for curved interfaces was addressed by many groups in the last years [113], no "standard" technique to incorporate the curvature could be achieved.

According to the statements in the previous chapters, there are essentially two possible starting points to derive Fresnel laws for curved interfaces, namely the ray picture (this section) and the wave picture (next section).

In this section, the objective is to find an qualitative and quantitative explanation for the deviations at curved interfaces in terms of a *ray-based* picture. The motivation for these considerations is that essential qualitative features of microcavities are, in general, well described by the ray picture as we will see throughout the second part of this thesis. Therefore, it is desirable to complete the ray model by a mechanism that explains the observed differences. Since the ray picture can be thought of as the zero-wavelength limit of wave mechanics, it is clear that for a light ray *any* interface will appear planar. The corresponding reflection and transmission coefficients are given by Fresnel's law, see Eqs. (7.4, 7.5), giving the wrong predictions when the ray model does not strictly apply, i.e. for light of finite wavelength. Therefore, in order to

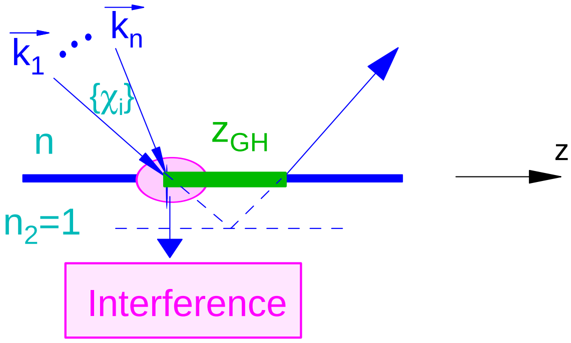

Figure 8.1: Goos-Hänchen shift at a planar interface. An incident beam containing contributions from plane waves of slightly different wave vectors appears to be reflected at a position that is shifted a distance z_{GH} away from the point of incidence. Alternatively, one can think of the beam to be reflected at a shifted interface indicated by the dashed lines.

obtain a more realistic point of view, we need to implement some *wave properties* that imply corrections of the ray picture in particular around the critical angle χ_c where we find the largest deviations between ray and wave picture, see Figs. 7.14, 7.15. The so-called *Goos-Hänchen effect* [116, 117, 118, 119, 120] possesses precisely the features we are looking for. It is an interference effect that occurs upon total internal reflection of plane waves with slightly varying wave vectors. The result is a *lateral shift of the reflected beam*, the so-called Goos-Hänchen shift (GHS), see Fig. 8.1. It is this interference effect that incorporates *wave* properties into the ray model. The according phase shift can be interpreted as lateral shift, and is accompanied by a time shift (*Wigner delay*) of the reflected beam that is of the order of 10^{-14} to 10^{-15} seconds that is accessible in, e.g., measurements at metallic gratings (cf. [121] and references therein).

The way slightly different wave vectors cause a lateral shift of the reflected beam can easily be understood within a simple calculation – this effect is already present at a planar interface [89]!. The necessary ingredients comprise a collection of (at least two) incident plane waves with slightly different transverse wave vectors (in other words, the corresponding rays cover a certain range of angles of incidence χ_i), see Fig. 8.1, and the phase shift $\Phi(\chi_i)$ that occurs upon total internal reflection, cf. Eq. (7.6). Therefore, each plane wave undergoes a slightly different phase change so that the sum of all reflected plane waves, comprising the real reflected beam, results to be laterally shifted. Another more physical explanation of this effect is based on the evanescent wave flowing parallel to the interface in the less dense medium in the case of total internal reflection. It can be shown [118] that energy will not be conserved if there is no lateral shift of the reflected beam.

The first analytical expression for the Goos-Hänchen shift z_{GH} of a *Gaussian beam*[1] of wave vector nk in the dielectric travelling in a medium with refractive index n and being reflected at a planar interface with vacuum, was obtained by Artmann as [117]

---

[1] Gaussian beams are exact solutions of the paraxial wave equation. They are characterized by a Gaussian-distributed electric field intensity along the beam wavefronts, and diffractive angular spread, giving rise to the existence of a so-called beam waist, cf. e.g. [122]. We will use the notation σ for the beam half width defined by intensity drop to $E_{\max}/e$.

$$z_{\mathrm{GH}}^{A} = \frac{2\mathcal{T}\tan\chi}{nk\sqrt{\sin^2\chi - \sin^2\chi_c}} \frac{\cos^2\chi_c}{\cos^2\chi + \mathcal{T}^2\left(\sin^2\chi - \sin^2\chi_c\right)} \tag{8.1}$$

with the polarisation-dependent constant

$$\mathcal{T} = \begin{cases} 1 & \text{TM polarized light} \\ n^2 & \text{TE polarized light}\,. \end{cases} \tag{8.2}$$

Clearly, this result diverges at the critical angle! Since a Gaussian beam contains a smooth and continuous spectrum of plane waves and the shift is expected to be finite and continuous, this behaviour is unphysical. This is particularly evident at $\chi = \chi_c$, where we have plane-wave components with angles of incidence both smaller and larger than the critical angle χ_c. When slightly varying χ, corresponding to a *slight* change of the amplitudes involved, we expect a *slight* change of the lateral shift as well [118].

Therefore, Lai et al. derived an improved expression for the Goos-Hänchen shift, that, due to fewer approximations, remains finite at the critical angle. Their more sophisticated result to order $(nk\sigma)^{-1}$ for a Gaussian beam of half width σ reads [118]

$$z_{\mathrm{GH}}(\chi) = \frac{\sigma}{\cos\chi} \frac{\operatorname{Re} a_1}{1 - \operatorname{Re} a_2}\,, \tag{8.3}$$

with

$$\begin{aligned}
a_1 &= \frac{e^{i\pi/4} \times e^{\beta_0^2/4}\left[-BD_{-1/2}(\beta_0) - \frac{2iE}{nk\sigma}D_{1/2}(\beta_0)\right] + \frac{2iC}{\sqrt{nk\sigma}}}{2\left[\sqrt{nk\sigma}A + Be^{i\pi/4} \times e^{\beta_0^2/4} \times D_{1/2}(\beta_0)\right]}\,, \\
a_2 &= \frac{-Be^{i\pi/4} \times e^{\beta_0^2/4} D_{-3/2}(\beta_0)}{4A\sqrt{nk\sigma}}\,, \\
\beta_0 &= ink\sigma\Delta\,, \\
A &= \cos^2\chi - \mathcal{T}^2\left(\sin^2\chi - \sin^2\chi_c\right)\,, \\
B &= -2\mathcal{T}\cos\chi\sqrt{\sin 2\chi}\,, \\
C &= \frac{-2\mathcal{T}^2}{G}\cos^2\chi_c \sin 2\chi\,, \\
E &= \frac{2\mathcal{T}}{G}\sin\chi\sqrt{\sin 2\chi}\left[\mathcal{T}^2(\cos^2\chi + \cos^2\chi_c) - \cos^2\chi\right]\,, \\
G &= \cos^2\chi + \mathcal{T}^2\left(\sin^2\chi - \sin^2\chi_c\right)\,, \\
\Delta &= \frac{\sin^2\chi - \sin^2\chi_c}{\sin 2\chi}\,.
\end{aligned}$$

The functions $D_\nu(\gamma)$ are parabolic cylinder functions of order ν and argument γ. In Appendix D we relate them to well-known Bessel functions suitable for practical applications[2].

Non-zero values $z_{\mathrm{GH}}(\chi)$ are found around the critical angle χ_c, whereby the maximum is reached at an angle slightly larger than χ_c. The result (8.3) was obtained under the general approximation

$$\tan\chi \ll nk\sigma \tag{8.4}$$

---

[2] Parabolic cylinder functions are not contained in standard numerical C-libraries like [123].

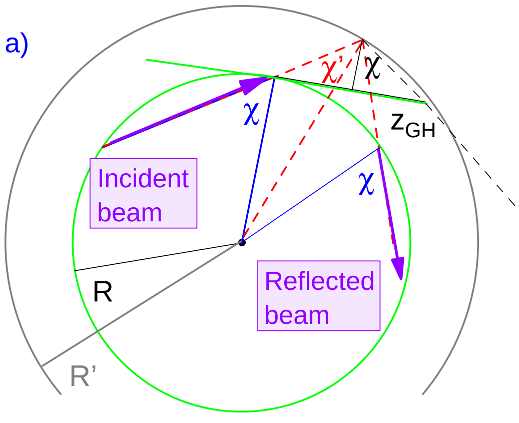

Figure 8.2: Two possible implementations of the Goos-Hänchen effect at a curved interface. The reflection seems to occur at an interface of larger curvature radius $R' > R$ under a smaller angle $\chi' < \chi$ of incidence. In a), the symmetry w.r.t. the reversed ray path is respected only for small lateral shifts $z_{\rm GH} < R$. It can be fully established when assuming that the lateral shift *follows* the interface as in b). Then the effective quantities are given by $\chi' = \chi - z_{\rm GH}/(2R)$ and $R' = R\,\sin\chi/\sin\chi'$.

and the additional condition for TE polarized light near the critical angle

$$G \gg \frac{n^4-1}{nk\sigma}\,\sin(2\theta)\,, \tag{8.5}$$

or $2(n^2+1)\sqrt{n^2-1} \ll nk\sigma$. This reduces the validity range of Eq. (8.3) for TE polarized light compared to TM polarization.

So far, we considered the Goos-Hänchen shift for a Gaussian beam at a *planar* interface. Since the reflection law (7.1) is not affected by the lateral shift and fulfilled for the mean angle of incidence and reflection, respectively, the angle-dependent Fresnel reflection coefficients (7.4, 7.5) are not changed at a planar interface. However, if we consider a *spherical* interface, the situation changes as shown in Fig. 8.2. In Fig. 8.2a, a lateral shift of the amount $z_{\rm GH}$ is assumed to occur at an interface that is tangent to the point of incidence. The intersection of the effective reflection plane (parallel to the tangent interface) with the incident ray defines an effective radius $R' > R$. We now assume that the ray is specularly reflected at this effective spherical interface with a larger radius of curvature, resulting in a smaller effective angle of incidence $\chi' < \chi$. Accordingly, for a ray incident under an angle χ we have to *evaluate* the Fresnel reflection coefficients (7.4, 7.5) at this *smaller angle* χ', which already provides an qualitative explanation of the shift in the reflection coefficient for curved interfaces. The same holds if we modify this construction by presuming the lateral shift to follow the curved interface as illustrated in Fig. 8.2b. The higher symmetry of this approach guarantees that the optical path is reversible.

We point out the $1/k$-dependence of the Goos-Hänchen shift in Eq. (8.1) implying that this effect vanishes for large k, i.e., in the ray limit $k \to \infty$, $\lambda \overset{\rm def}{=} 2\pi/k \to 0$. This is in agreement with the results shown in Figs. 7.14, 7.15, too, since we observed larger deviations from Fresnel's

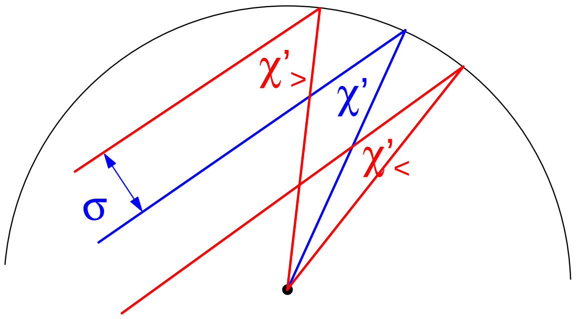

Figure 8.3: Beam of half width $\sigma \sim \lambda$ incident at a spherical interface with radius R of curvature. The range of angles of incidence $[\chi'_<, \chi'_>]$ is defined by the innermost and outermost beam, respectively. The value of $\chi'_{<(>)}$ is given by $\sin\chi'_{<(>)} = [1-(+)\sigma/(R'\sin\chi')]\sin\chi'$.

formulas for smaller k.

When we consider a Gaussian beam of finite half width σ incident on a spherical interface, curvature does not only enter by changing the effective angle of incidence from χ to χ' due to the Goos-Hänchen effect. In addition, a beam of finite extent *directly* experiences a certain range of angles of incidence that have to be integrated over[3], see Fig. 8.3.

In Figs. 8.4 and 8.5 we present the results of this Goos-Hänchen effect based approach. We find a very good agreement with the exact results obtained within the sequential model. Hence, we conclude that the *Goos-Hänchen effect* provides the desired qualitative and quantitative *extension* of the *ray picture for spherical interfaces.*

Eventually we comment on the relation between Gaussian beams and the exact wave picture solutions for the dielectric disk that are given in terms of Bessel functions, see Section 7.2. One can think of establishing a direct relation between Bessel functions and a Gaussian beam by adjusting the (wave front) parameters of the Gaussian beam according to the contour lines of the Bessel function. However, the results presented in Figs. 8.4 and 8.5 indicate that simply assuming a beam width of the order of one wavelength gives already very reasonable results, that furthermore depend only slightly on the precise width chosen. Consequently, the exact connection to Bessel functions is not necessary and would, furthermore, be in no relation to the approximations involved so far.

We conclude this section by briefly discussing the implications of a disk of refractive index $n < 1$. Then we have to apply the Goos-Hänchen effect to a light ray coming from *outside* the disk. This ray will appear to be reflected at a sphere of *smaller* radius and, accordingly, the angle of incidence at this effective sphere is larger than the original angle χ. To obtain a consistent picture, rays *inside* the disk have to be reflected at this effective sphere as well, which implies an increased angle of incidence. This behaviour is opposite to that for the optically

---

[3] This spread in the angles of incidence at a *planar* interface originally gave rise to the Goos-Hänchen effect, in particular to Eq. (8.3). However, for a spherical interface the distribution of angles will be different. In the simplest effective model we take this into account by integrating over all angles of incidence occurring for a given beam width. Each contribution is weighted according to the Gaussian beam profile.

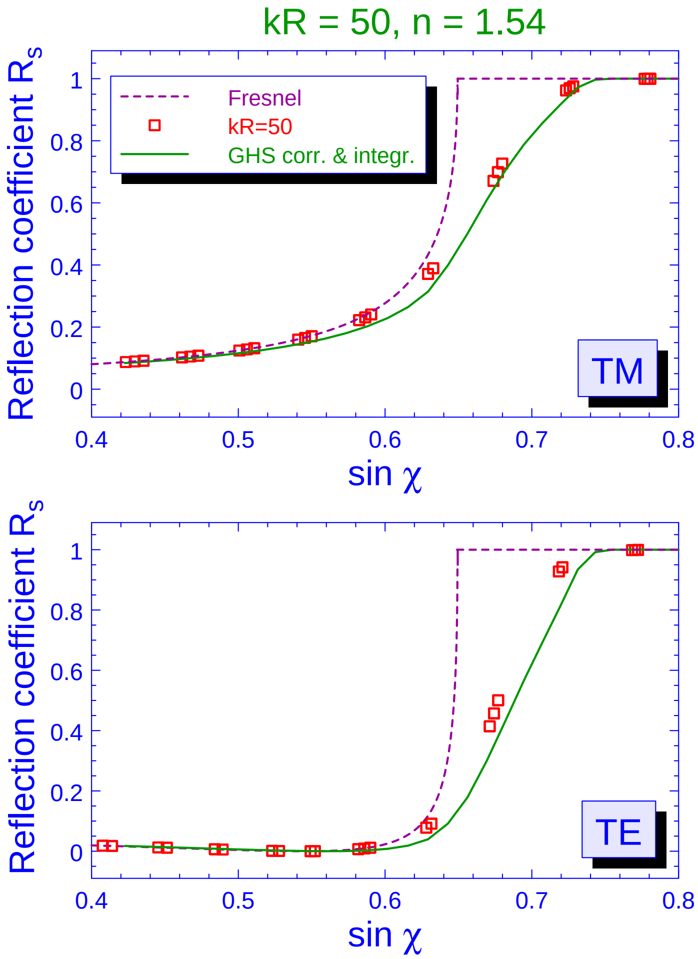

Figure 8.4: Goos-Hänchen-shift corrected and integrated Fresnel coefficient at a curved interface for kR=50 for a Gaussian beam of half width $\lambda/\sqrt{2} = \sqrt{2}\pi/nk$. The squares denote the numerical results for kR from Eqs. (7.32, 7.36) with real part close to 50 and the imaginary part (resonance width) expressed as reflection coefficient via the sequential reflection model, cf. Eq. (7.62). The approximations under which Eq. (8.3) was derived are not fulfilled for TE polarized light of this wavelength. Therefore, for the TM result, $R_s(\chi)$, we computed the angle $\bar{\chi}$ such that the Fresnel law gives the same value, $R_s(\chi) = R^{\mathrm{TM}}(\bar{\chi})$. The corrected TE reflection coefficient at the angle χ is now presumed to be $R^{\mathrm{TE}}(\bar{\chi})$, where $\bar{\chi} = \arccos\sqrt{(1/n^2-1)/[(1-\sqrt{R(\chi)})^2/(1+\sqrt{R(\chi)})^2-1]}$.

denser disk discussed above. It is in perfect qualitative agreement with the numerical results shown in Fig. 7.16.

The concept that both rays inside and outside the disk are reflected at an effective spherical interface larger ($n > 1$) or smaller ($n < 1$) than the real disk was used for example in [125] to explain qualitatively the spacing of morphology-dependent resonances in experiments with dielectric spheres. In [125], the penetration depth near total internal reflection is increased due to the Goos-Hänchen effect, leading to an increase in the round-trip optical path length.

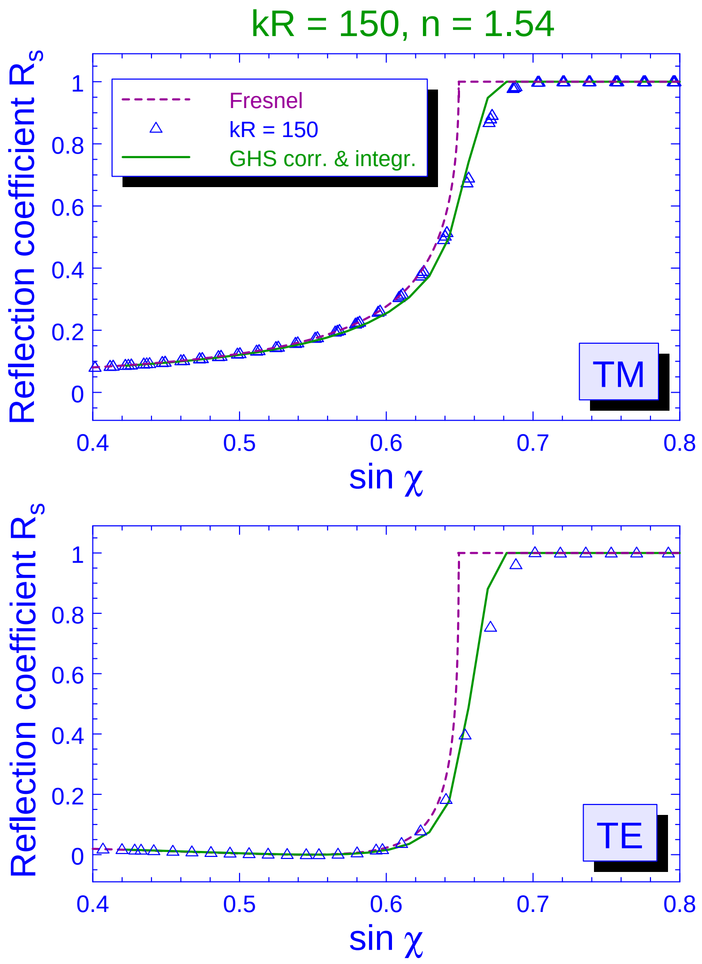

Figure 8.5: Same as Fig. 8.4 but for a wave vector $kR = 150$. As there, the integration procedure is carried out w.r.t. the effective interface, i.e., the sphere of radius $R' > R$.

Therefore, the effective optical size of the cavity is larger than its physical size, explaining the observed decrease in mode spacing.

Another interesting aspect of the Goos-Hänchen effect was investigated in [126] in the classical and quantum-mechanical scattering by a radially symmetric potential. It was found that incorporation of the Goos-Hänchen effect in the classical deflection function leads to an improvement over the classical result for, e.g., the cross section. In this section we confirmed this improvement for Fresnel reflection coefficients [128].

8.2 Description of narrow resonances in the wave picture

In the previous section, we employed a ray-based approach to account for the difference between Fresnel's reflections coefficients for planar and curved interfaces. The *exact* results for curved interfaces are obtained within the sequential reflection model, see Section 7.4 and the results shown in Figs. 7.14, 7.15. They are based on the *numerical* solution of the implicit Eqs. (7.32, 7.36) for the complex wave vectors of resonant states of the open system that were derived in

Section 7.2. For practical purposes like modelling microcavities it is, however, desirable to have an *analytical* expression for the resonance width if the resonance energy is given. In particular, this implies that an expression for the resonance width as function of a *continuous* energy variable is desirable. In terms of mathematics, this requires a kind of (smooth) interpolation between the discrete solutions, and leads to a different problem that *substitutes* the original one. The remaining part of this section is devoted to this problem.

A first possibility to obtain an analytical expression for the width y of *narrow* resonances is to expand Eqs. (7.32, 7.36) for small y. Applying the recursion formulas (7.34) for Bessel functions [56] leads to Eqs. (7.35, 7.37). For TM polarized light these equations read

$$nJ_{m-1}(nkR)H_m^{(1)}(kR) - J_m(nkR)H_{m-1}^{(1)}(kR) = 0\,, \tag{8.6}$$

and for TE polarized light we have

$$nJ_m(nkR)H_{m-1}^{(1)}(kR) - J_{m-1}(nkR)H_m^{(1)}(kR) = \frac{m}{kR}\left(n - \frac{1}{n}\right) J_m(nkR)H_m^{(1)}(kR)\,. \tag{8.7}$$

Note that in contrast to the TM case the rhs of Eq. (8.7) does *not* vanish, and on the lhs m and $m-1$ are interchanged. Expansion of Eq. (8.6) in $kR \overset{\text{def}}{=} x + iy$ to linear order in the resonance width $y \overset{\text{def}}{=} y_{\text{fl}}$ is straightforward and was performed in [108] for the TM situation[4]

$$iy_{\text{fl}}^{\text{TM}} = \frac{ac^2 + c + ad^2 + id}{(ac+1)^2 + a^2d^2}\,, \tag{8.8}$$

where

$$\begin{aligned} a &= \frac{1}{x}\,, \\ c &= \frac{1}{1-n^2}\left(\frac{J_{m-1}(x)J_m(x) + Y_{m-1}(x)Y_m(x)}{J_m^2(x) + Y_m^2(x)} - n\frac{J_{m-1}(nx)}{J_m(x)}\right)\,, \\ d &= \frac{1}{1-n^2}\,\frac{J_m(x)Y_{m-1}(x) - J_{m-1}(x)Y_m(x)}{J_m^2(x) + Y_m^2(x)}\,. \end{aligned}$$

For the case of TE polarized light we have to expand the more complex Eq. (8.7), resulting in

$$\begin{aligned} iy_{\text{fl}}^{\text{TE}} &= \frac{\frac{1}{x} + \frac{AC+BD}{A^2+B^2} - i\frac{AD+BC}{A^2+B^2}}{\left(\frac{1}{x} + \frac{AC+BD}{A^2+B^2}\right)^2 + \left(\frac{AD-BC}{A^2+B^2}\right)^2} \\ &= \frac{(A^2+B^2)\left(\frac{A^2+B^2}{x} + AC + BD - \mathrm{i}(AD-BC)\right)}{\left(\frac{A^2+B^2}{x} + AC + BD\right)^2 + (AD-BC)^2}\,, \end{aligned} \tag{8.9}$$

where

$$\begin{aligned} A &\overset{\text{def}}{=} J_{m-1}(nx)J_m(x) - nJ_m(nx)J_{m-1}(x) + \mathcal{A}J_m(nx)J_m(x) \\ B &\overset{\text{def}}{=} J_{m-1}(nx)Y_m(x) - nJ_m(nx)Y_{m-1}(x) + \mathcal{A}J_m(nx)Y_m(x) \\ C &\overset{\text{def}}{=} (n^2-1)J_{m-1}(nx)J_{m-1}(x) + 2\frac{m}{x}\mathcal{A}J_m(nx)J_m(x) \end{aligned}$$

---

[4] Note that iy_{fl} formally acquires a real part which can be understood as a correction to the resonance position x.

$$\begin{aligned} & -\mathcal{A}J_m(nx)J_{m-1}(x) - n\mathcal{A}J_{m-1}(nx)J_m(x) \\ D & \overset{\text{def}}{=} (n^2-1)J_{m-1}(nx)Y_{m-1}(x) + 2\frac{m}{x}\mathcal{A}J_m(nx)Y_m(x) \\ & -\mathcal{A}J_m(nx)Y_{m-1}(x) - n\mathcal{A}J_{m-1}(nx)Y_m(x) - \\ \mathcal{A} & \overset{\text{def}}{=} \frac{m}{x}\left(n - \frac{1}{n}\right) . \end{aligned}$$

These Eqs. (8.8, 8.9) can be either applied at a fixed quantum number m to yield the resonance width as a function of energy, or they are used to find the resonance width at fixed energy for increasing m, or $\sin\chi = m/(nkR)$, see Eq. (7.58). In the following figures we illustrate the latter dependence. In Eqs. (8.8, 8.9) we assumed y to be real which requires a purely imaginary rhs. This will only be fulfilled at true resonance positions, and leads to characteristic fluctuations of the calculated resonance width y_{fl} about the numerical values when only the imaginary part of the rhs is analyzed, see Fig. 8.6. In the vicinity of *exact* resonances possessing nearly the same x that is used for the evaluation of Eqs. (8.8, 8.9), the agreement is fully satisfying. The reason for the fluctuations in between the true resonance positions lies in the fact that the expansion condition of $y \ll x$ is not necessarily fulfilled there.

For TM polarized light one can additionally impose a consistency condition for the real part of the rhs in Eq. (8.8) [108] that in an effective manner cares for energy values that lie between the discrete solutions of Eq. (7.32). The result obtained in [108] can be further simplified to

$$y_{\text{sm}}^{\text{TM}} = \frac{2}{(1-n^2)\pi x}\frac{1}{J_m^2(x) + Y_m^2(x)} , \tag{8.10}$$

which provides indeed a smooth dependence of the resonance width on the energy between the discrete solution points. In the much more involved TE situation this procedure, however, fails.

The existence of angles of incidence where Eqs. (8.8, 8.9) yield obviously unphysical results is a drawback when one thinks about practical applications and one has to think about alternatives as we shall do in the following.

Another possibility [127] of dealing with Eqs. (8.6, 8.7) is to extract the ratio of the Bessel functions by transforming them into the form

$$\frac{J_{m-1}(nkR)}{J_m(nkR)} = \frac{1}{n\frac{H_m^{(1)}(kR)}{H_{m-1}^{(1)}(kR)}} = \frac{1}{n}\frac{H_{m-1}^{(1)}(kR)}{H_m^{(1)}(kR)} \tag{8.11}$$

for TM polarized light, and into

$$\frac{J_m(nkR)}{J_{m-1}(nkR)} = \frac{1}{n\frac{H_{m-1}^{(1)}(kR)}{H_m^{(1)}(kR)} - \frac{m}{kR}\left(n - \frac{1}{n}\right)} \tag{8.12}$$

if TE polarization applies, respectively. In both cases, the y-dependence of the rhs of Eqs. (8.11, 8.12) can be neglected to a very good approximation, see Fig. 8.7. Therefore, we evaluate the rhs at $y = 0$ and substitute the resulting value by $\sigma + i\tau$.

As a next approximation we rewrite the ratio of Bessel functions on the lhs of Eqs. (8.11, 8.12) using the Debye formula that is also refered to as approximation by tangents [56] for Bessel functions $J_m(nkR)$ which states

$$J_m\left(m\frac{nkR}{m}\right) = \sqrt{\frac{2}{\pi m \tan\beta^m}}\cos\left(m(\tan\beta^m - \beta^m) - \frac{\pi}{4}\right) , \tag{8.13}$$

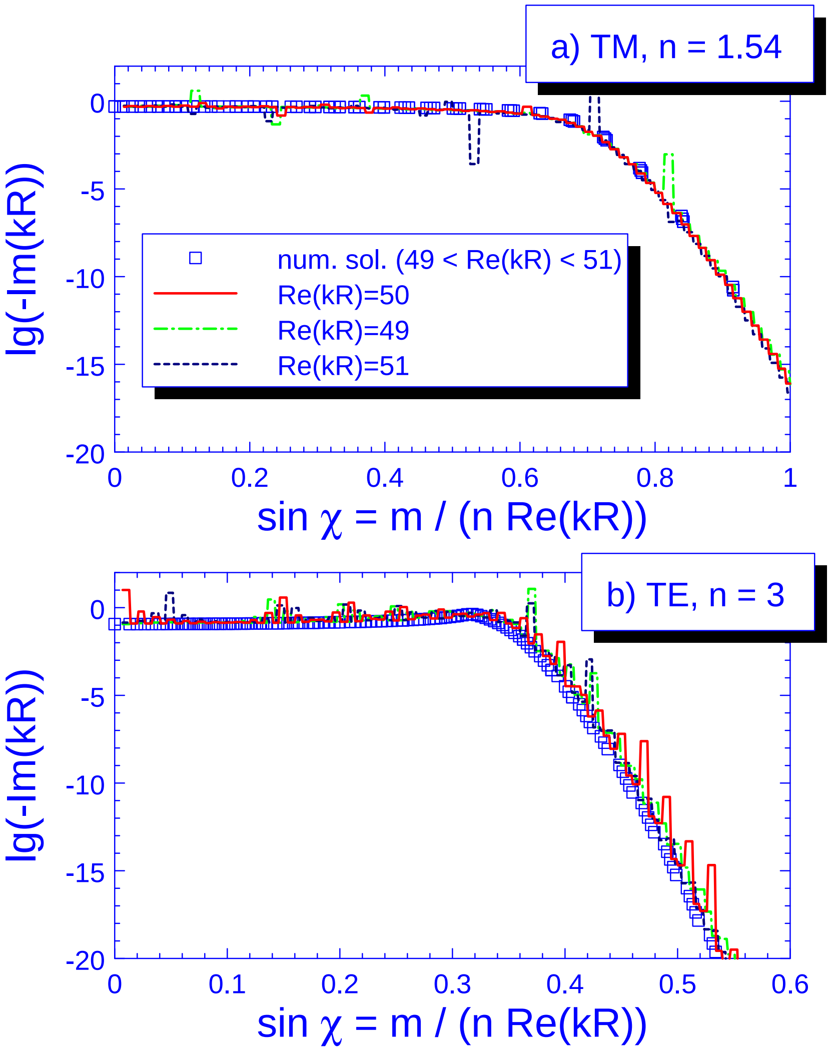

Figure 8.6: Comparison of exact and analytically determined resonance width y for a) TM and b) TE polarized light versus the angle of incidence deduced via the ray-wave correspondence. The squares denote the numerical solutions of Eqs. (7.32, 7.36) with real part in the interval $(49, 51)$. Since the resonance energy is kept approximately fixed, the x-axis shows the dependence on the angular momentum quantum number. The agreement between the numerical results (symbols) and Eqs. (8.8, 8.9) (lines) is very good if the condition under which Eqs. (8.8, 8.9) were derived is fulfilled, i.e., $\mathrm{Im}(kR) \ll \mathrm{Re}(kR)$. In between the discrete solutions of Eqs. (7.32, 7.36) this is not the case, giving rise to fluctuations. Consequently, the fluctuations depend on the value for which Eqs. (8.8, 8.9) are evaluated as is demonstrated for slightly different wave vectors $\mathrm{Re}(kR)$. Note also that the TM-resonance width is a monotonic function of $\sin\chi$ whereas a maximum is observed for the TE case. It corresponds to the Brewster angle introduced in Section 7.1.

where the angle β^m is provided by[5]

$$\frac{1}{\sin\chi} \equiv \frac{nkR}{m} \quad = \quad \sec\beta^m \equiv \frac{1}{\cos\beta^m}\,,$$

---

[5] Here and in the following we do not specify the real part of kR when confusion can be excluded.

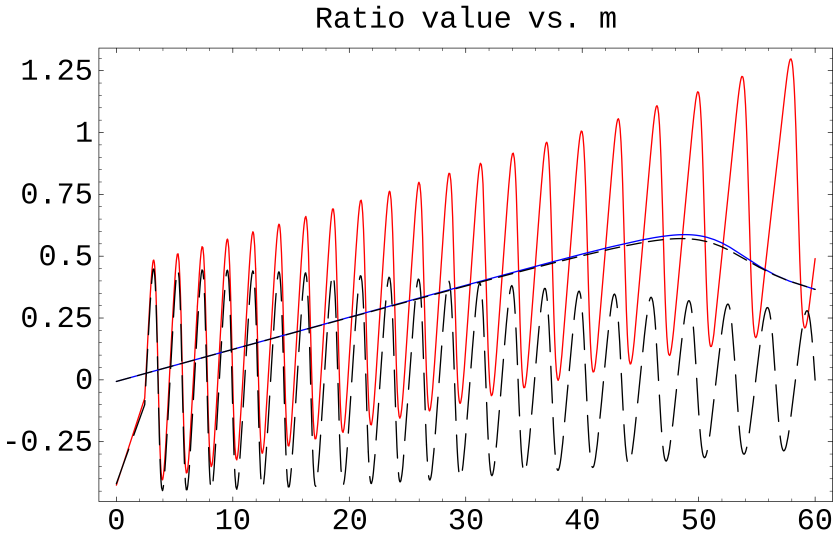

Figure 8.7: Limitations of the approximation of the ratios (8.11, 8.12) by the tangent for small refractive indices ($n = 1.54$). The monotonically increasing lines are the rhs of Eq. (8.12) evaluated at $kR = 50 - 0.5i$ (full line) and neglecting the imaginary part (dashed line) which proves to be a very good approximation. The full oscillating line is the lhs of Eq. (8.12), again evaluated at $kR = 50 - 0.5i$. Its approximation by the tangent is illustrated by the dashed oscillating line for the same kR. Whereas for $n > 2$ the two curves will (nearly) coincide, for smaller n there are deviations in the region $m \sim \mathrm{Re}(kR)$ that cause a failure of this approach.

$$\tan \beta^m = \sqrt{\frac{(nkR)^2}{m^2} - 1} \,. \tag{8.14}$$

We evaluate β^m using Eq. (8.14) in the form $\beta^m = \arctan(\cot \chi) = \chi - \pi/2$ up to 5th order in $\sin \chi$ to be

$$\beta^m = \frac{m}{nkR} + \frac{1}{6}\left(\frac{m}{nkR}\right)^3 + \frac{3}{40}\left(\frac{m}{nkR}\right)^5 - \frac{\pi}{2} \,. \tag{8.15}$$

Accordingly, we obtain for the ratio of the Bessel functions on the lhs of Eqs. (8.11) and (8.12), respectively,

$$\frac{J_m(nkR)}{J_{m-1}(nkR)} = \frac{\cos(\alpha^m - \frac{\pi}{2})}{\cos(\alpha^{m-1} - \frac{\pi}{2})} \,, \tag{8.16}$$

where α^m is given by

$$\begin{aligned} \alpha^m &= \sqrt{(nkR)^2 - m^2} + \frac{m^2}{nkR} + \frac{m}{6}\left(\frac{m}{nkR}\right)^3 + \frac{3m}{40}\left(\frac{m}{nkR}\right)^5 - m\frac{\pi}{2} + \frac{\pi}{2} - \frac{\pi}{4} \\ &\approx nkR\left(\sqrt{1 - \left(\frac{m}{nx}\right)^2} + \left(\frac{m}{nx}\right)^2 + \frac{1}{6}\left(\frac{m}{nx}\right)^4\right) - m\frac{\pi}{2} - \frac{\pi}{4} \,. \end{aligned} \tag{8.17}$$

In the last step we have neglected the 5th order term and made an expansion to linear order in nkR, or y, respectively.

Eq. (8.16) can be further simplified when approximating $\alpha^{m-1} \approx \alpha^m + \pi/2$. This will turn out to be inapplicable for small n ($n < 2$, say), and leads to wrong results in this regime, see Fig. 8.8. The reason for this is the (slight) difference in the arguments of the cosine functions in the numerator (α^m) and denominator (α^{m-1}). Consequently, when considered as a function of m, the real and imaginary part of the fraction do *not* need to be oscillating functions about the m-axis. Rather, their averaged values are allowed to possess an overall slope, see Fig. 8.7. In contrast to this behaviour, approximation by the tangent function leads to oscillations of both the real and imaginary part of the Bessel function ratio about the m-axis, corresponding to an average value of zero as is demonstrated in the same figure. Although neglecting the overall slope by performing the tangent approximation is a good approximation for $n > 2$, it fails for smaller n where the results presented below do not hold, see Fig. 8.8.

If we assume n to be not too small, we can approximate the Bessel function ratio (8.16) by the tangent and proceed further. Since we can obtain the TM result from the TE expression by interchanging m and $m-1$ and setting $\mathcal{A} = 0$ as discussed in the context of Eq. (8.7), we consider first TE polarized light and deduce the TM expression thereafter from symmetry considerations. Evaluating the rhs of Eq. (8.12) and using relation (8.16) yields

$$\frac{J_m(nkR)}{J_{m-1}(nkR)} \approx \tan\alpha^m \overset{\text{def}}{=} \sigma^{\text{TE}} + i\tau^{\text{TE}} , \tag{8.18}$$

with

$$\begin{aligned} \sigma^{\text{TE}} &= \frac{n(J_{m-1}(x)J_m(x) + Y_{m-1}(x)Y_m(x)) - \mathcal{A}(J_m(x)^2 + Y_m(x)^2)}{(nJ_{m-1}(x) - \mathcal{A}J_m(x))^2 + (nY_{m-1}(x) - \mathcal{A}Y_m(x))^2} , \\ \tau^{\text{TE}} &= \frac{n(J_{m-1}(x)Y_m(x) + Y_{m-1}(x)J_m(x))}{(nJ_{m-1}(x) - \mathcal{A}J_m(x))^2 + (nY_{m-1}(x) - \mathcal{A}Y_m(x))^2} \\ &\equiv -\frac{2n}{\pi x}\frac{1}{(nJ_{m-1}(x) - \mathcal{A}J_m(x))^2 + (nY_{m-1}(x) - \mathcal{A}Y_m(x))^2} . \end{aligned} \tag{8.19}$$

In the last step we used the relation $J_{m-1}(x)Y_m(x) + Y_{m-1}(x)J_m(x) = 2/(\pi x)$ [56]. Straightforward algebra and usage of Eq. (8.17) for the resonance width y yields[6]

$$\begin{aligned} ny\mathcal{F} &= \text{Im}\left[\arctan(\sigma + i\tau)\right] , \\ \mathcal{F} &= \sqrt{1 - \left(\frac{m}{nx}\right)^2 + \left(\frac{m}{nx}\right)^2 + \frac{1}{6}\left(\frac{m}{nx}\right)^4} . \end{aligned} \tag{8.20}$$

Using the relation $\arctan x = (1/2i)\ln\left[(1+ix)/(1-ix)\right]$, we obtain the final result for the resonance width of TE polarized light with a vacuum wave vector $x = \text{Re}\, kR$

$$y^{\text{TE}} = -\frac{1}{4n\mathcal{F}}\ln\frac{(1-\tau^{\text{TE}})^2 + \left(\sigma^{\text{TE}}\right)^2}{(1+\tau^{\text{TE}})^2 + \left(\sigma^{\text{TE}}\right)^2} , \tag{8.21}$$

where σ^{TE} and τ^{TE} are introduced in Eq. (8.19).

We now turn to the case of TM polarization. From Eq. (8.11) we obtain for sufficiently large n

$$\frac{J_{m-1}(nkR)}{J_m(nkR)} = \cot(\alpha^m) = -\tan\left(\alpha^m - \frac{\pi}{2}\right) \overset{\text{def}}{=} \sigma^{\text{TM}} + i\tau^{\text{TM}} , \tag{8.22}$$

where σ^{TM} and τ^{TM} are found from σ^{TE} and τ^{TE} by interchanging $m \leftrightarrow m-1$ and setting $\mathcal{A}' = 0$. Therefore,

$$\sigma^{\text{TM}} = \frac{J_{m-1}(x)J_m(x) + Y_{m-1}(x)Y_m(x)}{n(J_m^2(x) + Y_m^2(x))} , \tag{8.23}$$

---

[6] We are only interested in the relation for the imaginary part of kR. Taking into consideration the equation for the real part of kR, which would give a correction to the resonance energy, is beyond the scope of this work.

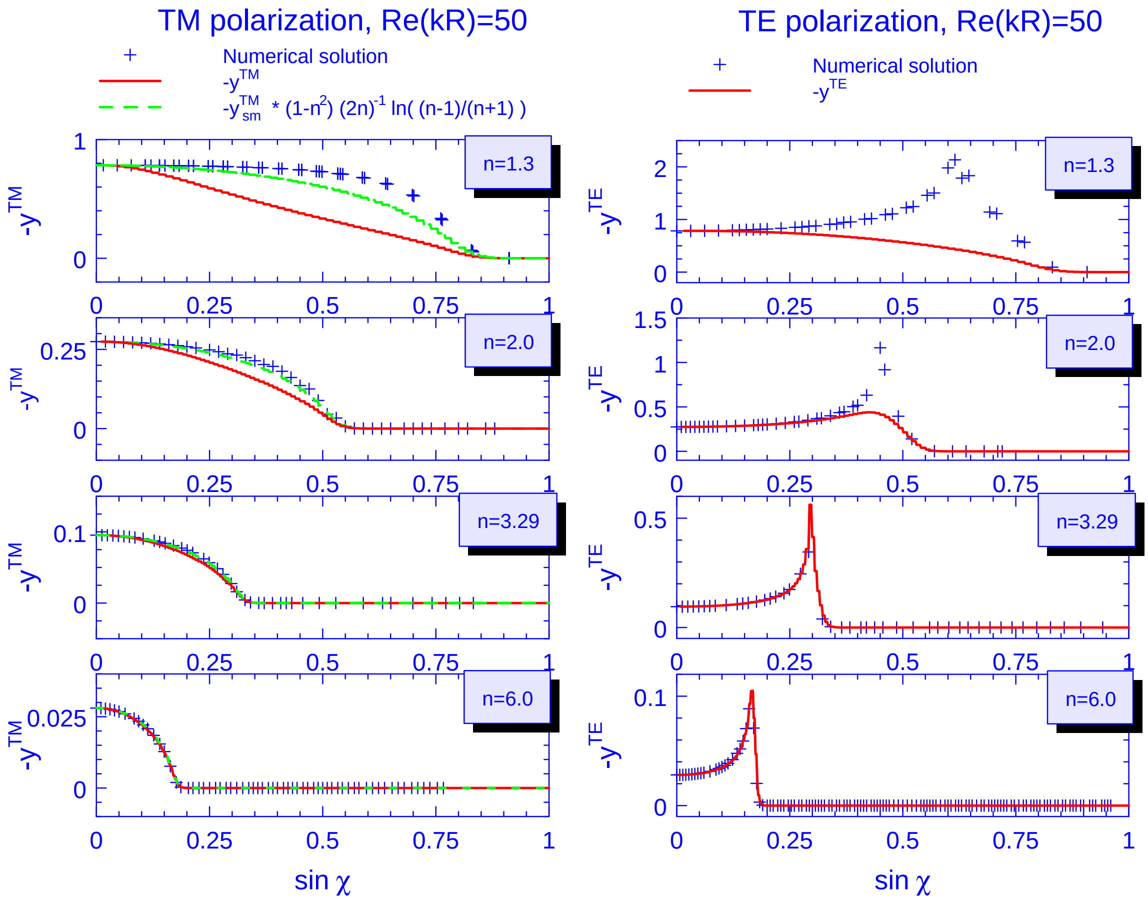

Figure 8.8: Analytically evaluated resonance widths $y^{\mathrm{TM}}, y^{\mathrm{TE}}$ (cf. Eqs. (8.21, 8.21), full lines) in comparison with the exact results (Eqs. (7.32, 7.36), crosses) for TM and TE polarized light. For $n > 3$, all curves coincide. However, the analytical expressions break down around $n = 2$ as discussed in the text. For TM polarization the result for $y_{\mathrm{sm}}^{\mathrm{TM}}$, modified by a phenomenological factor that ensures the right limiting behaviour [108] is also shown (dashed lines).

$$\begin{aligned}\tau^{\mathrm{TM}} &= -\frac{J_{m-1}(x)Y_m(x)+Y_{m-1}(x)J_m(x)}{n(J_m^2(x)+Y_m^2(x))} \\ &\equiv -\frac{2}{\pi n x}\frac{1}{J_m^2(x)+Y_m^2(x)} \,. \end{aligned} \tag{8.24}$$

To solve Eq. (8.22), we note that the change of $\pi/2$ in the argument w.r.t. the TE case does not affect the imaginary part, such that Eq. (8.21) applies now for $-y$, and we get the final result

$$y^{\mathrm{TM}} = \frac{1}{4n\mathcal{F}} \ln \frac{(1-\tau^{\mathrm{TM}})^2 + \left(\sigma^{\mathrm{TM}}\right)^2}{(1+\tau^{\mathrm{TM}})^2 + \left(\sigma^{\mathrm{TM}}\right)^2} \,. \tag{8.25}$$

Note that Eq. (8.10) can be rewritten in terms of σ, τ for n not too small ($1/(1-n^2) \approx -1/n^2$) as

$$y_{\mathrm{sm}}^{\mathrm{TM}} = \frac{\tau^{\mathrm{TM}}}{n} \,, \tag{8.26}$$

which is consistent with Eq. (8.21) in the limit $\tau \ll 1$, $\sigma \to 0$, and $\mathcal{F} \approx \infty$. This is immediately seen using the first-order expansion of $\ln[(1+x)/(1-x)] = 2x$. Again, applying Eq. (8.26) for $y_{\text{sm}}^{\text{TM}}$ to the case of TE polarized light fails to provide a smooth solution for y^{TE}, which underlines once more the significant analytical differences between TM and TE polarization.

In Fig. 8.8 we illustrate the results obtained by the tangent approximation. Apart from the failure for small n discussed above, the results agree very well with the numerical results, in particular for refractive indices relevant for semiconductor lasers ($n \approx 3.3$).

Summarizing this chapter we have derived new analytical expressions for Fresnel coefficients at curved interfaces that work well for $n > 2$; for $n < 2$ more careful approximations are in order. Furthermore, the results could be qualitatively and quantitatively explained in a novel ray-based model that was extended by the Goos-Hänchen effect as we saw in the previous section.

9 Ray-wave correspondence in the dielectric annular billiard

In this chapter we apply the methods outlined in Chapter 7 to the case of the *dielectric* annular billiard. We first study the ray dynamics in classical annular billiards with hard walls in terms of the Poincaré section. We generalize this approach to the *refractive* annular billiard by allowing light rays to enter the inner disk whenever the condition for total internal reflection is violated. Within the wave picture, we start our discussion with the case of the dielectric disk that we generalize by first placing another dielectric disk *concentrically* inside the system that is subsequently moved off the centre. We study the behaviour of resonances both in the delay time and in its Fourier transform. This allows us to identify the type of trajectory via its length. Besides a great variety whispering-gallery-type modes, we also find wave-mechanical realizations of other regular orbits. We study their signatures in the Poincaré section and their dependence on the ratio of the refractive indices that is used to control the openness of the system.

9.1 Classical and dielectric annular billiard: Ray picture

The system that we will consider in this chapter is shown in Fig. 9.1. Is consists of a (larger) dielectric disk of refractive index n_1 and radius R_1 in which a smaller disk (n_2, R_2) is eccentrically placed. The distance between the two disk centres is the eccentricity or displacement parameter δ. This system is embedded in air with n_0=1. Given a set of parameters $(n_0 \equiv 1, n_1, n_2)$, the same results hold for the scaled set $(\widetilde{n}_0, \widetilde{n}_1 = n_1\widetilde{n}_0, \widetilde{n}_2 = n_2\widetilde{n}_0)$ for wave vectors $\widetilde{k} = k/\widetilde{n}_0$, if the geometry is not changed. Concerning the geometry, a similar scaling applies. Fixing the dielectrica, the parameter sets $(R_1 \equiv 1, R_2, \delta)$ and $(\widetilde{R}_1, \widetilde{R}_2 = R_2\widetilde{R}_1, \widetilde{\delta} = \delta\widetilde{R}_1)$ are equivalent when $k \to \widetilde{k} = k/\widetilde{R}_1$.

The classical annular billiard, where the boundary of the inner and outer disk are hard walls that confine trajectories to the annular region, was studied by Bohigas [100]. Doron and Frischat investigated in particular the *doublet splitting* in the eccentric annular billiard in great detail [101]. We will comment on this effect in *open* systems below in the context of Fig. 9.11.

In the hard-wall systems [100, 101], the dielectric properties of the annular region do not play a role because refraction to other regions cannot occur. In the following we will, however, study open annular systems where refractive escape is allowed, and the confinement mechanism is provided by total internal reflection. The critical angle, Eq. (7.3), that distinguishes between total internal reflection and the possibility of refractive escape is determined from the ratio of the refractive indices of the dielectrica such that the relative material properties now become important.

In this section, we will study this interplay in terms of Poincaré sections, cf. Section 7.1. In Fig. 9.2 the Poincaré surface of section for a classical (hard wall) annular billiard ($R_2 = 0.6$, $\delta = 0.22$) is shown. We see a *mixed* phase space with several stability islands, typical representatives of which are shown on top and bottom illustrating the richness of the phase space. A major part of the phase space is taken by the so-called *chaotic sea* [75]. Near the values $\sin\chi = \pm 1$ we find the whispering gallery orbits.

Let us now address the question how to model and represent trajectories in a *dielectric* annular billiard. We will keep the *outer* boundary as a hard wall in order not to "loose" rays, but allow refractive coupling to the *inner* disk whenever the angle of incidence at the inner boundary is smaller than the critical angle for total internal reflection. Then the *full amplitude* shall enter the inner disk and there is no reflected ray. This assumption approximates Fresnel's law, Eqs. (7.4, 7.5), to a stepwise function. However, it has the great advantage to make things clear and to avoid an exponential increase of the number of rays involved. We will refer to this model as *refractive (annular) billiard.* The "real" situation will be somewhere in between the classical billiard where *each* ray is always reflected and the refractive billiard that neglects the reflection when refractive transmission is chosen. We will find that this combination is able to explain the wave-picture results very well in Section 9.3.

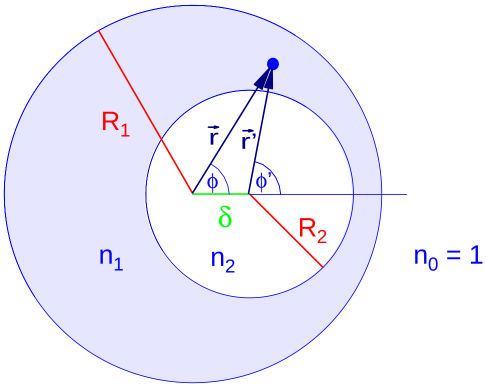

Figure 9.1: Geometry and notations in the dielectric annular billiard.

An example of the phase space of a refractive billiard is shown in Fig. 9.3. The parameters are the same as in Fig. 9.2, with the addition of refractive indices, $n_1 = 3$ in the annulus and $n_2 = 1$ in the inner disk, allowing for partial confinement in the annulus due to total internal reflection. The phase space[1] now possesses far less structure. Certain trajectories are lost because they are allowed to enter the inner disk which affects the orbit in a way that the trajectory cannot be closed any more. This applies in particular to orbits that hit the inner disk perpendicular clearly violating the condition for total internal reflection except for $n_1/n_2 \to \infty$ in which limit the classical annular billiard with hard walls is recovered. Indeed, we do not find those orbits represented in the phase space shown in Fig. 9.3. On the other hand, we find orbits that remain unchanged in comparison with the hard-wall situation. Besides the whispering gallery modes that are not at all affected by the inner disk (cf. Section 7.1.1), this applies to an orbit (Fig. 9.3 top right) that fulfills the condition of total internal reflection at the inner disk and, therefore, persits its refractive opening. Most interestingly, we discover a new type of *regular* orbit (Fig. 9.3 bottom right) the trajectory of which lies partly *within* the inner disk. Its appearance depends, of course, on the ratio of the refractive indices. For example, it is lost when increasing n_1 to higher values. The possibility to have regular trajectories that travel in both dielectrics is a new feature found in the phase-space structure.

In Section 9.3 we will discuss successes and limitations of the concepts outlined above in the context of the ray-wave correspondence in the dielectric annular billiard. In following Section 9.2 we firstly address the scattering approach to the annular billiard on which we will base the wave picture interpretation.

---

[1] As before the outer boundary is chosen as the surface of section.

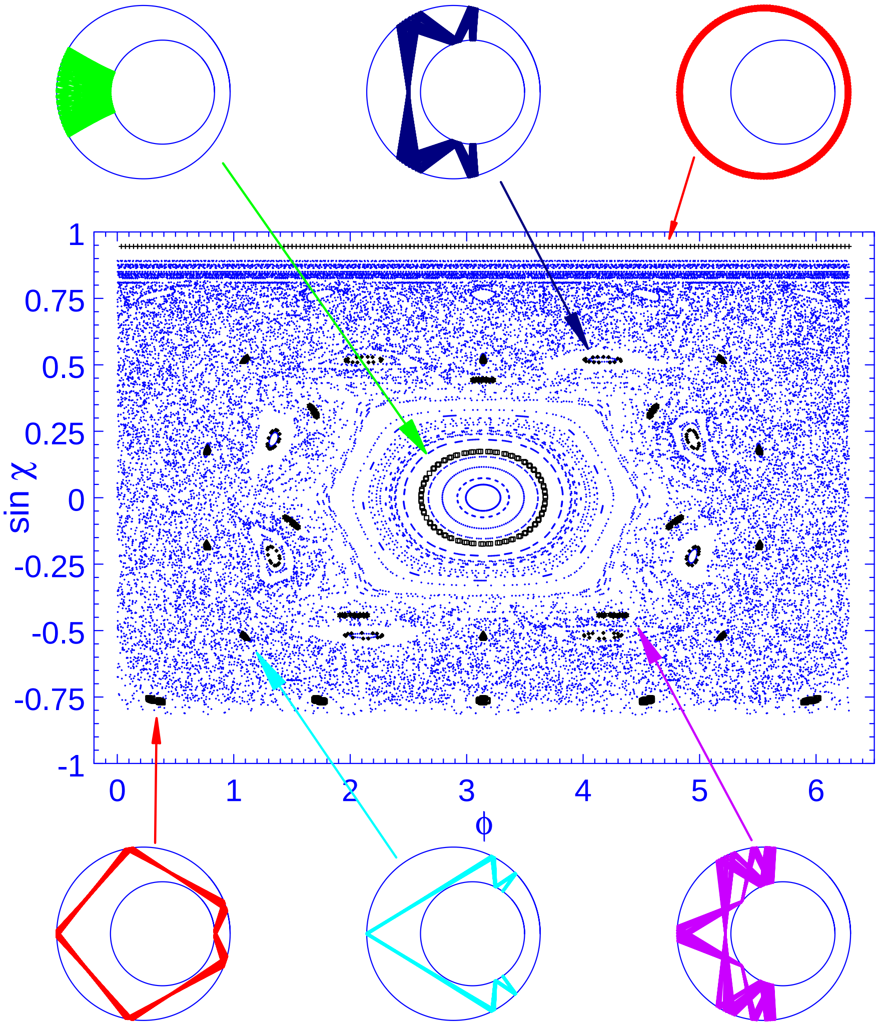

Figure 9.2: Poincaré section for the classical hard-wall annular billiard ($R_1 = 1, R_2 = 0.6, \delta = 0.22$) showing a highly structured mixed phase space. Typical representatives of stable orbits and the corresponding stable islands in phase space are shown on top and bottom.

9.2 Dielectric annular billiard in the wave picture

9.2.1 Scattering matrix

In this section we will generalize the ideas developed in Section 7.3 to the dielectric annular billiard in order to determine the S-matrix for the *eccentric* annular billiard. To this end, we start with an ansatz for the wave function for the (TM polarized) electric field Ψ. We will denote the three different regions by 0 (for the environment that is assumed to be air), 1 (for the annular region of refractive index n_1), and 2 (for the inner disk) to label the wave functions as well as the wave vectors that are $k_0, k_1 \overset{\text{def}}{=} n_1 k_0, k_2 \overset{\text{def}}{=} n_2 k_0$.

The problem of the S-matrix of the annular billiard can be divided into the scattering problem at the *outer* boundary (between refractive indices n_0 and n_1) and that at the *inner*

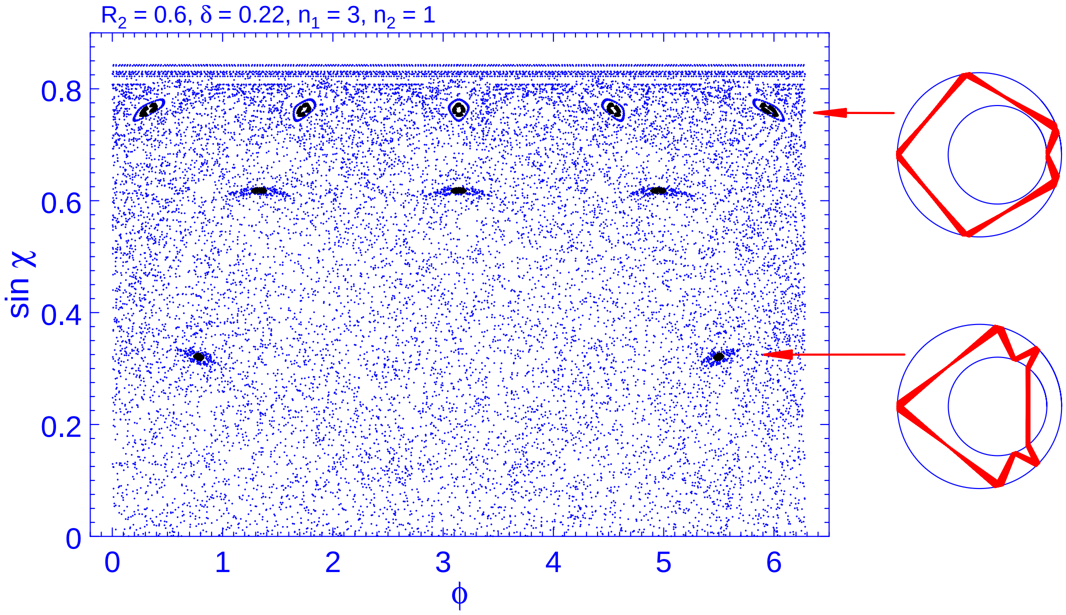

Figure 9.3: Poincaré section for the *refractive* annular billiard with the same geometry as in Fig. 9.2 and for refractive indices $n_1 = 3, n_2 = 1$. The part of phase space that is influenced by the refractive opening of the inner disk is completely re-structured. Whereas many regular orbits shown in Fig. 9.2 are lost, there is a new one (bottom right) that illustrates a new possibility for a periodic orbit that is inherent to the refractive billiard.

boundary (between refractive indices n_1 and n_2). Although the scattering at a dielectric disk was essentially solved in Section 7.3, the situation we are confronted with here is more complicated: first of all, the two disks lay one in the other, and, secondly, their centres will in general not coincide! We will begin with the scattering problem at the inner boundary and express the scattering matrix S^2 for the dielectric disk w.r.t. a coordinate system the origin of which does not coincide with the centre of the inner disk. This implies that the corresponding scattering matrix S^2 has *not only* entries along its diagonal. From Section 7.3 we already know the S-matrix of the inner disk w.r.t. *primed* coordinates, see Eq. (7.46),

$$S^{2c}_{ll'} = -\frac{H_l^{(2)\prime}(k_1 r') - n\frac{J_l'(nk_1 r')}{J_l(nk_1 r')} H_l^{(2)}(k_1 r')}{H_l^{(1)\prime}(k_1 r') - n\frac{J_l'(nk_1 r')}{J_l(nk_1 r')} H_l^{(1)}(k_1 r')} \delta_{ll'} \,, \tag{9.1}$$

and will now derive the relation between the (diagonal) S^{2c} and S^2. To this end we write the ansatz for the wave function in the annulus in *primed* coordinates, $\vec{r'} = \vec{r} - \vec{\delta}$, with $\vec{\delta}$ the vector from the centre of the large disk to the centre of the smaller disk, as

$$\Psi^{1c}(\vec{r} - \vec{\delta}) = \sum_{l=-\infty}^{\infty} a_l^c \left[H_l^{(2)}\left(k_1|\vec{r} - \vec{\delta}|\right) e^{il\phi} + \sum_{l'=-\infty}^{\infty} S^{2c}_{ll} H_{l'}^{(2)}\left(k_1|\vec{r} - \vec{\delta}|\right) e^{il'\phi} \right] \,, \tag{9.2}$$

where the coefficients a_l^c are to be chosen to yield the desired kind of incident wave. We use the

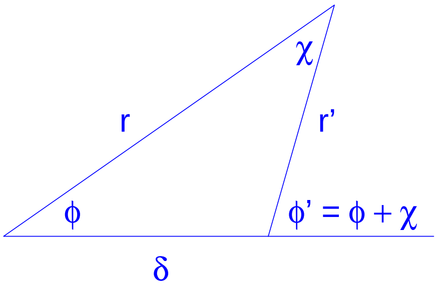

Figure 9.4: Addition theorem for Bessel functions.

addition theorem for Bessel functions[2] $Z_m \in \{J_m, Y_m, H_m^{(1)}, H_m^{(2)}\}$ to relate the arguments wr and wr' (w is a constant factor), see Fig. 9.4, [56]

$$Z_m(wr')e^{im\phi} = \sum_{k=-\infty}^{\infty} J_k(w\delta)Z_{m+k}(wr)e^{i(m+k)\phi} \, . \tag{9.3}$$

Inserting this into Eq. (9.2) we obtain the expression

$$\widetilde{\Psi}^1 = \sum_{l=-\infty}^{\infty} \sum_{k=-\infty}^{\infty} a_l^c \left[H_{l+k}^{(2)}(k_1 r) + S_{ll}^{2c} H_{l+k}^{(1)}(k_1 r) \right] \, J_k(k_1\delta) \, e^{i(l+k)\phi} \tag{9.4}$$

for the wave function in the annulus, now expressed w.r.t. the centre of the bigger disk, i.e., in unprimed coordinates. Now we specify the coefficients a_l^c by the requirement that the amplitude in front of an incident wave with angular momentum m shall be one in *unprimed* coordinates,

$$\sum_{l=-\infty}^{\infty} \sum_{k=-\infty}^{\infty} a_l^c H_{l+k}^{(2)}(k_1 r) J_k(k_1\delta) \, e^{i(l+k)\phi} \equiv H_m^{(2)}(k_1 r) \, e^{im\phi} \, . \tag{9.5}$$

With $\mu \overset{\text{def}}{=} l + k$, $l = \mu - k$, and using $\sum_k J_{m-(\mu-k)} J_k = \delta_{m\mu}$, we find that choosing

$$^{m}a_l^c = J_{m-l}(k_1\delta) \quad \forall l \tag{9.6}$$

provides a suitable set of coefficients *for a given m*. Accordingly, we write

$$\begin{aligned}
\widetilde{\Psi}^1 \; &= \; \sum_{m=-\infty}^{\infty} \left\{ \sum_{\mu,k=-\infty}^{\infty} \left[\delta_{m\mu} H_\mu^{(2)}(k_1 r) e^{i\mu\phi} + J_{m-(\mu-k)}(k_1\delta) S^{2c}_{(\mu-k)(\mu-k)} J_k(k_1\delta) H_\mu^{(1)}(k_1 r) e^{i\mu\phi} \right] \right\} \\
&\overset{\text{def}}{=} \; \sum_{m=-\infty}^{\infty} \left\{ H_m^{(2)}(k_1 r) e^{im\phi} + \sum_{\mu=-\infty}^{\infty} S^2_{m\mu} H_\mu^{(1)}(k_1 r) e^{i\mu\phi} \right\} \, ,
\end{aligned} \tag{9.7}$$

---

[2] The original form of this theorem reads [56]

$$Z_m(wr')e^{im\chi} = \sum_{k=-\infty}^{\infty} J_k(w\delta)Z_{m+k}(wr)e^{ik\phi}$$

for the general restriction $|\delta \exp(\pm i\phi)| < |r'|$ which is always fulfilled in the annular region if $R_2 > \delta$. If this is not the case, the addition theorem has to be applied in a modified form that we do not further consider here.

where we have read off the scattering matrix S^2 of the inner disk w.r.t. the centre of the big disk,

$$S^2_{m\mu} \stackrel{\text{def}}{=} \sum_{k=\infty}^{\infty} J_{m-(\mu-k)}(k_1\delta) S^{2c}_{(\mu-k)(\mu-k)} J_k(k_1\delta) \ . \tag{9.8}$$

The structure of this equation suggests a notation in terms of a transformation matrix U, namely $S^2 = U^{-1} S^{2c} U$, that describes the change of the origin of the coordinate system. Without going into the details of this approach, we read off $U_{l'l} = J_{l'-l}$ and $U^{-1}_{l'l} = J_{l-l'}$.

The scattering matrix S^2 allows us to describe the scattering at an off-centred disk, and we can now formulate the scattering problem of the annular billiard in the spirit of Section 7.3. Accordingly, we start with an ansatz for the wave function Ψ^0 outside the annular system ($|\vec{r}| > R_1$, using polar coordinates) in the form

$$\Psi^0(\vec{r}) = \sum_{M=-\infty}^{\infty} \Psi^0_M(\vec{r}) = \sum_{M=-\infty}^{\infty} \left[\Psi^-_M(k_0\vec{r}) + \sum_{M'=-\infty}^{\infty} S_{MM'} \Psi^+_{M'}(k_0\vec{r}) \right] \ , \tag{9.9}$$

where we have introduced the scattering matrix S of the (complete) system and the definitions

$$\begin{aligned} \Psi^-_M(k_0\vec{r}) &= H^{(2)}_M(k_0 r) e^{iM\phi} \ , & (9.10) \\ \Psi^+_M(k_0\vec{r}) &= H^{(1)}_M(k_0 r) e^{iM\phi} \ , & (9.11) \end{aligned}$$

for incoming and outgoing waves outside the disk. Note that we have used up here the freedom in fixing one of the amplitudes.

Similarly, we write for the wave function Ψ^1 in the annular region

$$\Psi^1(\vec{r}) = \sum_{l=-\infty}^{\infty} a_l \left[\Psi^-_l(k_1\vec{r}) + \sum_{l'=-\infty}^{\infty} S^2_{ll'} \Psi^+_{l'}(k_1\vec{r}) \right] \ , \tag{9.12}$$

with the amplitudes a_l, the abbreviations as in Eqs. (9.10, 9.11), and S^2 from Eq. (9.8).

Now, we determine S from the matching conditions[3] that require for continuity of the wave function itself as well as their derivative. To this end we introduce the notation of capital letters for functions of argument $k_0 r$ and reserve lower case characters for the argument $k_1 r$. Given an incident wave of angular momentum M, wave function matching for each angular momentum L in the scattered bunch yields

$$H^{(2)}_M e^{iM\phi} \delta_{ML} + S_{ML} H^{(1)}_L e^{iL\phi} = a^{(M)}_L h^{(2)}_L e^{iL\phi} + \sum_{l=-\infty}^{\infty} a^{(M)}_l S^2_{lL} h^{(1)}_L e^{iL\phi} \ , \tag{9.13}$$

where we point out that the amplitudes $a^{(M)}_j$ are now coefficients associated with an incoming function of angular momentum M, namely $H^{(2)}_M$. Since this has to hold for all M and at fixed M for all L, we write this as a matrix equation

$$\langle^{(M)} H^{(2)}| + \langle S^{(M)}| H^{(1)} = \langle a^{(M)}| \left(h^{(2)} + S^2 h^{(1)} \right) \ , \tag{9.14}$$

where S^2 is a matrix, $h^{(2)}$ and $h^{(1)}$ are diagonal matrices, $h^{(1,2)}_{lj} = h^{(1,2)}_l \delta_{lj}$, and we adopt the *bra*-notation for quantities that, at fixed M, are transposed vectors and gain matrix character once M is varied. With this notation we immediately write the matching condition for the derivatives as

---

[3] Note that Ψ stands for the electric field, see Chapter 7, and the matching conditions arise as a consequence of Maxwell's equations.

$$k_0 \left(\langle {}^{(M)}H'^{(2)}| + \langle S^{(M)}|H'^{(1)} \right) = \langle a^{(M)}| k_1 \left(h'^{(2)} + S^2 h'^{(1)} \right) . \tag{9.15}$$

From Eq. (9.14) we find after substituting $F \overset{\text{def}}{=} h^{(2)} + S^2 h^{(1)}$ that

$$\langle a^{(M)}| = \left(\langle {}^{(M)}H^{(2)}| + \langle S^{(M)}|H^{(1)} \right) F^{-1} . \tag{9.16}$$

Introducing furthermore $F' \overset{\text{def}}{=} h'^{(2)} + S^2 h'^{(1)}$ and $W \overset{\text{def}}{=} F^{-1}F'$, we write the S-matrix as the solution of the problem as

$$S = \left(k_1\, H^{(2)}\, W - k_0\, H'^{(2)} \right) \left(k_0\, H'^{(1)} - k_1\, H^{(1)}\, W \right)^{-1} . \tag{9.17}$$

This last equation allows us to apply the Wigner-delay-time approach to resonances, cf. Section 7.3.2, and we will study resonance signatures in the delay time $\tau(k_0)$ in the following. We recall that $\tau(k_0)$ is proportional to the derivative of the phase of $\det S$ w.r.t. the wave vector k_0, see Eq. (7.49).

Before we discuss the results in the remaining part of this chapter, we complete the discussion here with some comments on the wave functions. First of all, we have not given the wave function in the inner disk so far. The ansatz is as usual a sum of Bessel functions,

$$\Psi^{2c}(\vec{r'}) = \sum_{l=-\infty}^{\infty} b_l^c J_l(k_2 r') e^{il\phi'} , \tag{9.18}$$

where we adopted primed coordinates for convenience. The coefficients b_l are found from matching with the wave function in the annulus at the *inner* boundary. To this end, we have to rewrite the annular wave function (9.12) in terms of primed coordinates by applying the addition theorem (9.3) for Bessel functions. After straightforward algebra we find

$$\Psi^{1c}(\vec{r'}) = \sum_{l=-\infty}^{\infty} a_l^c \left[H_l^{(2)}(k_1 r') + S_{ll}^{2c} H_l^{(1)}(k_1 r') \right] e^{il\phi'} , \tag{9.19}$$

where the coefficients a_l^c are related to the a_l by

$$a_l^c = \sum_{l'=-\infty}^{\infty} a_{l'} J_{l'-l} \overset{\text{def}}{=} \langle a|U . \tag{9.20}$$

Another remark is in order concerning the validity of the addition-theorem-based expansion of the Bessel function when changing between primed and unprimed coordinates. For example, expansion of the annular wave function in *primed* coordinates fails near the outer boundary where $|\vec{r'}| > R_1 - R_2 - \delta$. Similarly, expanding the annular wave function in *unprimed* coordinates does not work near the inner boundary where $|\vec{r}| < R_2 + \delta$. The reason for this behaviour is that angular momentum is not conserved in the eccentric annular billiard; and the expansion breaks down at radii where this is "noticed" by the waves because interface boundaries are hit.

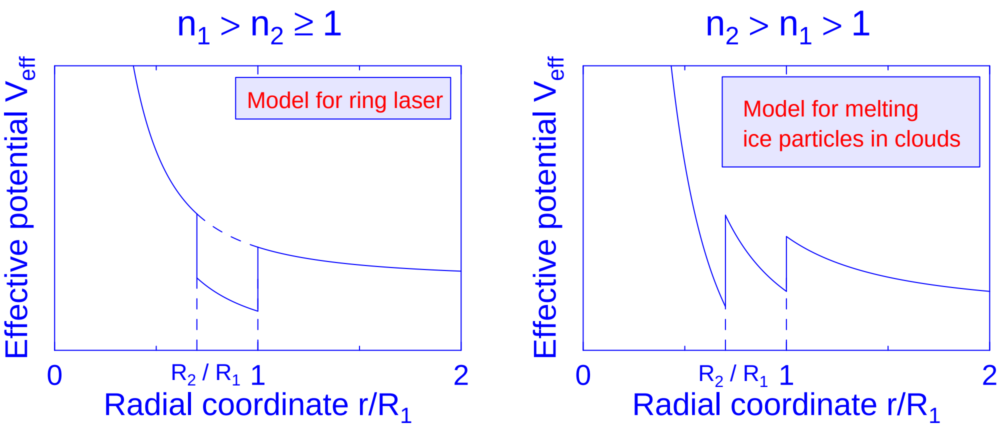

Figure 9.5: Effective potential for the concentric annular billiard. Assuming air outside, the two principal situations shown above are possible according to whether the refractive index in the annulus is highest ($n_1 > n_2 \geq n_0 \equiv 1$, left) or the refractive index of the inner disk ($n_2 > n_1 > n_0 \equiv 1$, right). In comparison with the disk (Fig. 7.6), in the first case the potential well is broadened whereas the latter case results in a double-well structure. Prominent examples are ring lasers and melting ice particles in clouds [106], respectively. Note that in the eccentric situation the position of the inner discontinuity varies as a function of the polar angle ϕ.

9.2.2 Concentric case and exact solution

In the concentric annular billiard, angular momentum is conserved due to rotational symmetry and provides a good quantum number. In this special situation we can find an exact solution in terms of the wave picture developed in Section 7.2. The basis for interpretation of these quasibound states, characterized by a complex wave number, is again the effective potential picture outlined there [see Eq. (7.16)]. The new aspect in the case of the annular billiard is that the refractive index changes *twice* discontinuously, giving rise to

$$V_{\mathrm{eff}}(r) = \begin{cases} k_0^2(1-n_1^2) + \frac{m^2}{r^2} & \text{if } R_2 < r < R_1 \\ k_0^2(n_1^2-n_2^2) + \frac{m^2}{r^2} & \text{if } r < R_2\,. \end{cases} \tag{9.21}$$

The resulting two principal possibilities are shown in Fig. 9.5. In the situation of $n_1 > n_2 \geq n_0 \equiv 1$, a potential well is formed in the annular region. In eccentric geometries, its size varies as the polar angle ϕ is followed. In terms of the ray picture, confinement on either side of the well is provided by total internal reflection; quantum mechanically, tunnelling escape is possible.

For $n_2 > n_1 > n_0 \equiv 1$, a double-well structure arises. The relative depth of the wells depends on the ratio of the refractive indices as well as on the ratio of the radii, R_2/R_1. In this situation, quasibound states might be localized in the left *or* in the right well, corresponding to whispering gallery modes of the inner and outer disk, respectively. Note that *locally* each of the wells corresponds to the potential we know from the dielectric disk, see Chapter 7. However, identifying the subsystem of the inner disk with the system of a (single) dielectric disk oversimplifies the situation in general since it neglects the effect of the second well. This is in particular not justified if the outer well dominates the structure of the potential.

Many resonant states will, however, be supported by *both* wells, and we will give an ray-model based explanation and examples below, cf. e.g. Fig. 9.8. In general, the number of resonant states is increased when the refractive indices give rise to a double-well structure of the effective potential as we shall see below.

The concentric case allows for an exact solution of Maxwell's equations, i.e., the matching conditions result in a complex equation the solutions of which are the complex wave vectors of quasibound states. Straightforward evaluation of the boundary conditions for the value and the derivative of the wave function, performed at the inner and the outer boundary, gives for TM polarized light

$$\begin{aligned} 0 \;=\; & n_1 J_m(k_2R_2){H'_m}^{(1)}(k_0R_1)\left[{H'_m}^{(2)}(k_1R_2)H_m^{(1)}(k_1R_1) - {H'_m}^{(1)}(k_1R_2)H_m^{(2)}(k_1R_1)\right] \\ & -n_1^2 J_m(k_2R_2)H_m^{(1)}(k_0R_1)\left[{H'_m}^{(2)}(k_1R_2){H'_m}^{(1)}(k_1R_1) - {H'_m}^{(1)}(k_1R_2){H'_m}^{(2)}(k_1R_1)\right] \\ & -n_2 J'_m(k_2R_2){H'_m}^{(1)}(k_0R_1)\left[H_m^{(2)}(k_1R_2)H_m^{(1)}(k_1R_1) - H_m^{(1)}(k_1R_2)H_m^{(2)}(k_1R_1)\right] \\ & +n_1 n_2 J'_m(k_2R_2)H_m^{(1)}(k_0R_1)\left[H_m^{(2)}(k_1R_2){H'_m}^{(1)}(k_1R_1) - H_m^{(1)}(k_1R_2){H'_m}^{(2)}(k_1R_1)\right] \end{aligned} \quad (9.22)$$

as the desired equation ($R_2 > 0$). Note that Eq. (9.22) reduces to Eq. (7.32) for $n_1 = n_2$ as expected for the situation in which the annular billiard reduces to the dielectric disk.

In Fig. 9.6 we compare the results obtained for the delay time $\tau(k_0)$ in the scattering matrix formalism, Eqs. (9.17, 7.49), with the exact solutions, Eq. (9.22). We start with the situation $n_1 = n_2$, i.e., the dielectric disk (solid line in Fig. 9.6). If we now turn to the concentric annular billiard, we find a systematic deviation of the resonance position to the right (left) if the refractive index of the inner disk is lower (higher) than that in the annulus. The fact that all three resonances are rather close to each other suggests that the resonances in the annular geometry are similar to those for the dielectric disk and mainly localized at the *outer* boundary, see Fig. 7.9. However, the resonant wave function *do* experience the change of the refractive index in the inner disk as indicated by the shift in the position. The direction of the shift is most easily seen when thinking in terms of an *effective* refractive index n_{eff},

$$n_{\text{eff}} \overset{\text{def}}{=} \left(1 - \frac{R_2^2}{R_1^2}\right) n_1 + \frac{R_2^2}{R_1^2} n_2 \,. \quad (9.23)$$

An inner disk of lower refractive implies $n_{\text{eff}} < n_1$ and a larger spacing in the resonances as is clearest seen when going back to the closed dielectric disk and noting that eigenvalues are defined by $nk \overset{\text{def}}{=}$ const. $\equiv$ zero of Bessel function, see Eq. (7.22). Obtaining the same constant value for a smaller n requires a higher k. In contrast, an inner disk of higher refractive index reduces the spacing between the resonances. Note that this effect is strongest for resonances of small angular momentum quantum number m since they do extend to the inner regions of the disk or the annular billiard[4], respectively. Accordingly, the effect reduces for increasing m and eventually vanishes if the inner disk is not seen any more. This behaviour is clearly seen in Figs. 9.6 and 9.7. In the latter plot, we start from the dielectric disk of refractive index $n_1 = 6$. Then we consider the annular situation with $n_2 = 5$ and increase the radius R_2 of the inner

---

[4] In terms of the ray picture, they correspond to smaller angles of incidence, leading to the same conclusion.

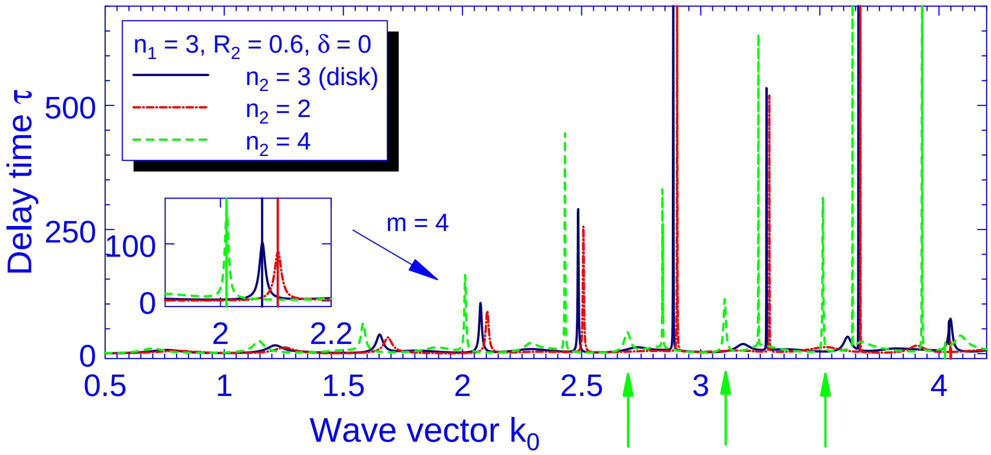

Figure 9.6: Resonances in the concentric annular billiard ($R_1 = 1, R_2 = 0.6, n_1 = 3$), essentially corresponding to the first family of whispering gallery modes. The “real” annular situations $n_2 = 2$ (dash-dot) and $n_2 = 4$ (dashed) are contrasted to the homogeneous disk $n_2 = 3$. Note the systematic deviation of the resonance position to larger (smaller) wave vectors for $n_2 = 2$ ($n_2 = 4$) that decreases with increasing angular momentum quantum number m since the inner disk becomes less important there. In the inset, we compare the properties of a peak in the delay time with the exact wave vector according to Eq. (9.22) for the resonances to $m = 4$. We find excellent agreement with the exact values $k_0 = 2.0108 - 0.0041i$ ($n_2 = 4$), $k_0 = 2.0753 - 0.0063i$ ($n_2 = 3$), and $k_0 = 2.1035 - 0.0075i$ ($n_2 = 2$). Note the existence of additional resonances for $n_2 = 4$, some of them marked by arrows from below. They are due to the double-well structure of the effective potential, see text.

disk. The impact of the inner disk is systematically enhanced, leading to deviations from the homogeneous system case.

Another feature in Fig. 9.6 is the emergence of a family of resonances exclusively for the case of a higher refractive index of the inner disk. The explanation of this effect lies in the corresponding double-well structure of the effective potential (see Fig. 9.5), originating from the jump in the refractive index at the inner disk. This structure allows for states in the outer (annular) well *and* in the inner well and for combinations of the two. One example of such a quasibound state with a corresponding trajectory in the ray picture is shown in Fig. 9.8 for the central arrow in Fig. 9.6. This family of resonances shows the characteristics discussed for whispering gallery modes in the context of Chapter 7. However, the ray picture suggests another type of dynamics for this orbit in the sense that the rays travel through the inner disk between two bounces at the outer boundary and simultaneously form the (whispering-gallery-type) pattern at the outer and inner boundary, see Fig. 9.8. A remark is necessary concerning the existence range of this family of orbits from the point of view of the ray picture. As we saw before (cf. Table 7.4), the angle of incidence increases corresponding to a sharpening of the resonance peak within each family of resonances. This implies, however, that we loose this family of states if the angle of incidence at the outer boundary becomes larger than $\arcsin(R_2/R_1)$, which defines the angle under which rays just *touch* the inner disk. This illustrates the rather

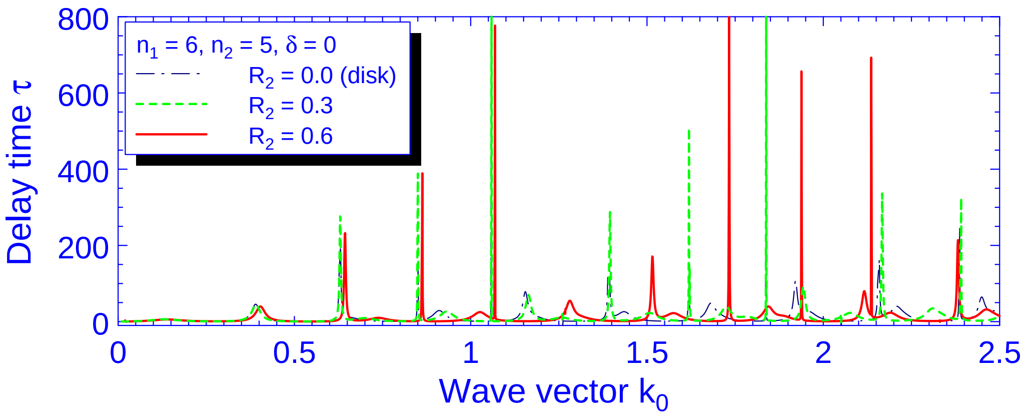

Figure 9.7: Influence of the inner disk on whispering gallery modes. We compare the dielectric disk (dash-dot) with concentric annular billiards of increasing radius R_2 of the inner disk ($n_1 = 6, n_2 = 5$). The resonance positions are increasingly affected, especially those of higher order families (radial quantum number $\rho > 1$) that extend further to the inner regions.

complicated interplay of the two disks already within the simple ray model. As for the wave picture, we can, therefore, expect subtle effects as well, initiated by the *double-well structure* of the effective potential. *For a given wave vector* k, the structure of V_{eff} directly reflects the chosen parametrization $(R_1, R_2, n_0, n_1, n_2)$ in terms of the relative width and depth of the both wells. Depending on the ratio of the refractive indices n_2/n_1 and on the ratio of the radii R_2/R_1, the peaks in the delay time correspond to whispering gallery modes of the inner or outer disk[5]. One possibility to obtain certainty about the kind of resonance corresponding to a particular peak is to check its sensitivity against a change of the parameters. For example, the resonance energy of whispering gallery modes of the *inner* disk are *less* sensitive against changes of the displacement δ than the position of whispering gallery modes at the outer boundary. The latter dependence is discussed in Section 9.2.3.

9.2.3 Eccentric case: Perturbation of whispering gallery modes

In this paragraph we briefly discuss the implications of an eccentrically placed inner disk. Our starting points are the dielectric disk and the concentric annular billiard studied in Section 9.2.2. As illustrated there, deviations of the refractive index n_2 of the inner disk from the value n_1 in the annulus cause (in general) a shift of corresponding resonance positions that we explained by means of an effective refractive index n_{eff}, see Eq. (9.23). For example, for $n_2 < n_1$ the resonance positions are shifted to higher wave vectors. In Fig. 9.9 we see that this effect is enhanced if the inner disk is shifted away from the centre. This can be understood by realizing that an eccentrically placed inner disk will affect the resonant mode in particular in the constricted region where the distance between inner and outer boundary is smallest. Therefore, an off-

---

[5] For example, in the concentric annular billiard with $R_2 = 0.6$, $n_1 = 3$, $n_2 = 4$ the first resonance peaks correspond to whispering gallery modes localized at the *outer* boundary, whereas for $n_2 = 6$ they are found in the *inner* disk.

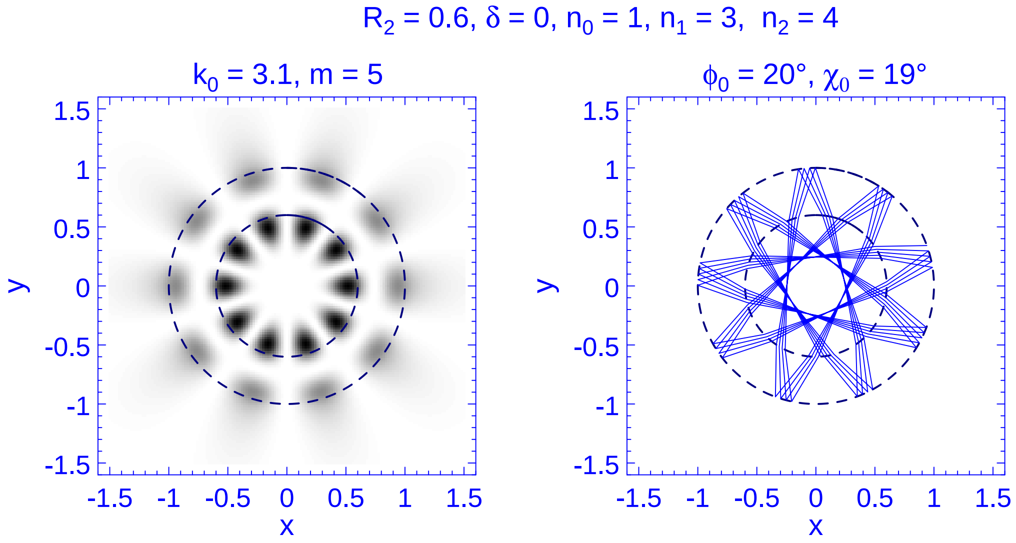

Figure 9.8: Wave intensity plot (left) for a state that is supported by both (concentric) disks and, therefore, is typical for the *dielectric* annular billiard. On the right a corresponding ray pattern is shown.

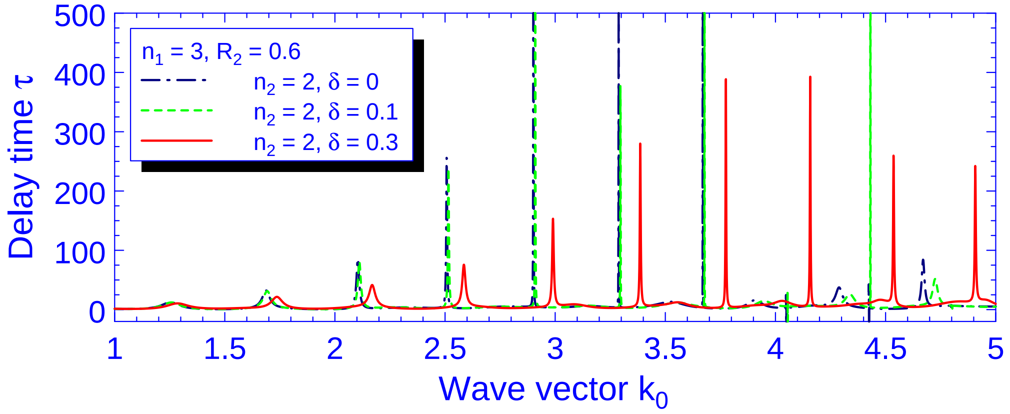

Figure 9.9: Resonance positions for increasing displacement δ in comparison with the concentric case (dash-dot) for an annular billiard with $n_2 < n_1$. Whispering gallery modes of the outer disk are increasingly shifted to higher wave vectors due to a decrease of the effective refractive index.

centred inner disk acts (locally) like a concentric inclusion with *larger radius* R_2^{eff}. This in turn gives rise to a decrease of the effective refractive index according to Eq. (9.23), and explains the observed behaviour for whispering gallery modes of the outer disk.

In Fig. 9.10 the same scenario is shown for an inner disk with higher refractive index, $n_2 > n_1$. Again, for the first resonances, corresponding to whispering gallery modes of the outer disk, we see an increasing shift with increasing displacement δ, in this case to the left. The explanation is as before. However, for the new family of resonances illustrated in Fig. 9.8, we observe the opposite behaviour for $\delta = 0.1$. This implies that for those modes the relative contribution from

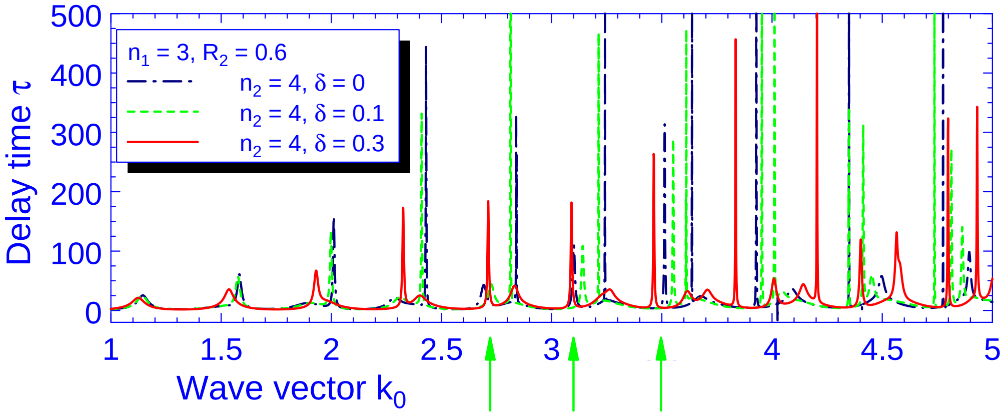

Figure 9.10: Resonance positions for increasing displacement δ in comparison with the concentric case (dash-dot) as in Fig. 9.10, but now for $n_2 > n_1$. Here, whispering gallery modes of the outer disk are increasingly shifted to the left due to an increase of the effective refractive index. However, other modes are affected in a different way, as for example the resonances marked by arrows as in Fig. 9.6 that belong to the family of resonances of the type in Fig. 9.8. In comparison with the concentric case, the resonance at $k_0 \approx 3.1$ is shifted to the right for $\delta = 0.1$, and shifted to the left for $\delta = 0.3$.

the annular region is enhanced with increasing displacement δ (in terms of the ray picture one would argue that the ratio of the ray paths in the annulus and in the inner disk, respectively, is shifted in favour of the annular region, the lower refractive index of which leads to a decrease of n_{eff}. However, we find this trend changed when we look at $\delta = 0.3$ where, moreover, resonances are shifted to the right (small m) *or* to the left (higher m) of the corresponding peaks in the concentric case, illustrating the limits of this simple picture.

Eventually, we give an example for a typical wave pattern of a whispering gallery mode that is slightly affected by the eccentric geometry, see Fig. 9.11. The correspondence to the ray model is evident as illustrated in Fig. 9.12. Note that both ray patterns were obtained with nearly the same initial conditions. Although their appearance is very different, they *both* have to be attributed wave patterns like the one in Fig. 9.11.

At this point a comment is in order concerning the well-studied doublet splitting in the eccentric annular billiard [101]. In the concentric annular billiard angular momentum doublets (states composed of angular momentum components m and $-m$) are degenerate in energy due to rotational invariance of the system. In the case of an eccentrically placed inner disk this symmetry is reduced to a reflection symmetry w.r.t. the x-axis, and the degeneracy is lifted. The exact quantum states have to be symmetric or antisymmetric under the corresponding symmetry operation and are just the even and odd parity states (symmetric and antisymmetric combination of angular momentum states to $\pm m$) introduced in Eq. (7.24). Since in the eccentric case the effective potential $V_{\text{eff}}(r)$ varies as a function of the polar angle ϕ, and even and odd parity states have different probability densities on the symmetry axis, see Fig. 9.11, we would expect the states in this figure to be *not* degenerate in energy. The reason that the doublet (tunnelling) splitting in energy is harder to observe in the *dielectric* annular billiard than in a

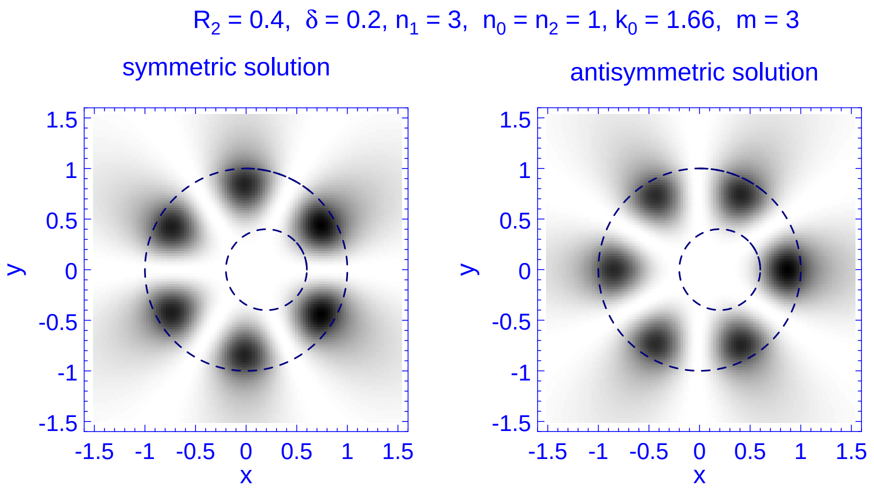

Figure 9.11: Symmetric and antisymmetric wave function for the annular billiard of $R_2 = 0.4$, $\delta = 0.2$, $n_1 = 3$, and $n_0 = n_2 = 1$. Shown is the first family mode with angular momentum $m = 3$ ($k_0 = 1.66$). Note the enhanced intensity in the constricted region of the annulus as expected from ray-model based considerations.

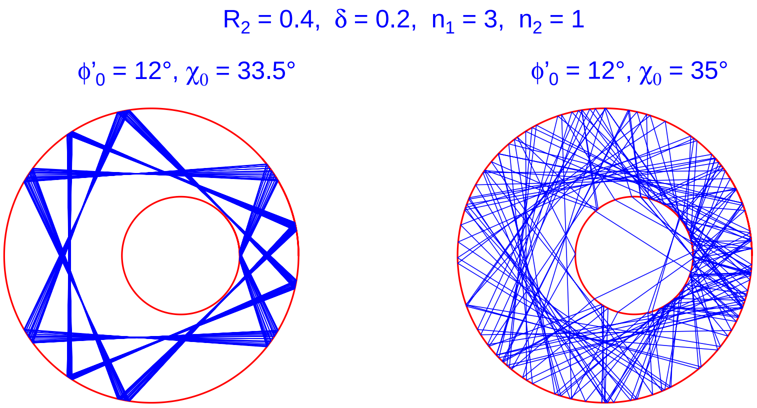

Figure 9.12: Perturbed whispering-gallery-type ray patterns in the refractive annular billiard $R_2 = 0.4$, $\delta = 0.2$, $n_1 = 3$, and $n_2 = 1$. The initial conditions are very similar for both trajectories. However, whereas the regular orbit (left) is localized on small islands that all fulfill the condition for total internal reflection, the chaotic trajectory (right) violates it a few times because it accesses regions in the Poincaré section where $|\sin\chi| < 1/n_1$. The density of rays in the constricted region of the annulus is enhanced.

closed system as in [101] lies in the possibility of tunnelling *escape* to the surroundings. This implies that for each resonance of the open system there is a competition between the *doublet splitting* and the *resonance width*. The latter is related to tunnelling escape from the annular system and to the outer barrier of the effective potential, cf. Fig. 9.5. The resulting width of the resonance can easily overwhelm the effect of the doublet splitting. This effect becomes especially clear when one *decreases* the width of the constricted region in order to enhance

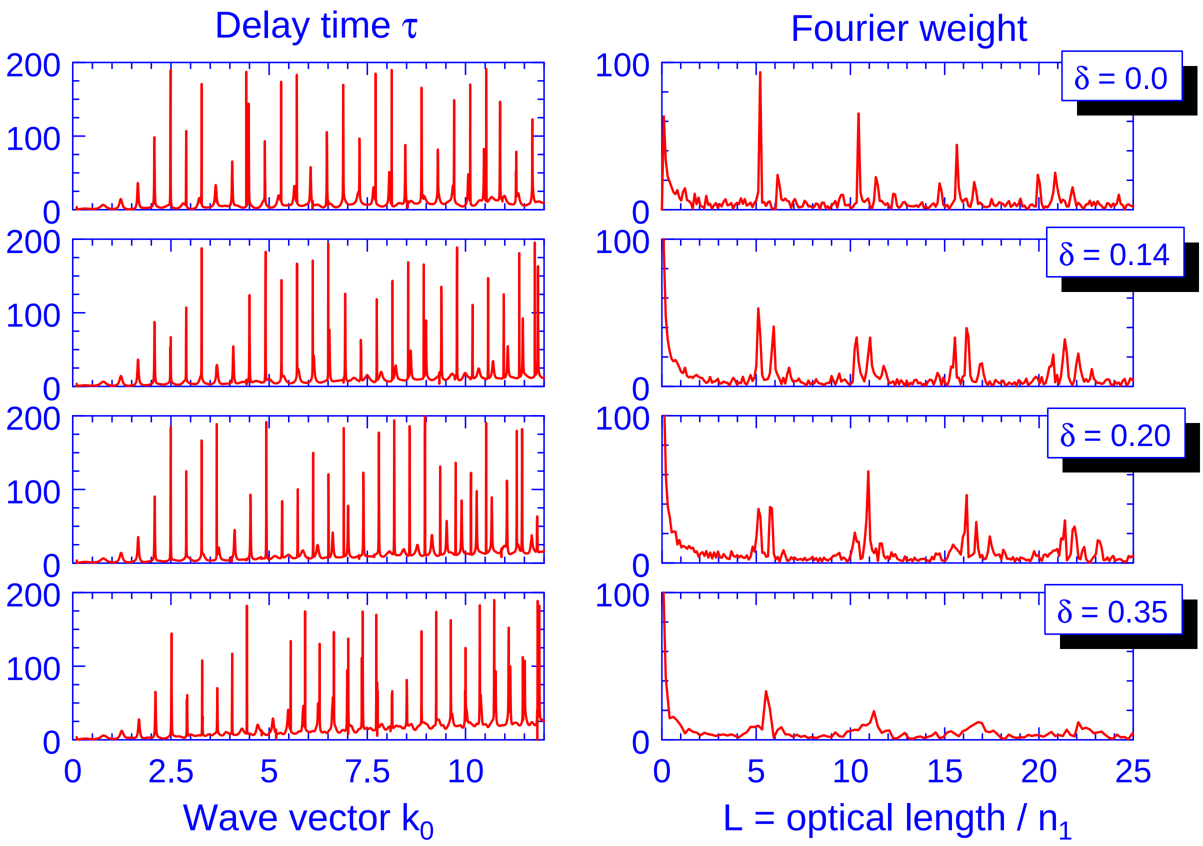

Figure 9.13: Delay time plots $\tau(k_0)$ (left) and Fourier transform (right) for the dielectric annular billiard $n_0 = 1, n_1 = 3, n_2 = 1$ with $R_2 = 0.4$, δ varied ($\Delta k = 0.005$). Families of whispering-gallery type orbits in $\tau(k)$ are increasingly shifted to higher wave vectors due to decreasing effective refractive index. The Fourier spectrum is essentially made up of two peaks and their higher harmonics. The first contribution corresponds to the geometric length of whispering gallery orbits at $L \approx 5.2$, the other peak at slightly higher length originates from the presence of several resonance families. Its weight is approximately constant, whereas the weight of the whispering gallery orbit decreases with increasing eccentricity. – The high intensity around $L = 0$ is due to the overall slope of the delay time representing the smooth part of the density of states.

the doublet splitting. Then at the same time the cavity will be more leaky there (as is, e.g., immediately verified in the ray picture) and the resonances will be broadened. Indeed we found this broadening to be the dominant effect. Another factor that limits the appearance of doublets is the general problem that studying the (Wigner) delay time one does not access the sharpest peaks where tunnelling *escape* is small and a doublet splitting might be seen, cf. also Fig. 7.12. Hence, the investigation of doublet splittings requires a rather closed system ($n_1 \gg n_0$) and a sufficient resolution Δk. It is, however, not of primary interest in the present work.

We end this section by a systematic investigation of the influence of increasing eccentricities on the resonance position in the delay time plot $\tau(k)$, see Fig. 9.13. Families of whispering-gallery type orbits are easily identified up to a radial quantum number $\rho = 4$ for the concentric case. With increasing eccentricity the spacing between the resonance peaks also becomes larger. The reason for this was discussed in detail in Section 9.2.3 in terms of the effective index of refraction, Eq. (9.23). We find this interpretation to hold also for large displacements of $\delta \approx R_2$ where, correspondingly, we find signatures of only three families when the same wave vector interval as for small displacements is chosen, see Fig. 9.13.

On the right of Fig. 9.13 we show the Fourier-transformed delay time data, i.e., the *length spectra* [97]. The general idea behind are the trace formulas that allow one to express the oscillatory part of the density of states as a sum over classical periodic orbits [57, 76, 97, 98]. Here, we apply the inverse procedure (assuming that the general idea holds for open systems as well), and extract the contributions of the different periodic orbits from the spectra ([59], see also the context of Eq. (7.63) for a relation between resonance spacing and orbit length). The Fourier transform yields peaks at the length of the contributing orbits, more precisely at their *optical* path length. We convert this into a geometric length L by division by n_1, which strictly speaking only applies for resonant modes localized in the annulus. If the refractive index of the annulus is highest, this is a good approximation due to the total internal reflection confinement at both boundaries.

In the concentric case, the spectrum is dominated by the peaks stemming from whispering gallery orbits, $L \approx 5.2$, see the top right plot in Fig. 9.13. This orbit length corresponds to a mean radius $R_{WG} \approx 0.83 < R_1$, in accordance with the naive expectation supported by Fig. 9.11, which was obtained for the $m = 3$ resonance at $\delta = 0.2$ ($k_0 = 1.66$). The position of this “whispering-gallery peak” remains unchanged when the eccentricity is increased, however, its height decreases since the modes become more and more affected by the constricted region leading to increased leakage loss, that is, broader resonances resulting in a reduced signature in the Fourier transform. Close to this whispering-gallery peak there is another peak that is less stable in position and merges with the first one at high displacements. This peak has to be attributed the interplay of the several families of resonances, in particular, it vanishes when only the first family is Fourier transformed.

We point out that there are no *visible* signatures of orbits other than of the whispering-gallery type, although the phase space of the classical annular billiard (hard walls) is very rich at the displacements chosen in Fig. 9.13. This is in agreement with the phase-space predictions of the refractive billiard, see Section 9.1. Trajectories of the classical annular billiard that hit the inner or the outer boundary under a right angle, have no (obvious) counterpart in the wave picture when we look at intermediate refractive indices. However, in the final Section 9.3 of this chapter we will correct the impression that the dielectric annular billiard does only accomodate whispering-gallery modes. We will reveal the great variety of resonant wave patterns that, depending on the parameters chosen, are similar to those known from the hard-wall system. Furthermore, we will establish the correspondence between resonances and stable trajectories in the refractive annular billiard.

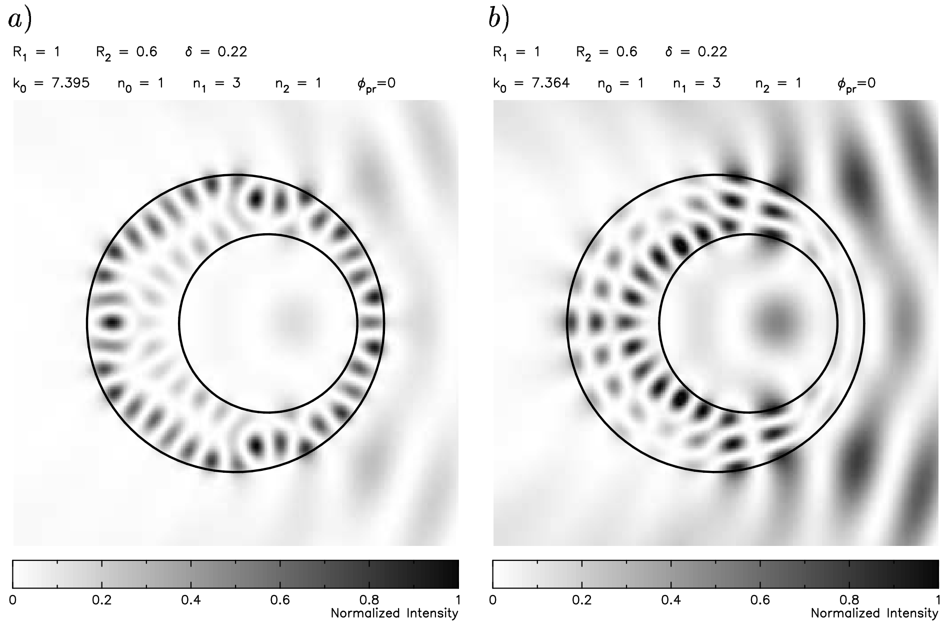

Figure 9.14: Typical resonant wave patterns for the dielectric annular billiard with an airy inclusion. The confinement to the annular region is due to the possibility of total internal reflection on either boundaries. For the examples shown here, high intensity is concentrated around regular orbits, in a) on a whispering-gallery-type orbit, whereas b) suggests to be a wave-mechanical realization of the arrow-like orbit shown in Fig. 9.3 (bottom right). In the delay time plot, the resonances are neighbouring and appear several times in this form with increasing wave vector. This suggests that they are regular modes. – ϕ_{pr} indicates the direction of incident plane wave (in radians) that excited the resonance.

9.3 Correspondence of ray and wave picture beyond whispering gallery modes

9.3.1 Dielectric ring embedded in air

As we saw in the previous section, there are major differences between annular billiards where the refractive index is highest in the annulus or in the inner disk, respectively. An illustrative explanation can be given in terms of the effective potentials, see Fig. 9.5. We will now focus on the situation where the annular region possesses the higher index of refraction, resulting in a single well in the effective potential, and turn to the other case in Section 9.3.2.

The regime $n_1 > n_2 \geq 1$ is characterized by the possibility of total internal reflection confinement to the annular region. As a consequence of this, we find the resonant wave patterns to live mainly in the annular region, cf. Fig. 9.14. This applies to whispering-gallery-type resonances (Fig. 9.14a) or resonances following regular orbits (Fig. 9.14b) as well as to all other resonant states (if the refractive indices are not too similar).

Let us now investigate the influence of changes of the refractive index of the annulus on

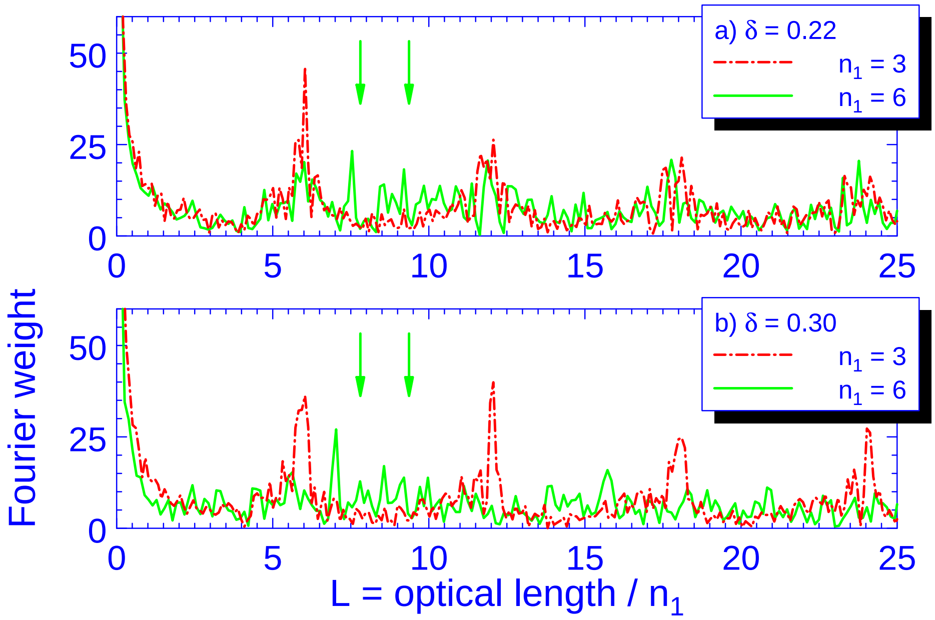

Figure 9.15: Fourier transform of the delay time (length spectrum) for two annular geometries ($R_1 = 1, R_2 = 0.6$, a) $\delta = 0.22$, b) $\delta = 0.3$), and two sets of refractive indices ($n_0 = n_2 = 1$, and $n_1 = 3$ (dash-dot) or $n_1 = 6$ (full line), respectively). The optical length is converted into (approximate) geometric length L by dividing by the refractive index n_1 of the annulus. There are signs of whispering gallery orbits in all four spectra (peaks around $L \approx 6, 12, 18$). However, for the higher n_1 we also find signatures of different orbits in the region marked by arrows. – Note the absence of very short (bouncing-ball) orbits like the upper left in Fig. 9.2 that can not be confined by total internal reflection.

the kind of resonances. To this end, we consider the Fourier-transform of the delay time for the annular billiard with $R_2 = 0.6$ at two displacements ($\delta = 0.22$, $\delta = 0.3$), and for two sets of refractive indices, namely for $(n_0, n_1, n_2) = (1, 3, 1)$ and $(1, 6, 1)$, where the latter set is closer to the hard-wall limit. In Fig. 9.15 we compare the resulting length spectra. Whereas for intermediate refractive index in the annulus ($n_1 = 3$) the spectrum is dominated by the whispering-gallery peaks[6] and its higher harmonics, for higher $n_1 = 6$ we find signatures (marked by arrows) that presumably *do not stem from whispering gallery orbits!* To identify this type of resonance mode we have several possibilities:

1. Scanning the corresponding delay time plot for the wave patterns at the resonances. We will do so by studying the response of the annular system to an incident plane wave that provides the system with a (well defined [56]) mixture of incident angular momenta at the same time[7].

---

[6] Its position is shifted to higher values $L \approx 6$ when compared with Fig. 9.13 where $R_2 = 0.4$. The reason is that the larger inner disk forces the whispering gallery orbits further to the outer boundary resulting in a longer path length. Correspondingly, the double peak structure discussed in Fig. 9.13 is lost.

[7] A more sophisticated method is to diagonalize the S-matrix at the resonance position and to deduce "eigen-delay times" τ_i. At each resonance, the main contribution to the total delay time τ will stem from a few τ_i only. The corresponding eigenvectors contain all information on the angular momenta that are needed to excite the

2. Studying the Poincaré section of the corresponding classical and *refractive* billiard. The geometric lengths found in the length spectrum might be useful as a characteristic trajectory property.

We will once more start with a ray approach, that is, the second possibility. For the set of refractive indices $(1,3,1)$ we already studied the Poincaré surface of section, see Fig. 9.3, and identified regular trajectories *other* than whispering galleries. First of all we have to explain why they do not leave signatures in the length spectrum. For the upper right orbit in Fig. 9.3 with stability islands at the beach of the chaotic sea we can argue that it is "almost" whispering-gallery-like in character such that no additional peaks in the length spectrum arise. (This also excludes this orbit as a candidate to explain the arrow-marked peaks in Fig. 9.15.) For the other, arrow-like, orbit (Fig. 9.3 bottom right), we find a geometric length of $\approx 6.15\ R_0$ for the central elliptic orbit of the stability island, corresponding to a length spectrum peak which cannot be distinguished from the whispering gallery contributions. Therefore, scanning of the delay time plot was used to obtain the representative wave patterns in Fig. 9.14.

We now address the other set of refractive indices, $(1,6,1)$, where the optical denser annular region causes a better confinement by total internal reflection, and look for candidates for the additional peaks in the length spectrum. Investigation of the Poincaré section of the corresponding refractive billiard reveals stability islands for an orbit similar to the one shown on the bottom right in Fig. 9.2. These islands are (practically) missing for $n_1 = 3$, and grow in size as the hard-wall system is approached. The corresponding orbit is shown in Fig. 9.16 (left). Its geometric length is about $8.5\ R_0$ and, therefore, falls into the length region marked by arrows in Fig. 9.15. We suggest the wave pattern in Fig. 9.16 (right) as a wave-mechanical counterpart. However, a comment is in order concerning the rather small size of the stability islands in the corresponding Poincaré section. It is well-known that quantum-mechanically these islands may appear larger [105] and, therefore, can be resolved with the wave vector chosen in Fig. 9.16 (cf. also the discussion at the end of Section 7.4). Studying the corresponding Husimi function would allow one to gain further insight, see Section 9.3.3.

Fig. 9.15 suggests that the behaviour for both eccentricities, $\delta = 0.22$ and $\delta = 0.3$, is approximately the same. If we look at the phase space plot of the refractive billiard (Fig. 9.17) we find, however, much more structure in it. A couple of stable orbits well-known from the classical annular billiard [100, 102] survive the refractive opening of the inner disk. However, they encounter the outer boundary at a right angle and one might argue that this implicates immediate escape when we think of this boundary as dielectric interface as well. Otherwise, we know from Fresnel's formulae (7.4,7.5) that at such an interface there is not only transmission, but also reflection is taking place. The *reflected* intensity for normal incidence is given by $(n-1)^2/(n+1)^2$ which means that for $n_1 = 6$ more than 50 % of the intensity are reflected[8].

---

resonance, and according choice of the amplitudes of the incident Hankel functions will give the resonant wave pattern. For whispering gallery modes, the main contribution comes from the corresponding angular momentum quantum number; this was used in Fig. 9.11. – The angular momentum content of a plane wave will in general not coincide with the one required according to the eigenvalue decomposition of the S-matrix. The hope is that the system "finds" the relevant components such that one gets some idea of the wave pattern, whereby a suitable angle of incidence for the plane wave has to be found.

[8] This applies, of course, also to the inner interface and has to be taken into account when interpreting the Poincaré sections of refractive billiards where this reflection is neglected.

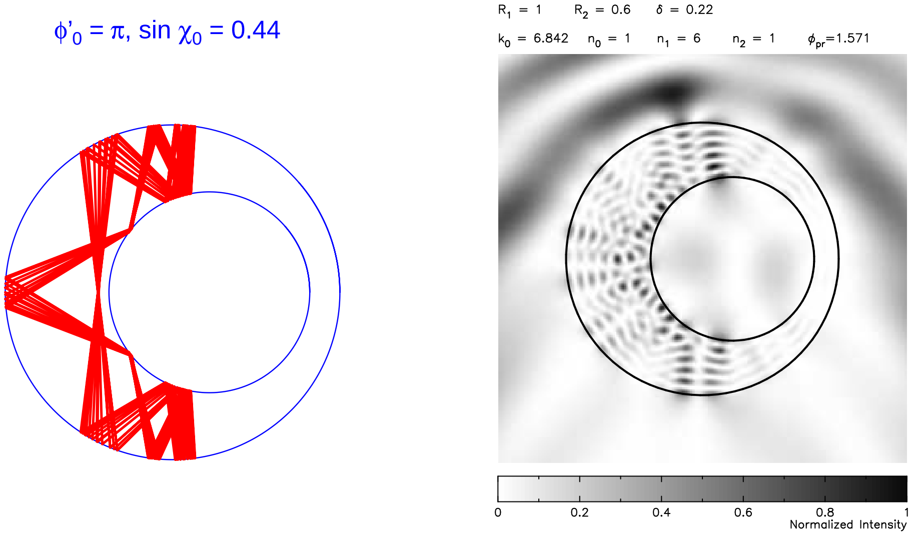

Figure 9.16: Stable trajectory (left) and wave-mechanical analogue (right) that might well account for the arrow-marked peaks in Fig. 9.15.

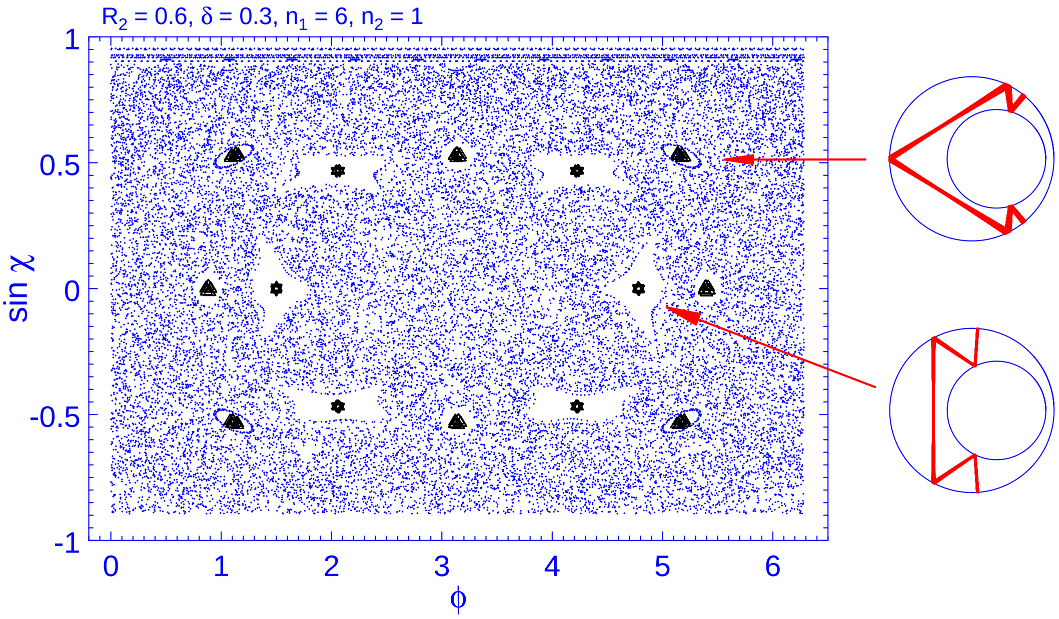

Figure 9.17: Poincaré section and two prominent regular trajectories for the refractive annular billiard $n_1 = 6$, $n_2 = 1$. The inner radius is $R_2 = 0.6$, the displacement is one half of this value, $\delta = 0.3$. The lower trajectory on the right is a typical representative of orbits at $\delta/R_2 \approx 0.5$.

Indeed do we find wave-mechanical counterparts of these characteristic orbits, see Fig. 9.18, that might well be responsible for the arrow-marked signatures in Fig. 9.15. Besides the favoured total internal reflection confinement at this refractive index, one might discuss another mechanism that favours the existence of those modes: The annular wave vectors k_1 for which we

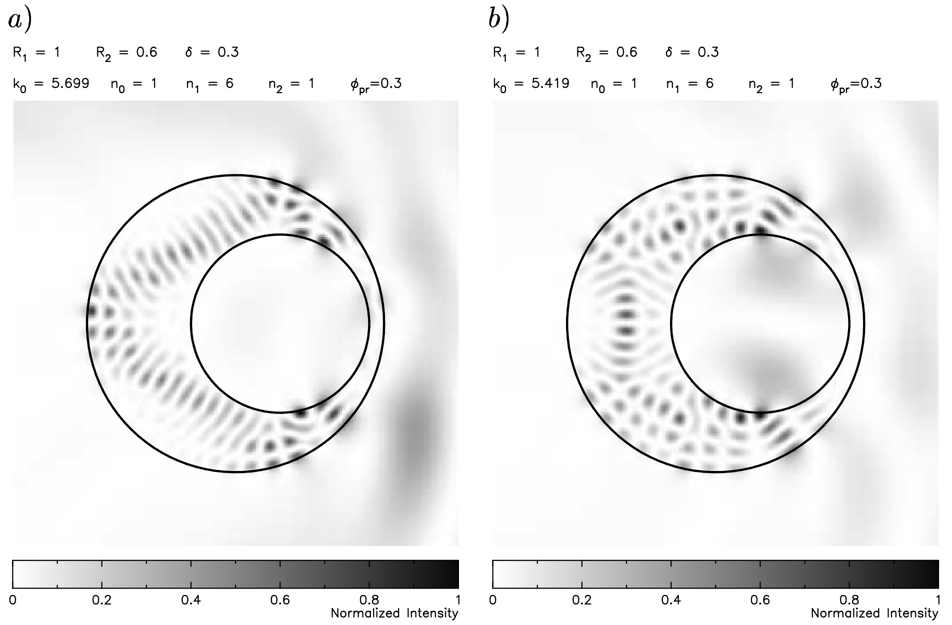

Figure 9.18: Wave-mechanical realization of orbits similar to the ones shown in Fig. 9.17 on a) top right, and b) bottom right. The (slight) deviations from the geometry of the regular orbits in Fig. 9.17 might be ascribed to the *openness* of the system and the interplay of reflection, transmission, and interference.

discussed the resonant wave patterns all correspond to wavelengths $\lambda_1 = 2\pi/(n_1 k_1) \sim 1/n_1$. The extension of the reflection points at the outer boundary is approximately of the same order, and one might argue that the wave "cannot see the exits". A quantitative formulation of this will be useful and is the subject of further investigations.

A more detailed interpretation of the special structure in the length spectra in Fig. 9.15 requires more careful Fourier transforms. As we saw in Fig. 9.13, there might be peaks in the spectrum that are *not* due to a particular orbit. Furthermore we want to point out that the Fourier transforms contain information about *optical* lengths that might be similar for several orbits although their *geometric* lengths are different, cf. also the context of Fig. 9.19.

9.3.2 Eccentric dielectric inclusion in a lower-index coating

We now turn to the case where the index of refraction is highest in the inner disk and lowest outside, $n_2 > n_1 > n_0 \equiv 1$. Well-known representatives of this situation are coated glass fibres [89] or melting ice particles in clouds [106]. Furthermore, in both examples non-concentric geometries are likely to be realized. In contrast to the situation of the previous section, the increase in the index of refraction when approaching the centre of the system implies that rays in the annular region are *not* confined by total internal reflection, but will enter the inner disk whenever the inner boundary is hit! Following the laws of geometric optics, those rays will leave the inner disk upon the next reflection. In contrast, whispering-gallery orbits, confined by total internal reflection, are now not only possible near the outer, but also near the *inner* boundary

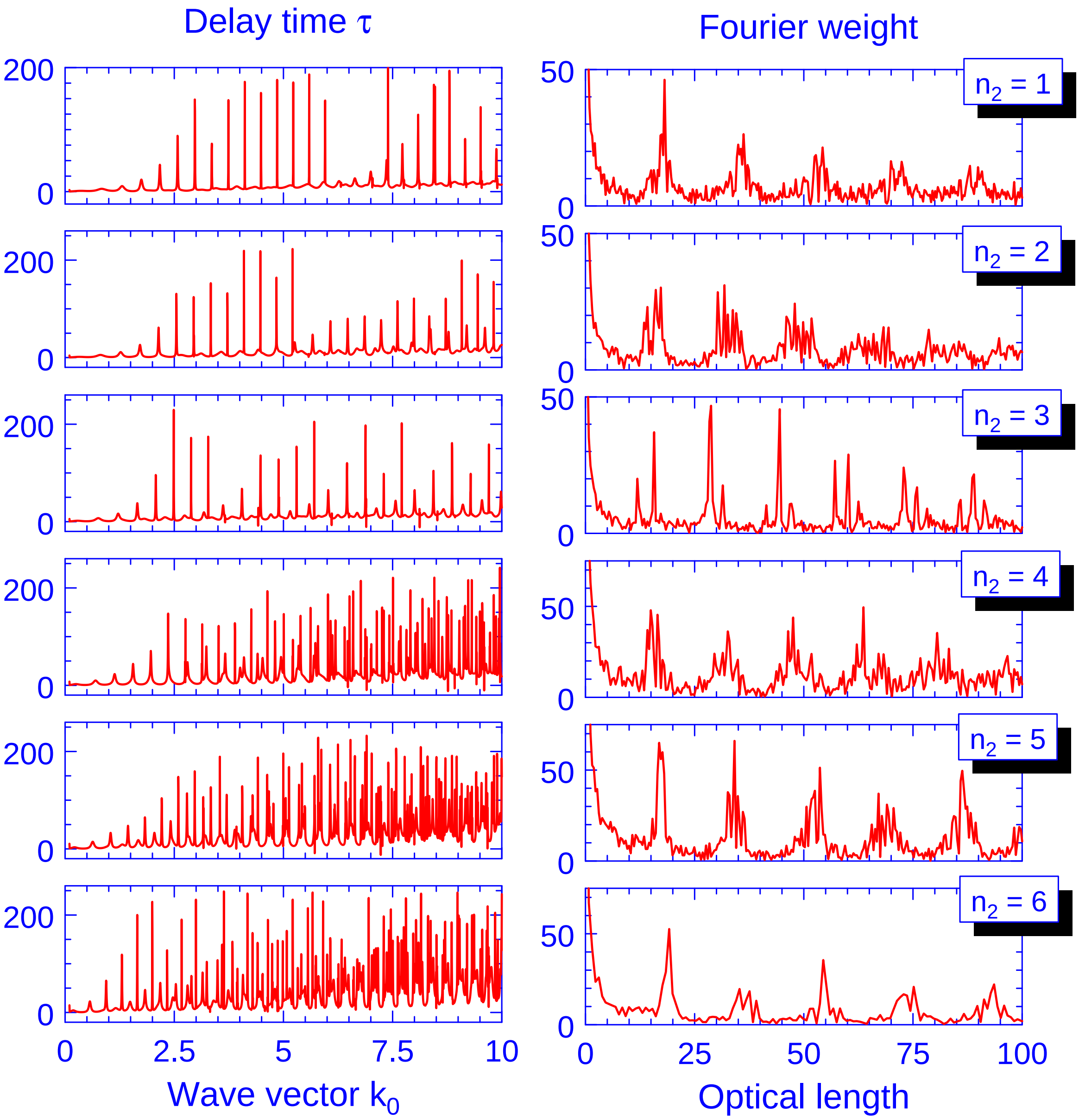

Figure 9.19: Delay time and its Fourier transform for varying index of refraction of the inner disk ($R_1 = 1, R_2 = 0.6, \delta = 0.22, n_0 = 1, n_1 = 3$). The delay time plots are dominated by families of whispering-gallery modes (near the outer boundary) for $n_2 \leq n_1$. For $n_2 > n_1$, the ray-model-predicted increase of possible confined modes is clearly visible in terms of a higher number of resonance peaks. As for the Fourier transform, we plot the weight against the *optical path length* because different indices of refraction are involved. Different (real space) paths may result in the same optical path length making it hard to identify clear signatures of the different orbits.

(cf. Fig. 9.20a). Consequently, this situation embodies much more resonances as we see in the delay time plots, cf. Fig. 9.19. Examples for resonant modes are shown in Figs. 9.20, 9.24, and 9.25.

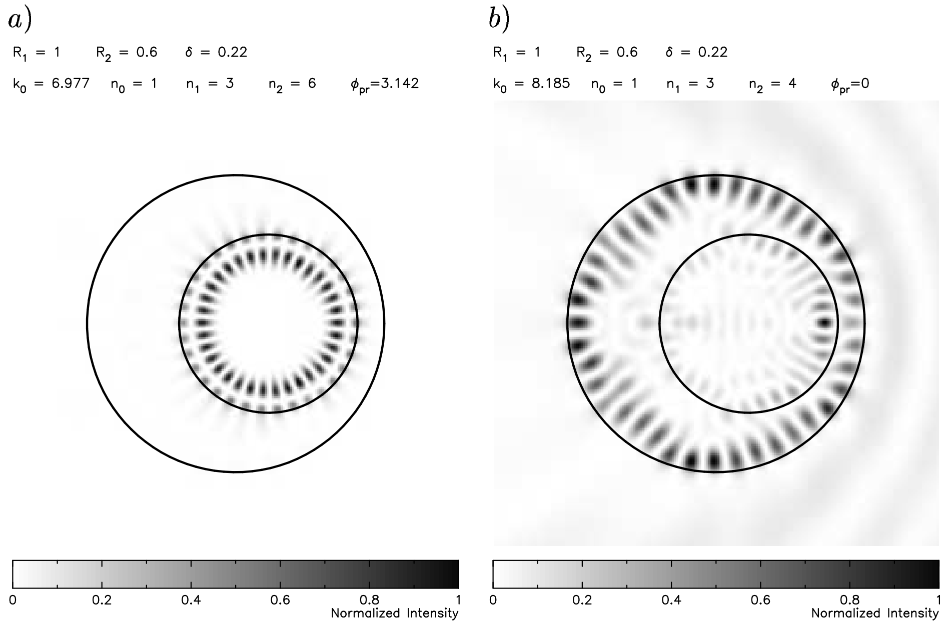

Figure 9.20: Characteristic properties of the annular billiard where the refractive index of the inner disk is highest are that a) whispering gallery mode of the inner disk are possible ($n_0 = 1, n_1 = 3, n_2 = 6$), and b) whispering gallery modes that do not fit through the constriction may go through the inner disk ($n_0 = 1, n_1 = 3, n_2 = 4$). Case a) is favoured for a rather big difference between n_1, n_2, whereas b) works preferably for similar values n_1, n_2. One (possible) ray picture analogue for b) is the upper right orbit in Fig. 9.21.

In Fig. 9.19 we present a systematic study of the implications of an increasing refractive index of the inner disk. The delay time plot clearly shows the transition from an airy inclusion ($n_2 = 1$) via the dielectric *disk* ($n_2 = 3$) to the situation $n_2 > n_1$ by a remarkable increase of resonance peaks. However, the signatures in the Fourier transforms are less conclusive. The length spectrum is dominated by whispering-gallery signatures in all cases. More precisely, other types of orbits do not differ significantly in length from the whispering gallery orbits, in particular appear the typical *optical* lengths to be rather similar.

We turn now towards a systematic study of the changes in the Poincaré section when increasing n_2, and concentrate on the identification of typical (regular) orbits and their wave-mechanical counterparts.

We begin with the example of the refractive billiard $n_1 = 3, n_2 = 4$ in the same geometry as for Fig. 9.19 (see Fig. 9.21). In this phase space plot only trajectories started at the *outer* boundary (and with positive momentum $\sin\chi > 0$) are shown. For those, the inner disk is *not* shadowed by total internal reflection and each ray hitting the inner boundary will be refracted into the inner disk! This implies, however, that each ray will leave the disk upon the next reflection (now hitting the inner boundary from inside) due to the principle of optical path reversion (and momentum conservation). Therefore, we have to discuss orbits *confined* to the

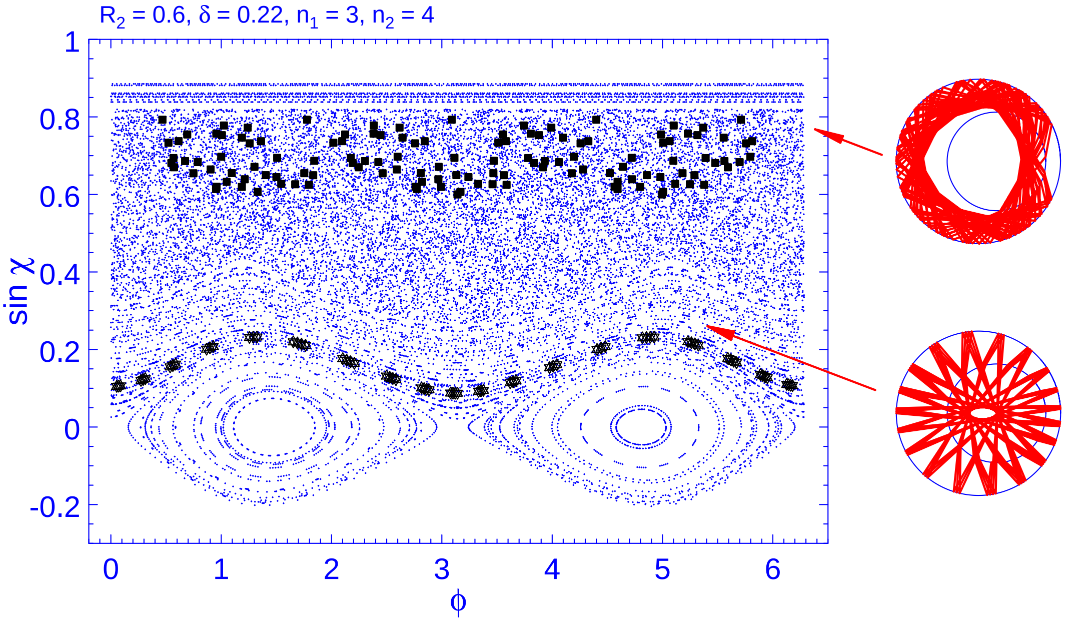

Figure 9.21: Poincaré section for a refractive annular billiard with $n_2 > n_1$ ($R_1 = 1, R_2 = 0.6, \delta = 0.22, n_1 = 3, n_2 = 4$). Typical are trajectories that cross the inner disk, which applies in particular to whispering gallery modes at the outer boundary that are supported by the inner disk in the region of closest approach of the interfaces, see the upper example on the right. Note also that the reflection points of this orbit, although in the *chaotic* region of phase space, they are rather close together and seem to follow an adiabatic invariant [108] *for the first few hundred* reflections where, in particular, no change in the sense of rotation occurs. The same applies with even more rigour to the lower orbit on the right that is a stable quasiperiodic orbit. Note that both orbits are well separated in momentum $\sin\chi$. – The stability islands around $\sin\chi = 0$ correspond to a "bouncing-ball orbit" involving the inner disk, see the example in Fig. 9.22 (lower right).

inner disk separately - and as we know from Chapter 7 these are just the whispering gallery modes[9] an example of which is shown in Fig. 9.20a).

The resonant mode shown Fig. 9.20b nicely illustrates the opportunity offered by the inner disk to "host" a whispering gallery mode of the outer one that otherwise would not fit into the constricted region. This requires, of course, $n_2 > n_1$, whereby for $n_2 \gg n_1$ the effect of refraction will become too big and destroy the hosting effect. In the case $n_2 < n_1$, the nodes of the whispering gallery modes "rearrange" for increasing quantum numbers m and ρ, eventually building up modes that only live in the wide region [129].

As for the star-like orbit, see Fig. 9.21 (lower right), we refer to Fig. 9.8 where we found a similar, regular, trajectory in the *concentric* case. In the eccentric case, the corresponding phase space curve follows an adiabatic invariant [86] if the displacement of the inner disk is not too large. Furthermore, the tolerated eccentricity depends on the ratio of the refractive indices.

---

[9] Note that for whispering gallery modes at the inner boundary R_2 takes the role of R_1 such that the same value "kR" now requires for a larger k_0.

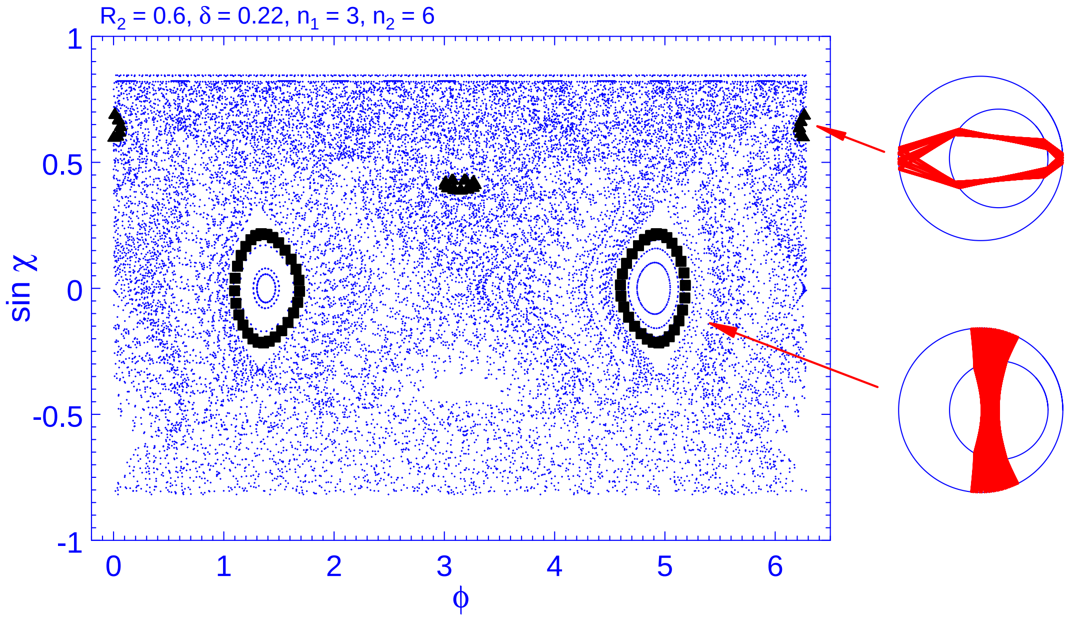

Figure 9.22: Poincaré section for a refractive annular billiard with the same geometry as in Fig. 9.21 but larger difference in the refractive indices ($n_1 = 3, n_2 = 6$). Typical are trajectories that cross the inner disk. The slight structure in phase space (besides the islands of stability) is partially a result of this choice but also a sign that some trajectories are rather close to a (nearly) periodic orbit for a high number of bounces before they are lost in the chaotic sea.

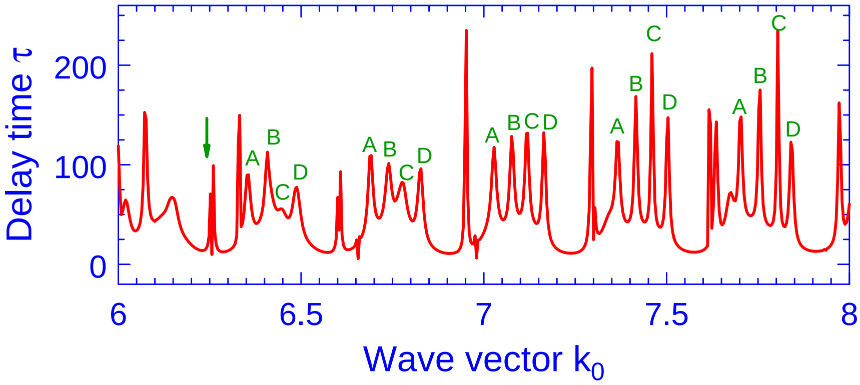

Figure 9.23: Delay time plot zoomed in from the last panel on the left in Fig. 9.19 ($R_1 = 1, R_2 = 0.6, \delta = 0.22, n_0 = 1, n_1 = 3, n_2 = 6$). Note the characteristic structure of four resonances (A,B,C,D) forming a group. Each of the four peaks corresponds to a characteristic wave pattern, see Fig. 9.25. The regular structure in the delay time and the fact that from group to group the number of nodes is increased by one suggests a correspondence to regular modes. – Marked by the arrow is the chaotic mode of Fig. 9.24.

Changing n_2 from 4 to 6 removes this orbit from the Poincaré section, cf. Fig. 9.22.

This brings us to the situation $n_1 = 3, n_2 = 6$. The Poincaré map for the corresponding

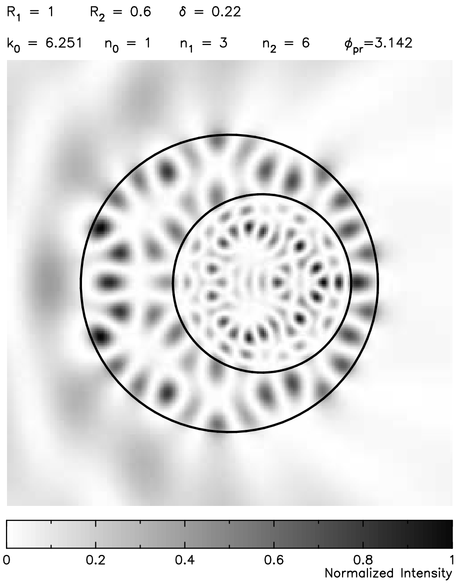

Figure 9.24: Chaotic mode with maxima and nodes nearly homogeneously distributed over the system. It corresponds to ray trajectories in the chaotic part of the phase space.

refractive billiard is shown in Fig. 9.22. Whereas the lower right orbit in this figure is generic for the refractive billiard with $n_2 > n1$, the upper one was not present for $n_2 = 4$, see Fig. 9.21. According to our experiences about the predicting power of the Poincaré section up to this point, we are optimistic to find wave-mechanical analogues of these regular orbits. Indeed is it tempting to relate a wave pattern like this in Fig. 9.25A to the upper one of the two orbits.

However, for the dielectric annular billiard with $n_2 > n_1 > n_0 \equiv 1$ things turn out to be more complicated. In the delay time plot, Fig. 9.23, we observe a characteristic arrangement of resonance peaks in groups of four, marked by A-D, for a certain range of wave vectors. The corresponding resonant modes are shown in Fig. 9.25, their sequence is the same in each group. From group to group, the number of nodes increases by one. This suggests that the modes are regular – but, apart from mode A, they do *not* form (visible) stability islands in the phase space of the refractive billiard. If we closer investigate the resonant modes, we find the pattern Fig. 9.25D to be based on a regular orbit well-known from the *hard-wall* annular billiard (cf. Fig. 9.2, centre of top row). However, now the inner disk is involved in the wave dynamics as well which causes a slight change in the geometry of the orbit; for example, the turning points are shifted towards the constricted region. This example makes clear that the simple picture of a stepwise Fresnel law is oversimplified, and a more realistic picture is required where both transmitted *and* reflected amplitudes are taken into account. The simplest way to achieve this is to take into consideration both the phase-space structure of the refractive and the hard-wall billiard (plus intuition). Then the examples in Fig. 9.25 can be understood as a nice illustration of the constructive interplay between interfering waves in the inner and outer disk, leading to reproduction and generalization of regular orbits known from studying the phase space of the hard-wall and the refractive annular billiard by a "suitable" adjustment of the orbit geometry.

So far we have only discussed regular modes. Since the phase space of the annular billiard

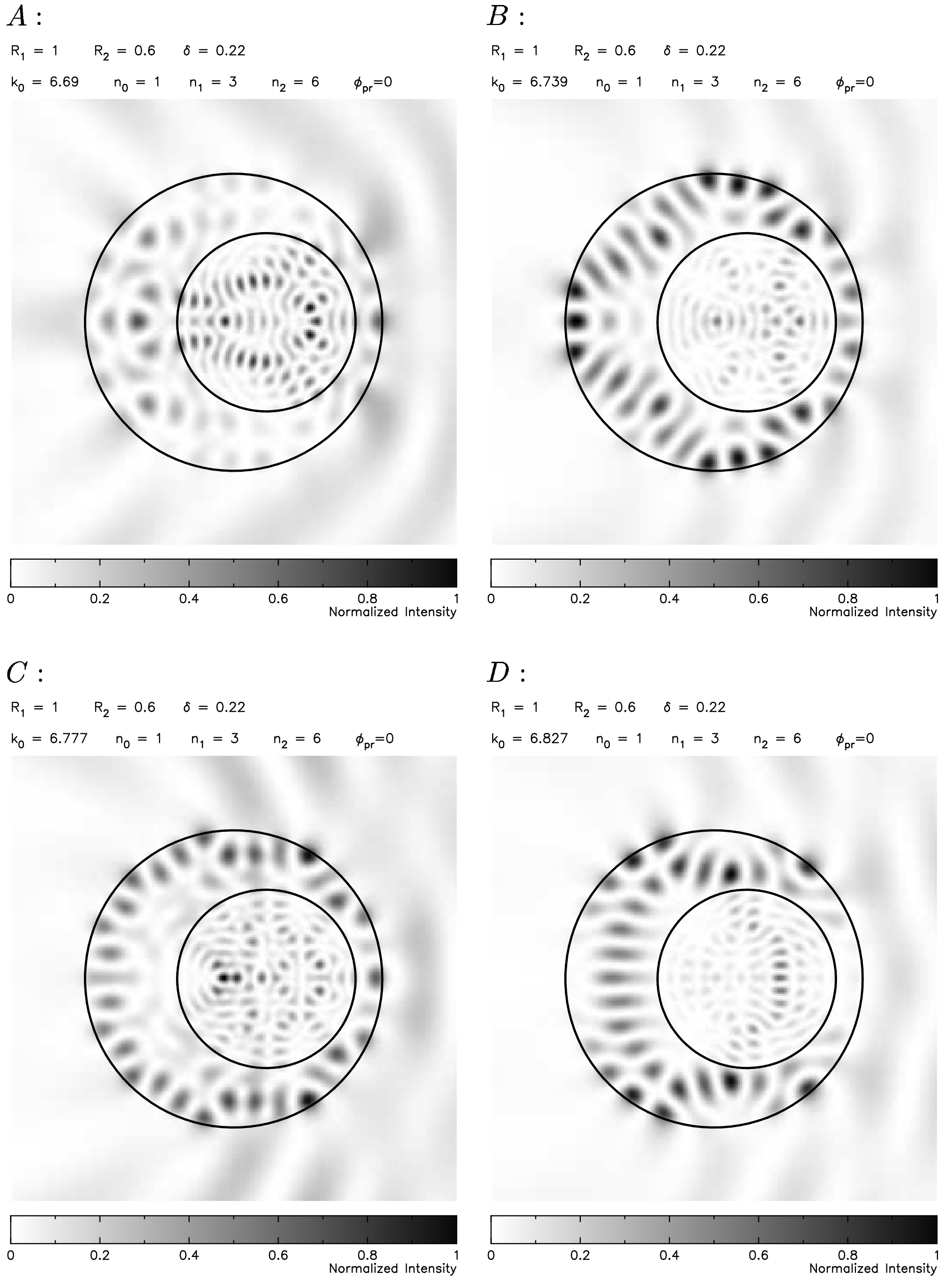

Figure 9.25: Characteristic resonant wave patterns associated with the group structure found in Fig. 9.23. All wave patterns are taken from the second group and named as above. The reflection-transmission interplay between inner disk and annular region goes beyond the prediction of the ray model. However, it is tempting to relate pattern A to the stable ray orbit that is shown in Fig. 9.22 on the lower right. – The wave patterns nicely illustrate how regular orbits known from the classical hard-wall annular billiard are recovered and *adopted* in the open dielectric system. Note in particular the role played by the inner disk in "completing" the annular patterns and the fitting of the wave patterns at the inner boundary.

is *mixed*, there must, of course, exist *chaotic* modes as well! Indeed this is the case, and one example is shown in Fig. 9.24. Concerning the occurence of chaotic modes, we point out that, in classical phase space, they will frequently cross the region of frustated total internal reflection at the outer boundary, $-1/n_1 < \sin\chi < 1/n_1$. Therefore, the confinement to the system is reduced, and regular modes dominate in the delay-time plot, cf. Fig. 9.23.

Note that there is no sharp transition in the interpretation of modes to be regular, chaotic or hierarchical [103, 105] when only real-space information is used. We will discuss possible improvements in the foolowing section.

9.3.3 Open problems

In this chapter we discussed the ray-wave correspondence in the dielectric annular billiard and proved in numerous examples that this is a fruitful concept. We used classical phase-space methods like the Poincaré surface of section, and studied wave properties of the systems using delay-time plots and real-space intensity plots. However, as already mentioned at the end of the previous section, several points are left for further investigation.

Concerning the geometrical-optics based phase-space approach, we used the Poincaré map of the hard-wall and the refractive system for a interpretation of the resonant modes. However, an improvement of the concept of the refractive billiard to account for realistic (wave-optical) situations where reflection *and* transmission occur at refractive index boundaries, is desirable. We expect the resulting phase space to contain elements both from the hard-wall and the refractive billiard.

In this context the question arises for a systematic classification of resonant modes in *phase space*, where information on the resonance *dynamics* is processed. The calculation of Husimi functions [75, 104] is necessary in order to reliably attribute a certain resonance to regular, chaotic, or even hierarchical [105] states. Another interesting issue not discussed in the present work is the existence of scarred wave functions.

Throughout this chapter we mainly discussed low-lying resonances. It remains for further studies to investigate the evolution of resonant modes to higher wave numbers k_0 where the ray limit is approached. In this context the influence of a decreasing wavelength on the size of the coupling region between dielectric and environment at the outer boundary, and its influence on the stability of orbits, will be an interesting subject.

Another problem that becomes important when discussing microlaser (see Section 10.2) is the far-field radiation characteristic of resonant modes. Methods working with complex wave vectors will be useful in this context. In any case, the dielectric annular billiard promises to remain an interesting model system.

10 Achievements of the ray model in microcavities: Examples

We end this second part of the thesis by demonstrating the strength of the ray model for two examples. First, we consider a recent glass-fibre experiment [130]. A remarkable filter effect has been observed in the response of a quadrupolar high-index fibre illuminated by a laser beam. The periodic filter characteristics found in a tiny window of far-field angles can be fully understood by numerical ray-tracing simulations [134].
The second example concerns microlasers where the ray model proved to yield reliable results in the bow-tie experiment [135]. Having in mind future applications that will require high output power and highly directional emittance, we use this concept and identify shapes that might even better suit future needs. Furthermore, we suggest a novel mechanism for out-coupling [137], namely a monolithically integrated light valve, and discuss its advantages compared to present realizations [136] relying on the violation of total internal reflection.

10.1 Multiple beam interference in a quadrupolar glass fibre

Optical fibres have attracted a lot of interest in recent years both in experimental and theoretical work. On one hand they are applied in microlasers as (active) lasing fibres, on the other hand they can be used as (passive) optical filters which are of great technological interest for planar integrated filter applications. Planar dielectric ring and disc cavities have been used as micron-sized optical filters mainly with evanescent light coupling, working with nearly total internal reflection. However, evanescent coupling between the cavity curved sidewall and the waveguide flat sidewall requires a very precise fabrication with a gap spacing in the sub-μm range. Therefore, filter techniques using non-evanescent coupling which allows gap sizes larger than sub-μm are technologically desirable.

Recent experiments [130] with using an oval-shaped microcavity have shown periodic output filter characteristics in a well defined, narrow window of far-field response. In this section we will present an analysis of the experimental data and, subsequently, of numerical ray-tracing simulations which allow a theoretical understanding of the experimental findings [134]. In the experiment, a passive (non-lasing) quadrupolar high-index glass fibre (refractive index $n = 1.8$) is illuminated by a laser beam, see Fig. 10.1. A tunable laser source with wavelengths λ_0 in the 670 nm range produces a Gaussian beam of TE-polarized light with a width (spot size) of 30 μm, that is shone onto the fibre allowing for different impact parameters. The cavity axes are 150 and 180 μm, and the shape is modelled by a quadrupole with polar-coordinate representation

$$r(\phi) = R_0(1 + \epsilon \cos 2\phi) , \qquad (10.1)$$

where R_0 is the mean radius of the quadrupole with eccentricity ϵ. According to the experimental data we have $R_0 \approx 82\,\mu m$ that we will use a unit length. The lengths of the half axes are then given by $R_0(1 \pm \epsilon)$ with $\epsilon \approx 0.1$. The corresponding size parameter $2\pi n R_0/\lambda_0$ is of the order of

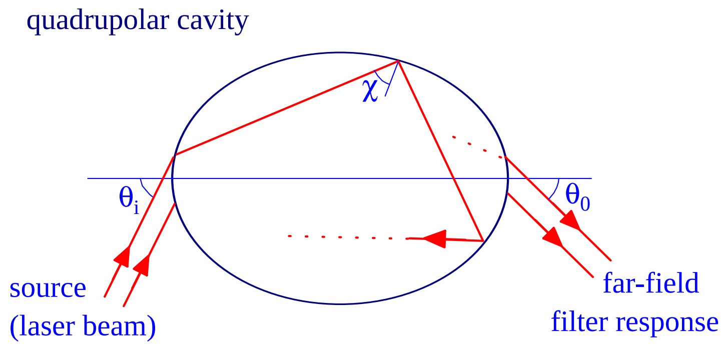

Figure 10.1: a) Schematic of the experimental setup used for the filter experiment in [130]. Shown is the cross section of the quadrupolar fibre with the definition of the input and output angles θ_i and θ_o. If the input is coming from a broadband source (indicated by arrows), the output shows periodic filter characteristics in a narrow "magic" window of far-field angles, see also Fig. 10.2. b) Typical orbits contributing to the far-field response, see text.

1400 such that we are well in the ray limit $\lambda_0 \ll R_0$ where quantum effects can assumed to be small.

The physical quantity of interest in the experiment is the far-field elastic scattering spectrum that is measured with a linear array detector that extends over a range of 5° of the output angle. The spectrum shows filter resonances as function of incoming wavelength with a good peak to background ratio of about 40, cf. Fig. 10.2a, but only under *very specific input and output coupling angles* $\theta_{i,o}$. The corresponding parameter region is called "magic window" [130]. The periodicity of the spectrum is a clear sign of the interference nature of the phenomenon; in addition the filter peaks display inhomogeneous broadening which is an indication of multimode interference. Therefore, we attribute the observed filter-characteristing behaviour to an interference scenario as is supported by the Fourier transform of the experimental data (Fig. 10.2b). This length-difference plot reveals that only a few, well defined length differences occur.

Before we discuss possible interference scenarios and their agreement with the experimental data, let us define the quantities and lengths that we will need for a length analysis of the contributing geometric paths, based on the assumption that the periodic output characteristics can be interpreted as interference of (classical) rays. We start by defining the amplitude-weighted length distribution $T(L)$ for the interfering rays,

$$T(L) = \sum_{\text{paths}\, i} A_i\, \delta(L - L_i)\,, \tag{10.2}$$

where A_i and L_i are the amplitude (at the detector) and the (total) *optical* length (from source to detector) of each path i hitting the detector. The interference pattern $J(k_0)$ as a function of the vacuum wave vector $k_0 = 2\pi/\lambda_0$ is given by

$$J(k_0) = \left| \int_{-\infty}^{\infty} \mathrm{d}L\, T(L)\, e^{ik_0 L} \right|^2 = \int \mathrm{d}l\, e^{-ik_0 l} \int \mathrm{d}L\, T(L)\, T^*(l+L) \overset{\text{def}}{=} \int \mathrm{d}l\, e^{-ik_0 l}\, S(l)\,. \tag{10.3}$$

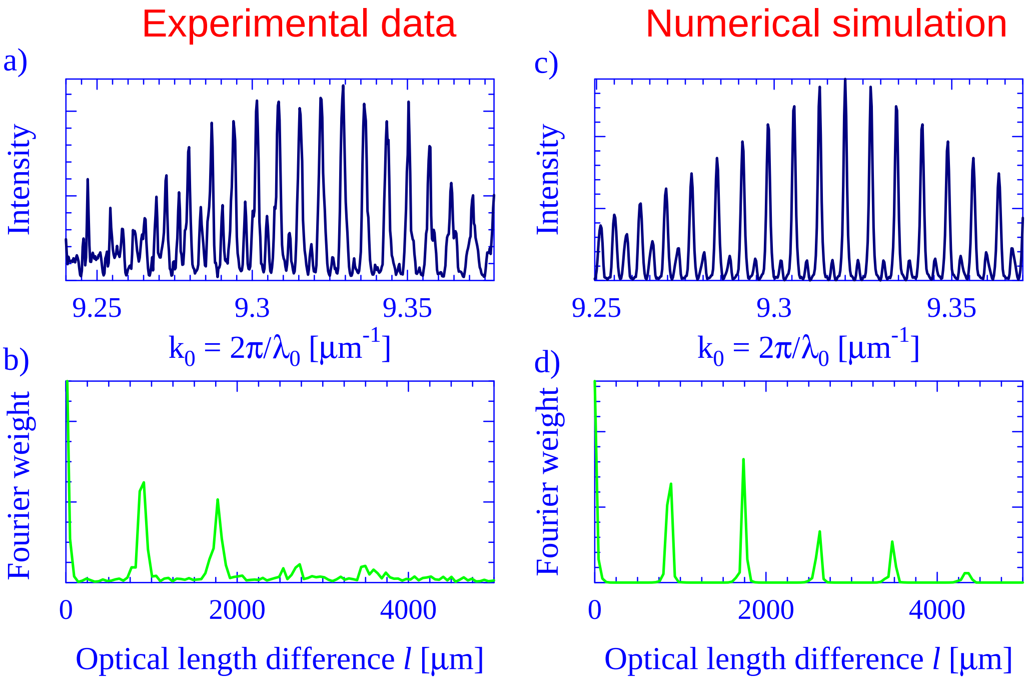

Figure 10.2: Representative experimental spectrum of [130]. a) raw interference data, $J(k_0)$, plotted as function of the wave vector k_0. The angles are chosen within the magic window, $\theta_i = 60^o$ and $\theta_o = 56^o$. b) Modulus^2 of the Fourier transform of $J(k_0)$ corresponding to the length-difference spectrum $S(l)$, see Eq. (10.3). The strong decay of the peak intensity for lengths l longer than 3 or 4 round-trips is a characteristic feature. Plots c), d) are as a), b) but for the theoretical ray-tracing result for $\theta_i = 60^o$, $\theta_o = 60^o$, and $\epsilon = 0.1$.

In the last step we have introduced the *length-difference spectrum* $S(l)$, given by the self-convolution (or correlation function) of $T(L)$ [123]. For discrete paths with lengths L_i the quantity $S(l)$ will be non-zero for length differences $l = L_i - L_j \ \forall i, j$. In the following we will mainly use the length-difference spectrum $S(l)$ for our analysis. It is related to the observed interference pattern $J(k_0)$ by Fourier transformation, see Eq. (10.3). The information about *absolute* path lengths is lost, but does, of course, not enter the interference result. Eventually, the optical length L_i of each path i from the source via the fibre to the detector is $L = n\widetilde{L}R_0 + L_{\text{ext}} + L_{\text{phase}}$, where $\widetilde{L}$ is the *geometrical* path length in the cavity measured in units of R_0. L_{ext} stands for the external paths between source and fibre and fibre and detector that are different for different input and output points of the interfering rays. Finally, L_{phase} comprises the phase shifts that occur upon the reflections.

The Fourier transform $S(l)$ of the (representative) set of experimental data in Fig. 10.2a is shown in Fig. 10.2b and shows large contributions to $S(l)$ at roughly equally spaced l values. Therefore, it is tempting to identify the spacing with the path length of one round-trip corresponding to a single dominating cavity orbit. The simplest possibility is interference of rays emerging (by refraction or by tunnelling) from a single stable orbit that is traced over and over again. In this case $T(L)$ contains equally spaced peaks with monotonically decreasing intensity

($\sim t(1-t)^{i-1}$ where t is the out-coupling rate and i the number of round-trips). A similar decay is then also found in the peaks of the difference spectrum $S(l)$. For the particular case of the quadrupolar fibre a candidate for a stable orbit is the so-called “diamond” (with reflection points at the intersection of the half axes with the boundary) where the tunnelling rate is rather small. Hence one would expect a slow, monotonous decay of the peak intensities in $S(l)$ which obviously is not in agreement with the experimental data. Furthermore, in the present experimental geometry the diamond-like orbit cannot be excited by *refractive* input coupling, but only by tunnelling – the resulting intensity is much lower than for refractive coupling, and is too small to account for the experimental observation the more so as we will see that refractive coupling to other orbits *is possible*. The same applies to other orbits like rectangular/trapezoidal modes or whispering-gallery orbits that are either unstable or can only be excited with evanescent coupling. We are therefore lead to consider another scenario, namely the interference of rays from multiple orbits as explanation for the observations in [130].

In our ray-tracing simulations we focus a two-dimensional geometry representing the quadrupolar cross-section of the fibre used in the experiment, see Eq. (10.1) and Fig. 10.1. The incoming beam is discretized into a sufficiently high number of equally spaced parallel rays. For simplicity we employ a rectangular beam profile that illuminates the whole lower left part of the fibre. The intensity fraction of each ray that penetrates into the quadrupole is given by Fresnel's formula[3] (7.5) for TE polarized light, its angle by Snell's law (7.2). The dynamics of each ray is then governed by the laws of a “Fresnel Billiard” [132, 133], that is, by straight propagation, specular reflection at the quadrupolar shaped boundary, and evolution of the intensity according to Fresnel's law for reflection and transmission. We assume perfectly reflecting walls for angles of incidence χ larger than the critical angle $\chi_c = \arcsin(1/n)$, and exclude leakage due to quantum tunnelling.

In the simulation, each ray of the incoming beam is traced numerically to construct the interference pattern [131, 132]. For angles $\chi < \chi_c$ we allow for refractive escape of the part of the ray that is determined by Fresnel's transmission amplitude, see Eq. (7.5), but follow further the remaining part inside the quadrupole until its intensity falls below a threshold of 10^{-6} of the initial intensity due to subsequent subcritical reflections. For the transmitted part, we determine the far field angle of the leaving ray again by Snell's law.

In Fig. 10.3 we show a couple of typical trajectories that are found upon scanning of the incoming beam. Due to the finite eccentricity and the finite beam width we find not only whispering gallery orbits. The typical orbit rather enters and escapes (by refraction) around the points of highest curvature of the quadrupole, as known from the study of asymmetric resonance cavities [132]. In particular, we find rays that undergo several polygonal-like round-trips (in which they come closer to the centre of the quadrupole than whispering gallery orbits) before their intensity eventually drops below the threshold. This process of intensity loss may happen at one single reflection after a few round-trips or (more likely) upon a couple of subsequent reflections and transmissions. Although each ray of the incoming beam follows another orbit in the *chaotic region of phase space*, the distribution of the orbit lengths, measured from entering the fibre until escape, is (surprisingly) sharply peaked at integer multiples of half the (mean) length of a round-trip. The reason for this lies in the preferred escape points near the highest

---

[3] Curvature effects may be neglected due to the large size parameter of the experiment $R_0 \gg \lambda_0/n$.

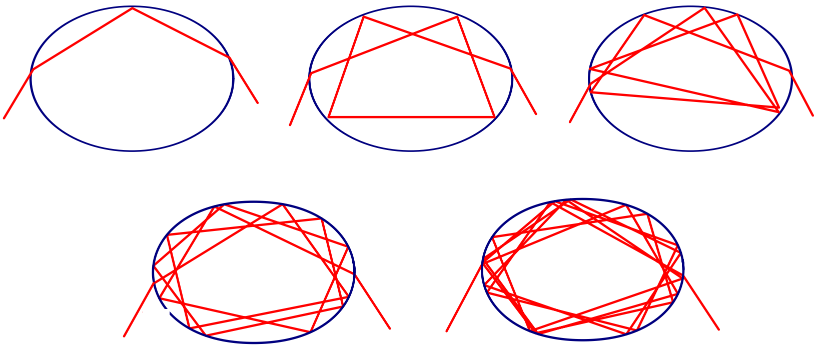

Figure 10.3: Orbits contributing to the multiple-beam interference scenario in the magic window. The orbits with 0.5, 1.5, and 2.5 round-trips (top row) come rather close to the centre of the quadrupole. In contrast, orbits exhibiting more round-trips before refractive escape (bottom row) rather resemble whispering-gallery type orbits.

wall curvature that the ray encounters every half a round-trip. Orbits with approximately 0.5, 1.5, 2.5 (top row) and 3.5, 4.5 (bottom) round-trips are shown in Fig. 10.3. These (and few longer) orbits contribute to the far-field interference for an output angle in the magic window. More precisely it is the existence of such a series of orbits that allows the filter-characteristics window in the far-field. We will see below that all orbits are excited by a rather small fraction of the incident laser beam. A similar interference effect with integer round-trip orbits is expected at the high curvature region near the incident laser beam but not accessible in the present experimental setup.

The primary result of the ray-tracing simulation are the ray trajectories, their escape points and geometrical path lengths $\widetilde{L}$, their output (transmission) intensities, and their far-field angle θ_o. The input angle is fixed at $\theta_i = 60^o$. We have neglected both L_{ext} and L_{phase} in the theoretical data analysis. These contributions to the optical length are of the order of one or several wavelengths, and are certainly smaller than the uncertainty in the fibre size or fabricational variation of the fibre cross-section. Of course, we cannot expect a *quantitative* agreement between theoretical and experimental interference pattern that really depends on the absolute optical lengths. However, in the length difference spectra $S(l)$ the corrections due to L_{ext} and L_{phase} will be small and we will use $L \approx n\widetilde{L}R_0$ in the simulations.

Since the filter-characteristics was found in the *far-field* total intensity where the detector is placed at a distance large compared to the cavity radius $R_0 \approx 82\,\mu m$, the precise *position* where the ray leaves the cavity is of no importance and the far-field angle θ_o alone determines whether a ray contributes to the magic window or not[4]. Accordingly, we analyse the ray-tracing data by summing up the intensities of geometrical path length that leave the cavity under a certain far-field angle θ_o. The result is intensity histogram plot ("Fresnel-weighted" histogram)

---

[4] In contrast, in a near field measurement (usually done with a focussing lens) a narrow interval of output positions is sampled, with a rather large range of output angles.

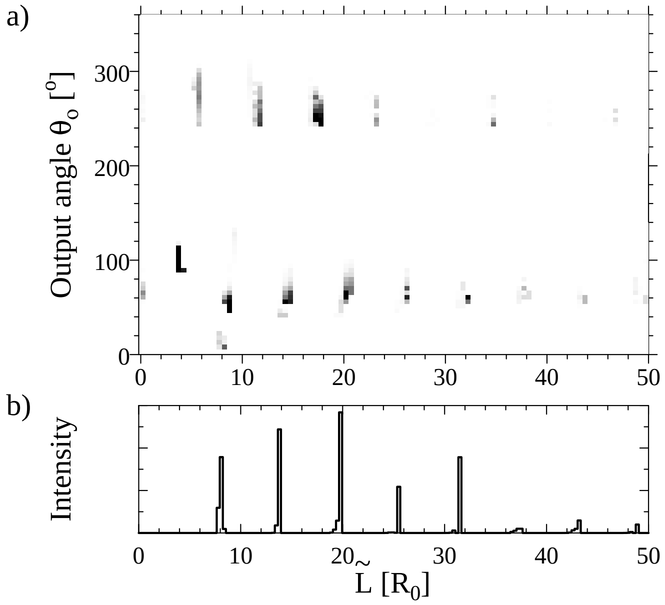

Figure 10.4: Results of the ray-tracing simulation. a) Intensity histogram showing the distribution of orbit lengths $\widetilde{L}$ vs. their output angle θ_o. The gray scale indicates the intensity (black for maximal intensity). The input angle is fixed at $\theta_i = 60^o$. b) Intensity vs. orbit length $\widetilde{L}$ at a specific detector position in the "magic window"obtained by integrating the above histogram over a narrow interval of output angles, $58^o < \theta_o < 62^o$. The result depends, of course, on the particular choice of these values; the qualitative features remain, however, unaffected. If external path differences are neglected this quantity is equivalent to the length distribution $T(L)$.

shown in Fig. 10.4a. It is (up to the factor R_0 of the unit length) the far-field-angle resolved version of the length spectrum $T(L)$ defined in Eq. (10.2) if we neglect external paths and phase effects. Clearly, there are two preferred output regions corresponding the high curvature points of the fibre. At most output angles there is low intensity that arises from short length $\widetilde{L}$. As for the region opposite the laser illuminated side ($\theta_o \approx 50^o$), we find a small ("magic") window with rather equal contributions from orbits up to 5.5 round-trips. This becomes clear in the histogram of Fig. 10.4b that was obtained by integrating the intensity-weighted lengths over a small range of far-field angles corresponding to the angle range covered by the detector. This quantity is equivalent to the length distribution $T(L)$ (again, up to the factor R_0 of the unit length and if external paths and phase effects are neglected). The peaks in Fig. 10.4 are easily found to correspond to orbits as shown in Fig. 10.3. After converting the geometric length $\widetilde{L}$ into optical length L, we obtain from $T(L)$ the length-difference spectrum $S(l)$ by self-convolution, and by Fourier transformation[5] the resulting interference pattern $J(k)$ as function of the wave vector $k_0 = 2\pi/\lambda_0$, cf. Eq. (10.3). The results for the theoretical length difference spectrum and the resulting interference pattern are shown in Fig. 10.2d and c.

Qualitative agreement between experiment and theory is most easily checked by comparing

---

[5] The Fourier transformations and convolutions are performed using the Fast Fourier Transform (FFT) method as described in [123].

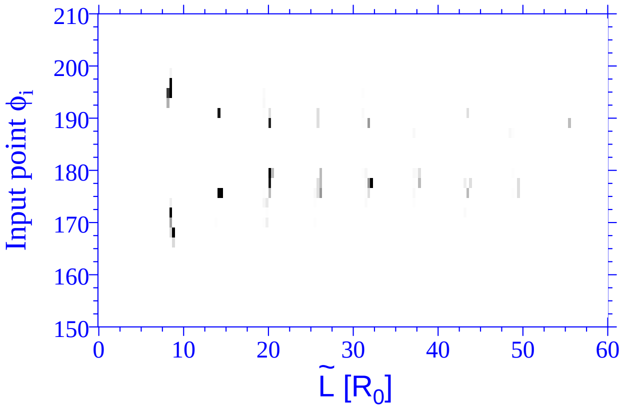

Figure 10.5: As Fig. 10.4, but now the different rays of the input beam are resolved: the vertical axis represents the input point of the individual incident rays, parametrized by their polar angle ϕ w.r.t. the main cavity axis. The input angle is again fixed at $\theta_i = 60^o$, the gray scale denotes the intensity for output angles in the window $58^o < \theta_o < 62^o$. This plot shows that only certain parts of the incoming beam contribute to the interference process.

the length-difference spectra $S(l)$, Fig. 10.2b and d. The main feature, namely a number of roughly equally spaced peaks with comparable intensity, but very little intensity at larger lengths, is nicely reproduced by the ray-tracing data.

As mentioned above, one cannot expect to reach a quantitative agreement with experiment due to the uncertainty in experimental parameters like size and eccentricity of the fibre and angle of the illuminating laser beam. The precise interference pattern depends strongly on these parameters, in particular it is extremely sensitive to length changes of the order of the light wavelength. We have checked that the interference pattern depends only slightly on the numerical discretization procedure used for the incoming beam.

It is important to point out that the far-field interference arises from orbits which have different input points on the cavity wall, i.e., the interfering rays come from different parts of the incoming beam. This becomes clear if we plot an amplitude histogram for far-field angles in the "magic window", but now as function of the input point, see Fig. 10.5. This is now the input-point resolved version of the length spectrum $T(L)$ where we can identify the parts of the incoming beam contributing to the interference. Two things are found: only a small part of the beam contributes, and the contributions for different orbit lengths originate from different (relatively small) parts of the (relatively broad) incident beam. Thus, the filtering effect will depend on the beam profile and will disappear when using more focussed laser beams not hitting a certain range of input points ($175^o < \phi_i < 195^o$ in Fig. 10.5).

By varying input and output angles, the simulation data clearly show that in most situations rays from all parts of the incident beam travel in polygonal cavity orbits only for a very short time (up to 2 round-trips) before they leave the cavity via refraction, mainly in the high-curvature regions. Only for a narrow range of input angles an appreciable part of the beam leads to polygonal orbits with a longer lifetime, which then are refractively output-coupled after a larger number of round-trips into a narrow window of far-field angles. The far-field output

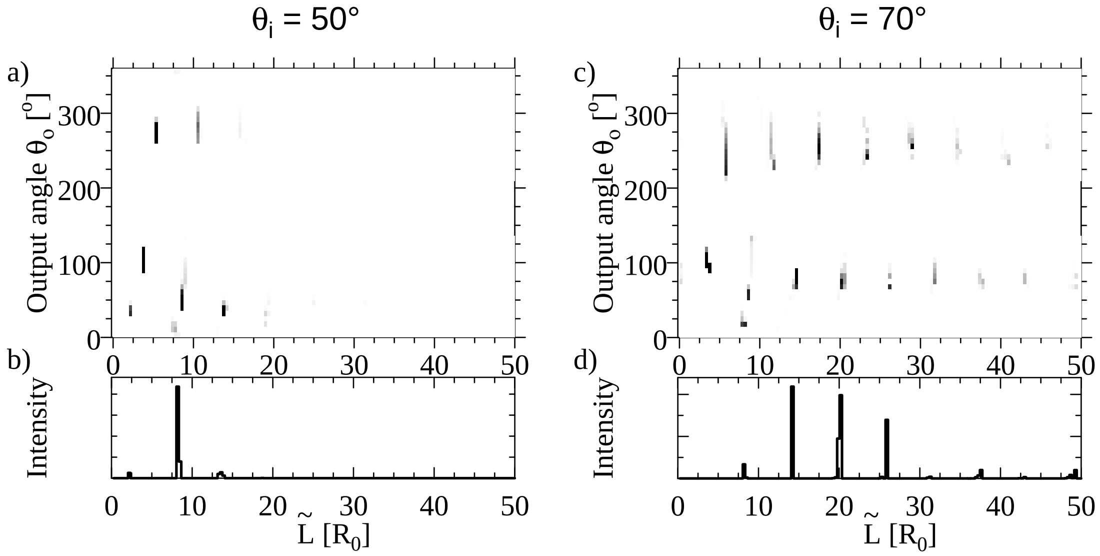

Figure 10.6: Results of the ray-tracing simulation as in Fig. 10.4, but now for input angles a), b) $\theta_i = 50^o$ and c),d) $\theta_i = 70^o$. a),c) Intensity histograms illustrating the distribution of orbit lengths $\widetilde{L}$ vs. their output angle θ_o. Whereas for $\theta_i = 50^o$ the filter effect practically disappears (a), it persits when the input angle is increased (c). This becomes clear when integrating these histograms over a narrow (detector) window of output angles, $41^o < \theta_o < 45^o$ in b), and $66^o < \theta_o < 70^o$ in d).

angle window depends sensitively on the input angle, so we predict that the "magic window" as observed in [130] will move (in the far-field angle) with varying input angle of the beam. In particular, for $\theta_i = 70^o$ we found the magic window at output angles 10° smaller than for $\theta_i = 60^o$, whereas for $\theta_i = 50^o$ the filter effect almost disappears. This corresponding far-field-angle-resolved length spectra are shown in Fig. 10.6.

We summarize the ray-tracing simulations by pointing the conditions that have to be met in order to observe the cavity filter effect:

1. A finite eccentricity of the fibre is needed to produce (chaotic) orbits which come close to the centre of the quadrupole. These modes leave the cavity by refraction preferably near the points of highest curvature.

2. The intensity loss per round-trip should be neither too small nor too large. In the former case, too many individual orbits (with slightly different lengths) contribute to the far-field interference leading to an incoherent response, whereas in the latter case the number of contributing beams is too small to produce a sharp interference pattern. This puts constraints on the refractive index of the fibre.

We have performed simulations with other fibre geometries and refractive indices which confirm both the points above: using for example a fibre of "normal" glass ($n = 1.5$), the filter effect disappears because the rays are lost too fast due to the higher critical angle ($\chi_c \approx 42^o$ instead of 34° for the high-index fibre) which implies poorer total internal reflection confinement.

To conclude this section, we state that a *ray*-tracing model well describes the main features found in the experiment [130]. In particular, the range of input and output angles, where far-field interference with filter characteristics can be observed, is rather small as was observed in the experiment ("magic window"). Moreover, the analysis of the length-difference spectrum allows for a clear distinction between our model of interfering rays from different orbits and other scenarios involving a single orbit only. It would be interesting to compare the results above with the case of TM polarization because of the special property of TE polarized light that allows for a very efficient Brewster-angle coupling to (and decoupling from) the fibre. As discussed in Section 7.1.2 light incident under the Brewster angle $\chi_{\mathrm{Br}} = \arctan(1/n)$ are completely transmitted into the medium they are incident on. We also point out a possible application of the filter effect for beam and/or cavity diagnostics.

10.2 Microlaser in the ray picture

Lasing in deformed microcavities has received increasing interest in the last years. Besides the paradigmatic example of the lasing "bow-tie" [135] in an oval-shaped cavity and, of course, lasing whispering-gallery-type modes (WGMs), another example for present work on microlasers are hexagonal fibres [84]. One (general) goal is to decrease the laser threshold power in order to eventually achieve lasing operation *without special activation.* The field of potential applications of those materials is huge and comprises "lasing" varnishes as well as communication devices.

At this point it is useful to make the distinction between the two basic components of a laser: first, there is the active material in which the laser light is generated by an external source such as electric current. The second part is the laser *resonator* that contains the active material and provides the feedback for the stimulated emission of light. It determines the special features of the emitted light such as its power, beam directionality, or spectral properties. As for the lasing mechanism, dye lasers and semiconductor lasers for example of the quantum cascade type [85] are widely used, mainly with Fabry-Perot resonators that, in turn, are the most common resonators. In the example of the bow-tie lasing mode a quantum cascade *microdisk* laser was used, other realizations are cylinders or droplets.

In this context we have to address the *coupling mechanism* between resonator and environment. The first possibility is *evanescent* coupling, used for example between optical cavities where light is confined by total internal reflection in WGMs and other elements like prisms [64], or fibres [68]. The general idea is a close approach (of the order of $50 \ldots 500\,nm$ in [64]) of the two elements such that light couples in or out the cavity. However, having in mind possible applications that require the coupling of *curved* disks and *planar* waveguides, the evanescent coupling requires a very precise fabrication with a gap spacing in the sub-μm range that is hard to achieve in mass production. Another possibility is to couple to modes that violate total internal reflection at certain reflection points upon reflection at an air-filled gap [136], that, however, results in the same technical difficulties. Here, we will introduce a completely different and new type of coupling. The method we suggest [137] does not require violation of total internal reflection or fabrication of a microgap. Rather, the waveguide directly plugs into the cavity, and the coupling *strength* is controlled via the *overlap* between the wave functions in the cavity and the waveguide.

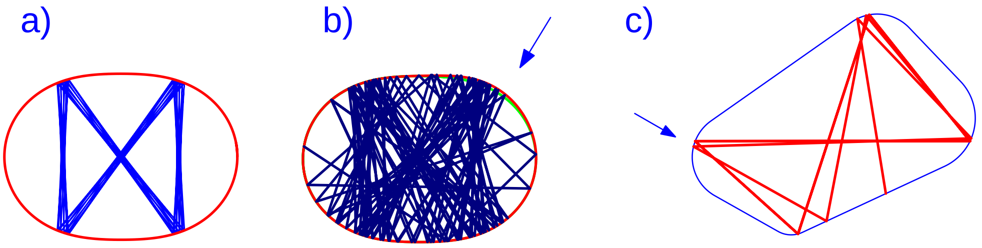

Figure 10.7: a) Stable bow-tie orbit in a quadrupolar billiard [135] with four equal points for refractive escape. In b) the shape was slightly deformed at the top right corner (arrow) in order to favour refractive output at this corner by, e.g., a decreased angle of incidence. The stability of the orbit is lost. The same happens in c) where a billiard consisting of four circles connected by their common tangents is constructed around a bow-tie skeleton. It is impossible to stabilize a bow-tie-like orbit in a billiard of this type, which will always possess a chaotic phase space [138].

In the following, we are not interested in the lasing mechanism but exclusively in the special output characteristics of certain resonator modes depending on the shape of the resonator. We will first discuss the implications of a coupling mechanism based on violation of total internal reflection, and then discuss the advantages of the integrated waveguide mentioned above.

Theoretical [132, 108] as well as experimental [135] investigations on asymmetric microcavities have highlighted the interesting properties of systems with reduced symmetries. We already discussed the lasing bow-tie mode [135] in an oval- or quadrupolar[6]-shaped cavity, see Fig. 10.7a. The out-coupling mechanism relies on the (slight) violation of total internal reflection at all four bouncing points. Since the mode can be followed in either direction, there are eight beams that leave the cavity and carry the output power.

It is tempting to think of a microlaser with just one output region where all power is concentrated. An obvious starting point is, of course, to deform the well-known bow-tie orbit in such a way that one corner is preferred for refractive escape because its angle of incidence is smaller than the critical angle and the angles of incidence at the other corners all lie above the critical angle. Two attempts are illustrated in Fig. 10.7. In Fig. 10.7b the quadrupolar shape is deformed at one corner (marked by the arrow) in order to locally decrease the angle of incidence – immediately resulting in a loss of stability. In c) a bow-tie based orbit with the desired properties was chosen as skeleton. It is, however, impossible to stabilize it by a billiard composed of four circles and their common tangents as indicated in the example of Fig. 10.7c.

As mentioned above, one future application of microlasers might be devices that couple light at a point where total internal reflection is frustated from the cavity via an air-filled gap into another cavity, or glass fibre, etc. [136]. Therefore, we look for regular orbits the reflection points of which have well-separated angles of incidence. Nanotechnologies allow nowadays to produce cavities of nearly any shape or even the annular type. In particular, we firstly choose a dipole-tripole combination, with a polar-coordinate representation

---

[6] The quadrupole is defined in Eq. (10.1); $\epsilon = 0.168$ in Fig. 10.7.

$$r(\phi) = R_0 \ (1 + \epsilon_1 \cos 2\phi + \epsilon_2 \cos 3\phi) \ . \tag{10.4}$$

A second model cavity is based on an elliptical billiard where we removed a part of the ellipse by a cut parallel to the minor axis and a distance x_w away from the centre of the ellipse. We define the ellipsoidal shape by the eccentricity ϵ_e that is related to the minor axis b via $b = (1-\epsilon_e^2)^{1/4}$ and to the major axis $a \overset{\text{def}}{=} 1/b$. The focal length is $c = \sqrt{a^2 - b^2}$, and we choose $x_w = -0.5c$. Eventually, we will use the annular billiard discussed in Chapter 9 as third example.

All shapes allow for a great variety of stable periodic orbits (cf. also [102]). Deformed cavities mostly have *similar* angles of incidence at all reflection points. However, for special parametrisations of the dipole-tripole cavity and the cut-ellipse, well separated stability islands were found [137]. They are shown in Figs. 10.8, 10.9. In the case of the dipole-tripole billiard the emergence of a stability island *below* the line of total internal reflection is bound to the (intermittent) separation of the period-three orbit islands into two around the special parameter choice $\epsilon_1 = 0.02, \epsilon_2 = 0.03$. In contrast, the triangular orbit found in the cut ellipse possesses well-separated stability islands over a wide parameter range ($\epsilon = 0.3 \ldots 0.9$, $|x_w| = 0.25 \ldots 0.85$, see [137] for details). We mention that the point where total internal reflection is violated lies mostly on the *flat* side of the microresonator.

Another type of suitable orbits with possibly highly favourable properties is known from the investigation of the annular billiard, where stable orbits with (nearly) normal incidence at the outer boundary exist, cf. Figs. 9.2 (centre of top and bottom row) and 9.17 (orbits on the right), and the corresponding *resonant modes* were also seen, cf. Figs. 9.18 or 9.25D. Note the freedom in combining different refractive indices – together with the geometric parameters this constitutes a large parameter space that allows for a suitable adjustment of the properties. Normal incidence removes the problem of the reversed path that (under typical pumping conditions) takes away half of the output intensity into another direction that normally cannot be used.

Let us now turn to the alternative coupling method that relies on a *monolithically integrated light valve* [137] instead of violation of total internal reflection. Here, resonator and waveguide are *directly* connected. The amount of light that is coupled out is controlled via the overlap between the cavity and waveguide that is determined by the ratio of their heights. In this situation violation of total internal reflection seems to be a disadvantage because then light may leak out of the cavity without being used. However, in Fabry-Perot quantum cascade lasers the amount of Fresnel reflected light with normal incidence, given by $R_\perp = (n-1)^2/(n+1)^2$ [72], is sufficient to ensure laser operation for refractive indices $n \approx 3.3$.

Besides saving the production of an air-filled microgap, the great advantage of a monolithically integrated light valve is that much more orbits are candidates for lasing modes, and the tolerance against fabrication errors is much better. This applies in particular when reflection points at the *device symmetry axis* are chosen because their position is *not* affected by slight variation of the orbit as might be caused by fabrication variance. There is a great variety of stable orbits that fulfill this requirement and have sufficiently large islands such that one might expect lasing of the corresponding mode. For example, the regular trajectories for the dipole-tripole billiard and the cut ellipse discussed above belong to this class of orbits. The annular

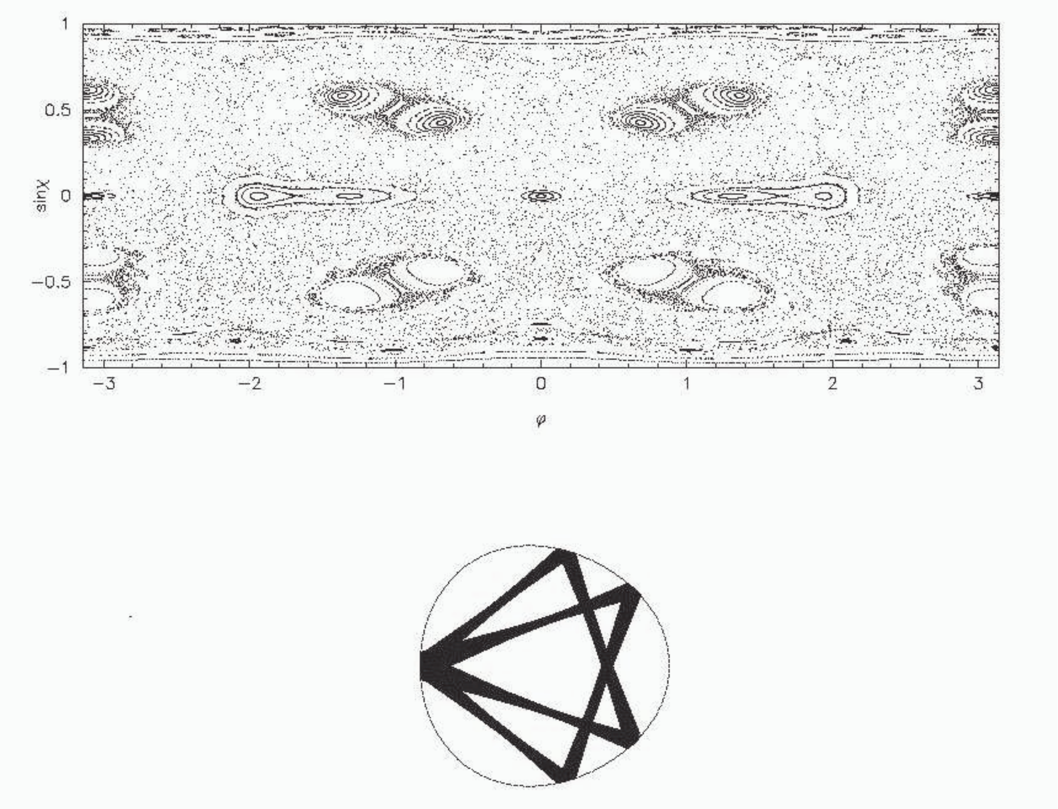

Figure 10.8: Poincaré section for a billiard of the dipole-tripole shape, Eq. (10.4). ϕ is the angle between the (Cartesian) x-axis and the boundary point and runs from 0 to π in the upper half-plane, and from 0 to $-\pi$ in the lower one. This shape supports a triangular orbit with nearly equal angles of incidence at all three reflection points in a wide parameter range (ϵ_1, ϵ_2). However, around $\epsilon_1 = 0.02$ and $\epsilon_2 = 0.03$ the corresponding island splits in accordance with an emerging double-triangular orbit where the angles of incidence form well separated and relatively big islands around $\sin\chi = \pm 0.5$. The lower-most island (at $\phi = \pm\pi$) extends down to $\sin\chi \approx 0.3 \equiv 1/n_{\mathrm{sc}}$ for typical semiconductor with refractive index $n_{\mathrm{sc}} = 3.3$. This is resembles the situation of the lasing bow-tie [135] where total internal reflection was violated in a small part of the corresponding phase-space structure. This region was just small enough to keep the mode lasing and large enough to allow a suitable amount of power to be coupled out. In the present situation, fine-tuning of ϵ_1, ϵ_2 might allow for a similar operation mechanism.

billiard proves to be a very rich and promising system in this respect, too, see the ray orbits and wave patterns shown in Chapter 9!

This brings us to a first extension of the ray model in microlasers, namely to consider the resonant states of the cavity that are potentially interesting as lasing modes. These will be modes of intermediate width where the relation between output power and gain necessary to assure lasing operation is most favourable. In this respect we recall that the S-matrix description will be especially useful here, because this approach is well-suited to determine the wave vectors of resonances of intermediate width.

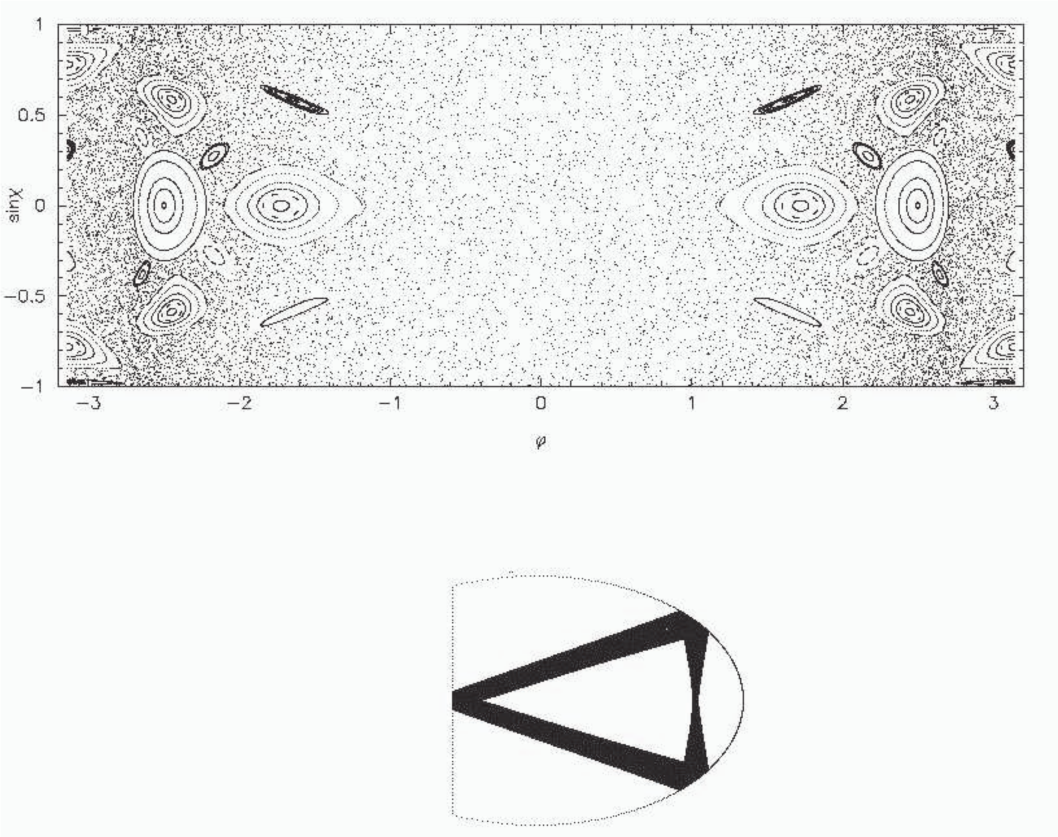

Figure 10.9: Poincaré section for the cut-ellipse billiard described in the text, $\epsilon_e = 0.8$; ϕ is defined as in Fig. 10.8. The stable islands corresponding to the triangular orbit are highlighted by a large number of clockwise-travelling ($\sin\chi > 0$) travelling trajectories started. The island representing the smallest angle of incidence appears splitted at $\phi = \pm\pi$. It lies around $\sin\chi \approx 0.3$ which makes this an attractive shape for lasers based on semiconducting materials as well. Furthermore, the islands are well separated in $\sin\chi$ and persist over a rather big parameter range.

A second extension is necessary when one really wants to take into account the special properties of *lasers*, namely the active (lasing) material or the pumping mechanism. For whispering gallery modes efforts towards this direction are reported in [139], where the non-linear interaction between the light field and the lasing medium was included in the description. The ideas presented in this section are guided by the example of the lasing bow-tie [135] where the ray-model approach proved to work well. However, future experiences and justifications for these approximations are needed.

An important question is to determine the far-field radiation characteristic of the laser, i.e., the angular dependence of the output power, especially if the conventional coupling via an air-filled gap or to vacuum is used. Assuming refractive out-coupling of rays might be misleading in certain cases [83]. Therefore, an interesting subject of further studies will be a situation where a *wave source* (described, e.g., by a singularity originating from a Bessel function) is placed within the cavity. The advantage of this setting is its close relation to experimental pumping situations in the sense that only *real* wave vectors enter the description. Eventually, we mention that it is not clear *a priori* which mode will start lasing once the system is pumped, pointing out yet another peculiarity of real microlasers that is beyond the possibilities of the ray model. However, with further experiences on the importance of classical phase-space properties (concerning, e.g., the size of stable islands) for lasing in microcavities, the ray model might become a valuable tool in microlaser design.

11 Summary & Outlook

In this work we have investigated various wave phenomena in mesoscopic systems of electronic and optical nature. We found them to be rich model systems, that largely inspire the field of mesoscopic physics and quantum chaos, both in theory and experiment.

In Part I, we have been interested in interference effects caused by Aharonov-Bohm and, in particular, geometric phases. Geometric phases are determined by the topological properties of the system and may accompany the transport of electrons with spin in the presence of inhomogeneous magnetic fields besides Aharonov-Bohm-like oscillations. Electrons in one-dimensional rings allow for an exact solution of the Schrödinger equation in the general non-adiabatic situation, taking into account all spin-flip effects of the electrons. This enabled us to consider spin-dependent transport in one-dimensional rings subject to a rotational invariant, non-uniform, magnetic field using a transfer-matrix formalism where unitarity is fully respected, in contrast to other approaches [34]. Studying the crossover between the diabatic and adiabatic regime, we have investigated the onset of geometric phase effects as adiabaticity is approached.

Application of the method to situations realized in recent experiments, where a central micromagnet is used to create a magnetic field with inhomogeneities on a mesoscopic scale [35], revealed the importance of adiabatic conditions in order to observe clear signs of geometric (or Berry) phases. Though this regime is hard to achieve with present micromagnets, stronger non-uniform magnetic fields should allow for the conclusive observation of geometric phases in electronic ring structures in future experiments. Those fields might be generated by suitably arranged ferromagnetic particles [50] or a perpendicular electric current through the ring as realized in the context of Oerstedt switching [51].

For mesoscopic rings subject to an in-plane rotational invariant magnetic field our calculations predict the existence of a *novel* spin-flip effect in the phase-coherent regime at low temperatures. One-dimensional analytical transfer-matrix and two-dimensional numerical tight-binding computations give quantitative agreement in the case of transport in one transverse channel. This assures the (qualitative) significance of one-dimensional calculations, where the spin-flip effect was proven analytically. The spin-flip effect exists in adiabatic as well as in non-adiabatic situations. It might become conceptually important in future spintronics development. In this context the question arises, whether the requirement of rotational invariance of the in-plane magnetic field might be relaxed to axial symmetry w.r.t. the lead axis. Two-dimensional calculations may point towards this direction.

Motivated by recent advances in the fabrication of high-mobility semiconductor heterostructures, we focussed here on ballistic systems. Extension of the investigations to diffusive systems is left for future studies. In particular, it will be interesting to address the question of conditions for adiabiticity in diffusive systems, cf. [32, 33]. Another extension of the present model involves the inclusion of the Rashba spin-orbit coupling that may be important for the description of certain semiconductor materials like InAs.

Optical mesoscopic systems were the subject of Part II, and we studied in particular the dielectric annular billiard. For the first time comparing the results of ray and wave description of this system, we deepened the understanding of this correspondence. The ray picture provides a simple method to obtain a first impression of the system properties, whereas the wave picture contributes corrections when the wavelength becomes of the order of the system size. We studied the resonances of the open system using both numerical evaluation of complex wave vectors and the S-matrix method. Within the S-matrix approach, all resonances are of the characteristic Breit-Wigner form. Families of resonances, characterized by (generalized) quantum numbers, are easily identified, cf. Chapters 7 and 9. Employment of the S-matrix method goes considerably beyond the method used in [108], where the variation in the plane-wave response at a single reference point was used to identify signatures of resonances.

The ray approach to the annular billiard was based on the investigation of the hard-wall and the refractive system. In the latter we kept the outer boundary fully reflecting, but Fresnel's law at the inner boundary was approximated by a stepwise dependence of the reflection coefficient on the angle of incidence (with full transmission below the critical angle and zero otherwise). *Combining* both models we gained a good understanding of the real-space appearance of the resonant modes. It will be challenging to extent the refractive model to account for more realistic Fresnel laws at both the inner and the outer boundary. In particular, it will be interesting to study the influence of the Brewster angle (cf. Fig. 7.5) that occurs for the case of *TE polarized* light that was not in the discussion of the ray-wave correspondence in the annular billiard. Due to reduced reflectivity near the critical angle the light will be less confined for those angles of incidence, and the resonant modes will, consequently, be affected, too. For further studies it will be very helpful to establish the ray-wave correspondence in phase space by representing the resonant modes as Husimi or Wigner functions. This will, possibly, also illuminate the structure of the underlying classical (ray) phase space.

An important extension would be to determine the *complex* wave vectors of the resonances (poles) of the eccentric annular billiard, especially if the focus is on the radiation characteristics. Alternatively, and in particular when microlasers are addressed, we suggest to place a source within the system which might simulate the laser pumping. In this context we refer to the Petermann factor [140] that describes the enhancement of the quantum-limited line width of a laser cavity due to the non-orthogonality of the cavity modes. It was studied for integrable and chaotic resonators [140], and it will be interesting to examine it in a mixed system like the annular billiard.

An outstanding property of optical systems is that their openness can be controlled by varying the refractive index of n of the cavity (leaving the surroundings unchanged at $n_0 = 1$). The cavity is transparent for $n = n_0$, whereas in the limit $n \to \infty$ the closed system with complete confinement by total internal reflection and just tunnelling escape is approached. Besides large refractive index, the system can be closed by including extra reflecting layers at the interface boundaries [107]. Closed systems are well-studied in the context of quantum chaos and the results, e.g., for the resonance counting function, are well-known. It will be interesting to investigate the behaviour of those quantities under opening of the system. Also, a systematic study of the evolution of the resonance width with increasing leakage ($n \to n_0$) as well as, for fixed refractive indices, increasing eccentricity of the annular billiard, remains for further studies. The inside-outside duality [92] provides a relation between the eigenvalues of the closed system and the resonances of the corresponding scattering problem, and a generalization towards optical systems is an open problem. Another question that is not especially discussed in the present work is the case of very high wave vectors, e.g., wave solutions in the semiclassical, or ray, limit [141] and the resolution of the phase-space structure with increasing wave vector. – As an example for the considerable potential of open, dielectric systems w.r.t. the field of quantum chaos we refer to quadrupolar-glass-fibre experiment that is interpreted in Section 10.1. An possible extension of optical microcavities is, e.g., their combination with a central quantum dot, where the coupling between whispering-gallery modes and the quantum dot can be studied.

New analytical expressions for Fresnel coefficients at curved interfaces were derived within a joint treatment of *both* polarizations, going beyond recent work [108]. Furthermore, we gave for the first time a ray-picture based qualitative explanation of the corrections to Fresnel's laws necessary at curved interfaces by taking into account the Goos-Hänchen effect. Performing the calculations, we find satisfying *quantitative* agreement with the wave picture results. The Goos-Hänchen shift is a lateral shift of the reflected beam upon total internal reflection of light. An interesting question is to study this effect in the case of Andreev reflection and at phase conjugating mirrors, in particular also the accompanying time delay [121].

Motivated by the principal agreement of the ray and wave picture results throughout Part II of the thesis we addressed the design of microlasers. We suggest a novel coupling mechanism between microcavity and subsequent wave guide [137] that does not require the violation of total internal reflection, in contrast to other concepts [136]. Accordingly, we recommend axially symmetric cavities with a reflection point on this axis as particularly suitable for applications because of the stability of this point against fabrication variations. Regular orbits with this property were identified in microcavities of different shapes. We assume those to be the dominant modes in the refractively opened system, and verified it for the dielectric annular billiard. The exact description of the active material and the investigation of the radiation characteristics of those lasers remains a subject for future studies.

One special property of optical systems arises when we interpret Maxwell's equations for two-dimensional systems as a Schrödinger equation, namely an energy dependence of the (effective) potential and polarization-dependent boundary conditions. The effective potential depends on the refractive indices and the geometry of the system, that can be chosen to model, e.g., single-, double-, or multi-well potentials with continuously changing properties. We point out that there is an alternative interpretation of the "Schrödinger equation for light", cf. Eq. (7.11), namely by *incorporating the refractive index into the metric*, that is, into the Laplace operator. A change in the refractive index appears then as a change in the metric, the light follows the corresponding geodesics, and the phase-space volume depends on the index of refraction. This approach appears particularly suitable for anisotropic materials where the tensor nature of the dielectric constant directly translates into an anisotropic metric.

Summarizing, the present thesis has explored a number of novel aspects of mesoscopic ring structures. Part I was devoted to geometric phases in ballistic electronic systems – here the main ingredients are understood, and we focussed on particular geometries where the experimental observation of such phases might be possible in the near future. Optical systems were the topic of

Part II. Using the annular billiard as model system, initial steps were undertaken to understand the interplay of wave effects and classical chaos in optical microcavities, but much work remains to be done.

Appendix

A Conserved quantities in a closed ring

The Noether theorem states the existence of a conserved quantity for each continuous symmetry in a physical system. For the one-dimensional ring considered in Chapter 3 it is the invariance under rotations about the z-axis (that is, perpendicular to the ring plane). We show that the z-component of the total angular momentum operator L_z,

$$L_z = -i\frac{d}{d\phi} + \frac{1}{2}\sigma_z,$$

is a conserved quantity. We verify this by computing its commutator with the Hamiltonian H, see Eq. (3.3). The commutator of L_z with the kinetic term vanishes because A^{ϕ}_{em} does not depend on ϕ. The Zeeman term reads for a magnetic field $\vec{B}$ of magnitude B,

$$-\mu\vec{\sigma}\cdot\vec{B} = -\mu B \begin{pmatrix} \cos\alpha & \sin\alpha e^{-i\phi_t} e^{-i\phi} \\ \sin\alpha e^{i\phi_t} e^{i\phi} & -\cos\alpha \end{pmatrix}.$$

Therefore, we find as contributions to the commutator

$$\left[-i\frac{d}{d\phi}, \vec{\sigma}\cdot\vec{B}\right] = B \begin{pmatrix} 0 & -\sin\alpha e^{-i\phi_t} e^{-i\phi} \\ \sin\alpha e^{i\phi_t} e^{i\phi} & 0 \end{pmatrix},$$

and

$$\left[\sigma_z, \vec{\sigma}\cdot\vec{B}\right] = B \begin{pmatrix} 0 & 2\sin\alpha e^{-i\phi_t} e^{-i\phi} \\ -2\sin\alpha e^{i\phi_t} e^{i\phi} & 0 \end{pmatrix},$$

indeed indicating that the angular momentum perpendicular to the ring, composed of a orbit and a spin contribution as given in Eq. (3.12), is conserved.

We emphasize the factor 1/2 in front of the spin contribution that is related to a fundamental difference of the groups $SO(3)$ (rotations in 3-dimensional space, elements are real, symmetric 3×3-matrices) and $SU(2)$ (rotations in spin space, elements are complex 2×2-matrices of unit determinant; refer to the Pauli spin matrices as example). Although both groups possess the same Lie algebra, the periodicity of $SO(3)$ is 2π, whereas $SU(2)$ is 4π periodic expressed in the additional factor one half. Mathematically , the difference between rotations in configuration and spin space is written as $SO(3) \cong SU(2)/\mathbb{Z}_2$, where $\mathbb{Z}_2$ is the kernel of the homomorphism $SU(2) \to SO(3)$.

B Electrons in a closed ring and Aharonov-Bohm effect

In Chapter 4 we discuss the transmission probability of electrons through a one-dimensional (1d) ring coupled to current leads in terms of a transfer matrix formalism. We find Aharonov-Bohm-like oscillations under variation of a homogeneous magnetic field perpendicular to the ring

(Section 4.3). Here we will give an alternative description based on the Schrödinger equation for electrons in a periodic potential. Furthermore, we will see how the electromagnetic vector potential entering the generalized momentum gives rise to an additional phase factor (besides the dynamical phase) that leads to the Aharonov-Bohm interference effect.

In the limiting situation of zero coupling between the ring and the leads ($\epsilon = 0$, cf. Section 4.1.3) there is an analogy [27] between the electrons in a 1d ring and electrons in a 1d periodic potential, where the potential fulfills the relation $V(x) = V(x + L)$. In the ring, the role of L is taken by the circumference of the ring. The Schrödinger equation for the ring of radius $a = L/2\pi$, with x being the coordinate along the ring (again in units $\hbar = c = 1$),

$$-\frac{1}{2m}\frac{d^2}{dx^2}\xi_n(x) = \epsilon_n \xi_n(x) \, ,$$

therefore has to be solved with periodic boundary conditions $\xi_n(x) = \xi_n(x + L)$, so that we find the eigenstates

$$\xi_n(x) = A_n e^{\pm i k_n x} \quad \text{with} \quad k_n = \frac{2\pi}{L} n \, , n \in \mathbb{Z} \, , \quad \text{and} \quad \epsilon_n = \frac{k_n^2}{2m} \, .$$

If the ring is subject to a homogeneous magnetic field B_z in z-direction, we have to include the electromagnetic vector potential $\vec{A}_{\text{em}}$ into the calculation. It can be expressed in terms of the magnetic (or, Aharonov-Bohm) flux $\Phi = \Phi^{AB} \overset{\text{def}}{=} \pi a^2 B_z$ as $\vec{A}_{\text{em}} = \frac{1}{2} a B_z \vec{e_x} = \Phi^{AB}/L \vec{e_x} \overset{\text{def}}{=} A^x_{\text{em}} \vec{e_x}$, cf. Section 3.1. The Schrödinger equation now reads

$$\frac{1}{2m}\left(-i\frac{d}{dx} - eA^x_{\text{em}}\right)^2 \xi_n(\phi) = \epsilon_n \xi_n(x) \, ,$$

and due to the additional contribution the generalized momentum, the quantized k values have to be replaced according to

$$k_n \longrightarrow k^{\Phi}_{n'} = \frac{2\pi}{L}\left(n' + \frac{\Phi}{\Phi_0}\right) \, , \tag{B.1}$$

where n and n' are related by

$$n = n' + \frac{\Phi^{AB}}{\Phi_0} \, . \tag{B.2}$$

The spectrum is periodic in Φ^{AB} with period of the *flux quantum* $\Phi_0 = hc/|e| \equiv 2\pi/|e|$ (in units $\hbar = c = 1$). Therefore, it suffices to consider only to the first "Brillouin zone" $(-\Phi_0/2, \Phi_0/2)$ with width $k_0 = 2\pi/L$. Also, the interpretation in terms of a band scheme holds, see [27, 28]. In Section 4.1.3 we extend this discussion to a 1d ring that is weakly coupled to leads.

Let us now turn to the phase change in the wave function that is associated with replacing the momentum by the generalized momentum in the presence of gauge fields,

$$\vec{p} \longrightarrow \vec{p} - e\vec{A} \, . \tag{B.3}$$

Consider a free electron with wave function $\exp(i\vec{p}\cdot\vec{r})$. Its phase is changed according to

$$\theta \longrightarrow \theta - e\vec{A}\cdot\vec{r} \, . \tag{B.4}$$

We generalize the last equation to arbitrary trajectories $\mathcal{C}$ in space and obtain the accompanying phase change as

$$\Delta\theta = -e\int_{\mathcal{C}} \vec{A}\cdot d\vec{r} \, . \tag{B.5}$$

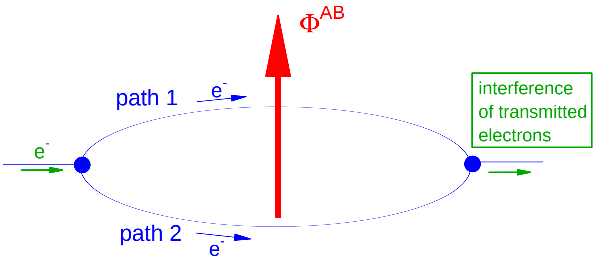

Figure B.1: Aharonov-Bohm effect in a ring subject to a magnetic flux Φ^{AB}. The interference pattern, created by the electrons travelling along the paths $1, 2$, is shifted due to the presence of a (varying) Aharonov-Bohm flux Φ^{AB}. For Φ^{AB}/Φ_0 integer, interference is constructive. Note that the arms need not to have equal lengths, cf. [26].

If we consider a closed trajectory that is splitted into two paths $1, 2$, we obtain the phase difference between the wave functions $1, 2$ as

$$\Delta = -e \oint_{1-2} \vec{A} \cdot d\vec{r} = -e \int_{1-2} \left(\vec{\nabla} \times \vec{A} \right) \cdot d\vec{S} \,, \tag{B.6}$$

where we have used Stokes' formula. In the special case of electromagnetism, $\vec{A} = \vec{A}_{\text{em}}$, we obtain

$$\Delta = -e \int_{1-2} \vec{B} \cdot d\vec{S} = 2\pi \frac{\Phi^{AB}}{\Phi_0} \,. \tag{B.7}$$

We illustrate formula (B.7) for electrons travelling along the two arms of a 1d ring of radius a, enclosing an Aharonov-Bohm flux $\Phi^{AB} = 2\pi a A^{\phi}_{\text{em}}$ (where we have now replaced the propagation along x-axis by propagation in ϕ-direction along the ring, cf. Section 3.1), see Fig. B.1. We obtain for the phase change along the first path

$$\Delta\theta_1 = -e \int_1 \frac{\Phi^{AB}}{2\pi a} \, a \, d\phi \,;$$

and for the second path, that is travelled in the opposite direction, we find

$$\Delta\theta_2 = e \int_2 \frac{\Phi^{AB}}{2\pi a} \, a \, d\phi \,.$$

The resulting *phase difference* between the two corresponding wave functions reads

$$\Delta = \Delta\theta_1 - \Delta\theta_2 = -e \oint_{\text{ring}} \frac{\Phi^{AB}}{2\pi} a d\phi = -e\Phi^{AB} \equiv 2\pi \frac{\Phi^{AB}}{\Phi_0} \,. \tag{B.8}$$

Accordingly, we find a phase shift of 2π whenever the Aharonov-Bohm flux Φ^{AB} through the ring equals an integer multiple of the flux quantum Φ_0, and a phase shift of π for half integer multiples. Hence, the shift in the conductance interference pattern is periodic under changes of the flux Φ^{AB} through the ring with period Φ_0. This effect is called Aharonov-Bohm effect [1].

C Magnetic field of a bar magnet

In this paragraph, we will derive the magnetic field of a permanent cylindrical-shaped magnet of magnetisation $\vec{M} = M\vec{e_z}$, see Fig. C.2. This problem of magnetostatics [53, 54] does not involve any currents nor electric fields, so we can think of the magnetic field $\vec{H}$ to originate from a magnetic scalar potential Φ_M in analogy to the situation one is familiar with in electrostatics[1].

The magnetic induction $\vec{B}$ is given by the sum

$$\vec{B} = \mu_0(\vec{H} + \vec{M}) \,, \tag{C.1}$$

with μ_0 being the permeability of vacuum, and the magnetic field $\vec{H}$. In regions where $\vec{M} \neq 0$, the magnetic induction is therefore not any more proportional to the magnetic field $\vec{H}$, but depends via (C.1) on the magnetization $\vec{M}$.

Maxwell's equations now read

$$\begin{aligned} \vec{\nabla} \times \vec{H} &= 0 \rightarrow \vec{H} = -\vec{\nabla}\Phi_M \,, && \text{(C.2)} \\ \vec{\nabla} \cdot \vec{B} &= \mu_0 \vec{\nabla}(\vec{H} + \vec{M}) = 0 \,. && \text{(C.3)} \end{aligned}$$

Inserting the first into the latter equation, we obtain

$$\vec{\nabla}^2 \Phi_M = \vec{\nabla} \cdot \vec{M} \overset{\text{def}}{=} -\rho_M \,, \tag{C.4}$$

the magnetostatic Poisson equation with ρ_M the effective magnetic charge density [54] defined in analogy to the charge density in electrostatics. Since Maxwell's equation $\vec{\nabla} \cdot \vec{B} = 0$ presupposes that $\vec{B}$ is continuous and differentiable, in the present situation of a bar magnet where $\vec{M} \neq 0$ only within the magnet, it is replaced by the condition that now the surface divergence of $\vec{B}$ vanishes, that is [53],

$$B_n + B_{n'} = 0 \,, \tag{C.5}$$

where B_n and $B_{n'}$ are the normal components of $\vec{B}$ on the surface. This equation yields with Eq. (C.3) that $H_n + H_{n'} = -\vec{M} \cdot \vec{n} \overset{\text{def}}{=} -M_n$, where for the cylindrical magnet with $\vec{M}$ pointing along the cylinder axis the right hand side is nonzero only for the top and botton boundary surfaces. Inserting Eq. (C.2), $\vec{H} = -\vec{\nabla} \cdot \Phi_M$, we eventually obtain the surface condition

$$\frac{\partial \Phi_M}{\partial n} + \frac{\partial \Phi_M}{\partial n'} = M_n \,. \tag{C.6}$$

Adding $\Phi_M = 0$ as a boundary condition at infinity, the solution to Eqs. (C.4, C.6) is [54, 55]

$$\Phi_M(\vec{r}) = -\int \frac{\vec{\nabla} \cdot \vec{M}(\vec{r'})}{4\pi\,|\vec{r} - \vec{r'}|} d^3r' + \oint \frac{M_n(\vec{r'})}{4\pi\,|\vec{r} - \vec{r'}|} d^2r' \,. \tag{C.7}$$

Here, $\vec{r}$ is the vector to the reference point, and $\vec{r'}$ is the vector that scans the magnetic polarisation (in the magnet), see Fig. C.2. The first term sums all magnetic densities ρ_M *inside* the magnet (and is the solution of the Poisson equation alone), the second term covers the surface densities on its *boundary*. For our bar magnet, M = const., and the first term vanishes. The contributions to the second term stem from the two end surfaces, see above. Considering a bar magnet of height $2H$ and radius R', approximate integration of (C.7) for large distances $|\vec{r}| \gg H, R'$ leads to the *far-field* expression

$$4\pi\, \Phi_M(\vec{r}) = M\pi R'^2 \left(\frac{1}{|\vec{r}_1|} - \frac{1}{|\vec{r}_2|} \right) \,, \tag{C.8}$$

---

[1] As usual, we use SI (or MKSA) units as in [53].

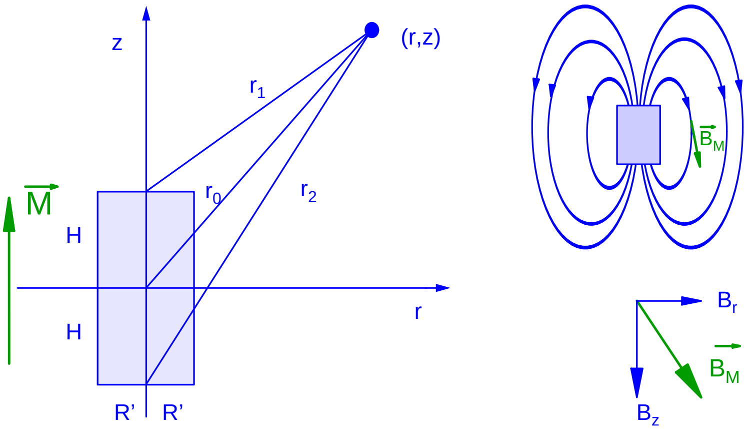

Figure C.2: Bar magnet of longitudinal magnetization M with a point (r, z) of reference on the outside. We use cylindrical coordinates (r, ϕ, z) and rotational symmetry about the z-axis. On the right, the magnetic field outside the magnet is sketched.

with $\vec{r}_1$ ($\vec{r}_2$) pointing from the top (and bottom, respectively) end surface to the reference point, cf. Fig. C.2. Series expansion of $1/|\vec{r}_1|$ and $1/|\vec{r}_2|$ gives the final result for the magnetic scalar potential in the far-field as

$$4\pi\,\Phi_M(\vec{r}) = 2\pi\,M\,HR'^2\,\frac{z}{r_0^3}\,, \tag{C.9}$$

which is the familiar and expected dipole result, with $r_0 \overset{\text{def}}{=} \sqrt{r^2+z^2}$ denoting the distance of the reference point (r, ϕ, z in cylindrical coordinates) from the centre of the bar. From (C.2) we obtain for the magnetic field in the far-field or dipole approximation

$$\vec{H}(\vec{r}) = -\frac{M}{2}HR'^2\left[\frac{-3rz}{(r^2+z^2)^{\frac{5}{2}}}\vec{e_r} + \frac{r^2-2z^2}{(r^2+z^2)^{\frac{5}{2}}}\vec{e_z}\right]\,. \tag{C.10}$$

There exist many possible ways for calculating the exact expression for the magnetic field from Eq. (C.7), including the expansion of $1/|\vec{r}-\vec{r'}|$ in terms of Legendre polynomials [54] or exploiting the cylindrical symmetry of the problem for an ansatz in terms of Bessel functions[2] [54]. Since there is no closed form of the solution for all regions in space, we briefly demonstrate yet another possibility based on direct (and partially numerical) evaluation of the integrals in the Poisson equation. Starting from Eq. (C.7), the exact result involves a contribution Φ_M^t from the top boundary surface (primed coordinates denote points on this surface) to Φ_M for a reference point (r, z) in the $x-z$ plane (i.e. $\phi = 0$) that contains an integral over r' of the form

$$\int_0^{R'} dr' \frac{r'}{\sqrt{r^2+(z-H)^2+r'^2-2rr'cos\phi'}}\,.$$

Performing the the r'-integration, leads to a complicated expression due to the presence of r' both in the numerator and denominator[3]. If we, however, choose to write $\vec{B} = \vec{\nabla} \times \vec{A}$ in order to automatically satisfy $\vec{\nabla}\cdot\vec{B} = 0$, we obtain via $\vec{\nabla}\times\vec{H} = \vec{\nabla}\times(\vec{B}/\mu_0 - \vec{M}) = 0$ a Poisson equation for $\vec{A}$, namely[4]

---

[2] We will briefly discuss this at the end of this chapter.

[3] The ϕ'-integration, in turn, results in Elliptic functions that are not of advantage.

$$\nabla^2\vec{A} = -\mu_0\vec{\nabla}\times\vec{M}\,. \tag{C.11}$$

Under the given boundary conditions, the solution again can be written as

$$\frac{4\pi}{\mu_0}\vec{A}(\vec{r}) = \int \frac{\vec{\nabla}'\times\vec{M}(\vec{r'})}{|\vec{r}-\vec{r'}|}d^3r' + \oint \frac{\vec{M}(\vec{r'})\times\vec{n'}}{|\vec{r}-\vec{r'}|}d^2r'\,,$$

involving a volume and a surface contribution. Since M = const., the first integral vanishes. The second term is now determined by the contribution from the *lateral* area of the cylinder and yields a ϕ-component (only) for $\vec{A}$ since $\vec{M}(\vec{r'})\times\vec{n'} = M\vec{e'_\phi}$. Again, straight forward algebra leads to the far-field result (C.10) that is now found via the rotation $\vec{\nabla}\times\vec{A}$ which makes the calculation slightly more involved.

In order to find the contribution of the surface term it suffices, because of symmetry, to consider a reference point in the $x-z$ plane such that $\vec{e_\phi} = \vec{e_y}$. Noting an additional factor $\cos\phi'$ due to the scalar product $\vec{e'_\phi}\cdot\vec{e_y}$) the according term reads

$$\frac{4\pi}{\mu_0}\vec{A}(\vec{r}) = M\int_0^{2\pi} R'\cos\phi' d\phi' \int_{-H}^{H} dz' \frac{1}{\sqrt{r^2+(z-z')^2+R'^2-2rR'cos\phi'}}\vec{e_\phi}\,. \tag{C.12}$$

Now, we can procede further by performing the z'-integration, that, after substituting $\zeta \overset{\text{def}}{=} z'-z$, yields (using $\int dx/\sqrt{C^2+x^2} = \operatorname{arsinh}(x/C)$, [55])

$$\begin{aligned}
\frac{4\pi}{\mu_0}\vec{A}(\vec{r}) &= MR'\int_0^{2\pi}\cos\phi' d\phi' \int_{-H}^{H} d\zeta \frac{1}{\sqrt{r^2+R'^2-2rR'cos\phi'+\zeta^2}} \\
&= MR'\int_0^{2\pi}\cos\phi' d\phi' \times \ldots \\
&\qquad \ldots\times\left[\operatorname{arsinh}\frac{H-z}{\sqrt{r^2+R'^2-2rR'cos\phi'}} - \operatorname{arsinh}\frac{-H-z}{\sqrt{r^2+R'^2-2rR'cos\phi'}}\right]\vec{e_\phi}\,.
\end{aligned}$$

From $\vec{H} = \vec{\nabla}\times\vec{A}/\mu_0$ we obtain the non-vanishing components of the magnetic field as $H_r = -\partial A_\phi/\mu_0\partial z$ and $H_z = A_\phi/\mu_0 r + \partial A_\phi/\mu_0\partial r$ resulting in

$$\begin{aligned}
H_r &= \frac{MR'}{4\pi}\int_0^{2\pi}\cos\phi' d\phi' \times\ldots \\
&\ldots\times\left[\frac{1}{\sqrt{r^2+R'^2-2rR'cos\phi'+(H-z)^2}} - \frac{1}{\sqrt{r^2+R'^2-2rR'cos\phi'+(H+z)^2}}\right]\vec{e_r} \\
H_z &= \frac{MR'}{4\pi r}\int_0^{2\pi}\cos\phi' d\phi' \times\ldots \\
&\ldots\times\left[\operatorname{arsinh}\frac{H-z}{\sqrt{r^2+R'^2-2rR'cos\phi'}} - \operatorname{arsinh}\frac{-H-z}{\sqrt{r^2+R'^2-2rR'cos\phi'}}\right] \\
&-\frac{MR'}{4\pi}\int_0^{2\pi}\cos\phi' d\phi' \frac{r-R'cos\phi'}{r^2+R'^2-2rR'cos\phi'}\times\ldots \\
&\left[\frac{H-z}{\sqrt{r^2+R'^2-2rR'cos\phi'+(H-z)^2}} - \frac{-H-z}{\sqrt{r^2+R'^2-2rR'cos\phi'+(H+z)^2}}\right]\,.
\end{aligned} \tag{C.13}$$

---

[4] We work in Coulomb gauge, $\vec{\nabla}\cdot\vec{A} = 0$.

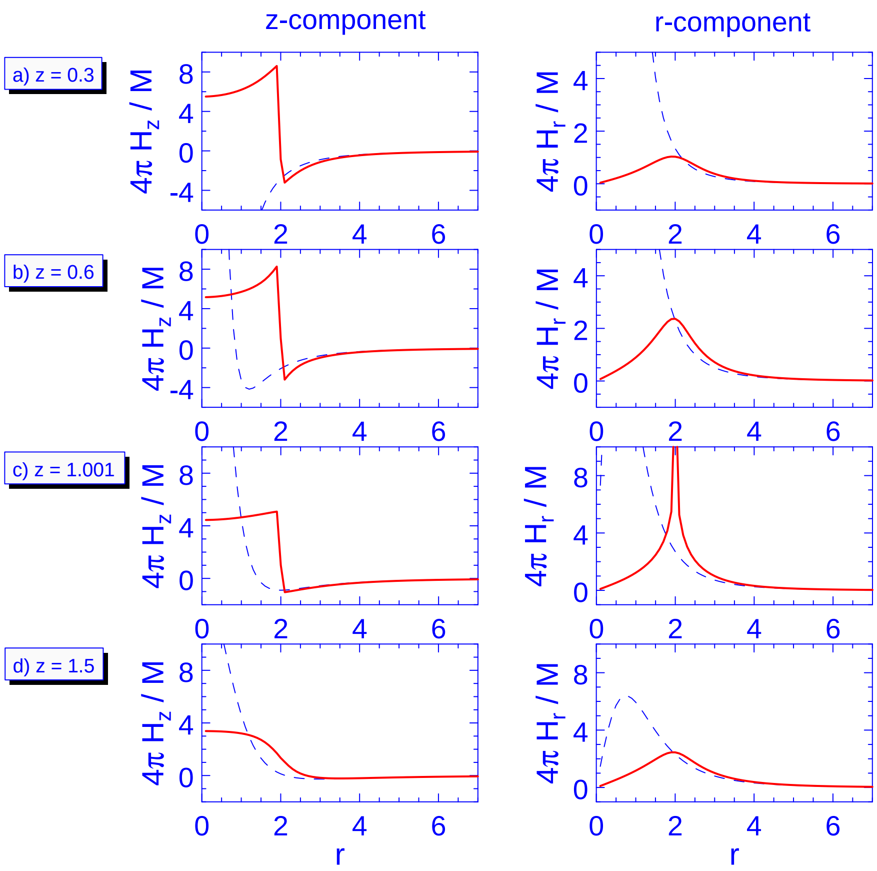

Figure C.3: Exact magnet field $\vec{H}$ (full lines) of a bar magnet of longitudinal magnetization M, height $2H$ and radius $R' = 2$ compared to a dipole field (dashed lines). Shown are the non-vanishing components H_z and H_r in scaled units as a function of the radial coordinate r for different reference planes $z = \text{const}$. Outside the magnet, the dipole result proves to be a reasonable approximation.

The exact result (C.13) and the dipole approximation (C.10) are compared in Fig. C.3. Whereas outside the bar magnet ($r > R'$) the dipole approximation describes the behaviour of the magnetic field resonably well, it clearly breaks down inside. The z-component H_z of the magnetic field jumps for $-H < z < H$ at the border of the bar magnet due to the jump in the magnetization, such that $\vec{B} = \mu_0(\vec{H} + \vec{M})$ changes continuously. The dipole approximation, of course, does not show this behaviour. The radial component H_r shows a maximum at $r = R'$ that becomes a singularity when $z = \pm H$.

For completeness, we give an expression for the magnetic field outside the bar magnet in terms of Bessel functions. One may start then from the ansatz for the *scalar* magnetic potential using [54]

$$\frac{1}{|\vec{r} - \vec{r'}|} = \frac{2}{\pi} \sum_{m=-\infty}^{\infty} \int_0^{\infty} dk e^{im(\phi - \phi')} \cos\left[k(z - z')\right] I_m(kr') K_m(kr) \,.$$

The result for $\vec{H} = H_r \vec{e_r} + H_z \vec{e_z}$,

$$H_r = 8MR' \int_0^{\infty} dk I_1 K_1(kr) \sin kz \, \sin kH \,,$$

$$H_z = -8MR' \int_0^\infty dk I_1 K_0(kr) \cos kz \, \sin kH \, , \tag{C.14}$$

is indeed absolutly equivalent to Eq. (C.13).

To judge the practical applicability of the dipole approximation we have to compare its prediction to the exact magnetic field at the position of the electrons, i.e., at the ring radius. The radius of the ring is several times ($\approx 2 \ldots 4$) greater then the radius of the micromagnet in typical experimental setups [35], such that we have to consider the far-field behaviour of the magnetic field. Although there exist major discrepancies between the two descriptions nearby and especially inside the micromagnet, see Fig. C.3, the far-field is rather well treated by the dipole approximation. For the geometrical situation realized in the experiment (Section 5.2) it is, therefore, sufficient to use the dipole picture.

D Parabolic cylinder functions

Parabolic cylinder functions $D_\nu(\gamma)$ are a special kind of confluent hypergeometric functions [124]. For real positive argument γ there exist simple relations to the modified Bessel function K of second kind, for example [124]

$$D_{-1/2}(\gamma) = \sqrt{\frac{x}{2\pi}} K_{1/4}\left(\frac{1}{4}\gamma^2\right) \, . \tag{D.1}$$

However, according to Eq. (8.3) the parabolic cylinder functions $D_\nu(\gamma)$ have to be evaluated at *complex* argument $\beta_0 = ink\sigma\Delta \overset{\text{def}}{=} iz$ with z real and positive[5]. The relation to real arguments is provided by [124]

$$D_{-\nu-1}(iz) = \frac{\Gamma(-\nu)}{\sqrt{2\pi}} e^{i\frac{\pi}{2}(\nu+1)} \left[D_\nu(z) - e^{-i\pi\nu} D_\nu(-z)\right] \tag{D.2}$$

where $\Gamma(\nu)$ is the Γ-function. While for real *positive* arguments the relation of the $D_\nu(z)$ to modified Bessel functions $K_{\nu'}(\gamma')$ is given in many textbooks [124] in the form of Eq. (D.1), these relations do not hold for real negative arguments of D_ν since the modified Bessel function K is not defined on the negative real axis. Furthermore, often *positive* arguments are *implicitely* used without notifying the restricted range of validity. We generalized the result to negative arguments and cross-checked the resulting formula with exact results obtained from "Mathematica". Without going into further detail, the following generalized equation for $D_{-1/2}$ was obtained (with $I_{\nu'}(\gamma')$ the modified Bessel function of the first kind)

$$D_{-1/2}(\pm z) = \frac{\sqrt{\pi z}}{2} \left[I_{-1/4}\left(\frac{z^2}{4}\right) \mp I_{1/4}\left(\frac{z^2}{4}\right)\right] \, . \tag{D.3}$$

Note that only positive arguments allow to write this equation in the form of Eq. (D.1)!

The results for $D_{1/2}$ and $D_{-3/2}$ are obtained from Eq. (D.3) by applying the recursion formulas for parabolic cylinder functions.

---

[5] This holds for angles of incidence larger than the critical angle, $\chi > \chi_c$. For $\chi < \chi_c$ a relation similar to Eq. (D.2) holds, confirm [124]

Bibliography

[1] Y. Aharonov, D. Bohm, Phys. Rev. **115** 485 (1959)

[2] M. V. Berry, Proc. R. Soc. Lond. A **392** (1984) 45

[3] A. Betat, V. Frette, I. Rehberg, Phys. Rev. Lett. **83** 88 (1999)

[4] M. Büttiker, Y. Imry, R. Landauer, Phys. Lett. **96A** 365 (1985)

[5] R. Akis, D. K. Ferry, Phys. Rev. B **59** 7529 (1999)

[6] J. Stein, H.-J. Stöckmann, Phys. Rev. Lett. **68** 2867 (1992)

[7] Y. Aharonov, J. Anandan, Phys. Rev. Lett. **58** 159 (1987)

[8] A. Shapere, F. Wilczek (editors): Geometric Phases in Physics, World Scientific, Singapore 1989

[9] M. Born, V. Fock, Z. Phys. **51** 165 (1928)

[10] A. C. Maggs, arXiv:cond-mat/0009182 (2000)

[11] S. Pancharatnam: Collected works of S. Pancharatnam, Oxford University Press 1975

[12] A. B. Ruffin, J. V. Rudd, J. F. Whitaker, S. Feng, H. G. Winful, Phys. Rev. Lett. **83** 3410 (1999); and references therein

[13] D. Dubbers, Physica B & C **151** 93 (1988)

[14] R. Chiao, Y.-S. Wu, Phys. Rev. Lett. **57** 933 (1986); A. Tomita, R. Chiao, Phys. Rev. Lett. **57** 937 (1986)

[15] M. V. Berry, J. Phys. A **18** 15 (1985)

[16] M. Nakahara: Geometry, Topology, and Physics, Institute of Physics Publishing, London 1990

[17] D. C. Brody, L. P. Hughston, J. Geom. Phys. **38** 19 (2001)

[18] T. W. B. Kibble, Commun. Math. Phys. **64** 73 (1978); Commun. Math. Phys. **65** 189 (1979)

[19] P. de los Rios, N. Manani, E. Tosatti, Phys. Rev. B **54** 7157 (1996)

[20] P. Facchi, A. G. Klein, S. Pascazio, L. S. Schulman, arXiv:quant-ph/9903102 (1999)

[21] J. Pachos, P. Zanardi, M. Rasetti, Phys. Rev. A **61** 010305(R) (2000); A. Blais, A.-M. S. Trembley, arXiv:quant-ph/0105006 (2001)

[22] S. Datta: Electronic Transport in Mesoscopic Systems, Cambridge University Press 1995

[23] T. Chakraborty, P. Pietiläinen: The quantum Hall effects: Integral and Fractional, Springer Series in Solid State Sciences **85**, Springer, Berlin, Second Edition 1995

[24] M. Imada, A. Fujimori, Y. Tokura, Rev. Mod. Phys. **70** 1039 (1998)

[25] A. F. Morpurgo, J. P. Heida, T. M. Klapwijk, B. J. van Wees, G. Borghs, Phys. Rev. Lett. **80** 1050 (1998)

[26] M. Persson, J. Pettersson, B. von Sydow, P. E. Lindelof, A. Kristensen, K. F. Berggren, Phys. Rev. B **52** 8921 (1995); S. Pedersen, A. E. Hansen, A. Kristensen, C. B. Sørensen, P. E. Lindelof, Phys. Rev. B **61** 5457 (2000)

[27] M. Büttiker, Y. Imry, M. Ya. Azbel, Phys. Rev. A **30** 1982 (1984)

[28] M. Büttiker, Y. Imry, R. Landauer, Phys. Lett. **96A** 365 (1983)

[29] Y. Aharonov, E. Ben-Reuven, S. Popescu, D. Rohrlich, Phys. Rev. Lett. **65** 3065 (1990)

[30] A. Stern, Phys. Rev. Lett. **68** 1022 (1992)

[31] Y. Aharonov, A. Casher, Phys. Rev. Lett. **53** 319 (1984)

[32] D. Loss, P. M. Goldbart, A. V. Balatsky, Phys. Rev. Lett. **65** 1655 (1990); D. Loss, H. Schoeller, P. M. Goldbart, Phys. Rev. B **48** 15218 (1993)

[33] S. A. van Langen, H. P. A. Knops, J. C. J. Paasschens, C. W. J. Beenakker, Phys. Rev. B **59** 2102 (1999)

[34] Y. Yi, T. Qian, Z. Su, Phys. Rev. B **55** 10631 (1997)

[35] P. D. Ye, S. Tarucha, D. Weiss, Proceedings of the EP2DS, Jerusalem (1998)

[36] W. Nolting: Grundkurs Theoretische Physik, Band 5, Verlag Vieweg, Braunschweig, Wiesbaden, 4. Aufl. 1997

[37] M. V. Berry: The quantum phase, five years after, in [8]

[38] R. Jackiw, Int. J. Mod. Phys. A **3** 285 (1988)

[39] D. Frustaglia, K. Richter, arXiv:cond-mat/0011161 (2000)

[40] D. Frustaglia, M. Hentschel, K. Richter, submitted to Phys. Rev. Lett.

[41] D. Frustaglia, PhD thesis, Technical University of Dresden (2001)

[42] R. Fiederling et al., Nature **402** 787 (1999); Y. Ohno et al., Nature **402** 790 (1999); P. R. Hammar, et al., Phys. Rev. Lett. **83** 203 (1999); C.-M. Hu et al., Phys. Rev. B **63** 125333 (2001)

[43] G. A. Prinz, Science **282** 1660 (1998)

[44] J. M. Kikkawa, D. D. Awschalom, Nature **397** 139 (1999)

[45] S. Das Sarma, J. Fabian, X. Hu, I. Žutić, arXiv:cond-mat/9912040 (1999), Superlattice. Microst. **27** 289 (2000)

[46] S. Datta, B. Das, Appl. Phys. Lett. **56** 665 (1990)

[47] M. J. Gilbert, J. P. Bird, Appl. Phys. Lett. **77** 1050 (2000)

[48] D. Loss, D. P. DiVincenzo, Phys. Rev. A **57** 120 (1998)

[49] A. Imamoglu et al., Phys. Rev. Lett. **83** 4204 (1999)

[50] A. Nogaret, S. J. Bending, M. Henini, Phys. Rev. Lett. **84** 2231 (2000)

[51] J. A. Katine, F. J. Albert, R. A. Buhrmann et. al. Phys. Rev. Lett. **84** 3149 (2000)

[52] D. K. Ferry, S. M. Goodnick, Transport in Nanostructures, Cambridge University Press 1997; D. J. Thouless, S. Kirkpatrick, J. Phys. C **14** 235 (1981)

[53] A. Sommerfeld: Lectures on Theoretical Physics, Vol. III, Academic Press, New York 1952

[54] J. D. Jackson: Classical Electrodynamics, John Wiley & Sons, New York, Second Edition 1975

[55] I. N. Bronstein, K. A. Semendjajew, G. Musiol, H. Mühlig: Taschenbuch der Mathematik, Verlag Harry Deutsch, Thun, Frankfurt am Main, 2. Auflage 1995

[56] I. S. Gradshteyn, I. M. Ryzhik, A. Jeffrey (editor): Table of integrals, series, and products, Academic Press, San Diego 1994

[57] H.-J. Stöckmann: Quantum Chaos, Cambridge University Press 1999

[58] C. M. Marcus, A. J. Rimberg, R. M. Westervelt, P. F. Hopkins, A. C. Gossard, Phys. Rev. Lett. **69** 506 (1992); Y. Alhassid, Rev. Mod. Phys. **72** 895 (2000)

[59] H. J. Stöckmann, J. Stein, Phys. Rev. Lett. **64** 2215 (1990)

[60] M. L. Mehta: Random Matrices, Academic Press, New York, Second Edition 1991

[61] F. Haake: Quantum Signatures of Chaos, Springer, Berlin 1991

[62] T. Guhr, A. Müller-Groeling, H. A. Weidenmüller, Phys. Rep. **299** 190 (1998)

[63] A. J. Campillo, J. D. Eversole, H. B. Lin, Phys. Rev. Lett. **67** 437 (1991); S. Schiller, R. L. Byer, Opt. Lett. **16** 1138 (1991)

[64] W. von Klitzing, R. Long, V. S. Ilchenko, J. Hare, V. Lefèvre-Seguin, arXiv:quant-ph/0011102 (2000)

[65] V. V. Klimov, M. Ducloy, V. S. Letokhov, Phys. Rev. A **59** 2996 (1999)

[66] T. A. Brun, H. Wang, Phys. Rev. A **61** 032307 (2000)

[67] G. C. Chen, M. M. Mazumber, R. K. Chang, J. C. Swindal, W. P. Acker, Prog. Energy. Combust. Sci. **22** 8010 (1997)

[68] M. Cai, O. Painter, K. J. Vahala, Phys. Rev. Lett. **85** 74 (2000)

[69] S. A. Backes, A. P. Heberle, J. R. A. Cleaver, K. Koehler, Phys. stat. sol. (b) **204** 581 (1997)

[70] M. Berry, Nature **403** 21 (2000)

[71] J. Sainhas, R. Dilão, Phys. Rev. Lett. **80** 5216 (1998)

[72] S. G. Lipson, H. Lispon, D. S. Tannhauser: Optical Physics, Cambridge University Press, Third Edition 1995

[73] C. W. J. Beenakker, Rev. Mod. Phys. **69** 731 (1997)

[74] P. B. Wilkinson, T. M. Fromhold, R. P. Taylor, A. P. Micolich, Phys. Rev. Lett. **86** 5466 (2001)

[75] L. E. Reichl: The Transition to Chaos, Springer, New York 1992

[76] M. C. Gutzwiller: Chaos in Classical and Quantum Mechanics, Springer, New York 1990

[77] D. Ullmo, M. Grinberg, S. Tomsovic, Phys. Rev. E **54** 136 (1996)

[78] C. Dembowski, H.-D. Gräf, A. Heine, T. Hesse, H. Rehfeld, A. Richter, Phys. Rev. Lett. **86** 3284 (2001)

[79] C. Dembowski, H.-D. Gräf, A. Heine, R. Hofferbert, H. Rehfeld, A. Richter, Phys. Rev. Lett. **84** 867 (2000)

[80] O. Brodier, P. Schlagheck, D. Ullmo, arXiv:nlin.CD/0104010 (2001)

[81] E. J. Heller, Phys. Rev. Lett. **53** 1515 (1984); E. B. Bogomolny, Physica D **31** 169 (1988); M. V. Berry, Proc. R. Soc. Lond. A **432** 219 (1989)

[82] S.-B. Lee, J.-H. Lee, J.-S. Chang, H. J. Moon, S. W. Kim, K. An, arXiv:physics/0106031 (2001)

[83] N. B. Rex, H. E. Tureci, H. G. L. Schwefel, R. K. Chang, A. D. Stone, arXiv:physics/0105089 (2001)

[84] I. Braun, G. Ihlein, F. Laeri, J. U. Nöckel, G. Schulz-Ekloff, F. Schüth, U. Vietze, Ö. Weiß, D. Wöhrle, Appl. Phys. B **70** 335 (2000)

[85] J. Faist, F. Capasso, D. L. Sivco, C. Sirtori, A. L. Hutchinson, A. Y. Cho, Science **264** 553 (1994)

[86] M. Robnik, M. V. Berry, J. Phys. A **18** 1361 (1985)

[87] A. N. Kolmogorov, Dokl. Akad. Nauk SSSR **98** 527 (1954); V. I. Arnold, Soviet Math. Dokl. **2** 501 (1961); J. Moser, Nachr. Akad. Wiss. Göttingen II, Math. Phys. Kl., 1 (1962)

[88] J. Greene, J. Math. Phys. **20** 1183 (1979)

[89] A. W. Snyder, J. D. Love: Optical waveguide theory Chapman & Hall Medical, London, Weinheim, New York, First Edition 1983

[90] W. Macke: Wellen, Akademische Verlagsgesellschaft Geest & Portig, Leipzig 1962

[91] B. R. Johnson, J. Opt. Soc. Am. **10** 343 (1993)

[92] E. Doron, U. Smilansky, Nonlinearity **5** 1055 (1992)

[93] J. R. Taylor: Scattering Theory, Robert E. Krieger Publishing Company, Malabar (Florida) 1983

[94] R. G. Newton: Scattering Theory of Waves and Particles, Springer, New York, Heidelberg, Berlin, Second Edition 1982

[95] Y. V. Fyodorov, H.-J. Sommers, J. Math. Phys. **38** 1918 (1997)

[96] W. I. Smirnov: Lehrgang der höheren Mathematik, Teil III(2), Deutscher Verlag der Wissenschaften, Berlin 1955

[97] U. Smilansky, in: Mesoscopic Quantum Physics, Les Houches, Session LXI 1994 (Editors: E. Akkermans, G. Montambaux, J. L. Pichard, J. Zinn-Justin)

[98] R. B. Melrose: Geometric scattering theory, Cambridge University Press 1995

[99] A. Kohler, R. Blümel, Ann. Phys. **267** 249 (1998); A. Kohler, R. Blümel, Phys. Lett. A**238** 271 (1998)

[100] O. Bohigas, D. Boosé, R. Egydio de Carvalho, V. Marvulle, Nucl. Phys. **A560** 197 (1993)

[101] S. D. Frischat, E. Doron, Phys. Rev. Lett. **75** 3661 (1995); Phys. Rev. E **57** 1421 (1998)

[102] A. Bäcker, PhD thesis, University of Ulm (1998)

[103] R. Schubert, PhD thesis, University of Ulm (2001)

[104] J. Kurchan, P. Leboeuf, M. Saraceno, Phys. Rev. A **40** 6800 (1989)

[105] R. Ketzmerick, L. Hufnagel, F. Steinbach, M. Weiss, Phys. Rev. Lett. **85** 1214 (2000)

[106] M. P. Ioannidou, D. I. Bakatsoula, D. P. Chrissoulidis, J. Quant. Spectrosc. Ra. **63** 585 (1999)

[107] G. Hackenbroich, J.-U. Nöckel, Europhys. Lett. **39** 371 (1997)

[108] J. U. Nöckel, PhD thesis, Yale University (1997)

[109] A. W. Snyder, J. D. Love, IEEE Transactions on microwave theory and techniques MTT **23** 134 (1975)

[110] Y. Z. Ruan, L. B. Felsen, J. Opt. Soc. Am. A **3** 550 (1986)

[111] N. C. Fraetschi, A. F. J. Levi, Appl. Phys. Lett. **66** 2932 (1995); J. Appl. Phys. **80** 644 (1996)

[112] J. J. Monzón, L. L. Sánchez-Soto, arXiv:physics/0105013 (2001)

[113] A. L. Cullen, Ann. Télécommunic. **31** 359 (1976)

[114] N. Fiedler-Ferrari, H. M. Nussenzweig, W. J. Wiscombe, Phys. Rev. A **43** 1005 (1991)

[115] T. Kudou, M. Yokota, O. Fukumitsu, Electron. Lett. **24** 1520 (1988)

[116] F. Goos, H. Hänchen, Ann. Physik **1** 333 (1947)

[117] K. Artmann, Ann. Physik **8** 270 (1951)

[118] H. M. Lai, F. C. Cheng, W. K. Tang, J. Opt. Soc. Am. A **3** 550 (1986)

[119] B. R. Horowitz, T. Tamir, J. Opt. Soc. Am. **61** 586 (1971)

[120] H. K. V. Lotsch, Optik **32** 116 (1970); 189 (1970); 299 (1971); 553 (1971)

[121] D. Chauvat, O. Emile, F. Bretenaker, A. Le Floch, Phys. Rev. Lett. **84** 71 (2000)

[122] A. E. Siegmann: Lasers, University Science Books, Sausalito 1986

[123] W. H. Press et al.: Numerical Recipes in C, Cambridge University Press 1992

[124] W. Magnus, F. Oberhettinger, R. P. Soni: Formulas and Theorems for the Special Functions of Mathematical Physics, Third enlarged Edition, Springer, Berlin, Heidelberg 1966

[125] D. Q. Chowdhury, D. H. Leach, R. K. Chang, J. Opt. Soc. Am. A **11** 1110 (1994)

[126] J. Herb, P. Meerwald, M. J. Moritz, H. Friedrich, Phys. Rev. A **60** 853 (1999)

[127] M. Hentschel, J. U. Nöckel, in: Quantum Optics of Small Structures (Editors: D. Lenstra, T. D. Visser, K. A. H. van Leeuwen), Edita KNAW (2000)

[128] M. Hentschel, H. Schomerus, in preparation

[129] R. Hofferbert, PhD thesis, Technical University of Darmstadt (1999)

[130] A. W. Poon, P. A. Tick, D. A. Nolan, R. K. Chang, submitted to Opt. Lett., A. W. Poon, R. K. Chang, private communication

[131] J. A. Lock, C. L. Adler, B. R. Stone, P. D. Zajak, Appl. Optics **37** 1527 (1998)

[132] J. U. Nöckel, A. D. Stone, Nature **385** 45 (1997)

[133] M. V. Berry, Eur. J. Phys. **2** 91 (1981)

[134] M. Hentschel, M. Vojta, submitted to Opt. Lett.

[135] C. Gmachl, F. Capasso, E. E. Narimanov, J. U. Nöckel, A. D. Stone, J. Faist, D. L. Sivco, A. Y. Cho, Science **280** 1556 (1998)

[136] M. F. Booth, A. Schremer, J. M. Ballantyne, Appl. Phys. Lett. **76** 1095 (2000)

[137] H. Heidrich, M. Hentschel, D. G. Rabus, M. Hamacher, K. Richter, Patent application filed at 3rd of July, 2001 under filing number DE 101 32 479.0 (Deutsches Patent- und Markenamt, Germany)

[138] L. A. Bunimovich, Commun. Math. Phys. **65** 295 (1979)

[139] T. Harayama, P. Davis, Phys. Rev. Lett. **82** 3803 (1999)

[140] H. Schomerus, K. M. Frahm, M. Patra, C. W. J. Beenakker, Physica A **278** 469 (2000)

[141] V. M. Babič, V. S. Buldyrev: Short-wavelength diffraction theory: Asymptotic methods, Springer, Berlin, Heidelberg, 1991

Acknowledgements

First of all I would like to thank Prof. Klaus Richter for his supervision in the last years, and for introducing me to mesoscopic physics and quantum chaos. He always found the time to answer my questions. I thank Prof. Peter Fulde for giving me the possibility to write my PhD thesis at the Max-Planck-Institut für Physik komplexer Systeme in Dresden. The institute's financial support allowed me to attend several conferences and summer schools. I thank Dr. Jens-Uwe Nöckel for pointing out interesting questions in the context of optical systems.

My special thanks go to Prof. Uzy Smilansky for his help and advice that stimulated the second part of the work. I thank Dr. Holger Schanz for his patience in answering the never ending flood of questions. The same applies to Dr. Henning Schomerus who helped me with fruitful discussions on various subjects. I thank Prof. Shmuel Fishman for suggesting a systematic study of annular geometries, as well as Prof. Michael Berry, Prof. Thomas Dittrich, Prof. Bruno Eckhardt, Dr. Roman Schubert, Dr. Martin Sieber and Prof. Hans-Jürgen Stöckmann for useful discussions and advice.

Thanks are due to Diego Frustaglia, Dr. Helmut Heidrich, Dr. Klaus Hornberger, Dr. Sang Wook Kim, Dominik Rabus, Prof. Ingrid Rotter, Dr. Peter Schlagheck, Dr. Gisela Timmermann, Dr. Jan Wiersig, and Dr. Oleg Yevtushenko for stimulating discussions and help. I thank Prof. Douglas Stone and Prof. Richard Chang from Yale University as well as Prof. Uzy Smilansky from the Weizmann Institute for their hospitality.

My thanks go to all colleagues from the institute for their help on a variety of things, including literature supply, flight booking, bicycle repairs, increasing the disk quota, or proof-reading parts of the manuscript. In particular I thank Christian Siedschlag for sharing the office.

Especially I would like to thank my family, my mother and father, my brother Heiko and my sister Kristina, and my grand mother, who encouraged me throughout the last years with their confidence and support. With Matthias I enjoyed weekends in New York and much more. I thank my friends for their understanding, help, and wonderful experiences not only in the mountains.

Versicherung

Hiermit versichere ich, daß ich die vorliegende Arbeit ohne unzulässige Hilfe Dritter und ohne Benutzung anderer als der angegebenen Hilfsmittel angefertigt habe; die aus fremden Quellen direkt oder indirekt übernommenen Gedanken sind als solche kenntlich gemacht. Die Arbeit wurde bisher weder im Inland noch im Ausland in gleicher oder ähnlicher Form einer anderen Prüfungsbehörde vorgelegt.

Die Arbeit wurde am Max-Planck-Institut für Physik komplexer Systeme in der Nachwuchsgruppe Quantenchaos und mesoskopische Systeme angefertigt und von Prof. Klaus Richter und Prof. Peter Fulde betreut.

Ich erkenne die Promotionsordnung der Fakultät Mathematik und Naturwissenschaften der Technischen Universität Dresden vom 20. März 2000 an.